Interactions between downslope flows and a developing cold-air pool

Paul Burns

Centre for Atmospheric & Instrumentation Research (CAIR)

School of Physics, Astronomy and Mathematics (PAM)

University of Hertfordshire

submitted to the University of Hertfordshire in partial fulfilment of the requirements of the degree of PhD

Doctor of Philosophy

June 2014

I would like to dedicate this thesis to my family.

Abstract

Downslope flows and regions of enhanced cooling have important impacts on society and the environment. Parameterisation of these often subgrid-scale phenomena in numerical models requires a sound understanding of the underlying physical processes, which has been the overarching aim of this work. A numerical model has been used to characterise the development of a region of enhanced cooling in an idealised alpine valley with width and depth of order 10 and 1 km, respectively, under stable, decoupled, poorly-drained conditions. A focus of this work has been to remove the uncertainty surrounding the forcing mechanisms behind the development of regions of enhanced cooling. The average valley-atmosphere cooling has been found to be almost equally partitioned between radiative and dynamics effects. Complex interactions between the downslope flows and the region of enhanced cooling have been quantified for the first time. For example, relatively large variations in the downslope flows are generally restricted to the region of enhanced cooling and cannot solely be attributed to the analytical model of [McNider, 1982a]. These flow variations generally coincide with return flows above the downslope flows, where a thin region of unstable air occurs, as well as coinciding with elongated downslope flow structures. The impact of these interactions on the dispersion of passive pollutants has been investigated. For example, pollutants are generally trapped within the region of enhanced cooling. The concentration of pollutants within the region of enhanced cooling, emitted over the lower half of the slopes, increase as the emission source moves away from the ground-based inversion that expands from the bottom of the valley. The concentration of pollutants within the region of enhanced cooling is very similar when varying the location of the emission source over the top half of the valley slopes. This work includes a test of the effects of varying the horizontal numerical grid resolution on average valley-atmosphere temperature changes.

Acknowledgements

In particular I would like to acknowledge the contribution of my principal supervisor Charles Chemel, whose efforts and energy have significantly improved this document and helped to make the experience of creating it rewarding and enjoyable. I would also like to acknowledge the support of my family and friends as well as the useful discussions had with colleagues at the University of Hertfordshire, especially those members of the CAIR (Centre for Atmospheric & Instrumentation Research) and PAM (School of Physics, Astronomy and Mathematics) community, all of which was important and much appreciated. This work has made use of the University of Hertfordshire, Science and Technology Research Institute, high-performance computing facility.

Table of contents

I

Main Introduction

In essence this study considers the downward flows of relatively dense air that form adjacent to sloping landforms, such as hills and mountains (complex terrain), and the development of regions of enhanced cooling towards the bottom of topographic depressions. In small-scale terrain, such as hill environments, the regions of enhanced cooling are equivalent to regions of relatively cold air, commonly referred to as cold-air pools (CAPs), with the reference points often taken as the air temperatures immediately above the depressions [e.g. Gustavsson *et al.*, 1998].

The term 'downslope flow' will be used hereafter to refer to the currents of dense air that flow down the sides of complex terrain. The term will exclude the larger-scale flows along valley axes and through complex systems of valleys and other landforms, which will be called 'down-valley winds' and 'drainage flows', respectively. The term 'katabatic wind' is reserved here for the large-scale flows that can be found moving down the Earth's major glaciers, such as those of Antarctica and Greenland. It is acknowledged that this nomenclature might not be universally accepted, however, it ensures consistent terminology in this document.

Figure I.1 illustrates a downslope and down-valley flow (denoted by u_s and u_y, respectively), as well as a CAP or region of enhanced cooling. The top schematic of Fig. I.1 shows the early onset of downslope flows and the typical circulations that result in order to conserve mass. Figure I.1 is an over-simplification of the system, even when considering idealised examples, and is used here mainly to illustrate the key terms defined above. The detail of Fig. I.1 approximates what can generally be found in standard texts on the subject [e.g. Whiteman, 2000].

Downslope flows form essentially due to a net loss of longwave radiation from the ground surface to space, cooling the surface, which in turn cools the atmosphere immediately adjacent to the surface. Over sloping terrain this creates a horizontal temperature gradient and so a horizontal pressure gradient, with higher pressures occurring with lower temperatures [e.g. Fleagle, 1950; Zardi & Whiteman, 2013]. Conceptually, parcels of air are forced horizontally away from the ground surface, soon finding themselves amongst lighter neighbours, before being drawn downslope by gravity.

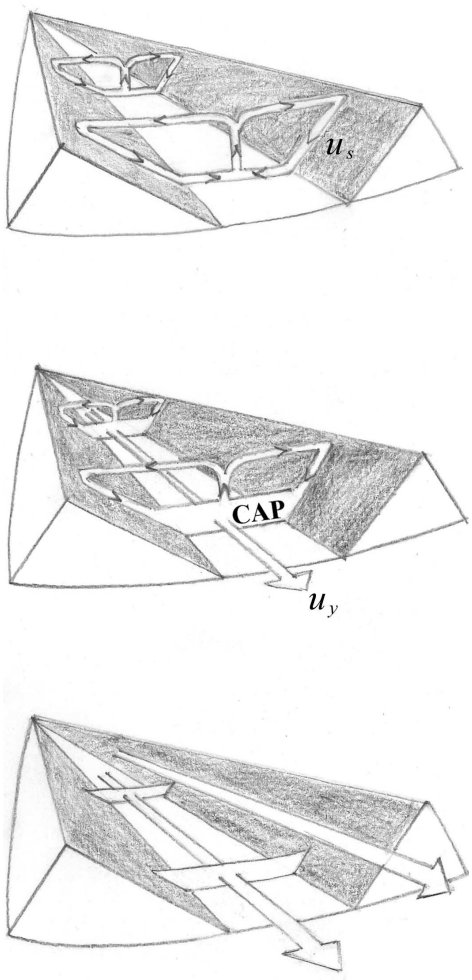

Figure I.1: Schematic showing downslope flows (denoted by u_s), down-valley winds (denoted by u_y), and a cold-air pool (denoted by CAP) or region of enhanced cooling. The schematic shows the early onset of downslope flows and the resulting circulations (top figure), the development of a region of enhanced cooling that may co-exist with downslope and down-valley flows (middle figure), and the possible situation where u_s and the region of enhanced cooling have been generally eroded/destroyed by a strengthening along-valley flow (bottom figure). The schematic is an over-simplification of the system, even when considering idealised examples, and is used here mainly to illustrate key terms. The apparent increasing valley width is deceptive and in fact a perspective effect. In nature valley configurations include those with either near-constant widths and those with increasing widths in the down-valley direction (see text for examples). The schematic has been adapted from Defant [1949, 1951].

The middle schematic of Fig. I.1 shows the development of a region of enhanced cooling that may co-exist with downslope and down-valley flows [e.g. Whiteman & Zhong, 2008]. Down-valley flows are often part of a larger mountain-to-plain flow system, which forms due to pressure and gravitational forces. Complex terrain cools the atmosphere above it more effectively than a plain creating a pressure difference between the two landforms, inducing air flows. The relatively dense air that forms

in complex terrain is also forced downslope towards the plain by gravity. These low-level mountain-to-plain flows are often accompanied by higher-level return plain-to-mountain flows (not shown in Fig. I.1), in order to conserve mass [e.g. Whiteman, 2000; Zardi & Whiteman, 2013]. The apparent increasing valley width, in Fig. I.1, is deceptive and in fact a perspective effect. The observation campaigns discussed by Neff & King [1989]; Eckman [1997]; Chazette *et al.* [2005]; Whiteman & Zhong [2008]; Price *et al.* [2011] provide examples of valleys with near-constant widths. There are also many examples of increasing valley widths in the down-valley direction [e.g., see Neff & King, 1989; Price *et al.*, 2011].

The bottom schematic of Fig. I.1 shows the possible situation where u_s and the region of enhanced cooling have been eroded/destroyed by a strengthening along-valley flow [e.g. Whiteman & Zhong, 2008]. The above description does not account for air flows intruding into the complex-terrain atmosphere from the 'free atmosphere' above. Such intrusions can occur, for example, due to geostrophic wind systems, passing fronts, mountain waves, upper-level disturbances [e.g. Whiteman, 2000], seabreezes and marine-air intrusions. These mesoscale and synoptic systems and effects can also erode and destroy downslope flows and regions of enhanced cooling (as well as down-valley flows). Mesoscale and synoptic systems are flow systems with length scales of the order of 10 to 100 km, and 1000 km, respectively. The degree to which these larger-scale non-local systems force the complex-terrain atmosphere is largely controlled by the size of the forcing (e.g. wind speeds), and how well the complex-terrain atmosphere is shielded from these larger-scale systems. The latter is controlled largely by the configuration of the terrain (scale, shape and orientation), and the possible existance of stable layers of air towards the top of the complex-terrain atmospheres. Conditions that exist when complex-terrain atmospheres are not forced by the ambient free-atmosphere above are termed decoupled conditions.

The development of downslope flows and regions of enhanced cooling favour clear-sky conditions, which maximise the loss of longwave radiation to space, increasing the cooling of the ground surface and the atmosphere above. Clear and calm conditions often occur under anticyclonic conditions [e.g. Zardi & Whiteman, 2013].

The topics introduced above are part of the larger subject of mountain meteorology, which also considers daytime upslope flows and the two transition periods. These transition periods often occur close to local sunrise (when slope flows reverse from downslope to upslope) and local sunset (when slope flows reverse from upslope to downslope). The wind systems described above are sometimes refered to as 'thermal winds' [e.g. Whiteman, 2000; Zardi & Whiteman, 2013].

I.1 Motivations

It has been estimated that complex terrain covers 34 % of Earth's land surface (excluding the Antarctic and Greenland glaciers), directly supporting some 39 % of the growing global human population [Maybeck *et al.*, 2001]. Those people not living in these environments may nevertheless partially depend upon them, for example, for a wide range of goods and services including water and energy resources, for biodiversity maintenance, as well as for recreational opportunities [Blyth *et al.*, 2002].

Slope flows and regions of enhanced cooling create a number of challenges and perhaps opportunities for society. They must be accounted for in order to achieve more accurate weather predictions within complex terrain regions, and most likely to achieve more accurate weather predictions outside of these regions [Noppel & Fiedler, 2002; Price *et al.*, 2011]. An improved forecast capability for complex terrain regions has a number of important applications.

A more accurate description of the structure and evolution of the atmosphere, within complex terrain, has the potential to improve the management of airborne pollutants, which pose a serious threat to both people and the environment [Anquetin *et al.*, 1999; Brulfert *et al.*, 2005; Chazette *et al.*, 2005; Szintai *et al.*, 2010]. Malek *et al.* [2006] investigated one of the worst air pollution episodes in the US that occurred on 15 January 2004 in Logan (Utah), a settlement of approximately 100,000 people located in the Cache Valley, which has a width of approximately 50 km and a depth of about 1370 m. Instantaneous concentrations of particulate matter with a diameter less than 2.5 μm [$PM_{2.5}$, i.e., small solid and liquid particles (excluding water vapour), also known as aerosols, from natural and anthropogenic sources], were found to be comparable to $PM_{2.5}$ concentrations recorded during previous wild fire events.

The potential health effects of $PM_{2.5}$ are well documented and include respiratory and cardiovascular morbidity, such as aggravation of asthma, respiratory symptoms and an increase in hospital admissions, mortality from cardiovascular and respiratory diseases and from lung cancer [World Health Organisation, 2013]. Long-term exposure to $PM_{2.5}$ is associated with an increase in the long-term risk of cardiopulmonary mortality by 6 to 13 % per 10 μg m^{-3} of $PM_{2.5}$ [Pope *et al.*, 2002; Beelen *et al.*, 2008]. Susceptible groups with pre-existing lung or heart disease, as well as elderly people and children, are particularly vulnerable. For example, exposure to PM affects lung development in children, including reversible deficits in lung function as well as chronically reduced lung growth rate and a deficit in long-term lung function [World Health Organisation, 2013].

The pollution event in Logan was essentially caused by the production of $PM_{2.5}$ by acid-based reactions between gas-phase precursors from vehicle emissions and livestock, and the trapping of this pollutant close to the ground surface by long-lived

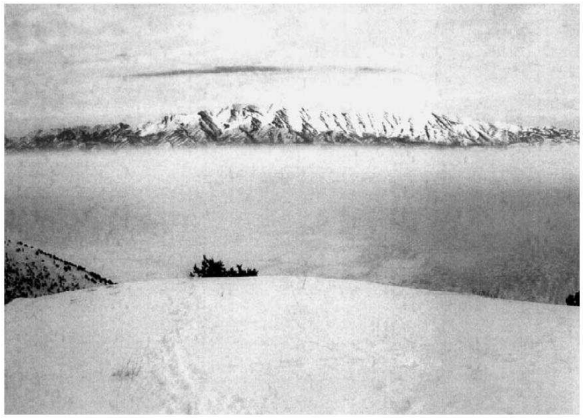

Figure I.2: Photograph looking westward across the 50-km wide, 1370-m deep Cache Valley in Utah, USA, from the eastern valley slopes on 6 February 2004. A stable layer containing the trapped pollutants obscuring the ground surface can be seen towards the valley bottom. Visual investigations indicated that the layer top was 250–350 m above the valley floor [reproduced from Malek *et al.*, 2006].

stable layers. The field campaign was restricted to near-surface measurements only and so the spatial and temporal evolution of pollutants higher in the valley atmosphere [$>$ 2 m above ground level (a.g.l.)] can only be implied. Figure I.2 shows a photograph looking westward across the Cache Valley taken from the eastern valley slopes on 6 February 2004. A stable layer containing the trapped pollutants obscuring the ground surface can be seen towards the valley bottom. Visual field investigations indicated that the layer top was 250–350 m above the valley floor. It would be useful to carry out a more in-depth study of the evolution of the Cache Valley winter atmosphere.

More accurate weather predictions in complex terrain would enhance road transport and aviation safety, particularly within complex terrain, where snow and ice covered roads, low-level cloud and fog, as well as the occurrence of atmospheric icing conditions (all affected by slope flows and regions of enhanced cooling), pose a serious hazard. This presumably has significant economic effects; however, the subject is not well represented in the scientific literature.

The accurate prediction of near-surface air temperatures, frost and snow in complex terrain, would help to create a more sustainable agricultural industry by preventing the loss, or damage, of crops and cattle [e.g. Price *et al.*, 2011; Zardi & Whiteman, 2013]. Accurate weather predictions in complex terrain are also likely to affect the tourism industry, which forms an important source of revenue in some regions, for example, in many Alpine settlements, such as Chamonix in the French Alps. An accurate consideration of slope flows is thought to be important for the development of new settlements and structures as well as for the management of fires both wild and prescribed [Zardi & Whiteman, 2013]. Slope flows and regions of enhanced cooling

are expected to modulate the effects of climate change (see § I.2.2), and to affect the phenology, distribution and diversity of plant and animal species [Daly *et al.*, 2009], and so there is an interest in improving our ability to predict them.

The distribution of length scales of slope flows and regions of enhanced cooling mean that they are often too small to be modelled explicitly, in either low-resolution climate and earth-system models or high-resolution weather prediction models, which is likely to be the case for the foreseeable future. The resolved model variables must be adjusted to account for their effects and this parameterisation is an active area of research.

Existing parameterisation schemes account for the drag effect of complex terrain on the low-level flow. These schemes also account for the generation of internal gravity waves (IGWs), expected in a stable atmosphere when parcels of air are forced over a terrain obstacle, displacing them from their equilibrium positions. IGWs can break above a terrain surface disrupting the flow [Lott & Miller, 1997]. However, these schemes are limited to an implicit consideration of momentum fluxes and do not account for fluxes of heat, moisture, pollutants or other scalars. They do not account for the mixing effects of slope flows and valley circulations. Vertical fluxes induced by slope winds can be significant, as pointed out for instance by Noppel & Fiedler [2002] and Weigel *et al.* [2007]. Comparison of the results from existing operational forecasting models to available observations indicates that a cold-bias is often present in the predicted near-surface temperatures [Price *et al.*, 2011]. In order to develop a parameterisation scheme that accounts for the effects of slope flows and regions of enhanced cooling, a sound understanding of the associated physical processes must be gained.

The next section discusses the factors that affect downslope flows and regions of enhanced cooling. The aim of § I.2 is to put the research conducted by this project into its proper context, to demonstrate why the research is required and to enable comparisons with previous work. This is essentially a numerical modelling project and § I.2 will also help to set up the numerical model. Generally, the topics introduced in the opening paragraphs of this chapter are discussed further. It is not the intention to review all of the scientific literature on the subject. Downslope flows and regions of enhanced cooling are important phenomena for a wide range of landforms and timescales, which reflects how § I.2 has been structured. § I.3 derives and discusses two of the existing analytical models for downslope flows, which are relevant elsewhere in this document. The specific objectives of this study are presented in § I.6. This is essentially a numerical modelling study, and more details of the tool used, as well as the justification for using it, will be provided in Chapter II. Chapters III to V meet the objectives defined at the end of this chapter, and are presented essentially in the form they were published in. Inevitably, this has resulted in a small amount of

repetition. Some additional discussions have been added to the published material to clarify points or to provide further comparisons. This additional material is provided as supporting information at the end of each chapter, for relatively short comments, or in a set of Appendices for more lengthy discussions. Chapter VI summarises the key results of this project.

I.2 Factors affecting downslope flows and regions of enhanced cooling

Much research has been carried out to improve understanding of downslope flows and regions of enhanced cooling, for example, see the review by Zardi & Whiteman [2013]. This section focuses on a number of studies which included a field campaign or which made use of observations, and these studies (excluding review papers) are listed chronologically in Table I.1. Table I.1 includes the key factors that were discussed using each of the chosen references. The studies used to help setup the numerical simulation completed for this work, or which were used for specific comparisons, are indicated in the table.

Table I.1 includes the types of equipment used in the studies. The reader is referred to the original papers for detailed equipment specifications that are not provided in Table I.1. Table I.1 is not intended to be a complete list of past field campaigns, however, it appears to be comprehensive enough to reveal the general increased use of remote sensing equipment. In particular sonic detection and ranging (SODAR), radio detection and ranging (RADAR) and light detection and ranging (LIDAR) systems, as well as radiometers (frequently carried on satellite vehicles), have led to significant recent improvements to the understanding of complex terrain atmospheres [Banta *et al.*, 2013]. In particular these remote sensing systems have improved the areal coverage of observations, providing access to previously inaccessible areas. Table I.1 shows the continued use of near-surface stations and towers, which are in general a relatively inexpensive option, an advantage that is hard to ignore given the inevitable constraints on field campaign resources. The use of complex arrays of both in situ and remote sensors reflects the difficulty of observing complex terrain atmospheres, which are, in general, neither stationary nor horizontally homogeneous. By generally neglecting the equipment details Table I.1 cannot show the advancements in sensor technology that are carried on the identified measurement platforms.

Study	In situ						Remote						Topics
	Nss	Twr	Ts	Rs	Ms	Air	Rad	Sdr	Rdr	Ldr	C	Sat	
Doran & Horst [1981]	-	#	-	-	-	-	-	-	-	-	-	-	Drainage flow oscillations
Doran & Horst [1983]	-	#	#	-	-	-	-	-	-	-	-	-	u_s profiles over a steep near-uniform (i.e. angle) slope □
Gryning *et al.* [1985]	-	#	-	-	#	-	-	-	-	-	-	-	Effects of marine flows on drainage winds
Thompson [1986]	#	#	-	-	-	-	-	-	-	-	-	-	CAP forcing mechanisms in hilly terrain
McKee & O'Neal [1988]	-	-	#	-	-	-	-	-	-	-	-	-	Theory and observations of pooling and draining valleys
Neff & King [1989]	-	-	#[1]	-	-	-	-	#[1]	-	-	-	-	Drainage flow profiles in alpine terrain, pooling conditions, layering □, mixing effects, static stability □, parameterisation
Sakiyama [1990]	#	#	#	-	#	-	-	-	#	-	-	-	Drainage flow profiles in alpine terrain, TAF, along-valley geometry curvature effects, ambient flow effects
Gudiksen *et al.* [1992]	-	#	#	-	-	-	-	#	-	-	-	-	Drainage flows, ambient wind effects
Guardans & Palomino [1995]	-	#	-	-	-	-	-	-	-	-	-	-	Seasonal variation of CAPs
Helmis & Papadopoulos [1996]	#	#	-	-	-	-	-	-	-	-	-	-	u_s profiles over a non-uniform (i.e., angle) slope □
Eckman [1997]	-	#	-	-	-	-	-	-	-	-	-	-	Deep broad valleys, ambient wind effects
Whiteman *et al.* [1997]	#	-	#	#	-	-	-	-	#	#	-	-	Drainage flows, static stability □, ambient winds
Gustavsson *et al.* [1998]	#[2]	-	#	-	-	-	-	-	-	-	-	-	CAP forcing mechanisms in hilly terrain, snowfall and forests effects
Whiteman *et al.* [1998]	-	#	-	#	-	#	-	-	#	-	-	-	Plateaus surrounded by mountains, static stability, ambient wind effects, parameterisation
Dai *et al.* [2002]	#[3]	-	-	#	-	-	-	-	-	-	-	#	Variation of moisture in troposphere □
Heinemann [2002]	#	#	-	#	-	-	-	-	-	-	-	-	Depths of downslope flows over glaciers (low-angle slopes)
Renfrew & Anderson [2002]	-	#	-	-	-	-	-	-	-	-	-	-	Downslope flow speeds over a glacier
Seemann *et al.* [2003]	#[3]	-	-	#	-	-	-	-	-	-	-	#	Tropospheric moisture profiles □
Brulfert *et al.* [2005][6]	#	-	-	-	-	-	-	-	-	-	-	-	Pollution impacts in complex terrain, dataset of near-surface air temperatures close to valley bottom in the Alps □
Chazette *et al.* [2005]	#[1,5]	-	-	-	-	#	#	-	-	#	-	-	Valley shape, GBI depths and pollutants, snow cover effects
Forbes & Hogan [2005]	-	-	-	#	-	-	-	-	#	-	-	-	Cooling from evaporation and sublimation of rain and snow
Malek *et al.* [2006]	#[2]	-	-	-	-	-	-	-	-	-	-	-	Deep and broad valleys, daily-averaged near-ground pollution concentrations
Whiteman *et al.* [2007]	#	-	#	-	-	-	-	-	-	-	-	-	Dewfall and frostfall effects in small basins
Whiteman & Zhong [2008][7]	#	#	#	-	-	-	-	#	#	#	-	-	Downslope flows over gentle slopes in a deep and broad valley, static stability □, along-valley geometry
Daly *et al.* [2009]	#	-	-	-	-	-	-	-	-	-	-	-	CAPs and climate change, deep GBIs, seasonal variation of CAPs
Gohm *et al.* [2009]	#[2,5]	#	#[5]	#	-	#[5]	-	-	-	-	-	-	Deep GBIs, quasi-vertical profiles of pollutant concentrations □
Martínez *et al.* [2010]	#	#	-	-	-	-	-	-	-	-	-	#[3]	Cooling and flow patterns over a large plateau surrounded by mountains
Szintai *et al.* [2010]	#	-	-	-	-	-	-	#	-	-	-	-	Pollution transport in complex terrain
Whiteman *et al.* [2010][8]	#	#	#	-	-	-	#	#	-	-	-	-	Ambient winds, density currents, parameterisation
Wood *et al.* [2010]	-	#[5]	-	-	-	-	-	-	-	-	-	-	Urban heat islands, static stability
Price *et al.* [2011]	#[4]	#	-	#	-	-	#	-	-	#	-	-	CAP forcing mechanisms in hilly terrain, ambient winds, impact of CAPs, along-valley geometry
Cuxart & Jiménez [2012]	#	-	-	-	-	-	-	#	-	-	-	#	Cloud and fog effects in complex terrain
Nadeau *et al.* [2012]	#[4,5]	#	#	-	-	-	#	-	-	-	-	-	Evening transition in alpine terrain □, shading front, downslope flow initiation
Silcox *et al.* [2012]	#[5]	#	-	#	-	-	-	-	-	-	#	-	Long-lived stable layers in a deep and broad valley, daily-averaged pollution concentrations

= a number of, Nss = near-surface station, Twr = tower, Ts = tethersonde, Rs = radiosonde, Ms = minisonde and theodolite, Air = airborne, Rad = radiometer, Sdr = sonic detection and ranging (SODAR) system, Rdr = radio detection and ranging (RADAR) system, Ldr = light detection and ranging (LIDAR) system, C = Ceilometer, Sat = Satellite system, □ = studies used for model setup or for comparisons to numerical results.

[1] Mobile system used, [2] Fixed and mobile systems used, [3] Surface radiative measurements, [4] Soil measurements made [5] Composition of air measured,
[6] Chemel & Chollet [2006] used the same field campaign, [7] Princevac *et al.* [2008] used the same field campaign, [8] Haiden *et al.* [2011]; Hoch *et al.* [2011a] used the same field campaign

Table I.1: Equipment inventory for observation campaigns of studies used to discuss factors affecting cold-air pooling processes

I.2.1 Complex terrain length scales

An important question is how do variations in terrain length scales affect the evolution of thermodynamical processes in complex terrain, and in particular, the evolution of downslope flows and regions of enhanced cooling? The answer to this question is likely to influence a possible future parameterisation of these often subgrid-scale effects.

I.2.1.a Variation of terrain length scales

Efforts at elucidating cold-air pooling processes include those which considered small-scale (i.e., hilly) terrain, with typical depths of about 100 m. For example, Thompson [1986] discussed observations from Utah, USA and Ontario, Canada, Gustavsson *et al.* [1998] analysed observations taken in southern Sweden, and the Cold-Air Pooling Experiment (COLPEX) campaign deployed both observational and numerical systems to study cold-air pooling in the UK [see Price *et al.*, 2011, for an overview].

Previous studies have considered alpine valleys, which are typically deep but narrow. For example, Nadeau *et al.* [2012] analysed observations from the Slope Experiment near La Fouly (SELF-2010) field campaign, which took place in the Swiss Alps in 2010. Observations were made to investigate the evening transition of slope flows on clear-sky days during summer and autumn. The valley considered by Nadeau *et al.* [2012] has a depth and width of approximately 1 and 6 km, respectively.

Past work has considered relatively deep and broad valleys such as those studied by Eckman [1997], Malek *et al.* [2006], Princevac *et al.* [2008], and Whiteman & Zhong [2008]. Eckman [1997] used observations and numerical simulations to study flow patterns in the Tennessee river valley, USA, a valley over 50-km wide, with a maximum depth of roughly 1800 m. Princevac *et al.* [2008] and Whiteman & Zhong [2008] used field observations from the Vertical Transport and Mixing Experiment (VTMX) campaign [see Doran *et al.*, 2002], to improve understanding of slope flows within Utah's Salt Lake Valley, USA; a valley with a width and depth of roughly 25- and 1-km, respectively.

Previous studies include those of large basin landforms, such as the examples studied by Whiteman *et al.* [1998] and Martínez *et al.* [2010]. Whiteman *et al.* [1998] used radiosonde data to investigate the evolution of deep surface-based stable layers during winter in the Colorado Plateau, USA. This is one of North America's major landforms, covering an area of approximately 225,000 km^2, and surrounded by a ring of mountains, which to the west, rise approximately 1500 m above the basin floor. Martínez *et al.* [2010] studied nocturnal air flows and cooling rates in the Duero basin on the Iberian Peninsula, using tower observations and satellite imagery [from the National Oceanic and Atmospheric Administration (NOAA), and from the European Organisation for the Exploitation of Meteorological Satellites (EUMETSAT)]. The Duero

basin has a radius of approximately 160 km and is surrounded by mountain ranges rising above the valley floor by as much as 1750 m. The Duero basin was the subject of the Stable Atmospheric Boundary-Layer Experiment in Spain (SABLES-98) campaign [see Cuxart *et al.*, 2000].

Whereas some studies have focused on individual terrain depressions [e.g. Thompson, 1986; Gustavsson *et al.*, 1998; Eckman, 1997; Princevac *et al.*, 2008; Whiteman & Zhong, 2008], others have considered the more complex case of a system of valleys and other landforms, where the slope flows from individual elements of the system combine and interact with one another. Examples of investigations into the latter case include the work of Doran & Horst [1981], Neff & King [1989], Sakiyama [1990], Gudiksen *et al.* [1992] and Whiteman *et al.* [1997]. Doran & Horst [1981] analysed the temporal variations of along-valley flows observed from a tower in the Geysers area of northern California, USA, during the 1979 Atmospheric Studies in Complex Terrain (ASCOT) campaign, sponsored by the US Department of Energy. Neff & King [1989] built on the work of the 1984 ASCOT field campaign, making further observations, to investigate the pooling of air along the Colorado River, USA. Sakiyama [1990] made observations to study air flows and cooling patterns in the Alberta mountains, Canada. Gudiksen *et al.* [1992] also used field data captured during one of the ASCOT campaigns, in a joint effort by the Lawrence Livermore National Laboratory and the NOAA Wave Propagation Laboratory, as well as numerical simulations, to study flow and cooling patterns in the Mesa Creek valley, Colorado, USA. Whiteman *et al.* [1997] made observations in the Grand Canyon (part of the Colorado River catchment) for the Winter Visibility Study (WVS) of 1989–1990. The WVS was designed to determine the effects on the Grand Canyon atmosphere of the Navajo Generating Station, a coal-fired power plant located at Page, Arizona. The Colorado River and Mesa Creek valleys are located on the north western edge of the Colorado Plateau.

Some studies have considered observations made over isolated slopes rather than in terrain depressions, such as the studies of Doran & Horst [1983] and Helmis & Papadopoulos [1996]. Doran & Horst [1983] analysed observations taken over a near idealised two dimensional (2D) ridge, near Richland city, Washington state, USA, as part of the ASCOT campaign. The ridge was located approximately 595 m above mean sea level (a.m.s.l.), with its base near 150 m a.m.s.l., and the slope angle at the observation points was approximately 21°. Measurements were taken in two separate campaigns using Gill three-component anemometers and Climate cups and vanes at various levels (approximately 5) depending on the campaign and slope position. Helmis & Papadopoulos [1996] analysed observations made over the slopes of Mount Hymettos, Athens, Greece, an isolated hill roughly 500 m high with its base close to 250 m a.m.s.l. The slope angles at the base and half-way up the slope were estimated to be 9 and 34°, respectively. A mast some 30-m high was erected at the base of the

slope, with cup and propeller anemometers and wind vanes mounted at different levels to one another (a total of 8 mount points were set-up for the instruments). Renfrew & Anderson [2002] used near-surface stations, upper-air soundings and satellite data to study katabatic winds in Coats Land, Antarctica, over a gentle slope (less than 5.5 % or 2.9°) with a length of approximately 150 km.

I.2.1.b Length-scale thermodynamic effects

Though detailed observations of downslope flows are rare, the available evidence indicates that, under decoupled conditions, the shape of the underlying terrain has an important influence on the length and velocity scales of downslope flows. The angle of the slope is known to significantly affect the scales of the flow adjacent to it (see below and Zardi & Whiteman [2013]), and the maximum slope angle is essentially determined by the length scales of the terrain, although more length scales may need to be considered than the width and depth scales of the topographic features.

Doran & Horst [1983] displayed profiles of the downslope wind component with respect to vertical distance above the ground. The depth of the downslope flow was found to increase from approximately 5 to 15 m between 193 and 422 m from the top of the slope (measured along the slope), and between the vertical heights of 526 and 444 m a.m.s.l., respectively. The profiles demonstrate the presence of a cold-air jet (CAJ), with maximum flow speeds in the CAJ positioned from less than a metre to slightly over 2 m a.g.l., with maximum speeds ranging from approximately 0.4 to 4 m s^{-1}. Helmis & Papadopoulos [1996] reported increasing flow depths in the downslope direction, from 10 m near the mid-slope point to 20–30 m at the foot of the slope, a CAJ usually observed close to 6 m a.g.l., and typical downslope flow speeds of 1–2 m s^{-1}. Whiteman & Zhong [2008] observed downslope flows over a 1.6° slope on the western side of Utah's Salt Lake Valley using tethered balloons during clear and calm October nights. The downslope flows were observed to be 100–150-m deep, with a CAJ 10–15 m a.g.l., with jet speeds of approximately 5–6 m s^{-1}.

The study by Renfrew & Anderson [2002] is unique in the studies considered here in that the effects of the Earth's rotation could not be neglected due to the length of the slope (see below). The typical slope angles observed by Renfrew & Anderson [2002] and Whiteman & Zhong [2008] are similar, as are the characteristics of the two slope flows. Renfrew & Anderson [2002] focused on the case of weak synoptic flows and found mean katabatic wind speeds to be 5.1 and 7.5 m s^{-1} for a 0.6° and 2.9° slope, respectively. Renfrew & Anderson [2002] did not focus on the depth of the katabatic flow, however, these flows are known to be typically several hundred metres deep [e.g. Heinemann, 2002].

The work of Doran & Horst [1983], Helmis & Papadopoulos [1996] and Whiteman & Zhong [2008] indicates that downslope flows are generally deeper and faster over

more gentle slopes. The motions of air parcels moving down a slope are controlled by several forces; pressure, buoyancy and friction. The Coriolis term is often interpreted as a force, however, over the typical length scales of the slopes considered by these studies, rotation effects can be safely neglected (e.g., see Holton [2004] and § I.3). McNider [1982b] used theory to demonstrate that the pressure force can generally be neglected over gentle slopes (where a hydrostatic balance can be assumed in the direction perpendicular to a slope). This study demonstrates numerically that the pressure force is also relatively small for steeper slopes away from slope extremities (see Chapter IV). If friction forces are assumed similar for different simple slopes (e.g., slopes with a constant slope angle and roughness) then differences in the average speed of downslope flows over different slopes must be due to differences in the buoyancy force. This case has been considered in the literature [e.g. Zardi & Whiteman, 2013] to explain the differences in flow speeds over different slopes.

The buoyancy force acting on parcels depends on the ability of the slope to cool the air parcels above it relative to their ambient environment, and the effect of the buoyancy force depends on the slope angle. For the same height change, air parcels must move a greater distance along more gentle slopes, increasing the slope's ability to cool the air parcels above it. Also, for a given displacement along the slope the warming of parcels due to adiabatic effects will be less for more gentle slopes. Adiabatic warming of parcels occurs as they move downslope due to the increasing pressures of their environment (i.e., the environment transfers energy to the air parcels by doing work on them). As the slope angle decreases further the effect of the buoyancy force will be increasingly nullified by the terrain. Therefore, to maximise wind speeds a balance must be reached.

The studies of Doran & Horst [1983], Helmis & Papadopoulos [1996] and Whiteman & Zhong [2008] also demonstrate the increasing depths of downslope flows along the slope. Baines [2008] conducted laboratory experiments of gravity currents flowing down uniform slopes (constant slope angles and roughness) in stratified non-rotating liquids. A dense fluid was released at the top of the slope, which is generally different to how downslope flows form in the atmosphere, where the dense fluid is generated by the cold surface of the slope. Nevertheless, gravity currents in liquids can be used to investigate the mechanical mixing effects of downslope flows in the atmosphere. Generally, the work by Baines [2008] revealed a detrainment of fluid out of the gravity current for sufficiently gentle slopes (typically less than 12°). For steeper slopes fluid was generally entrained except for a broad region of detrainment centered on the level of neutral buoyancy; this case was termed the 'plume regime'. Increasing the slope roughness was found to delay the onset of the plume regime until larger slope angles were reached. Baines [2008] found surface friction to dominate the friction term for the gravity current regime in contrast to the plume regime where mixing at the top of

the downslope flow was dominant.

Given the change of mixing effects with changing slope angle it would be useful to confirm that the friction force can be neglected when explaining the increase of flow speeds with decreasing slope angles, up to some limiting value. It seems likely that faster downslope flows are also deeper partly due to the greater kinetic energy of these flows close to the ground. Diffusion processes then transport kinetic energy to greater heights. However, this is speculative and should be confirmed by future work.

It is clear from recent observations that variations of topographic length scales can contribute to significant localised thermodynamical effects within complex terrain. For example, Whiteman & Zhong [2008] found the downslope flow they observed to weaken, become more variable and more shallow in the late evening (after 2100 MST), which generally coincided with the establishment of down-valley flows, as well as the development of a ground-based temperature inversion (GBI) that expanded from the bottom of Salt Lake Valley. Whiteman & Zhong [2008] confirmed the presence of large wind shears when the down-valley flows interacted with the downslope flows, suggesting that the downslope flows were eroded from above by shear-induced turbulent mixing. The relative importance of shear-induced mixing and buoyancy for controlling the flow speed, flow stationarity and flow depth remains to be confirmed. Whiteman & Zhong [2008] recorded only small changes in the structure and intensity of the GBI, adjacent to the slope, in the late evening. Gradients in potential temperature θ were found to become more variable above the downslope layer at the different measurement sites in the late evening. Significant changes in the GBIs, adjacent to the slope, did not occur before 0300 MST.

Wherever the length scales of a complex terrain system allow for a significant down-valley flow, it is reasonable to expect similar effects to occur. The impact of these localised subgrid-scale effects on resolved near-surface temperatures and larger-scale mixing processes is not clear. The effects may be largely insignificant, or perhaps the presence of down-valley flows act to suppress the upward expansion of a region of enhanced cooling, whilst increasing exchanges of momentum, heat and scalars between the downslope flows and the valley atmosphere above. It is not clear if a down-valley flow would significantly affect exchanges of momentum, heat and scalars between the valley atmosphere and the free atmosphere above. The presence of down-valley flows might be used to modify a parameterisation scheme of complex terrain effects.

McKee & O'Neal [1988] presented observations of both very weak (less than 0.5 m s^{-1}) and strong (6–8 m s^{-1}) along-valley winds observed in different valleys. Analytical theory was used to demonstrate that the different wind speeds could be explained by different down-valley changes in the width to (cross-section-) area ratio W_v/A_v of the valleys, neglecting any variation in the surface-energy budgets. Valleys with W_v/A_v increasing down the valley leads to increasing cooling rates in the down-valley

direction. This leads to the formation of cooler air further down the valley, which effectively blocks the down-valley flow. McKee & O'Neal [1988] demonstrated that the magnitudes of the forcing mechanism outlined above (termed the intra-valley force), can exceed the magnitudes of forces due to mountain-plain temperature differences, or the magnitudes of forces due to temperature differences caused by sloping valley floors.

Neff & King [1989] observed the formation of a CAP that grew from the floor of the De Beque Canyon, located along the Colorado River. Drainage flows must exit the catchment through the narrow canyon but are partially blocked and forced to flood back into the surrounding valleys. Observations confirmed that down-valley flows with a distinctive CAJ were forced above the growing CAP. Approximate down-valley flow volume flux calculations and the assumption of volume conservation indicated a vertical transport of cold air by two likely mechanisms; vertical displacement of air within the CAP by incoming denser down-valley flows, and/or erosion of the CAP from above by overflowing drainage flows and ambient winds. Vortices and instability-like structures revealed by fog towards the top of the CAP indicated the presence of the latter mechanism, which is similar to that observed by Whiteman & Zhong [2008].

Neff & King [1989] estimated the volume flux of cold air to be linearly proportional to the catchment area above the measurement point. In general, this supports and enhances the results of Gustavsson *et al.* [1998] who found the lateral expansion of CAPs, observed in southern Sweden, to be proportional to the widths and catchment areas of the valleys. This lateral expansion was assumed to be due to downslope flows. Neff & King [1989] observed a general reduction of atmospheric stability within the De Beque Canyon through the night, assumed to be due to shear-induced mixing.

The rate of growth and maximum depth of a region of enhanced cooling must depend on the rate at which dense air accumulates in a topographic depression (either from slope flows or in situ radiative cooling), on the rate at which dense air is removed, and on the volume that the region of enhanced cooling can expand into. The input of mass from slope flows depends on the size of the catchment above or adjacent to the topographic depression. The loss of mass will depend on the existence or absence of terrain restrictions, as well as possible erosion of the region of enhanced cooling by ambient winds. Smaller volumes formed by topographic depressions will force an expanding region of enhanced cooling higher into the atmosphere, the effects of which have not been fully quantified. The highly-complex system investigated by Neff & King [1989] has a large input of dense air from many tributaries and a restricted outflow region, however, a large volume that the CAP can expand into, as well as some likely erosion by ambient winds. Given its size, presumably the system studied by Neff & King [1989] has a significant effect on the wider atmosphere, however, the ability of existing operational forecast models to represent these effects must be questionable.

The catchment area is comprised of many valleys which have length scales similar to that of the horizontal grid resolution of existing operational forecasting models, and the same can be said of the system's outflow region. It is questionable that parameterising the subgrid-scale mixing effects of the catchment's deep and relatively narrow valleys will improve the representation of the growth of the CAP and its effects on the wider atmosphere. Cases like these may need to be dealt with on a more case-by-case basis, if required, preceding the arrival of greater model grid resolutions.

Sakiyama [1990] suggested that down-valley wind observations with a clear cross-valley component could be explained by an oscillation or 'sloshing' of the down-valley flow, caused by a sharp bend in the valley upstream. It is unclear what effect complex flow features such as these have on near-surface temperatures and larger-scale mixing patterns. Sakiyama [1990] explained the variation in temperature ranges between a relatively wide U-shaped valley and a relatively narrow V-shaped tributary canyon using the so-called topographic amplification factor (TAF). The TAF is defined as the valley drainage area to volume ratio divided by the plain area to volume ratio. The factor estimates the ability of a topography to change the heat energy content of the volume of atmosphere it encloses, with larger surface areas and smaller volumes (typical of V-shaped valleys) resulting in larger changes of atmospheric heat energy with the evolution of solar and thermal radiation.

Sensitivity studies of the effects of complex terrain are rare. Hoch *et al.* [2011a] used MYSTIC; a three-dimensional radiative transfer scheme based on a Monte Carlo technique, which can account for the effects of clouds, complex terrain shapes and variations in surface albedo. Significant variations of average basin- and valley-atmosphere longwave radiative cooling rates were found between idealised 500-m deep topographies with widths ranging from 1 to 6 km, for two times during the night. The variation of average atmosphere radiative cooling rates was attributed to two key effects. For increasing terrain widths, the importance of near-ground cooling (associated with ground-air temperature deficits) decreases, whereas the importance of cooling due to the general temperature stratification in a depression atmosphere increases. The latter occurs since back radiation from nearby basin and valley sidewalls has a greater effect in more narrow terrain. It was argued that the former effect dominates the variations, which explains how radiative cooling rates for smaller depressions approach the flat-terrain case, and how radiative cooling rates in narrow (500-m wide) terrain can exceed those for flat terrain. The results are dependent on simplified atmospheric vertical temperature profiles and temperature deficits between the ground surface and the adjacent atmosphere. Dynamics effects were not explicitly accounted for (see also Chapter III). The study by Hoch *et al.* [2011a] demonstrated that one-dimensional radiative transfer schemes can significantly over-estimate average valley-atmosphere longwave radiative cooling rates compared to three-dimensional schemes. This is an

important error source that should be considered in future studies.

Katurji & Zhong [2012] tested the sensitivity of characteristics of downslope flows and regions of enhanced cooling to variations in topographic length scales and the ambient atmospheric stability, using the Advanced Regional Prediction System (ARPS) numerical model. The depth of the valley was held constant at 1 km whilst varying the width of the valley (2 to 16 km), slope angle (5.7 to 26.5°), and ambient stability (0.2 and 6 K km^{-1}). The total average valley-atmosphere cooling decreased as the volume of the valley and the ambient stability increased. The idealised simulations carried out by Katurji & Zhong [2012] were 2D (i.e., only one model grid point was used in the cross-flow direction), and did not represent microphysical processes. The horizontal model grid resolution Δx, and Δz adjacent to the ground surface, were 100 and 10 m, respectively. $\Delta z = 10$ was not fine enough to resolve a CAJ in most of the simulations, and so the generality of the results should be confirmed. The dependency of the average valley-atmosphere cooling on the chosen horizontal resolution is demonstrated in Appendix B, highlighting the need to select Δx with care in future work.

I.2.2 Time-scale effects

Downslope flows and regions of enhanced cooling are thought to significantly affect the climatology of mountainous regions, and a quantification of these effects can be valuable information for the agricultural industry [see Zardi & Whiteman, 2013, and references therein]. Downslope flows and regions of enhanced cooling appear to have a strong seasonal dependency. These local effects appear most pronounced during summer for generally more exposed topography, such as wide valleys and large basins [e.g. Guardans & Palomino, 1995; Martínez *et al.*, 2008]. This is due to the generally greater frequency of anticyclones during the summer months when day–night heating contrasts are largest [Zardi & Whiteman, 2013]. There is some evidence to suggest that in more sheltered atmospheres (e.g., relatively narrow and deep valleys) downslope flows and regions of enhanced cooling can be more pronounced during winter [e.g. Daly *et al.*, 2009].

Sub-mesoscale future climate estimates obtained by applying downscaling techniques to the results of general (global) circulation models (GCMs) have a strong regional bias. The relatively low grid resolution of GCMs prevents an accurate prediction of downslope flows, regions of enhanced cooling, or other sub-mesoscale (and most mesoscale) phenomena. However, these local-scale processes and effects are likely to significantly modulate climate change estimates and so should be accounted for [Daly *et al.*, 2009].

Daly *et al.* [2009] assumed that monthly-averaged surface temperatures $\langle T_0 \rangle$ ob-

served at points over the Oregon Cascades, USA, a region of mountainous terrain, could be expressed as a function of the average synoptic conditions. The latter were expressed using an index of the form $I = N_a - N_c$, where N_a and N_c correspond to the number of anticyclonic and cyclonic days occurring during a month, respectively. Any zonal flow-days were neglected. The index was calculated using reanalysis data from NOAA and the National Centre for Atmospheric Research (NCAR). Linear regression was used to define the function f for $\langle T_0 \rangle = f\ (I)$, the accuracy of which was shown to depend on the position of a point on the complex terrain surface, which affected whether the atmosphere adjacent to the point was, in general, decoupled from the synoptic flows or not. Future estimates of $\langle T_0 \rangle$ and $\langle \partial T / \partial z \rangle$ could then be obtained by adjusting I according to the expected general changes of the large-scale circulations. $\langle \partial T / \partial z \rangle$ was then set as the dependent variable in a multiple linear regression function, using height z and an index of local topographic type (lower numbers corresponding to more sheltered positions), as the independent variables. When added to the expected regional increase of $\langle T_0 \rangle$, this provided a spatial representation of the estimated future surface temperature changes over a region of the Oregon Cascades.

The results of Daly *et al.* [2009] reflect the variation of decoupling, predicting large spatial variations in the temperature changes estimated due to a warmer climate. The results implicitly assume that the relationship between average surface temperatures and synoptic conditions f does not change during global warming, neglecting any non-linearity in the system. In theory, it should be possible to investigate cold-air pooling processes, in future climates, using large-eddy simulation (LES) by adjusting the initial conditions and radiative transfer scheme to represent future conditions, if these conditions can be estimated with reasonable accuracy.

I.2.3 Additional key factors

Table I.2 aims to summarise the factors that affect downslope flows and regions of enhanced cooling. Time-scale effects (denoted by t in Table I.2) and length-scale effects (all factors in the 2$^{\text{nd}}$ column except for latitude Φ), have been addressed to some degree in the previous sections of this chapter. The remaining factors are considered in the following subsections.

I.2.3.a Atmospheric stability (γ)

It is known that the atmospheric stability of the boundary-layer, within complex terrain (as well as over flat terrain), will approach a neutral state close to sunset, given sufficient daytime convection. Cessation of convective motions together with relatively intense cooling close to the ground surface, essentially due to longwave radiation losses to space, will stabilise the boundary-layer, sometimes creating temperature inversions

Single case	Other geometries	Error sources
t γ shadows q_v, clouds, rain, snow z_0, α_r, ϵ_r, M_s, Q_E, Q_H, Q_G, ΔQ_S forests urban heat island pollutants $\mathbf{u_a}$	W_v, H 2D depression shape 3D depressions Φ	1D vs 3D radiation scheme surface-layer scheme Δx, Δz

t = time, γ = static stability, q_v = water vapour mass-mixing ratio, z_0 = aerodynamic roughness length, α_r = albedo, ϵ_r = emissivity, M_s = surface moisture, Q_E and Q_H are the latent and sensible heat flux at the ground surface, respectively, Q_G and ΔQ_S are the flux of heat through the soil and the storage of heat within the ground, respectively, $\mathbf{u_a}$ denotes the ambient wind velocity above the complex terrain, W_v and H denote the width- and depth-scales of the topographic depression, Φ denotes latitude, Δx and Δz are the horizontal (along x) and vertical grid resolution, respectively. 1D and 3D denote one-dimensional and three-dimensional. Note that γ in this context generally refers to an ambient or initial state. The orange text highlights those factors that seem to be particularly important for cold-air pooling processes within some limited range of latitudes, chosen by considering the literature review made in this chapter, factors that might be given priority if sampling the parameter space (see § I.4).

Table I.2: Factors affecting the evolution of regions of enhanced cooling

(i.e., $\partial T/\partial z > 0$) [e.g. Stull, 1988]. This assumes that mechanical mixing from larger-scale systems (e.g., synoptic systems) is not large enough to keep the fluid well mixed. Near-neutral layers close to sunset have often been observed in complex terrain [e.g. Whiteman *et al.*, 1997; Chemel & Chollet, 2006; Whiteman & Zhong, 2008].

Ground-based temperature inversions frequently occur in complex terrain at night, and sometimes during daylight hours given the right conditions (see § I.2.3.c). Inversion depths can vary greatly and depend on the past atmospheric state (i.e. static stability), the amount of cooling at a given time, as well as the ability of the atmosphere to mix and advect heat energy. A degree of mixing will serve to deepen the inversion by enabling the cooling of higher layers, however, intense mixing may erode an inversion.

Inversions over sidewalls of terrain depressions, away from the bottom of depressions, have depths of 1–20 m and maximum strengths of 3–7 °C [Zardi & Whiteman, 2013]. Inversion strengths are defined as the difference between the temperature of the ambient air away from the slope and the air temperature close to the sloping ground. GBIs that grow from the bottom of terrain depressions can be considerably deeper.

Neff & King [1989] present SODAR and Tethersonde data collected at three progressiveley lower locations within the De Beque basin of western Colorado (see also § I.2.1.a). The first site, located relatively high-up in the De Beque basin, within

a relatively small tributary valley (with depth and width of approximately 400 and 1000-m, respectively), had GBIs at the center of the valley that were about 50–100 m deep, in the early night before midnight. A down-valley wind existed over a similar depth range with maximum strength of about 2 m s^{-1}. The second site, located lower down in the basin, in a larger valley (with depth and width of approximately 700-m and 15 km, respectively), had inversions at the center of the valley between 300–500-m deep, in the late night within a few hours of sunrise. An approximate 200-m deep near-ground down-valley flow occurred concurrently with the inversions, as well as an elevated flow also about 200-m deep with a CAJ maximum positioned about 450 m above the surface. Maximum wind speeds were in the range of 1–4 m s^{-1}. The elevated flow was positioned above the most intense part of the GBI, as well as the major terrain obstacle inhibiting flows out of the basin (i.e., the De Beque canyon). The third site was within the 400-m deep, 1-km wide De Beque canyon, where GBIs were observed to be approximately 100-m deep during the early night, concurrent with drainage flows several hundred meters deep with maximum speeds between 2 and 8 m s^{-1}. The stability of the canyon atmosphere generally decreased during the night.

Chemel & Chollet [2006] present tethered-balloon soundings made close to the center of the Chamonix valley, in the French Alps, under calm and clear-sky summer conditions, for the POllution in Alpine Valleys (POVA) field campaign. The soundings show early- and late-night temperature inversions with depths of approximately 100 and 450-m deep, respectively. A down-valley flow occurred over approximately the same depths, with maximum wind speeds of about 3 m s^{-1}. Chazette *et al.* [2005] present GBIs in the Chamonix valley during winter (January 2003) lasting all day, with similar depths to those found by Chemel & Chollet [2006] in the late night, under similar conditions (see also § I.2.3.c). The results of Chazette *et al.* [2005] were found by constructing morning and afternoon quasi-vertical temperature profiles from airborne measurements. Gohm *et al.* [2009] present a GBI, constructed from ground-based and airborne measurements, with a depth of approximately 1.1 km, observed in the Inn valley, Austria, January 2006, under calm and clear high-pressure conditions, with a snow-covered surface. A down-valley wind was present with a depth and maximum strength of approximately 800 m and 7 m s^{-1}, respectively. A possible cause of this deep temperature inversion is the combined effects of snow cover and quiescent synoptic conditions leading to a rapid stabilisation of the boundary layer. If these conditions persist then the stability of the boundary layer may build enough to generate such deep temperature inversions.

Daly *et al.* [2009] used near-surface air temperatures (1.5–2 m a.g.l. [Daly *et al.*, 2007]) close to a valley floor and mountain top location, in the Oregon Cascades, to argue for the regular occurrence of deep [$\mathcal{O}(1)$ km] temperature inversions, assuming a

linear gradient of temperature with height. The analysis also uses daily minimum and maximum temperatures at each location so the results are dependent on the times of minimum and maximum being roughly coincident at each location. Since the inversions reported by Daly *et al.* [2009] occurred during both summer and winter, it is difficult to attribute their relatively large depth to the presence of snow cover alone, which is generally only present in the Oregon Cascades during the winter months. Another possible candidate is the advection of higher-θ air by elevated flows. Warm and wet Pacific maritime air is advected over the Oregon Cascades, which are considered to have a Mediterranean climate. The advection of air is due to sea breezes as well as mainly winter cyclonic systems carried by the Polar Jet Stream. A large amount of rain falls onto the Cascades, presumably partitioning more energy into latent fluxes, reducing sensible heat fluxes, especially at greater altitudes.

In some cases complex terrain atmospheres remain well-mixed despite the loss of solar radiation. Whiteman *et al.* [1997] suggest that the likely mechanism for this in parts of the Grand Canyon is drainage of air into the canyon from adjacent snow-covered plateaus. As well as the effects of ambient winds, clouds also reduce static stability by reducing the loss of longwave energy from complex terrain surfaces Chazette *et al.* [e.g. 2005] (see also § I.2.3.c).

The effects of changes in ambient atmospheric stability on downslope flows at points along slopes, are now well known from observations, numerical-modelling studies and analytical work. The downslope flows analysed by Whiteman & Zhong [2008], observed over the western slope of Utah's Salt Lake Valley in 2000, were found to be generally weaker with higher γ. The maximum CAJ speed was 5–7 m s^{-1} on 2 October with γ = 1–2 K km^{-1}, and 4–5 m s^{-1} on 8 October with γ = 5–8 K km^{-1}. The downslope flow was found to weaken later in the night (after 2121 MST) on 2 October, suggested to be caused by the increase in γ in a region expanding from the valley bottom. There is some evidence to suggest that the flow also became more variable during this period. Catalano & Cenedese [2010] used a numerical model run in LES mode to investigate the development of regions of enhanced cooling in idealised valleys with constant slope angles. The simulated downslope flows, analysed at a point, were found to weaken later in the night, stated to be caused by the growth of stable boundary layers from the valley floor. The two-layer (hydraulic) analytical model of McNider [1982a] (derived and discussed in § I.3) demonstrates that the strength of downslope flows are inversely proportional to γ.

Despite the now established understanding of the effects of γ on downslope flows at points along slopes, a thorough four-dimensional investigation of the interactions between downslope flows and developing regions of enhanced cooling is still required.

I.2.3.b Shadowing effects

For downslope flows mainly restricted to nocturnal hours shadows can significantly offset the start time of the flows from the time of local sunset. Shadowing effects vary with latitude, time of year, general terrain orientation and local site aspect [e.g. Nadeau *et al.*, 2012]. The observations analysed by Nadeau *et al.* [2012] revealed near-zero flow speeds close to sunset during what was termed the 'early-evening calm' period. The initiation of the downslope flows was found to be controlled by the movement of a shading front from the bottom towards the top of the valley slopes.

The pattern of shadows across a landscape is likely to be related to some degree to the development of regions of enhanced cooling. Chazette *et al.* [2005] cite shadows, together with snow-cover, clear skies and poorly-drained conditions, as one important factor in the development of relatively deep GBI layers in the French Alps (see also § I.2.3.a and § I.2.3.c).

Given the need to parameterise the effects of regions of enhanced cooling in complex terrain, it would be useful to confirm the importance of shadows for the development of these regions.

I.2.3.c Atmospheric moisture

The general reduction in atmospheric water content with height in the troposphere is well known [e.g. Seemann *et al.*, 2003], as is the large variation of water in the atmosphere [Dai *et al.*, 2002]. Figures I.3**(a)** and I.3**(b)** demonstrate both of these atmospheric characteristics by presenting quasi-vertical profiles of q_v and relative humidity (RH), respectively. The profiles are from radiosonde soundings launched from the floor of Salt Lake valley, Utah, USA, on 1 and 2 October 2000 at 1115 UTC (1615 MST; approximately 2 h before sunset). The valley floor is located about 1300 m a.m.s.l. and mountains rise up to approximately 2500 m and 3000 m a.m.s.l. on the western and eastern sides of the valley, respectively. The radiosondes were launched at the same time as the VTMX field campaign was being conducted [Whiteman & Zhong, 2008], during a period of generally quiescent synoptic conditions and clear skies.

Figure I.3**(a)** shows relatively large variations of q_v over small spatial scales, for example, on 1 October changes of $|q_v| \approx 1$ g kg^{-1} occurred over height changes of less than 200 m between approximately 3.5 and 6 km a.m.s.l. The possible large variability of RH in even fairly quiescent synoptic clear-sky conditions is clear from Fig. I.3**(b)**.

Layers of near constant q_v can occur within the atmospheric boundary layer near the ground close to sunset after daytime convective mixing [e.g., see Fig. I.4**(a)**]. Figures I.4**(a)** to I.4**(d)** show quasi-vertical profiles of q_v, RH, T, and θ, respectively. The profiles were taken or derived from Tethersonde launches made from the floor of the Chamonix valley at Les Praz de Chamonix on 8 July 2003 at 2057 UTC (approxi-

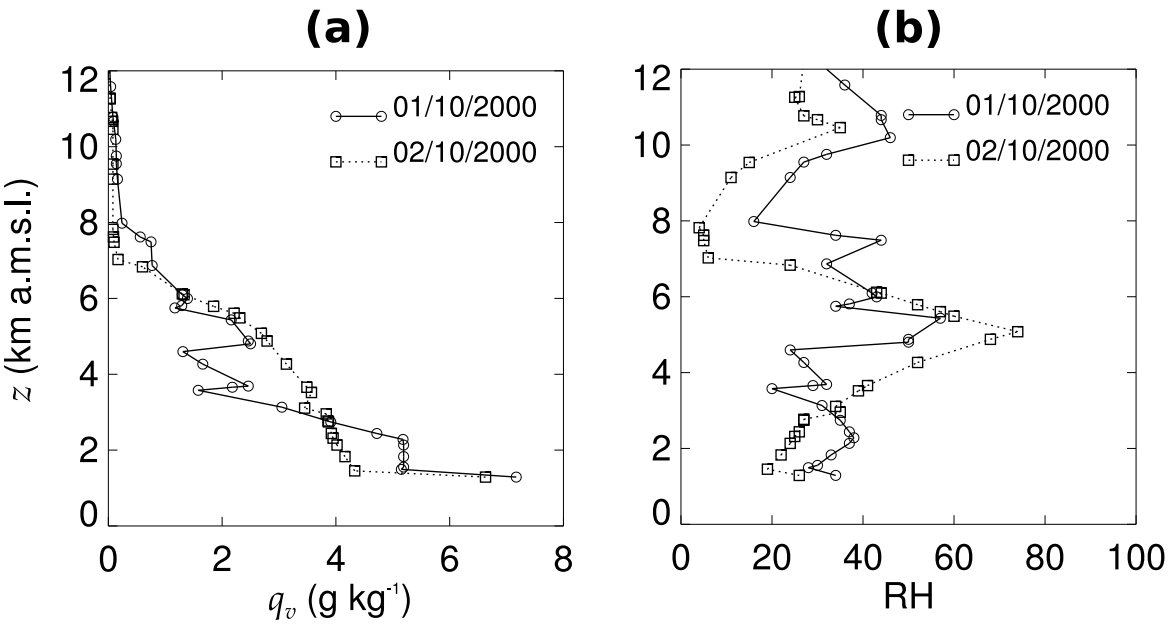

Figure I.3: Quasi-vertical profiles: **(a)** water-vapour mass mixing ratio q_v, **(b)** relative humdity (RH). The profiles are from radiosonde launches made from the floor of Salt Lake valley, Utah, USA, on 1 and 2 October 2000 at 1115 UTC (1615 MST; approximately 2 h before sunset). The valley floor is located about 1300 m a.m.s.l. and mountains rise up to approximately 2500 m and 3000 m a.m.s.l. on the western and eastern sides of the valley, respectively. The radiosondes were launched during a period of generally quiescent synoptic conditions and clear skies. The data was extracted from UoW [2014].

mately 30 min before sunset). The data was captured during the POVA field campaign [see Brulfert *et al.*, 2005; Chemel & Chollet, 2006], under generally quiescent synoptic conditions and clear skies. Measurements were averaged using a sliding 20-m vertical window. The Tethersonde site was a field close to the valley centre within a suburban area with a population of less than 10,000 people.

Figure I.4**(a)** was created by converting the available RH data to q_v, using $q_v = (\mathrm{RH}/100)\ q_{v_s}$, where q_{v_s} is the saturated mass mixing ratio. The latter was calculated using $q_{v_s} = \epsilon\, e_s/\,(p - e_s)$, where ϵ is the ratio of the molecular weights of water and dry air ($\epsilon = M_w/M_d$). p is the total pressure and e_s is the saturated vapour pressure, which was calculated using the approximation

$$e_s = 6.11\, e^{19.83 - 5417/T} \tag{I.1}$$

[see Tsonis, 2007], which assumes that the latent heat of vaporisation is constant and independent of T. This approximation is reasonable for a temperature range of -20 to 30°C, which is appropriate for the Tethersonde data considered here [see Fig. I.4**(c)**]. In Eq. (I.1), e_s and T have units of hPa (mbar) and Kelvin, respectively.

Although q_v is shown to be well-mixed close to the ground within the boundary layer within the Chamonix valley, this can not be said of T [Fig. I.4**(c)**], which decreases

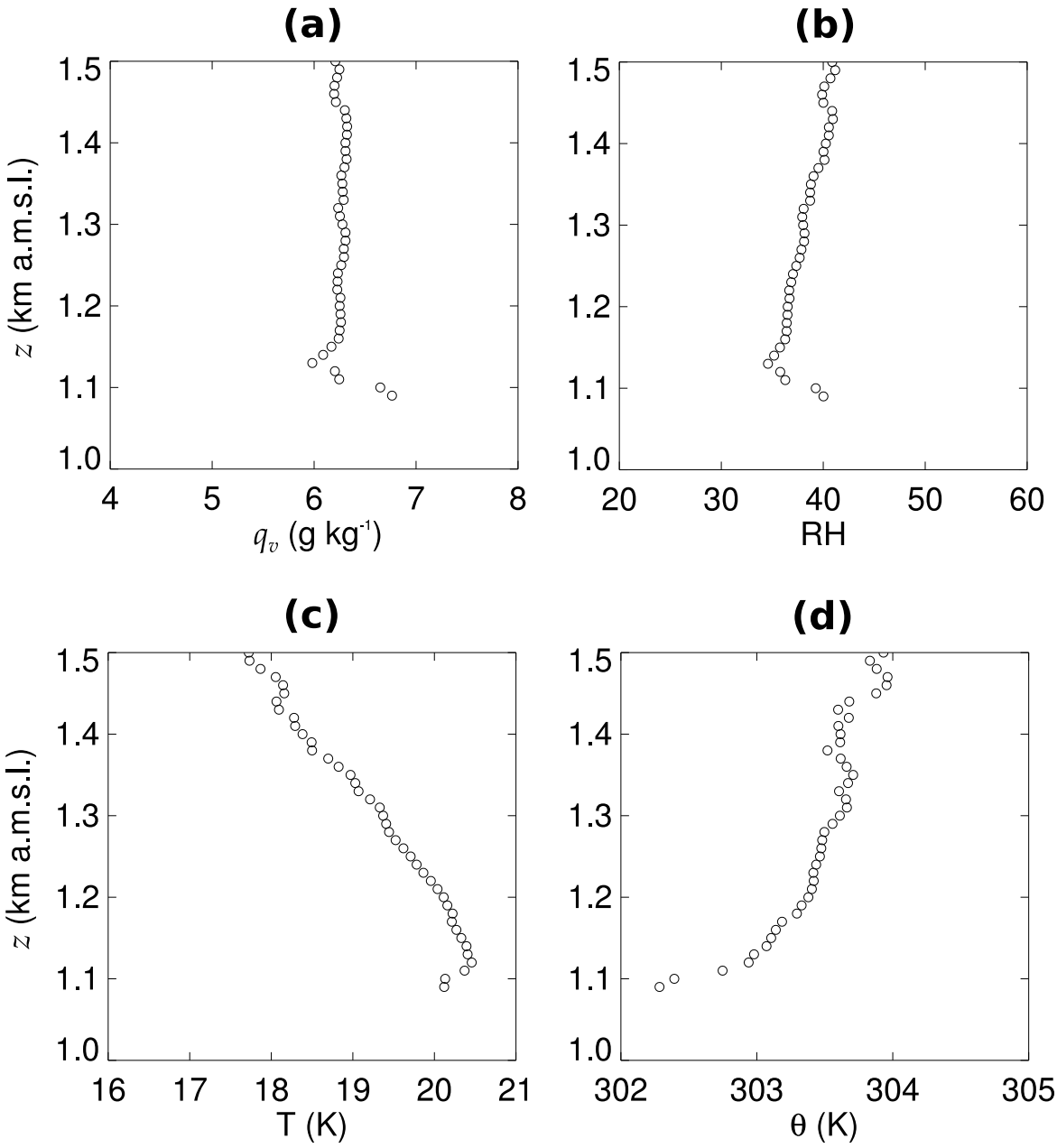

Figure I.4: Quasi-vertical profiles: **(a)** q_v, **(b)** RH, **(c)** temperature T, **(d)** potential temperature θ. The profiles were taken or derived from Tethersonde launches made from the floor of the Chamonix valley at Les Praz de Chamonix on 8 July 2003 at 2057 UTC (approximately 30 min before sunset). The data was captured during the POllution in Alpine Valleys (POVA) field campaign [see Brulfert *et al.*, 2005; Chemel & Chollet, 2006], under generally quiescent synoptic conditions and clear skies. Measurements were averaged using a sliding 20-m vertical window. The Tethersonde site was a field close to the valley centre within a suburban area with a population of less than 10,000 people.

with height. From the above discussion, this must result in a slight increase of RH with height close to the ground (RH increases by approximately 7 % over a height change of about 380 m). Evidently, the air adjacent to the valley floor has already been stabilised by the cooling surface even though the sounding started 30 min before

sunset. Figure I.4**(d)** shows a stable layer [including an inversion layer some 20-m thick adjacent to the ground, Fig. I.4**(c)**] up to a height of about 1.3 km a.m.s.l., with a near-neutral residual layer about 120-m thick above this. Figure I.4**(d)** was created by transforming the captured temperature data using

$$\theta = T\ (p_0/p)^{R_D/c_{p_d}}\ , \tag{I.2}$$

[e.g. Tsonis, 2007], where $p_0 = 100000$ pa (corresponding to a pressure at mean sea level), R_D is the gas constant for dry air, and c_{p_d} is the specific heat capacity at a constant pressure for dry air.

It is worth noting that an overall reduction in q_v with height is expected in the boundary-layer, due to the evaporation of moisture from the ground surface and the entrainment of relatively dry air at the top of the boundary layer. High atmospheric water content close to the ground is evident in Fig. I.3**(a)** and Fig. I.4**(a)**, and the general reduction in q_v across the boundary layer is evident in Fig. I.3**(a)**.

Figure I.5 aims to demonstrate how changes in the distribution and phase of water in complex terrain has a complex effect on the depression atmosphere temperature evolution. The following discussion focuses on near-surface and depression-atmosphere average quantities, however, can generally also be applied to points in space; therefore no averaging notation has been used. The box labelled (1) indicates an increase in a depression atmosphere average q_v, which might be due to evaporation from the ground surface (i.e. $Q_E > 0$), or it could represent a relatively moist atmosphere in some location compared to a drier environment. A greater q_v will, in theory, correspond to a greater cooling rate [denoted by $|\partial T/\partial t| \uparrow$ in box (2)]. Haiden *et al.* [2011] used MYSTIC, a three-dimensional radiative transfer model, to demonstrate that large variations in the average moisture content of valley atmospheres significantly affects but does not dominate the average valley-atmosphere instantaneous cooling by longwave radiation. By increasing q_v from 3.25 to 4.875 g kg^{-1} (a 50 % increase), in a valley with a width and depth of approximately 5 km and 500 m, respectively, increased the longwave cooling rate by approximately 17 %.

If an atmosphere is cooled to its dew-point temperature T_d (the value of which depends on some intitial T and q_v), then clouds and fog may form. This conditional event is indicated by a dashed line in Fig. I.5. The effects of clouds and possible subsequent precipitation are discussed below. If cooling rates are large enough then surface temperatures T_0 may decrease below the dew point of the adjacent atmosphere (the value of which depends on some initial T and q_v). If this happens then moisture will condense onto surface elements (a process known as dewfall or frostfall); water molecules are bonded into their less energetic fluid (or solid) form, releasing latent energy, and so reducing the cooling rate [boxes (3) and (4)]. Whiteman *et al.* [2007]

demonstrated that dewfall (represented by Q_E in Table I.2) can significantly reduce the average depression-atmosphere cooling rates, in small-scale topography. Whiteman *et al.* [2007] made Tethered balloon soundings in the Gruenloch basin, Austria, a depression with a width and depth of approximately 1 km and 150 m, respectively. The basin atmosphere total q_v fell by 2–3 g kg^{-1} overnight, resulting in a latent heat release that was 33–53 % of the overall basin sensible heat loss. Theory was used to indicate that the effects of dewfall and frostfall will be less during winter, when ambient air temperatures are lower. It is unclear whether dewfall and frostfall can have such a large impact in larger-scale topography. Note that dewfall depends on some initial T and q_v as well as T_0, where the latter is proportional to ground heat storage ΔQ_S, which is controlled by the surface energy balance $\Delta Q_S = R_n - Q_H - Q_E - Q_G$, where R_n, Q_H, Q_E and Q_G are fluxes of net radiation, sensible heat, latent heat and ground heat, respectively [e.g. Oke, 1987a].

During dewfall, the ground acts as a sink for water, reducing q_v, and so reducing the cooling rate further [boxes (5) and (6), respectively]. Since dewfall and frostfall deplete atmospheric moisture, it is reasonable to expect these processes to limit or prevent cloud formation within complex terrain. The prescence of clouds is likely to limit heat loss from complex terrain atmospheres [Cuxart & Jiménez, 2012], limiting the decrease of T_0 [boxes (7) and (8)], and so the ability of the surface to extract moisture from the air. Since cloud droplets are almost black-body radiators, clouds effectively absorb and re-emit longwave radiation back towards the ground surface (reducing the loss of longwave radiation to space). Although in general, it is reasonable to expect dewfall and cloud formation to occur separately, it is presumably possible for both processes to occur at different times during the night, or even at different locations at the same time. Furthermore, there are processes that can effectively reduce cloud mass in complex terrain, for example, cloud droplet deposition on ground surfaces [boxes (9) to (11)], as well as processes associated with snowfall [Whiteman *et al.*, 2007]. The latter includes the Bergeron Findeisen process, and Riming. The Bergeron Findeisen process includes the growth of ice crystals at the expense of water droplets, due to the lower saturated vapour pressure of ice crystals compared to water droplets. Riming involves the freezing of water droplets onto falling ice crystals, thereby removing cloud mass from an atmosphere [boxes (22) to (24)].

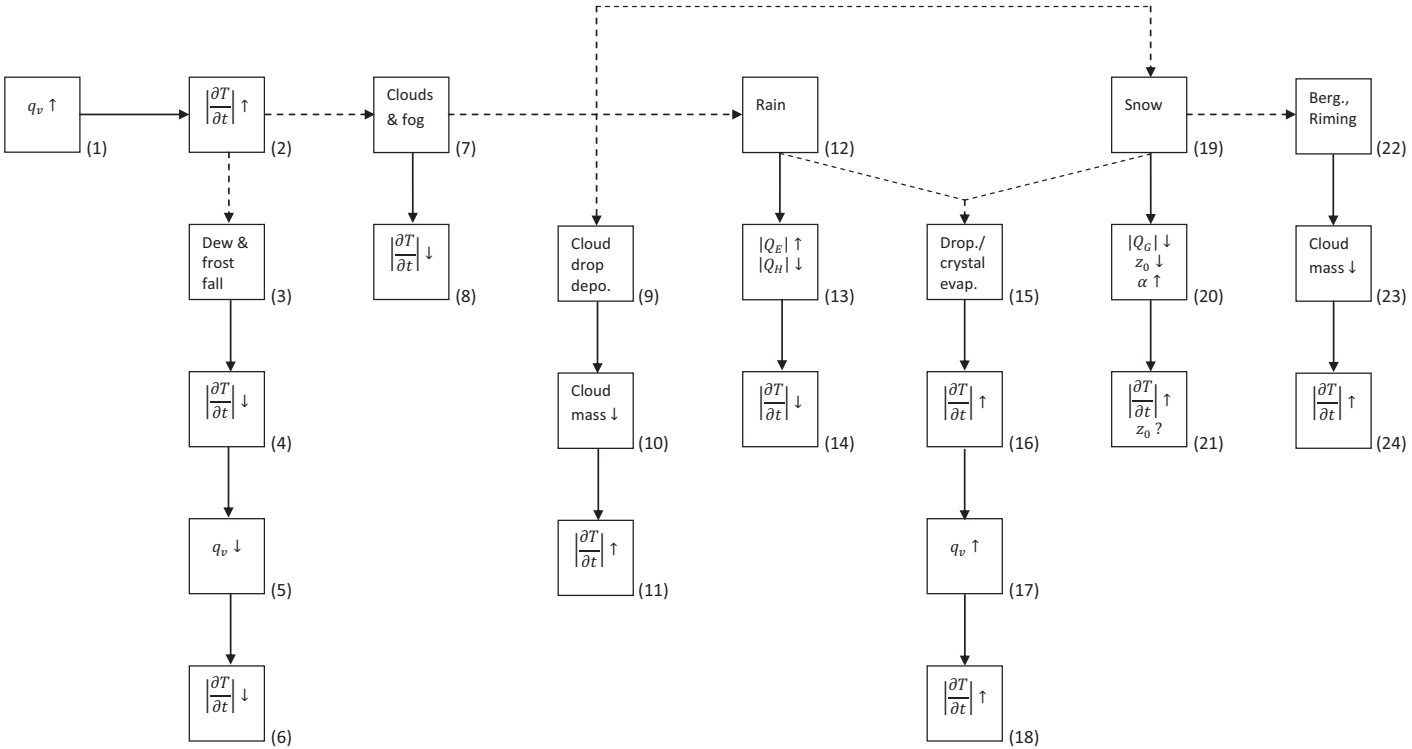

Figure I.5: Schematic diagram of processes affecting the nocturnal temperature evolution of complex-terrain atmospheres by changing the distribution and phase of water. Changes in cooling rates by the identified processes are denoted by $|\partial T/\partial t| \uparrow$ or $|\partial T/\partial t| \downarrow$. The diagram focuses on near-surface and depression-atmosphere average quantities, however, can generally also be applied to points in space; therefore no averaging notation has been used. Dashed lines represent conditional events (see text). The diagram aims to demonstrate the complex nature of moisture effects at night in complex terrain.

Radiation fog may form close to the ground if the surface is able to cool the adjacent atmosphere to its dew point. The formation of radiation fog is aided by the presence of a moist air mass close to the ground surface with drier air above, as well as a particular range of wind speeds. The former factor enhances radiation loss from the near-surface air, as moist air radiates longwave energy more effectively than either the cooler ground surface beneath or the drier air above it. Light winds transfer heat from the near-surface air to the ground by turbulent motions (i.e. $Q_H < 0$), however, stronger winds may weaken inversion strengths and/or dilute near-surface moisture concentrations [Oke, 1987a]. Presumably radiation fog reduces $|\partial T/\partial t|$ by reducing the loss of longwave energy to space.

Rainfall is likely to increase surface moisture (M_s), increasing the flux of latent heat at the ground surface Q_E, and reducing fluxes of sensible heat Q_H, thereby reducing cooling rates [boxes (12) to (14)]. Gustavsson *et al.* [1998] found snow-covered ground to increase the intensity of cold-air pools in small-scale terrain, argued to be due to the poor thermal diffusivity of snow packs (reducing the magnitude of the ground heat flux $|Q_G|$). It was noted that heavy snowfall creates a smoother effective ground surface (represented by the aerodynamic-roughness length z_0 in Table I.2 and Fig. I.5), which is likely to increase downslope flow speeds, although the effect of this latter factor on complex terrain cooling rates is less clear (see also § I.2.3.d). Rain and snowfall are likely to increase the emissivity ϵ_r of a surface (increasing losses of thermal radiation), and heavy snowfall will increase its albedo α_r (reducing absorption of solar energy). These effects are summarised in boxes (19) to (21).

Chazette *et al.* [2005] show that snow covered Alpine valleys, under clear skies, can suppress daytime convection, due to increased α_r and ϵ_r. The conditions prevented the growth of near-neutral (mixed) layers from the valley floor, allowing (approximately 450-m deep) GBIs to exist during daylight hours. Chazette *et al.* [2005] made measurements during daylight hours in the morning and afternoon in two Alpine valleys; one snow covered (Chamonix valley) and the other free of snow (Maurienne valley), the latter also under clear skies. Both sets of measurements were made in January 2003 and the two valleys have similar depths and breadths. Given the weak convection within the snow covered valley, it is likely that the morning profiles are representative of the nocturnal period, for this case. Note that Fig. I.5 was developed for the nocturnal case and part of it would need to be adjusted for daylight hours. For example, the presence of clouds during daytime reduces the development of mixed layers, which may help to create persistent cold-air pools [essentially in contrast to boxes (7) and (8)].

Evaporation of rain drops and sublimation of snow crystals can occur if these hydrometeors fall through subsaturated air [e.g. Forbes & Hogan, 2005]. The transformation of water from its liquid (or solid) form into its vapour phase requires an energy

input, which comes from the surrounding atmosphere, thereby increasing the cooling rate [boxes (15) and (16)]. The subsequent increase of q_v should in theory cause a further increase of cooling rates [boxes (17) and (18)]. However, these processes need enough space to occur, that is, a layer of subsaturated air beneath a cloud bank; they might not therefore be an important factor in small-scale terrain. The nature and importance of the processes, summarised in Fig. I.5, which affect the temperature evolution of complex terrain atmospheres, and how exactly they interact with one another in different topographies and ambient conditions, remains to be fully examined.

I.2.3.d Land-surface effects

Many topographic depressions are wooded [e.g. Blyth *et al.*, 2002]. The frictional effects of hills completely covered in trees on the flow above is reasonably well understood and modelled [see Belcher *et al.*, 2012, for a review]. Ross & Baker [2013] investigated the case of partially forested hills and found that the flow above the terrain is sensitive to the position of the forest on the slopes. The net drag on the ambient flow from the partially forested terrain was found to be modified from the case of fully forested slopes. Kiefer & Zhong [2013] examined the effects of sidewall forest canopies on the formation of CAPs using a 2D numerical simulation. Generally the cooling within the valley was found to be reduced by the presence of the forest. The rate of cooling of canopy elements was assumed to be equal to that of the adjacent canopy air spaces.

The complexity of urban areas may also be placed under the topic of land-surface effects. Solar energy accumulates in urban surfaces during the day and is subsequently released to the atmosphere during nocturnal hours. In addition there is an input of heat to the atmosphere from anthropogenic sources. This makes the lower layers of the atmosphere over large urbanised areas often near-neutral or slightly unstable [Roth, 2000]. Nevertheless, there can be occasions of temperature inversions, even in large cities [Wood *et al.*, 2010]. A detailed investigation into the effects of urban heat islands on the development of regions of enhanced cooling is required.

Urban areas are a key source of pollution in complex terrain, together with road transportation. Most of the scientific literature about air pollution in complex terrain focuses on how environmental conditions affect pollution concentrations and transport, particularly during daylights hours and close to the ground surface (see Chapter V for further discussion on this subject). Presumably pollutants can also affect the development of regions of enhanced cooling, for example, by modifying radiative transport processes, however, this subject is not well representated in the scientific literature.

Different land-use types may significantly change z_0, α_r, ϵ_r, M_s, Q_E, Q_H, Q_G, and ΔQ_S [e.g., see Oke, 1987a].

I.2.3.e Ambient winds (u_a)

A number of studies have discussed the effects of synoptic flows on complex terrain atmospheres [e.g. Doran & Horst, 1983; Gryning *et al.*, 1985; Sakiyama, 1990; Gudiksen *et al.*, 1992; Eckman, 1997; Whiteman *et al.*, 1997, 1998; Vosper & Brown, 2008; Price *et al.*, 2011].

Sakiyama [1990] analysed tethered balloon and Minisonde soundings tracked by Theodolites in the foothills of the Rocky Mountains, Alberta, Canada, during clear-sky days in September 1982. Sakiyama [1990] found a clear erosion of the down-valley flow by ambient winds directed up-valley, an effect not present when the ambient winds were directed mainly across the valley. This erosion effect is similar to that found by Whiteman & Zhong [2008] and Neff & King [1989].

In some complex terrain atmospheres elevated inversions form and persist close to the top of the terrain. Whiteman *et al.* [1997] describe four processes explaining the creation of elevated inversions; warming of air above terrain depressions by large-scale advection, cooling of complex terrain atmospheres, subsidence of air above terrain, and the growth of mixed layers from the bottom of complex terrain (starting from sufficiently strong atmospheric stability). Whiteman *et al.* [1997] analysed data from tethered and free-flying balloon ascents from the floor of the Grand Canyon region of Utah, New Mexico, Arizona, and Nevada, between 12 January and 3 March 1990. The measurements indicate that the first process usually caused the capping inversions close to the top of the Grand Canyon. Capping inversions are likely to trap pollutants within a complex terrain atmosphere, or inhibit pollutants from entering said atmosphere.

Despite the fragmented nature of the ring of mountains surrounding the Colorado Plateau, Whiteman *et al.* [1998] found the atmosphere above the plateau during mid-winter to exhibit characteristics of a basin atmosphere. Relatively high atmospheric stability was sometimes observed above the Colorado Plateau up to the maximum altitude of the highest mountains surrounding the plateau (2500 m a.m.s.l.) compared to the atmosphere above this height. The stable boundary-layer depth was observed to be significantly lower (approximately 600 m) outside of the Colorado Plateau. The observations indicate that the atmosphere close to the ground surface within the Colorado Plateau is largely decoupled from the atmosphere above 2500 m a.m.s.l., during mid-winter, and that this decoupling effect is likely to be greater than in the atmosphere outside of the plateau. Despite this decoupling effect, the evolution of the deep stable layer above the Colorado Plateau was found to be largely controlled by the passage of synoptic systems, and the associated advection of warm and cold air across the basin top. The lower regions of the stable layer were observed to be modulated by local effects including daytime growth of shallow convective boundary layers containing upslope winds, and the development of relatively intense nocturnal stable layers

and inversions, containing downslope and down-valley winds. Whiteman *et al.* [1998] note that the observed deep stable layer has too small a gradient to warrant the use of the term CAP.

The results of Whiteman *et al.* [1998] indicate that existing operational forecasting models will accurately represent the larger variations of the basin stable layer during mid-winter, however, will not be able to accurately capture all of the smaller localised modulating effects. Improved representation of these smaller variations might be gained from a parameterisation of slope flows.

Vosper & Brown [2008] used idealised 2D numerical simulations (with $\Delta x = 62.5$ m, and $\Delta z = 5$ m close to the ground surface) to study the formation of CAPs in hills. The width W_v of the valley was held constant whilst allowing the valley depth H, radiative cooling strength and $\mathbf{u_a}$ to vary. For a given radiative cooling strength and $\mathbf{u_a}$ the CAP intensity was found to increase with H as the valley floor becomes increasingly decoupled from the free flow above. A critical H was found beyond which no further increase in the CAP intensity occurred, and this critical value was found to correspond to a critical value of the inverse Froude number.

I.2.3.f Further external factors

The factors listed in the first column of Table I.2 may all be varied for one particular topographic depression. The development of regions of enhanced cooling might also be expected to depend on latitude Φ. Large changes in Φ can be expected to cause large changes in solar insolation, which is likely to alter the ambient atmospheric stability and surface conditions.

I.3 Analytical modelling of downslope winds

Despite the completion of field campaigns and advances in technology, the atmosphere continues to be undersampled, leading to ambiguity in the interpretation of observations, which is likely to be the case for the foreseeable future [Banta *et al.*, 2013]. In general, an improved understanding of downslope flows and regions of enhanced cooling has resulted from the combined efforts of observational, analytical and numerical studies. Analytical solutions to the simplified set of governing equations help to 'fill in the gaps' left by observations, and to confirm our understanding of particular atmospheric systems.

The essential physics explaining the initiation of downslope flows is now widely regarded to be well understood. Above a sloping surface a horizontal temperature gradient is created at night between the air adjacent to that surface and the ambient air further away from the slope, due to radiative heat loss from the ground to space.

A horizontal flow moving away from the slope is induced and a parcel soon finds itself surrounded by lighter neighbours and so is forced down the slope by gravity. The motion of a fluid parcel in such a system, expressed in a linear-orthogonal framework (x, y, z, t, i.e. a Cartesian system) can be expected to be described by

$$\frac{d\,\mathbf{u}}{dt} = -\frac{\nabla\, p}{\rho} - \nabla\,\phi - f_c\,\mathbf{e}_z \times \mathbf{u} + \nu\nabla^2\,\mathbf{u}, \tag{I.3}$$

[e.g., see Holton, 2004], where $\mathbf{u}$ is the velocity of the parcel, p is the pressure field, ρ is the air density, $\phi = g\,z$ (the geopotential), and g is the acceleration due to Earth's gravitational field. $f_c = 2\,\Omega_v$ is the Coriolis parameter, where $\Omega_v = \Omega \sin\Phi$ (the vertical component of Earth's angular speed Ω), and Φ is latitude. $\mathbf{e}_z$ is the basis vector for the local vertical, and ν is the kinematic viscosity of the fluid. This simplified form of the friction term assumes that the velocity field is non-divergent, that is, the fluid is assumed to be incompressible. This is reasonable given the relatively small height ranges considered in most cases.

Downslope flow analytical models fall into two main categories; those that assume a stationary flow in order to investigate its spatial structure, and those that assume spatial invariance and integrated characteristics in order to solve for the temporal changes of the flow (such as the models of Fleagle [1950] and McNider [1982a]). The former category can be subdivided further; that is, into models that solve for the variation of the flow through its depth [e.g. Prandtl, 1942], and those considering changes along the direction of the flow [e.g. Manins & Sawford, 1979]. The model of McNider [1982a] (that built on the work of Fleagle [1950]), and the model of Prandtl [1942] are considered below, respectively.

I.3.1 Downslope flow temporal variations

In contrast to earlier work, McNider [1982a] made the important step of incorporating an ambient lapse rate in potential temperature $\gamma \equiv \partial\theta/\partial z$, external to the downslope flow layer, and thus the restoring buoyancy force into the prediction of the downslope flow speed.

A slope-orientated coordinate system (s, y, n, t) is now introduced, by applying a linear orthogonal rotation to (x, y, z, t), so that $\mathbf{e}_x \cdot \mathbf{e}_n = -\sin\alpha$ and $\mathbf{e}_z \cdot \mathbf{e}_s = \sin\alpha$ (i.e. α is negative for clockwise rotations). s is directed down the slope and n is normal to and pointing away from the ground.

The simplified set of governing equations used by McNider [1982a] has the form

$$\frac{\partial u_s}{\partial t} = g \frac{\theta'}{\theta_a} \sin\alpha - k_t u_s,$$

$$\frac{\partial \theta}{\partial t} = -u_s \gamma \sin\alpha + L_c, \tag{I.4}$$

where $u_s(n,t)$ is the along-slope flow speed, $\theta'(n,t)$ is the potential temperature perturbation from the ambient/base state, that is, $\theta(n,t) - \theta_a$, where $\theta_a = \theta_0 + \gamma \delta z$, where θ_0 is a constant reference temperature (assumed here to be at the bottom of the slope), and γ is a constant stratification. k_t is a damping (friction) coefficient, and L_c a local diabatic warming/cooling rate. k_t, L_c and α were set constant in the analytical model.

A number of assumptions and simplifications were required to arrive at the set of equations (I.4), which are stated here, followed by a more detailed discussion of these assumptions below. Beginning with Eq. I.3, the effects of the Earth's rotation were neglected, as were variations and motions along y, that is, in the direction across the flow, so that $\partial/\partial y = 0$ and $v = 0$, making the problem 2D. The Boussinesq approximation was then applied, with conservation of mass reducing to conservation of volume. The vertical component of friction was neglected, which implies that vertical motions are small compared to horizontal ones, typical of more gentle slopes. After a transformation to a slope-orientated coordinate system (as above), variations along s were neglected, which together with the Boussinesq approximation, made the fluid hydrostatic along n (i.e., a quasi-hydrostatic state was reached). This also eliminated the pressure force along s. A first-order approximation was made to reduce the number of variables, to allow for a solution (i.e., $\rho'/\rho_r \approx -\theta'/\theta_a$, where ρ' is the perturbation density from the constant reference density ρ_r). The friction force was represented simply as $F_{f_x} = -k_t u$, to allow for a solution. These manipulations gave the momentum equation in Eq.-set (I.4).

Irreversible changes in a parcel's heat energy were assumed to occur at a constant rate L_c, due to the cooling effect from a homogeneous surface. Moisture effects were only considered implicitly through this term. The model does not explicitly account for heat transfers between the ground skin layer and the deep soil. The stratification was assumed to be linear (setting γ constant), and variations in temperature along the slope were assumed to be only due to the constant ambient temperature field. This leads to the energy equation in Eq.-set (I.4). Variables representing the flow at a point in space were assumed to represent layer-averaged quantities (denoted by $\overline{\zeta}$, where ζ is any variable), transforming partial derivatives into ordinary derivatives.

The equations in Eq.-set (I.4) could then be combined to find

$$\frac{d^2\overline{u_s}}{dt^2} + k_t \frac{d\overline{u_s}}{dt} + \left(\frac{g\,\overline{u_s}\,\gamma}{\theta_a}\right)\sin^2\alpha = \frac{g}{\theta_a}\overline{L_c}\sin\alpha, \tag{I.5}$$

a second-order linear ordinary differential equation with constant coefficients and non-zero right-hand side. Note that initially θ_a is a function of z, and so a representative ambient value is then chosen to set θ_a constant.

If $k_t^2 \geq 4\,(g\,\gamma/\theta_a)\sin^2\alpha$, that is, the case of critically or overdamped motion, the flow is subjected to a strong damping force and proceeds directly to an equilibrium state for which $\overline{u_s}$ is proportional to the forcing $\overline{L_c}$. This can only be the case for extremely small slope angles or near-neutral conditions. For most cases $k_t^2 < 4\,(g\,\gamma/\theta_a)\sin^2\alpha$, that is, the motion is under-damped or oscillatory and the general solution to Eq. (I.5) has the form

$$\overline{u_s} = A_1\, e^{-\frac{1}{2}k_t\,t}\cos\left(\omega_d\,t - \varphi\right) + \frac{\overline{L_c}}{\gamma\,\sin\alpha}, \tag{I.6}$$

where ω_d is the damped frequency of the oscillation, given by

$$\omega_d = \left(\frac{g\,\gamma}{\theta_a}\sin^2\alpha - \frac{1}{4}k_t^2\right)^{1/2}, \tag{I.7}$$

and where A_1 and φ are arbitrary constants, that given the initial conditions $\overline{u_s}\,(t=0) = 0$, and $d\overline{u_s}\,(t=0)\,/dt = 0$, are

$$A_1 = -\frac{\overline{L_c}\,(k_t^2 + 4\,\omega_d^2)^{\frac{1}{2}}}{2\,\omega_d\,\gamma\,\sin\alpha}, \quad \varphi = -\arctan\left(-\frac{1}{2}\frac{k_t}{\omega_d}\right),$$

which yields

$$\overline{u_s} = \frac{\overline{L_c}}{\gamma\sin\alpha}\left[1 - \left(k_t^2 + 4\,\omega_d^2\right)^{\frac{1}{2}} e^{-\frac{1}{2}k_t\,t}\cos\left(\omega_d\,t - \varphi\right)/\left(2\omega_d\right)\right], \tag{I.8}$$

It can be seen from Eq. (I.8) that $\overline{u_s}$ is directly proportional to $\overline{L_c}$, but inversely proportional to γ and $\sin\alpha$. Also the period of the oscillation is dependent on γ, $\sin^2\alpha$, and k_t^2, however the effect of k_t on ω_d is negligible. The exponential term indicates that the oscillations will decrease over time until $\overline{u_s} = \overline{L_c}/\left(\gamma\sin\alpha\right)$, which is the steady-state or particular solution that remains after the transient has vanished.

Figure I.6 shows $\overline{u_s}$ given by Eq. (I.8) for three stratifications and illustrates that both the period of the oscillations as well as the speed of the downslope flow are strongly dependent on the ambient stratification.

The oscillatory behaviour of downslope winds was first explained physically by Fleagle [1950]. As a parcel accelerates under the influence of an increasing pressure gradient, it increases in speed until the pressure gradient vanishes; at this time the

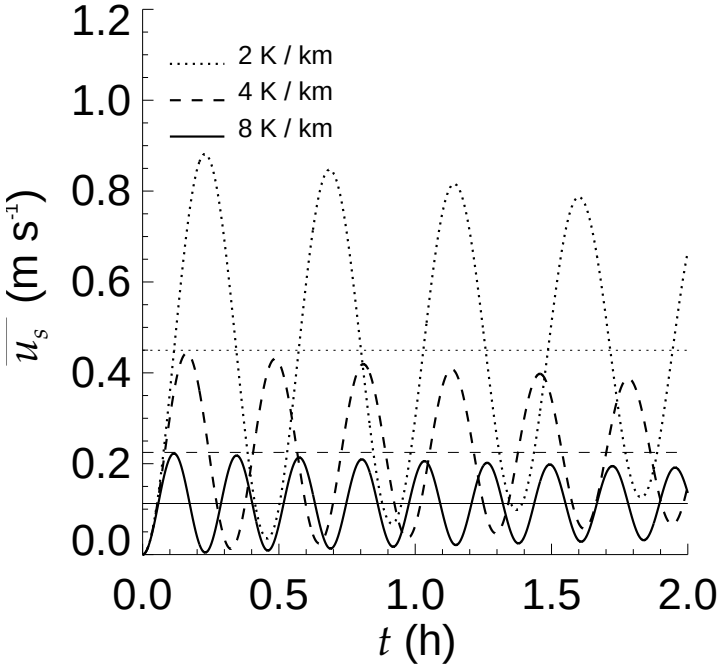

Figure I.6: Time series of the layer-averaged downslope velocity component from the analytical solution (I.8) derived by McNider [1982a], for three ambient lapse rates in potential temperature, where $\theta_0 = 288$ K, $\delta z = 500$ m, $\overline{L_c} = 1.5$ K h^{-1}, $\alpha = 27.6°$, and $k_t = 10^{-4}$ s^{-1} (see text for details).

adiabatic heating exceeds the radiational cooling. Continued downslope flow and consequent adiabatic heating result in an oppositely directed pressure gradient which slows the particle until radiational cooling again reverses the pressure gradient. The incorporation of an ambient atmospheric stratification by McNider [1982a] enhances this oscillation. As the parcel moves downslope it will encounter air with a lower potential temperature (in stable fluid) and so its motion will be opposed by a positive buoyancy force.

The assumptions made to arrive at Eq. (I.8) have been noted above. The importance of ambient rotation can be ascertained by reference to the Rossby number $Ro = U/(\Omega L)$. Assuming a representative flow speed $U = 2$ m s^{-1}, and length scale $L = 3$ km, where Ω is taken to be 10^{-4} rad s^{-1}, gives $Ro \approx 7 > 1$; therefore, with these scales the Coriolis 'force' can be safely neglected.

Whether or not it is reasonable to assume no variations or motions along y depends on the particular case considered (i.e., on the geometry of the terrain and whether or not there are any complicating factors that must be accounted for). For example, without any complicating factors, such a simplification might have been justified for

the downslope flow investigated by Doran & Horst [1983] where the flow was observed to exist over a near-idealised and approximately 2D slope. With such a geometry the major component of the downslope flow can be expected to exist in, or be very close to, the (x, z) plane, with only relatively small variations and motions occurring along y. This assumes that the Cartesian x-axis is aligned with the maximum gradient of the slope, where the directional derivative $dz/ds = \nabla z \cdot \mathbf{n}$ is maximised. ds is an element of distance, and $\mathbf{n} = \mathbf{e}_x\, x + \mathbf{e}_y\, y + \mathbf{e}_z\, z$ a unit vector in a given direction. The downslope flow can be expected to deviate from the (x, z) plane by small amounts due to a very small Coriolis acceleration term, small variations in surface characteristics, and turbulence effects. In the example investigated by Doran & Horst [1983], the complicating effects of ambient winds are likely to have deflected the downslope flow further away from the (x, z) plane.

The assumption of incompressibility is reasonable given the small height ranges usually considered, together with the expected speeds of the flow. The application to less steep slopes is restrictive if a consideration of steep slopes is required. The neglect of variations along s is highly questionable as is a constant cooling rate $\overline{L_c}$ (see Chapter IV). It has been noted by Noppel & Fiedler [2002] that variations in radiational cooling are likely to have a significant effect on the flow dynamics.

There is numerical evidence to suggest that away from the valley sidewalls and within a developing region of enhanced cooling, the assumptions of a constant γ and horizontal isentropes are valid [e.g. McNider, 1982a]. However, the assumption of a stationary stratification cannot be justified since it is the sidewall cooling, subsequent downslope flows and radiative divergence within the valley atmosphere which help to build the valley stable layer. The analytical solution developed by [McNider, 1982a] is likely only valid for time intervals when the change in stratification is small. Seiches within confined valleys, breaking waves, or shear instabilities may all be candidates for producing short period surges in downslope flows [McNider, 1982a].

I.3.2 Downslope flow profiles

The derivation of the analytical model by Prandtl [1942] is initially identical to that of McNider [1982a]. Equation-set I.4 can then be modified to give a more accurate representation of the friction force and the diabatic cooling rate. $-k_t\, u_s$ is replaced by $\nu_t\, \partial^2 u_s/\partial n^2$ (compare to the friction term in the Navier-Stokes equation, Eq. I.3), and similarly L_c is replaced by $\kappa_t\, \partial^2\theta'/\partial n^2$. ν_t and κ_t are turbulent mixing coefficients for momentum and heat energy, respectively, and are set constant in the analytical model. Therefore, the two terms are given a form analogous to that expected for molecular diffusion. By making Eq.-set I.4 a stationary system, these partial derivatives may be re-written as ordinary derivatives, enabling a solution. The modified equation set can

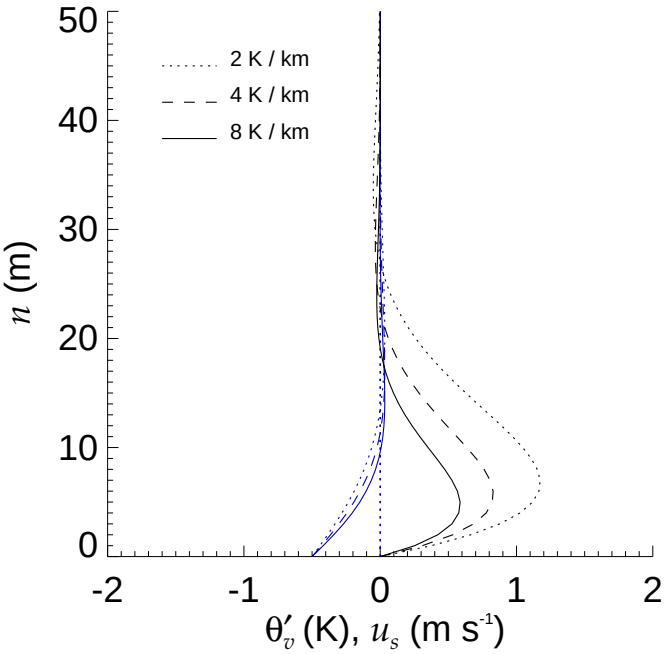

Figure I.7: Profiles of stationary downslope flow speed and potential temperature perturbation from the analytical model of Prandtl [1942], in a slope-oriented coordinate system (s, y, n), for three ambient stratifications. The required constants were set as $A_2 = -0.5$ K, $\alpha = 27.6°$, $\theta_0 = 288$ K, $\delta z = 500$ m, $\nu_t = 0.08$ s^{-1}, and $\kappa_t = 0.25$ s^{-1}, see text for details.

then be combined to find

$$\frac{\nu_t \, \kappa_t}{\gamma \, \sin\alpha} \, \frac{d^4 \, \theta'}{dn^4} + \frac{g \, \sin\alpha}{\theta_a} \, \theta' = 0, \tag{I.9}$$

a linear fourth-order ordinary differential equation with constant coefficients and no forcing term on the right-hand side. Note that θ_a is first allowed to vary with z, with $\theta' = \theta - \theta_a$, and so a representative ambient value is then chosen to set θ_a constant. Given the required boundary conditions $n \to \infty : \ \theta'$ and $u_s \to 0$, and $n = 0 : \ \theta' < 0$, $u_s = 0$, the particular solution to Eq. I.9 has the form

$$\theta' = A_2 \, e^{-n/l} \, \cos\left(n/l\right), \tag{I.10}$$

where it is clear that $A_2 = \theta' \, (n = 0)$. The constant l has the form

$$l = \left(\frac{4 \, \nu_t \, \kappa_t \, \theta_a}{g \, \gamma \, \sin^2 \alpha} \right)^{1/4}, \tag{I.11}$$

the solution for θ' can then be substituted into the momentum equation, modified

from Eq.-set I.4, to solve for u_s, which is given by

$$u_s = -A_2 \left(\frac{g\,\kappa_t}{\theta_a\,\nu_t\,\gamma} \right)^{1/2} e^{-n/l} \sin\left(n/l\right). \tag{I.12}$$

Figure I.7 shows θ' and u_s, using Eq. I.10 and Eq. I.12, respectively, for three ambient stratifications (as indicated), with $A_2 = -0.5$ K, $\alpha = 27.6°$, $\theta_0 = 288$ K, $\delta\,z = 500$ m (used to calculate θ_a), $\nu_t = 0.08$ s^{-1}, and $\kappa_t = 0.25$ s^{-1}. The chosen parameters enable a comparison with the results of the numerical simulation performed for this study, a comparison which is provided in Appendix E.

More recent work has removed some of the limitations of the model derived by Prandtl [1942], for example, Stiperski *et al.* [2007] included the Coriolis acceleration in their model, and Grisogono & Oerlemans [2001] included a gradually varying eddy diffusivity.

I.4 Notes on parameterisation of complex terrain effects

Development of a parameterisation scheme falls beyond the scope of this work, however, it is useful to make some initial notes. Progress has been made at parameterising the effects of downslope flows. For example, Haiden *et al.* [2011] developed an analytical model based on the conceptual mass-flux model of Whiteman *et al.* [2010], developed from observations, to parameterise the evolution of the atmospheric vertical temperature profile in the Arizona Meteor Crater, starting several hours after sunset. The model considers clear calm conditions, dynamics effects only, and is designed for the more unusual case of a continuous source of dense air falling into a depression atmosphere. Many downslope flows are formed of dense air created along a section of sloping ground by radiative cooling of the ground surface. Comparisons between numerical results and observations confirmed that the analytical model accurately predicts the evolution of the crater's atmospheric vertical temperature profile, later in the night, under the assumed conditions. Accurate results from the analytical model are dependent on an accurate initial temperature profile and knowledge of surface wind speed and temperature. The model assumes a constant downslope flow depth and a constant entrainment coefficient, and was derived by a transformation between a Lagrangian and Eulerian coordinate system.

Parameterisation of the effects of complex terrain on near-surface temperatures and larger-scale mixing in operational forecasting models will presumably need to be largely independent of existing surface meteorological variables and temperature profiles within the topographic depressions.

The above sections have demonstrated the complexity of cold-air pooling processes, and the large number of factors that effect these processes. Two diagnostic quantities of interest, associated with cold-air pooling processes, are near-surface and valley-averaged air temperatures (denoted by ΔT_{sgs} in Table I.3). The second row (excluding the first two columns) of Table I.3 lists those factors that are likely to be important for the evolution of ΔT_{sgs}, and factors which are likely to be available in a numerical weather prediction (NWP) model to parameterise ΔT_{sgs}. It should be possible to derive these factors from the land-surface model (LSM) used by a NWP model, as well as from the resolved fields (i.e., above the complex terrain).

		Slope flows, SEB[1]			Pooling/Draining		Ambient flow effects			Cooling potential[2]	
Dimension	ΔT_{sgs}	$1/z_0$	$1/F_{r_a}$	F_{s_a}	$\frac{d}{dy}\left(\frac{W_v}{A_v}\right)$	$1/\Delta p_a$	$1/\mathbf{u_a}$	H	$1/W_v$	$1/I_{\downarrow a}$	t
L	0	-1	2	-2	-2	1	-1	1	-1	0	0
T	0	0	1	-1	0	2	1	0	0	3	1
M	0	0	-1	1	0	-1	0	0	0	-1	0
Θ	1	0	0	0	0	0	0	0	0	0	0

First column contains the list of relevant dimensions for the system in question, that is, L = length, T = time, M = mass, Θ = temperature, where symbols have been used to represent the dimensions to simplify the analysis. F_{r_a} and F_{s_a} are the flux of rain and snow mass, respectively, through a surface above the complex terrain atmosphere. All subscript 'a' denote ambient conditions above the complex terrain atmosphere. $I_{\downarrow a}$ is the irradiance (i.e., energy per second per unit area; flux density) downwelling through a surface above the complex terrain atmosphere.

[1] SEB = surface energy balance. The terrain slope angle should be included in this group. Taking the sine or cosine of this angle makes it dimensionless, excluding the factor from this table. The mean slope angle of the terrain can be found from H and W_v (see text).
[2] The TAF and RH_a, which are dimensionless, should be included in this group.

Table I.3: Dimensional matrix

An attempt has been made to give the basic proportionality between ΔT_{sgs} and the controlling factors, and some brief discussion of this is of use. The key factors have been grouped by considering the key physical effects they have on cold-air pooling processes (see first row of Table I.3).

$\Delta T_{sgs} \propto 1/z_0$ has been assumed following the results of Kiefer & Zhong [2013], however, it should be noted that Gustavsson *et al.* [1998] found that forests shelter the atmospheres of hilly terrain from ambient winds, which enhances the cooling. $\Delta T_{sgs} \propto 1/F_{r_a}$ assumes that the main effect of rainfall is to partition more energy into latent heat by modifying ground-air energy fluxes. The resulting increased moisture contents of complex terrain atmospheres is assumed to be a smaller effect, which is perhaps indicated by the work of Hoch *et al.* [2011a]. Given the complexity of moisture effects, demonstrated above (§ I.2.3.c), this assumption would need to be confirmed by further work. There is little doubt that $\Delta T_{sgs} \propto F_{s_a}$, for example, indicated by the work of Gustavsson *et al.* [1998], Chazette *et al.* [2005] and Chemel & Chollet [2006]. It seems reasonable to assume that poorly-drained valleys will be more effectively cooled and therefore, from the work of McKee & O'Neal [1988], $\Delta T_{sgs} \propto \frac{d}{dy}\left(\frac{W_v}{A_v}\right)$. The ability of a valley to drain air also depends on the strength of mountain-to-plain

pressure differences [McKee & O'Neal, 1988], denoted by Δp_a in Table I.3 (where all subscript 'a' denote ambient conditions above the complex terrain atmosphere). It is therefore assumed that near-surface pressure differences are well correlated with pressure differences above the complex terrain atmosphere. It is now well known that $\Delta T_{sgs} \propto 1/\mathbf{u_a}$ and $\Delta T_{sgs} \propto H$ [e.g. Vosper & Brown, 2008; Price *et al.*, 2011], where the direction of the ambient flow is important as well as its strength (speed). The effects of ambient winds might be expected to generally decrease for more narrow valleys. Hoch *et al.* [2011a] found that near-surface radiative cooling dominates changes in average-valley atmosphere radiative cooling when reducing the width of complex terrain atmospheres. Given similar valley depths, a greater portion of depression atmospheres will be affected by near-surface radiative cooling in more narrow valleys; these arguments were used to set $\Delta T_{sgs} \propto 1/W_v$. More cooling can be expected with reduced radiative energy inputs from above complex terrain ($\Delta T_{sgs} \propto 1/I_{\downarrow a}$), which can be expected to occur, for example, at night, during the winter season, at greater Φ, or when cloud cover exists above complex terrain atmospheres during daylight hours. A general timescale t has also been added, with the expectation that the identified variables cannot account for all of the variations of ΔT_{sgs}.

Since the exact forms of the relationships between ΔT_{sgs} and the key identified factors are not known, or at least not fully known, a first straightforward step towards developing a parameterisation of ΔT_{sgs} is to conduct a dimensional analysis for the system of interest, which might be used to scale the problem. The Buckingham Pi theorem [Vaschy, 1892; Riabouchinsky, 1911; Buckingham, 1914] states that the n variables involved in a problem combine to form exactly $(n - r)$ independent non-dimensional variables, known as Π numbers (i.e., non-dimensional products), where r is the rank of the dimensional matrix (Table I.3). The fundamental dimensions of length, time, mass and temperature (denoted by L, T, M and Θ, respectively) are given in the first column of the table, where symbols have been used to simplify the analysis. In other words, a function $f(q_1, q_2, \ldots, q_n) = 0$ can be re-expressed as $f(\Pi_1, \Pi_2, \ldots, \Pi_{n-r}) = 0$. For the problem defined above, $n = 11$ and $r = 4$, giving 7 possible Π numbers (shown below), where the last two numbers were already known without recourse to formal dimensional analysis. Note that Π_6 can be used to compute a mean slope angle, which is known to have an important effect on the characteristics of downslope and down-valley flows. Alternatively, a more accurate measure of a depression's range of slope angles might be obtained from the available LSM. The latter could be used to compute the mean, maximum and range of slope angles, or the shape of the slope, for different terrain depressions, variables that could be used to better represent the effects of slope flows. Π_9 has been included to account for the effects of clouds above complex terrain atmospheres at night, since this is likely to reduce the cooling.

It is important to realise that the Π numbers are not necessarily the most physically meaningful for the problem in question, however, they may be manipulated and/or combined into more useful forms. For example, $\Pi_2\,\Pi_3 = F_{s_a}/F_{r_a}$ represents the competing effects of rainfall and snowfall, $1/\Pi_7 = H/(\mathbf{u_a}\,t)$ represents the competing effects of ambient winds and terrain depression depth (together with a timescale), $\Pi_3^2\,\Pi_5\,\Pi_6\Pi_7\,\Pi_7^{-4} = H^4\,F_{s_a}^2/\left(I_{\downarrow a}\,\Delta\,p_a\,W_v\,t^3\right)$ includes the effects of large-scale pressure gradients and downwelling radiation above the depression atmosphere.

$$\Pi_1 = \frac{H}{z_0} \qquad \Pi_2 = \frac{I_{\downarrow a}}{\mathbf{u_a}^2\,F_{r_a}} \qquad \Pi_3 = \frac{\mathbf{u_a}^2\,F_{s_a}}{I_{\downarrow a}} \tag{I.13}$$

$$\Pi_4 = H^2\,\frac{d}{dy}\left(\frac{W_v}{A_v}\right) \qquad \Pi_5 = \frac{I_{\downarrow a}}{\mathbf{u_a}\,\Delta\,p_a} \qquad \Pi_6 = \frac{H}{W_v} \tag{I.14}$$

$$\Pi_7 = \frac{\mathbf{u_a}\,t}{H} \qquad \Pi_8 = \mathrm{TAF} \qquad \Pi_9 = \mathrm{RH}_a \tag{I.15}$$

Further work might consider the development of an optimised set of Π numbers and aim to determine the relationships between the different Π numbers, for example, by sensitivity studies using numerical simulations and field experiments. The key factors above were identified based on their assumed availability in a NWP model and it is important to note that they may well not describe the full variability in the system of interest. More variables may need to be considered (see Table I.2) in order to fully describe the system and the relationships between the Π numbers.

Those factors that seem to be particularly important for cold-air pooling processes, chosen by considering the literature review above, have been highlighted in orange in Table I.2. Note that a number of surface variables (α_r, ϵ_r, M_r, Q_E, Q_H and Q_G) are partially dependent on other factors, for example, q_v, rain and snow. As in § I.2.3.c, Q_E represents dewfall and frostfall processes. t, Φ, shadows and clouds can be expected to strongly affect ambient radiative fluxes. 2D depression shape might be represented by the TAF and 3D depressions might be represented by the strength of any along-valley flow, for example. Note that possible error sources within the numerical model have been neglected when considering the parameter space.

Even considering the reduced set of factors identified in Table I.2 a future sensitivity study conducted by varying these factors in a numerical simulation is a daunting task. If it is assumed that a numerical model is used with the same grid as that used herein, then from Table B.1, in Appendix B, a single simulation for the full nocturnal period can be expected to take approximately 104 hours. Considering 14 factors for the sensitivity study, each with say 10 values gives 10^{14} simulations, which is clearly

unpractical. Another approach might be to manually conduct the sensitivity study, identifying near-linearities and non-linearities in the system to reduce the parameter space as the study develops. Further work might consider trying to optimise (reduce) the number of factors in Table I.2. Alternatively, it might be possible to use stochastic methods to reduce the time required for the sensitivity study.

Lee *et al.* [2011] used a Gaussian process emulator to estimate a multi-dimensional parameter space, using information from a small number of numerical model runs at points chosen using a Latin hypercube space-filling design. Gaussian process emulation is a Bayesian approach that uses information from the model runs along with some prior assumptions about the model behaviour to predict model output everywhere in the uncertainty space. This is a subject for future research.

Given the complexity of the system, it remains to be seen whether or not an effective general parameterisation scheme can be developed before advances in computing platforms. It might be more realistic to aim for incremental improvements in the representation of cold-air pooling processes in operational weather and climate models.

I.5 Main scope of the study

Whilst the physics behind the initiation of flows on simple isolated slopes is now considered to be reasonably well understood, much uncertainty remains about the forcing mechanisms controlling the evolution of regions of enhanced cooling in terrain depressions, as well as the complex interactions these regions have with slope flows. The effects these interactions have on the dispersal of airborne pollutants needs to be quantified. These subjects are the focus of the work presented hereafter.

The approach taken here was to define a simple idealised alpine valley, together with its initial overlying atmosphere, which are appropriate for a winter period. The work considers the case of decoupled conditions, where local processes and effects dominate the system, with slope flows and regions of enhanced cooling, interacting with one another, being two key examples. To simplify the problem, this study considers the case of negligeable down-valley flows, and avoids cloud formation, precipitation, and dewfall/frostfall. The full list of initial and boundary conditions used for this study, together with the justification for using them, are provided in Chapter III. The justification for using many of the chosen initial and boundary conditions has effectively been presented above. Due to time constraints the analysis considers half the nocturnal period and so considers the early growth and development of the region of enhanced cooling.

Essentially the idea was to set up a well controlled experiment, which has allowed the system's essential thermodynamical atmospheric processes to be quantified. Although only one numerical set-up has been used here, its idealised nature lends itself

to future sensitivity studies. Studies based on real topographies and atmospheres have proved invaluable for improving understanding of the physics of particular cases (as the above discussions demonstrate), however, the greater complexity of these cases can make it more difficult to quantify the essential physical processes. The usefulness of the approach taken by this study, together with some discussion of the great value and problems of real case studies was made by Zardi & Whiteman [2013]. It seems reasonable to start with a simple case, to fully understand it, before adding complexity and then re-examining the evolution of the system, allowing the effects of greater complexity to be more clearly understood. The aim and objectives of this work are as follows:

I.6 Aims and Objectives

Aim

To elucidate the evolution of key atmospheric thermodynamical processes, and their interactions with passive scalars emitted close to the ground surface, for an idealised alpine valley topography, under stable, decoupled, poorly-drained, and simplified microphysical conditions.

This aim will be met by the following objectives:

Objectives

1. To quantify the key atmospheric thermodynamical processes focusing on the depression atmosphere as a whole.
2. To quantify the evolution of key thermodynamical processes across the complex terrain atmosphere, including the interactions between slope flows and the region of enhanced cooling.
3. To quantify the interactions of key valley-atmosphere thermodynamical processes and passive tracers emitted close to the complex terrain surface.

In the next chapter, the modelling approach used for this work will be explained, together with some introductory material about the chosen model itself.

II

Computational methods

II.1 Methodology

Computational fluid dynamics (CFD) models, NWP models and global climate models (GCMs) solve the Navier-Stokes equations in order to simulate the atmosphere, however, they are designed for different domain length and time scales, and applications.

Here the term CFD models refers to models that consider microscale domains (i.e., domains with lengths of about 1 km or less). CFD models are frequently used in the manufacturing industry, for example, to investigate the aerodynamics of vehicles, to quantify combustion inside internal-combustion engines and gas turbines, or to examine flows inside rotating passages and diffusers [Versteeg & Malalasekera, 2007]. However, CFD codes have a wide range of applications and are also used within atmospheric science. Skyllingstad [2003] conducted a CFD simulation with a domain length along s, y and z of 765, 150 and 35.5 m, respectively, to investigate the characteristics of downslope flows. A consideration of microscale domains makes the use of turbulence resolving grids practical. CFD codes typically assume an incompressible atmosphere and neglect atmospheric physical processes such as radiative transfer, land surface processes, microphysics and unresolved surface roughness (e.g. Skyllingstad [2003]). These models often use boundary-fitted curvilinear or unstructured grids, and effectively simulate fluid flow above complex boundaries. CFD models most commonly use an eddy-viscosity type of turbulence closure, either based on a Reynolds-Averaged Navier-Stokes (RANS) or a LES approach.

NWP and GCMs are designed for mesoscale (of the order of 10 to 100 km) to global domains where it is not practical to resolve turbulence with existing computing platforms. Instead turbulence effects must be parameterised. NWP models usually consider a non-hydrostatic fully compressible atmosphere, whereas GCMs use the hydrostatic approximation. NWP and GCMs parameterise physical processes occurring in the atmosphere and near-surface ground. The governing equations of NWP and GCMs are written for spherical coordinates and are then projected onto planar surfaces using map projections. Vertical coordinates can be based on pressure, height or θ

and are commonly terrain-following. Such coordinate systems are limited in their ability to accurately simulate the atmosphere close to complex terrain surfaces, especially using the grid resolution of NWP and GCMs. Steep slopes distort the computational grid causing errors, for example, in the approximations of horizontal gradients. The immersed-boundary method (IBM) avoids the grid distortion problem and has now been partly implemented in the Weather Research and Forecasting (WRF) model [Lundquist *et al.*, 2012]. This is the first time the method has been used in a NWP model. Further work is required to complete and verify the implementation and the option is not yet generally available to the atmospheric science community.

This study considers a mesoscale domain which makes the use of a full CFD code impractical. Furthermore the problem considered requires an accurate simulation of physical processes such as radiative transfer, land surface processes and microphysics. In the past the ratio of turbulent length scale to filter width (grid resolution) was either very large of small, however, advances in computing have led to simulations where the ratio is on the order of one. The simulation completed for this work, using the WRF model, is an example of this. It has been noted that many research questions remain about such simulations [Zardi & Whiteman, 2013]. It can be said that WRF has generally been run in LES mode for this study [made possible by using a high-performance computing (HPC) system], however, this can probably not be said of the atmosphere close to the ground surface (see Appendix A).

An introduction to the WRF model is now provided together with a derivation of the WRF model governing equations. The derivation is restricted to a transformation from the Navier-Stokes equation in Cartesian coordinates to the hydrostatic-pressure terrain-following coordinate system. The use of a terrain-following grid (i.e., a structured curvilinear, or body-fitted grid) has several advantages over the linear orthogonal (Cartesian) coordinate system. Use of a body-fitted grid avoids the waste of computer memory and resources that can occur with the Cartesian system due to the occurrence of grid cells in regions where they are not needed, for example, within the terrain. Body-fitted grids enable the grid spacing to be varied across the domain allowing a more effecient use of the available computing resources; the grid resolution can be increased locally wherever the solution is expected to show large variations. Body-fitted grids improve the representation of complex boundaries and so the physical interactions between the boundary and the atmosphere. One disadvantage of body-fitted grids is that they make the governing equations of motion more complex (see Versteeg & Malalasekera [2007], or similar texts, for more details).

II.2 Basics of the Weather Research and Forecasting Model

The WRF model was designed for both research and operational numerical weather prediction, and was partly developed to promote discussions between the two sectors, from which both might benefit. The WRF model began as a collaborative effort between the NCAR Mesoscale and Microscale Meteorology (MMM) division, NOAA's National Center for Environmental Prediction (NCEP) and Earth System Research Laboratory (ESRL), the US Department of Defense's Air Force Weather Agency (AFWA) and Naval Research Laboratory (NRL), the Center for Analysis and Prediction of Storms (CAPS) at the University of Oklahoma, and the US Federal Aviation Administration (FAA), with the participation of university scientists. The development of the WRF model is now an international effort. WRF was developed as a portable Fortran code, capable of running on powerful parallel systems or a single computer, and suitable for simulating a wide range of atmospheric systems [see Skamarock *et al.*, 2008, for a complete description of the WRF model].

WRF has two dynamics solvers; the Non-hydrostatic Mesoscale Model (NMM) and the Advanced Research WRF (ARW) solver, the latter of which is considered hereafter.

The prognostic equations in the WRF model are written using a terrain-following hydrostatic-pressure vertical coordinate, consider a fully compressible atmosphere, account for moisture effects, include map projections enabling transformations from spherical to planar coordinates, and are cast in a perturbation form.

The WRF model prognostic equations can be derived by first considering the compressible Navier-Stokes equations, using a linear orthogonal (Cartesian) coordinate system (x, y, z, t),

$$\frac{\partial \mathbf{u}}{\partial t} + \mathbf{u} \cdot \nabla \mathbf{u} + \alpha_\rho \nabla p + \nabla \phi + f_c \, \mathbf{e}_z \times \mathbf{u} = \mathbf{F}, \tag{II.1}$$

$$\frac{\partial \rho}{\partial t} + \nabla \cdot (\rho \, \mathbf{u}) = 0, \tag{II.2}$$

where $\alpha_\rho = 1/\rho$ (the inverse density), and $\mathbf{F}$ includes any additional forcing terms such as molecular and turbulent diffusion, and model physics. The Coriolis term will be neglected hereafter (see § I.3.1).

II.2.1 Transformation to hydrostatic pressure coordinates

The derivation is made in a number of steps; first Eqs. II.1 and II.2 are transformed to a hydrostatic-pressure coordinate system, before a transformation to terrain-following

coordinates is made.

Let a scalar function $f(x_j)$, with the sequence $x_j = (x_1, \ldots, x_N)$, be given, and if there exists

$$x_j = x_j(u_1, \ldots, u_M), \quad \text{j=1,...,N,} \tag{II.3}$$

then according to Leibniz

$$\frac{\partial f}{\partial u_m} = \sum_{j=1}^{N} \frac{\partial f}{\partial x_j} \frac{\partial x_j}{\partial u_m}. \tag{II.4}$$

Setting $x_j = (x, y, z, t)$, and defining a curvilinear coordinate system $\left(\hat{x}, \hat{y}, \hat{z}, \hat{t}\right)$, with $\hat{x} = x$, $\hat{y} = y$, $\hat{z} = \pi = f(x, y, z, t)$, $\hat{t} = t$, and with $z = f\left(\hat{x}, \hat{y}, \hat{z} = \pi, \hat{t}\right)$, then the transformations for gradients of a with respect to x and t take the form

$$\left(\frac{\partial f}{\partial x}\right)_\pi = \left(\frac{\partial f}{\partial x}\right)_z + \frac{\partial f}{\partial z}\left(\frac{\partial z}{\partial x}\right)_\pi, \tag{II.5}$$

$$\left(\frac{\partial f}{\partial t}\right)_\pi = \left(\frac{\partial f}{\partial t}\right)_z + \frac{\partial f}{\partial z}\left(\frac{\partial z}{\partial t}\right)_\pi, \tag{II.6}$$

where the same form applies to gradients with respect to y, and the subscripts denote the vertical coordinate being held constant for the partial differentiation. Substitution of Eqs. II.5 and II.6 into the material derivative for the Cartesian system, together with

$$\frac{\partial f}{\partial z} = \frac{\partial f}{\partial \pi}\frac{\partial \pi}{\partial z}, \tag{II.7}$$

gives an expression for the material derivative in the curvilinear system, with respect to the orthogonal framework

$$\begin{aligned}\left(\frac{d f}{d t}\right)_\pi = & \left(\frac{\partial f}{\partial t}\right)_\pi - \frac{\partial \pi}{\partial z}\left(\frac{\partial z}{\partial t}\right)_\pi \frac{\partial f}{\partial \pi} \\ & + u\left[\left(\frac{\partial f}{\partial x}\right)_\pi - \frac{\partial \pi}{\partial z}\left(\frac{\partial z}{\partial x}\right)_\pi \frac{\partial f}{\partial \pi}\right] \\ & + v\left[\left(\frac{\partial f}{\partial y}\right)_\pi - \frac{\partial \pi}{\partial z}\left(\frac{\partial z}{\partial y}\right)_\pi \frac{\partial f}{\partial \pi}\right] \\ & + w\frac{\partial \pi}{\partial z}\frac{\partial f}{\partial \pi},\end{aligned} \tag{II.8}$$

distributing the x and y velocity components to the terms inside the square brackets,

and comparing the result to

$$\frac{d}{dt} = \left(\frac{\partial}{\partial t}\right)_{\pi} + \mathbf{u} \cdot \nabla_{\pi} + \dot{\pi}\frac{\partial}{\partial \pi}, \tag{II.9}$$

indicates the relationship between the curvilinear-coordinate velocity component and the vertical velocity w

$$\dot{\pi} = \frac{\partial \pi}{\partial t} = \frac{\partial \pi}{\partial z}\left[w - \left(\frac{\partial z}{\partial t} + u\,\frac{\partial z}{\partial x} + v\,\frac{\partial z}{\partial y}\right)_{\pi}\right], \tag{II.10}$$

which can be easily solved for w. Using the chain rule and Eq. II.9, the vertical gradient of w can be simplified to

$$\frac{\partial w}{\partial z} = \frac{\partial w}{\partial \pi}\,\frac{\partial \pi}{\partial z} = \frac{\partial \pi}{\partial z}\left[\frac{d}{dt}\left(\frac{\partial z}{\partial \pi}\right) + \frac{\partial u}{\partial \pi}\,\frac{\partial z}{\partial x} + \frac{\partial v}{\partial \pi}\,\frac{\partial z}{\partial y}\right]_{\pi} + \frac{\partial \dot{\pi}}{\partial \pi}. \tag{II.11}$$

The transformations of spatial and temporal derivatives enable transformation of the momentum equation. As is customary, both the horizontal and vertical components of the momentum equation are provided

$$\left(\frac{d\,\mathbf{u}}{dt}\right)_{\pi} + \alpha_{\rho}\nabla_{\pi}\,p + \alpha_{\rho}\frac{\partial p}{\partial \pi}\left(\nabla_{\pi}\,z\right)\frac{\partial \pi}{\partial z} = \mathbf{F}_{h}, \tag{II.12}$$

$$\left(\frac{d\,w}{dt}\right)_{\pi} + \alpha_{\rho}\frac{\partial p}{\partial \pi}\frac{\partial \pi}{\partial z} + g = F_{v}, \tag{II.13}$$

Assuming the curvilinear coordinate is the hydrostatic pressure, that is

$$\frac{\partial \pi}{\partial z} = -\rho\, g, \tag{II.14}$$

allows a further simplification of the momentum equation

$$\left(\frac{d\,\mathbf{u}}{dt}\right)_{\pi} + \alpha_{\rho}\nabla_{\pi}\,p + \frac{\partial p}{\partial \pi}\nabla_{\pi}\,\phi = \mathbf{F}_{h}, \tag{II.15}$$

$$\left(\frac{d\,w}{dt}\right)_{\pi} + g\left(1 - \frac{\partial p}{\partial \pi}\right) = F_{v}, \tag{II.16}$$

where horizontal variations in g have been neglected.

Re-writing Eq. II.2 as $d\left(\ln \rho\right)/dt + \nabla \cdot \mathbf{u}$, and substitution of Eqs. II.5 and II.11 lead to

$$\frac{d}{dt}\ln\left(\rho\,\frac{\partial z}{\partial \pi}\right) + \nabla_{\pi} \cdot \mathbf{u} + \frac{\partial \dot{\pi}}{\partial \pi}, \tag{II.17}$$

which can be rewritten as

$$\left[\frac{\partial}{\partial t}\left(\rho\frac{\partial z}{\partial \pi}\right)\right]_{\pi} + \nabla_{\pi}\cdot\left(\rho\,\mathbf{u}\frac{\partial z}{\partial \pi}\right) + \frac{\partial}{\partial \pi}\left(\rho\,\dot{\pi}\frac{\partial z}{\partial \pi}\right) = 0, \tag{II.18}$$

and simplified further by using the hydrostatic pressure coordinate

$$\nabla_{\pi}\cdot\mathbf{u} + \frac{\partial \dot{\pi}}{\partial \pi}, \tag{II.19}$$

where variations in g have been neglected.

II.2.2 Transformation to terrain-following coordinates

Whilst pressure coordinates intersect complex terrain, terrain-following (η) coordinates do not, which effects how the lower boundary conditions are implemented. In WRF the η coordinate is defined to be zero at the top of the domain and unity at the terrain surface, and takes the form

$$\eta = \left(p_h - p_{ht}\right)/\mu, \quad \mu = p_{hs} - p_{ht}, \tag{II.20}$$

where $p_h\left(\mathbf{r},t\right) = \pi$ is the dry hydrostatic pressure, $\mathbf{r}$ is the position vector, p_{hs} is the surface pressure, and p_{ht} is the pressure at the top of the domain and is set constant. μ is equivalent to the mass of fluid in a column of atmosphere per unit area, if g is assumed constant.

The transformations of spatial and temporal derivatives are analogous to those for the z and π coordinate systems (Eqs. II.5 and II.6),

$$\left(\frac{\partial f}{\partial x}\right)_{\eta} = \left(\frac{\partial f}{\partial x}\right)_{\pi} + \frac{\partial f}{\partial \pi}\left(\frac{\partial \pi}{\partial x}\right)_{\eta}, \tag{II.21}$$

$$\left(\frac{\partial f}{\partial t}\right)_{\eta} = \left(\frac{\partial f}{\partial t}\right)_{\pi} + \frac{\partial f}{\partial \pi}\left(\frac{\partial \pi}{\partial t}\right)_{\eta}, \tag{II.22}$$

which together with

$$\frac{\partial f}{\partial \pi} = \frac{\partial f}{\partial \eta}\frac{\partial \eta}{\partial \pi}, \tag{II.23}$$

can be used to transform the horizontal and vertical components of the momentum equation to the form

$$\left(\frac{d\,\mathbf{u}}{dt}\right)_{\eta} + \alpha_{\rho}\left[\nabla_{\eta}\,p + \left(\nabla_{\eta}\,\pi\right)\frac{\partial \eta}{\partial \pi}\frac{\partial p}{\partial \eta}\right] + \frac{\partial \eta}{\partial \pi}\frac{\partial p}{\partial \eta}\left[\nabla_{\eta}\,\phi - \left(\nabla_{\eta}\,\pi\right)\frac{\partial \eta}{\partial \pi}\frac{\partial \phi}{\partial \eta}\right] = \mathbf{F}_h, \tag{II.24}$$

$$\left(\frac{d\,w}{dt}\right)_\eta + g\left(1 - \frac{\partial\eta}{\partial\pi}\frac{\partial p}{\partial\eta}\right) = F_v, \tag{II.25}$$

$$\left[\frac{\partial}{\partial t}\left(\frac{\partial\pi}{\partial\eta}\right) + \frac{\partial}{\partial x}\left(u\frac{\partial\pi}{\partial\eta}\right) + \frac{\partial}{\partial y}\left(v\frac{\partial\pi}{\partial\eta}\right)\right]_\eta + \frac{\partial}{\partial\eta}\left(\dot{\eta}\frac{\partial\pi}{\partial\eta}\right) = 0. \tag{II.26}$$

The definition of the η coordinate in Eq. II.20 gives $\partial\eta/\partial\pi = 1/\mu$, which gives $\partial\phi/\partial\eta = -\alpha_\rho\,\mu$, by starting with $\partial\phi/\partial z = g$ and applying the chain rule. These expressions allow the momentum and continuity equations to be simplified further to the following forms (the change to the vertical momentum equation is trivial and so has been omitted),

$$\mu\left(\frac{d\,\mathbf{u}}{dt}\right)_\eta - \frac{\partial\phi}{\partial\eta}\nabla_\eta\,p + \frac{\partial p}{\partial\eta}\nabla_\eta\,\phi = \mu\,\mathbf{F}_h, \tag{II.27}$$

$$\left[\frac{\partial\mu}{\partial t} + \frac{\partial(\mu\,u)}{\partial x} + \frac{\partial(\mu\,v)}{\partial y}\right]_\eta + \frac{\partial(\mu\,\dot{\eta})}{\partial\eta}. \tag{II.28}$$

In the WRF model the momentum equation (Eq. II.24) is re-expressed into the following conservation form

$$\left[\frac{\partial(\mu\mathbf{u})}{\partial t}\right]_\eta + \nabla_\eta\cdot(\mu\mathbf{u}\otimes\mathbf{u}) + \frac{\partial}{\partial\eta}(\mu\dot{\eta}\mathbf{u}) - \frac{\partial}{\partial x}\left(p\frac{\partial\phi}{\partial\eta}\right) + \frac{\partial}{\partial\eta}\left(p\frac{\partial\phi}{\partial x}\right) = \mu\mathbf{F}_h, \tag{II.29}$$

$$\left[\frac{\partial(\mu\,w)}{\partial t}\right]_\eta + \nabla_\eta\cdot(\mu\,\mathbf{u}\,w) + \frac{\partial}{\partial n}(\mu\,\dot{\eta}\,w) - g\left(\frac{\partial p}{\partial\eta} - \mu\right) = \mu\,F_v, \tag{II.30}$$

where $\otimes$ is the tensorial (dyadic) product. This form of the momentum equation is reached by first re-arranging Eq. II.26 to $\partial\mu/\partial t = -\nabla_\eta\cdot(\mu\,\mathbf{u}) - \partial(\mu\,\dot{\eta})/\partial n$ and multiplying it by $\mathbf{u}$. The term(s) on the (left-) right-hand side were then (added) subtracted (to) from the momentum equation. The term $p\,\partial/\partial x\,(\partial\phi/\partial\eta)$ is also added and subtracted to the horizontal momentum equation only, and the order of the partial differentiation is changed. The identities $\nabla\cdot\left(f\,\overline{\overline{\zeta}}\right) = \overline{\overline{\zeta}}\cdot\nabla f + f\nabla\cdot\overline{\overline{\zeta}}$, $\nabla\cdot\overline{\overline{\zeta}} = \mathbf{f}\,(\nabla\cdot\mathbf{f}) + \mathbf{f}\cdot\nabla\mathbf{f}$, and $\overline{\overline{\zeta}}\cdot\mathbf{f} = \mathbf{f}\,(\mathbf{f}\cdot\mathbf{f})$, were required, where $\overline{\overline{\zeta}} = \mathbf{f}\otimes\mathbf{f}$, and $\mathbf{f}$ is some vector.

In addition to the prognostic equations for momentum and mass, an equation predicting the evolution of potential temperature θ is also solved, and has the form

$$\left[\frac{\partial(\mu\,\theta)}{\partial t}\right]_\eta + \nabla_\eta\cdot(\mu\,\mathbf{u}\,\theta) + \frac{\partial}{\partial\eta}(\mu\,\dot{\eta}\,\theta) = F_\theta, \tag{II.31}$$

the pressure field is then diagnosed from the equation of state (the ideal gas law)

$$p = p_0 \left(\frac{R_D \, \theta}{p_0 \, \alpha_{\rho_d}} \right)^{\varsigma}, \tag{II.32}$$

where p_0 is the reference pressure (usually taken as 1000 mb to approximate mean sea-level pressure), R_D is the specific gas constant for dry air, α_{ρ_d} is the inverse density for dry air, and $\varsigma = C_{p_d}/C_{v_d}$ is the ratio of heat capacities for constant pressure (C_{p_d}) and constant volume (C_{v_d}) for dry air.

The governing equations in WRF are further manipulated to a perturbation form, account for moisture effects and include map factors [see Skamarock *et al.*, 2008].

The next chapter targets the first objective of this work (see § I.6), that is, to quantify the key atmospheric thermodynamical processes for the case considered by considering the valley atmosphere as a whole.

III

Evolution of Cold-Air-Pooling Processes in Complex Terrain

This chapter is a reproduction of Burns & Chemel [2014a] and maps onto the first objective of this work (see § I.6). Note that the appendix has been moved to the set of appendices at the end of the thesis.

Paul Burns · Charles Chemel

Received: 18 July 2013 / Accepted: 7 November 2013 / Published online: 5 December 2013

Abstract Elucidating cold-air-pooling processes forms part of the longstanding problem of parametrizing the effects of complex terrain in larger-scale numerical models. The Weather Research and Forecasting model has been set-up and run at high resolution over an idealized alpine-valley domain with a width of order 10 km, to investigate the four-dimensional variation of key cold-air-pooling forcing mechanisms, under decoupled stable conditions. Results of the simulation indicated that the total average valley-atmosphere cooling is driven by a complex balance/interplay between radiation and dynamics effects. Three fairly distinct regimes in the evolution of cold-air-pooling processes have been identified. Starting about one hour before sunset, there is an initial 30-min period when the downslope flows are initiated and the total average valley-atmosphere cooling is dominated by radiative heat loss. A period of instability follows, when there is a competition between radiation and dynamics effects, lasting some 90 min. Finally, there is a gradual reduction of the contribution of radiative cooling from 77 to 53 %. The maximum cold-air-pool intensity corresponds to the time of minimum radiative cooling, within the period of instability. Although, once the flow is established, the valley atmosphere cools at broadly similar rates by radiation and dynamics effects, overall, radiation effects dominate the total average valley-atmosphere cooling. Some of the intricacies of the valley mixing have been revealed. There are places where the dynamics dominate the cooling and radiation effects are minor. Characteristics of internal gravity waves propagating away from the slopes are discussed.

Keywords Cold air pools · Downslope flows · Numerical simulation · Radiative heat loss

P. Burns
Centre for Atmospheric & Instrumentation Research (CAIR),
University of Hertfordshire, College Lane, Hatfield, AL10 9AB, UK

C. Chemel
National Centre for Atmospheric Science (NCAS), Centre for Atmospheric & Instrumentation Research (CAIR),
University of Hertfordshire, College Lane, Hatfield, AL10 9AB, UK
email: c.chemel@herts.ac.uk

III.1 Introduction

There is a need to understand and accurately model atmospheric processes in hilly and mountainous terrain (i.e., complex terrain). More specifically, accurate simulations are important, for example, for effective weather and storm predictions, road transportation and aviation safety, as well as for the agricultural industry [e.g. Price *et al.*, 2011]. Accurate simulations are required at the local scale for the prediction of air quality [Anquetin *et al.*, 1999; Brulfert *et al.*, 2005; Chazette *et al.*, 2005; Szintai *et al.*, 2010], avalanches [Lundquist, 2010], wild and prescribed fires, for impact assessments for proposed new settlements and structures [Zardi & Whiteman, 2013], and for climate change estimates [Daly *et al.*, 2009]. Regions of complex terrain are also thought capable of affecting the evolution of atmospheric systems on a wider scale [Noppel & Fiedler, 2002; Price *et al.*, 2011].

For the foreseeable future, the representation of the effects of complex terrain, in both high-resolution forecast models and low-resolution climate and earth-system models, is likely to require varying levels of parametrization, which requires a sound understanding of the underlying physical processes. One key process in complex terrain is cold-air pooling, ultimately driven by a net loss of longwave radiation from the ground surface to space, typically during nocturnal hours and the winter season. Cold air pools (CAPs) can create large temperature variations over short distances in even small-scale terrain. For example, Gustavsson *et al.* [1998] reported near-surface air temperature variations of approximately 7 K over length scales of order 1 km, in terrain with elevation variations less than 100 m, where in some places temperatures decreased by 8.5 K in one hour from sunset. Such temperature variations are currently not well represented in forecast models [Price *et al.*, 2011].

The present work considers cold-air-pooling processes in a valley atmosphere that is not subject to any synoptic forcing, which approximates the case of weak synoptic flows, or where the valley atmosphere is shielded from larger-scale flows by the terrain and possibly a stable layer. In these conditions the local weather and climate are driven by downslope flows and in situ cooling [Whiteman, 2000], but uncertainty remains over their respective contributions and their variations in space and time [Price *et al.*, 2011].

Previous observational and modelling studies have described characteristics of CAPs in relation to their environment [see Zardi & Whiteman, 2013, for a review, and references therein]. However, these studies have generally not focused on quantifying the respective contributions of CAP forcing mechanisms. Several measurement campaigns have aimed at elucidating cold-air-pooling processes for broadly similar mid-latitude climates and conditions [e.g. Price *et al.*, 2011; Sheridan *et al.*, 2013]. Price *et al.* [2011] argued that the dominant process is in situ cooling for small-scale valleys (i.e., valleys about 100-m deep and 1- to 3-km wide). The argument is that the

valley air is decoupled from the atmosphere above, due to the sheltering effect of the valley geometry, reducing turbulence within the valley and preventing heat transfer from above, allowing the valley atmosphere to cool by radiative heat loss to a greater degree than on more exposed ground. The coupling between atmospheric stability and turbulence is made clear, however, a detailed investigation into the characteristics of downslope flows and the valley radiation field was not made. Thompson [1986] used wind and temperature observations collected from Utah, USA and Ontario, Canada, to argue that downslope flows were not the cause of CAPs found in valleys of a very similar scale to those investigated by Price *et al.* [2011]. Thompson [1986] indicated that accurate observations made with bi-directional wind vanes positioned 0.3 m above ground level, targeted at detecting any downslope flow, did not detect any flows. However, no detailed information about the equipment was provided, and given the terrain over which the atmosphere was measured, and the low heights of the instruments above ground level, it is possible that the wind speeds were close to the threshold values of the wind vanes. The Utah measurements found that valley flows began after the development of the valley temperature inversion suggesting that downslope flows were not the cause of it. However, weak downslope flows could have contributed to the development of the valley temperature inversion in the first instance. Ambient wind-speed data was not provided, and the stability of the atmosphere was not discussed. The site characteristics, such as land use, surface roughness, soil type, and moisture content were not considered, although Gustavsson *et al.* [1998] provided evidence that suggests these latter variables have only a modulating effect on the formation of CAPs.

In contrast to the conclusions of Price *et al.* [2011] and Thompson [1986], Gustavsson *et al.* [1998], who made measurements in similar terrain to the former two studies, in southwestern Sweden, pointed out that downslope flows can be important for the development of CAPs. The lateral extent of the observed CAPs was found to increase during the night. The dependence of this lateral expansion on valley width and drainage area was clearly shown. However, without further investigation, it is difficult to assert that this lateral expansion was due to downslope flows rather than due to radiation effects. Gustavsson *et al.* [1998] found a strong correlation between valley drainage area and the strength of the CAP, measured by comparing near-surface air temperatures, and also demonstrated the complicating effects of forested regions on cold-air pooling, the tree canopy apparently enhancing the cooling process due to a sheltering effect.

There have been a number of numerical modelling works focused on improving our understanding of downslope flows and cold-air-pooling processes [e.g. Anquetin *et al.*, 1998; Skyllingstad, 2003; Smith & Skyllingstad, 2005; Vosper & Brown, 2008; Catalano & Cenedese, 2010; Smith *et al.*, 2010; Vosper *et al.*, 2013]. Hoch *et al.* [2011b] used the MYSTIC (Monte Carlo code for the physically correct tracing of photons

in cloudy atmospheres) code [Mayer & Kylling, 2005; Mayer, 2009], which accounts for inhomogeneous surface albedo and topography, to investigate longwave radiation heating and cooling rates in different topographies. The accuracy of the results is dependent on the assumed atmospheric temperature profiles and simplified ground-air temperature differences. Contributions to heating rates from dynamical processes was not explicitly investigated. The nocturnal radiative contribution to cooling rates was investigated by comparing MYSTIC-computed average-basin-atmosphere cooling rates in the Arizona meteor crater, USA, to the observed average-basin-atmosphere total temperature tendency. The observed total rates were estimated by constructing hourly vertical temperature profiles from a meteorological station on the crater floor, time-interpolated 3-hourly tethersonde and radiosonde launches, and a mid-latitude standard atmosphere above 20 km, beyond the range of the radiosonde system. Horizontal uniformity was assumed, based on previous measurements in the crater. The vertical profiles were also used as initial conditions for the MYSTIC simulations, which assumed a rotationally symmetric crater geometry to reduce computational time. Average basin heating and cooling rates were calculated by weighting the vertical profile points according to the proportion of the basin volume they represented. Hoch *et al.* [2011b] found that the radiative contribution, defined above, averaged over one night, was 28 %. The percentage contribution reached a maximum value of 75 % shortly before sunrise when wind speeds were low. A minimum percentage contribution of 9 % occurred during an air intrusion into the basin atmosphere in the middle of the night. The accumulated radiative cooling contribution was found to decrease from approximately 30 to 22 % during the course of the night. These latter values were found to lie within a factor of three of comparable estimates of a few earlier studies [see Hoch *et al.*, 2011b, and references therein]. The crater is approximately 150 m deep and 1.2 km across, and so has a very similar scale to the terrain investigated by Gustavsson *et al.* [1998] and Price *et al.* [2011]. There is a clear difference in geometries, however, Hoch *et al.* [2011b] did not find any large difference in cooling rates between valleys and basins of similar scales and under similar atmospheric and boundary conditions. The Arizona meteor crater lies at about 30 °N and has a semi-arid climate. The lack of moisture close to the ground/air interface is likely to enhance the ground-air temperature excesses and deficits relative to more northerly regions, where a greater portion of the available energy is stored as latent heat [Hoch *et al.*, 2011b].

Despite considerable effort and progress, it is apparent that uncertainty remains about the physical processes controlling CAPs. Detailed investigations of these processes are needed. In the present work, a numerical model is used to examine the variation of key cold-air-pooling forcing mechanisms in an idealized alpine-valley domain with a width of order 10 km under decoupled stable conditions. The set-up of the model and the design of the numerical simulation are presented in Sect. III.2.

Numerical results are analyzed in Sect. III.3 and a summary is given in Sect. V.4.

III.2 Design of the numerical simulation

The numerical simulation presented herein was performed with the Weather Research and Forecasting (WRF) model [Skamarock *et al.*, 2008], version 3.4.1. The WRF model is specifically designed for research and operational forecasting on a range of scales.

III.2.1 WRF numerical formulation

The WRF model is a fully compressible and non-hydrostatic model that uses a terrain-following hydrostatic-pressure vertical coordinate with a constant pressure surface at the top of the domain and a staggered grid of type Arakawa-C. A number of dynamics options are available [see Skamarock *et al.*, 2008, for details]. For the present work, time integration is performed using a third-order Runge-Kutta scheme using a mode-splitting time integration technique to deal with the acoustic modes. Momentum and scalar variables are advected using a fifth-order Weighted Essentially Non-Oscillatory (WENO) scheme with a positive definite filter [Shu, 2003] with no artificial diffusion. Here, the valley atmosphere is not subjected to any synoptic forcing, and so the relevant Rossby number is that based on the downslope flow, that is $Ro = U/(f_c\,L)$, where U and L are the typical velocity and length scales of the downslope flow and f_c is the Coriolis parameter. Given the scales of the problem ($U \approx 2$ m s^{-1}, $L \approx 3$ km and $f_c \approx 10^{-4}$ s^{-1}, see Sect. III.2.2 and III.3.2.a), the Rossby number is $\gg 1$ ($Ro \approx 7$), and so Coriolis effects were neglected by setting $f_c = 0$.

The model was run in a large-eddy simulation (LES) mode (i.e., with no boundary-layer parametrization scheme) with a vertical grid resolution Δz selected to capture the downslope flows (see also Sect. III.2.3). The vertical length scale of the downslope flows is given by the height of the wind maximum, denoted by n_j hereafter. For the relatively steep slopes of the terrain considered here (see Sect. III.2.2), n_j is expected to be of order 1–10 m. This range was drawn from appropriate observational studies [e.g. Doran & Horst, 1983; Helmis & Papadopoulos, 1996].[1] To minimize errors due to large grid-cell aspect ratios, a high horizontal resolution is therefore required (see Sect. III.2.3). A turbulent kinetic energy 1.5-order closure scheme [Deardorff, 1980] was used to model the subgrid scales. The constant 'C_k' in the subgrid-scale parametrization scheme was set to 0.10 [see Moeng *et al.*, 2007].[2]

Because of the anisotropy of the grid, the width of the filter for the subgrid scales

[1] see supporting information (§ III.5)
[2] see supporting information (§ III.5)

was modified following Scotti *et al.* [1993] [see also Catalano & Cenedese, 2010].

The WRF model includes a number of physics modules, which have a number of formulations that can be selected. The physics schemes used for this work are listed below.

- The Dudhia [1989] scheme was chosen to represent shortwave radiation processes. The scheme performs downward integration of solar flux, accounting for clear-air scattering, water vapour absorption [Lacis & Hansen, 1974], and cloud albedo and absorption, using look-up tables for clouds from Stephens [1978]. Slope effects on the surface solar flux, and slope shadowing effects, were deactivated. As well as simplifying the problem, this allows for later investigation into the importance of these effects.

- The Rapid Radiation Transfer Model (RRTM) was chosen to represent longwave radiation processes. This spectral-band scheme uses the correlated-k method [Iacono *et al.*, 2008], and pre-set tables to accurately represent the effects of water vapour, carbon dioxide, ozone, methane, nitrous oxide, oxygen, nitrogen and halocarbons. The two radiation schemes were called every minute, a compromise between the need to keep computational time within acceptable limits, and the need to update radiation variables on a time scale similar to the typical time scale over which these variables change significantly. Both schemes were set to account for the impact of clouds on optical depths.

- The National Severe Storms Laboratory (NSSL) two-moment microphysics scheme was selected. The scheme predicts the mass mixing ratio and number concentration for six hydrometeor species: cloud droplets, rain drops, ice crystals, snow, graupel, and hail [see Mansell *et al.*, 2010]. The scheme is intended for cloud-resolving simulations where the horizontal resolution Δx is greater than 2 km.

- The revised MM5 Monin-Obukhov surface-layer scheme by Jiménez *et al.* [2012] was chosen. The scheme uses the similarity functions of Cheng & Brutsaert [2005] and Fairall *et al.* [1996], which are suitable under strongly stable and unstable conditions, respectively. Both similarity functions range from neutral conditions, enabling the full range of atmospheric stabilities to be accounted for. Momentum fluxes are calculated by the surface-layer scheme, which also calculates exchange coefficients for momentum, heat and moisture (C_d, C_h and C_q, respectively) that are passed to the specified land-surface model (LSM), which then calculates the surface fluxes of heat and moisture. The thermal roughness length z_{0h}, over land surfaces, was set to depend on vegetation height rather than being set constant. Since z_{0h} helps to determine C_h and C_q, this leads to a more accurate representation of surface-atmosphere interactions [Chen & Zhang, 2009]. The

Obukhov length scale, L_O, is used to scale the fluxes. Although friction acts at inclined surfaces, turbulence production is dominated by the downslope flow wind maximum at n_j, which is the relevant length scale with which to scale the fluxes [Grisogono *et al.*, 2007]. Turbulence above the wind maximum is decoupled from the surface [Zardi & Whiteman, 2013]. Whenever $L_O > n_j$, the length scale of the turbulent eddies that determine the fluxes is not the most relevant length scale. Grisogono *et al.* [2007] demonstrated that this is more likely to occur as the slope angle and/or stratification are increased. However, for the present work, $L_O \leq n_j$ (not shown).

- The community Noah LSM [Chen & Dudhia, 2001] was chosen with four soil layers. The United States Geological Survey (USGS) land-use table was chosen, which provides 24 different land-use categories, and 16 soil categories were included. Both the land-use and soil category were set constant across the model domain (see Sect. III.2.4).

III.2.2 Idealized terrain

An idealized U-shaped valley, with its axis orientated north-south, was implemented with a maximum slope angle of 27.6°, flanked on either side by a horizontal plateau extending 2.25 km from the top of the valley slopes. The terrain height above sea level (a.s.l.) is given by

$$h\left(x,y\right) = H\ h_x\left(x\right)\ h_y\left(y\right) + z_{\text{ref}}, \tag{III.1}$$

where x and y are the west-east and south-north components of the model curvilinear coordinate system, respectively, H is the maximum depth of the valley, z_{ref} is the height of the bottom of the valley, and $h_x\left(x\right)$ and $h_y\left(y\right)$ are defined as

$$h_x\left(x\right) = \begin{cases} 0.5\left\{1 - \cos\left[\pi\ \left(\left|x - V_x\right|\right)/S_x\right]\right\}, & V_x \leq \left|x\right| \leq S_x + V_x \\ 0, & \left|x\right| < V_x \\ 1, & \left|x\right| > S_x + V_x \end{cases}, \tag{III.2}$$

and

$$h_y\left(y\right) = 0.5\left[1 + \tanh\left(y/S_y\right)\right], \tag{III.3}$$

where V_x is the half width of the valley floor, S_x is the x-dimension slope length, and S_y is the y-dimension slope length. To simplify the problem, $h_y\left(y\right)$ was held constant at unity, making the topography uniform in y, though y was given a length of 1.2 km.

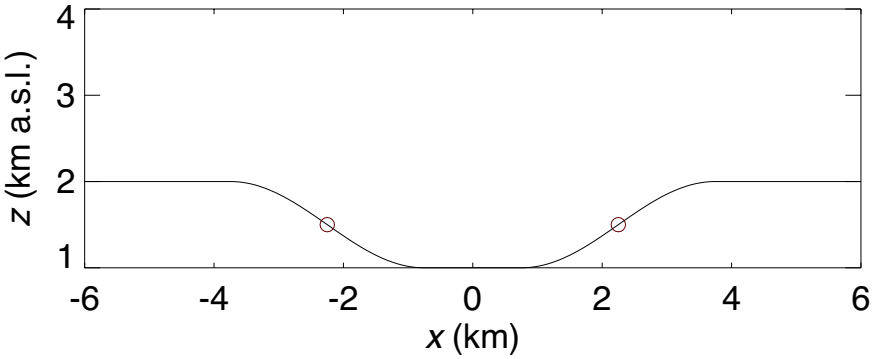

Figure III.1: Terrain height. The red circles mark the slope inflection points. The terrain is uniform along y (into the page), though y was given a length of 1.2 km.

We set $z_{\text{ref}} = 1000$ m, $H = 1000$ m, $V_x = 750$ m and $S_x = 3000$ m. These values approximate the environment of the lower Chamonix Valley, located in the French Alps (45.92 °N, 6.87 °E) and all model points were assigned these coordinates.[3] Figure III.1 illustrates the geometry of the terrain.

III.2.3 Model grid

The model was discretized using 101 staggered grid points along the z-direction. The vertical coordinate (defined by η levels) was stretched using a hyperbolic tangent function, from Vinokur [1980], defined by

$$\eta\,(k) = -\tanh\left[c_1\left(\frac{k-1}{k_{\max}-1} - 1\right)\right] / \tanh\,(c_1), \tag{III.4}$$

where k is the vertical staggered grid point number (ranging from 1 to $k_{\max} = 101$), and c_1 is a coefficient used to adjust the stretching, given a value of 3.134, with larger c_1 values providing greater vertical grid resolutions. This function provides decreasing resolution with increasing z, with a model top located at 12 km a.s.l., and $\Delta\, z$ values adjacent to the ground surface, denoted by $\Delta\, z_s$, of approximately 1.52 and 1.62 m over the plateaus and valley floor, respectively, with $\Delta\, z_s$ ranging between these two limits over the slopes of the valley. To obtain numerically stable results, this range of $\Delta\, z_s$ values demanded a model time step $\Delta\, t = 0.05$ s. The acoustic timestep was set equal to $\Delta\, t/10$. Given the relatively steep slopes of the terrain considered here (see Sect. III.2.2), the parameter 'β', used in the model to damp vertically propagating sound waves, was set to 0.9 [see Dudhia, 1995].

Mahrer [1984] demonstrated that, when using a terrain-following coordinate system, errors in the approximation of horizontal gradients are more likely to occur at large grid-cell aspect ratios, when the lengths of the grid cells are larger than their heights. This makes it more common for the change in z, caused by moving between

[3] see supporting information (§ III.5)

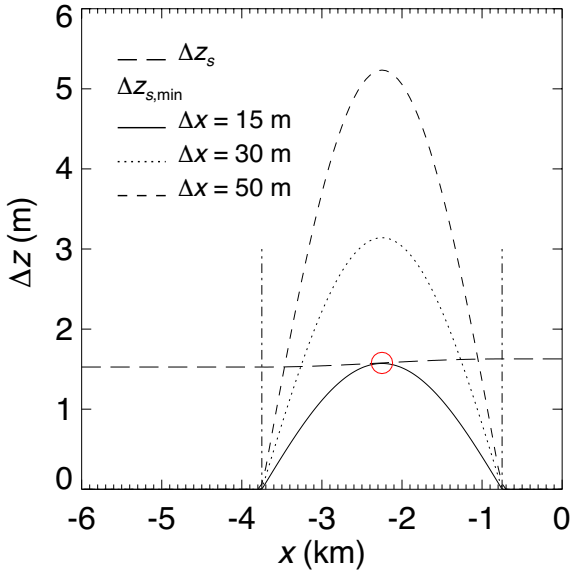

Figure III.2: Comparison of the vertical grid resolution adjacent to the ground surface, denoted by Δz_s, against the minimum acceptable Δz_s, denoted by $\Delta z_{s,\min}$, given by Eq. III.5 with $c_2 = 5$, for three values of horizontal resolution Δx. The vertical dot-dashed lines mark the start and end of the western slope, and the red circle marks the position of the slope inflection point.

neighbouring x points (holding η constant), denoted by $\Delta z_{\Delta x}$, to be larger than the vertical resolution Δz. To avoid errors in the approximations of horizontal gradients, Δz should be set so that $\Delta z \geq \Delta z_{\Delta x}$. Noting that $\Delta z_{\Delta x} = \Delta x \tan|\alpha|$ at the ground surface, where α is the slope angle, and introducing a parameter c_2 allowing for a range of acceptable grid cell distortions,[4] this gives

$$|\alpha| \leq \arctan\left(c_2 \frac{\Delta z_s}{\Delta x}\right). \tag{III.5}$$

Equation III.5 can be used to estimate the minimum Δz_s for given values of α and Δx. The parameter c_2 is commonly set in the range 1–5, with 5 providing the minimum acceptable Δz_s, denoted by $\Delta z_{s,\min}$. Figure III.2 compares the implemented Δz_s against $\Delta z_{s,\min}$, given by Eq. III.5 with $c_2 = 5$, for three values of Δx. It shows that only the $\Delta x = 15$ m resolution satisfies Eq. III.5 with $c_2 = 5$. An initial sensitivity study, not reported here, has revealed that the results from simulations using the $\Delta x = 15$-m and 30-m resolutions are qualitatively the same.[5] Therefore the lower and computationally less expensive horizontal resolution of 30 m, resulting in 402 and 82 staggered grid points in the x- and y-directions, respectively, was used to generate the results reported in Sect. III.3. The even number of horizontal grid points enabled the model to be symmetric about its mass points.

[4] see supporting information (§ III.5)
[5] see supporting information (§ III.5)

III.2.4 Initial and boundary conditions

The simulation was provided with an initial weakly-stable linear lapse rate in virtual potential temperature, $\partial\theta_v/\partial z = 1.5$ K km^{-1}, an environmental lapse rate in temperature, Γ, slightly less than the adiabatic rate. Therefore the simulation represents cases where there is no pre-existing residual layer, or inversions, in the valley atmosphere at the start of the night, indicative of well-mixed post-convective conditions.[6] The model is run for an 8-hr period starting at 1430 UTC on 21 December (that is about one hour before sunset at the latitude of the Chamonix valley).[7] The atmosphere at the bottom of the idealized valley was assigned an initial $\theta_v = 288$ K, a temperature of approximately 279.3 K (about 6 °C). This temperature value was chosen to approximately match measurements made in the Chamonix valley, at a similar time of day and year (see Fig. III.3). The time rate of change of the 2-m air temperature at the centre of the valley was compared to that of the data in Fig. III.3. To make the comparison fair, only the clear-sky observations were considered (i.e., excluding day 19 to 21), and those that did not experience any large shift in the synoptic wind direction (i.e., excluding day 16 and 18). The observed cooling rate averaged over the common time period and over days 15 and 17 is -1.2 K hr^{-1}. The corresponding model value is -0.9 K hr^{-1}, which given the idealized model set-up, is remarkably similar. The atmosphere was initialized with a spatially constant relative humidity of 40 %, which resulted in a moisture flux at the ground/air interface, but avoided any condensation of water in the atmosphere.

The temperature of the ground/air interface, or skin temperature, is initialized by extrapolation of the air temperature of the first three layers above the ground. A random negative thermal perturbation to the extrapolated skin temperatures, with a maximum value of 0.05 K, was applied at the initial time across the valley slopes. This reduced the spin-up time of the simulation, important given the short simulated time period, enforced by the computationally expensive integrations. The thermal perturbation also made the flow three-dimensional (3D), which would not otherwise have been the case, due to the y-independent valley geometry, the initial zero wind field (see below), no Coriolis effects, and the otherwise y-independent thermal forcing at the surface. Since turbulence is 3D it is important that the flow is 3D too.

For a deep valley under stable conditions, the valley atmosphere is often decoupled from the air above the valley [see, for instance, Whiteman, 2000], and so no synoptic forcing was prescribed. It is not known what the velocity field should be within the idealized valley, since this is the problem under investigation, and imposing a zero velocity field within the valley space and some non-zero velocity field above would likely lead to unrealistic results. Model grid nesting is beyond the scope of this work,

[6] see supporting information (§ III.5)
[7] see supporting information (§ III.5)

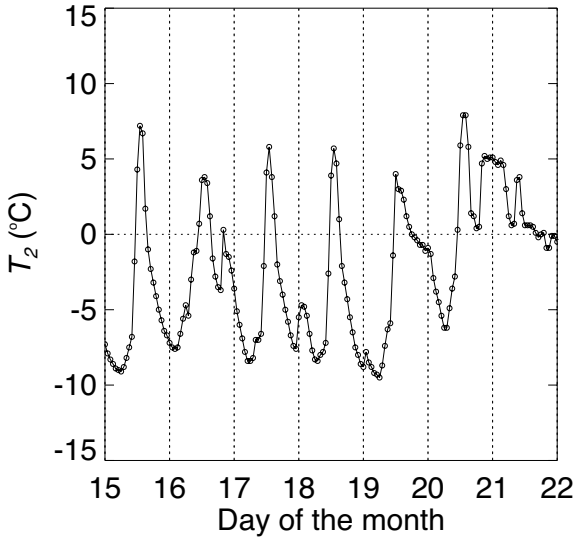

Figure III.3: Time series of 2-m air temperature above the floor of the Chamonix valley for a week during January 2003. The time series has a temporal resolution of one hour. Vertical dotted lines mark the start of each day (0000 UTC). The measurements were taken by Météo France during the POllution in Alpine Valleys (POVA) field campaign [see Brulfert *et al.*, 2005].

and so the wind field was set to zero everywhere at the initial time.

The model deep soil temperature, at a depth of 8 m (denoted by T_{deep}), is at the maximum depth of penetration of the annual solar temperature wave. A depth of 8 m for T_{deep} is reasonable for a soil with low to medium thermal diffusivity, typical of sand-free clay soils, as used for this work (see below). T_{deep} at the bottom of the valley was set to the annual mean surface air temperature of 281.4 K (that is 8.25 °C), a typical value for a mid-latitude Alpine site at this altitude. This proxy value is regarded as an accurate approximation, based on the premise that long-term thermal equilibrium exists between the soil and atmosphere [e.g. Oke, 1987b; Chen & Dudhia, 2001]. Green & Harding [1980] have shown, from numerous measurements across western and central Europe, that the gradient of soil temperature with altitude, during winter, is on average approximately -2 K km^{-1}, and that the differences between the gradients in these regions are not large. Gradients were calculated by considering station pairs, with one element of the pair on low ground and the other on high ground. It was found in an earlier study [Green & Harding, 1979] that the differences in soil temperature, observed between such a pair of stations, are dominated by the effects of altitude, provided that the height difference between them exceeds 200 m, and that they are in a broadly similar climatic regime. This was found to be the case despite large differences in terrain type, ranging from humus to broken rock. All of the station pairs used by Green & Harding [1980] satisfied the above two criteria. This study also suggests that the gradients of soil temperature with altitude are similar for different soil depths (considering soil depths of 0.1, 0.5 and 1 m), and that this pattern generally extends

throughout the year. This is important given that the soil temperature measurements were made at different depths, between 0.2 and 1 m, although most were made at 0.5 m. This also suggests that the vertical soil temperature profile does not change greatly with altitude, and so not with changes in average annual temperature, which varies with altitude. The -2 K km^{-1} gradient was used to vary T_{deep} with altitude across the idealized terrain.

Given a known skin and deep soil temperature the shape of the temperature variation between these boundary values was sought. A linear variation would be easy to implement, however, a better approximation is to decrease the temperature exponentially from T_{deep} towards the ground surface, which is what can generally be observed during the winter months [Lemmelä *et al.*, 1981]. Hillel [1982] showed that the variation of soil temperature with depth and time, due to an infinitely periodic surface heat wave, assuming a constant thermal diffusivity, is of the form

$$T\left(z,t\right) = \langle T_0 \rangle + A_0\, e^{z/d} \sin\left(2\,\pi\, f_{rps}\, t + \frac{z}{d} + \varphi\right), \tag{III.6}$$

where $z \leq 0$, $\langle T_0 \rangle$ is the mean soil surface temperature, A_0 represents the amplitude of the surface wave, f_{rps} is the wave frequency and φ is the signal phase shift. The parameter d is the damping depth, given by $d = \sqrt{D_h / \left(f_{rps}\,\pi\right)}$, where D_h is the (constant) thermal diffusivity.

Since the sinusoidal variation was applied for an infinite time, there is no transient part to Eq. III.6; the soil at any depth is synchronized to the surface signal, or in other words, the soil is in a quasi-steady state. This is not an accurate representation when the surface forcing is applied for some finite time, where the different depths exhibit a transient and more complex behaviour. However, for many systems the quasi-steady state approximation is reasonable, as exemplified by the analysis of Droulia *et al.* [2009]. This model was extended by Droulia *et al.* [2009] to account for both the daily and annual heat waves, which involves the superposition of two waves. The final solution is essentially a sum of terms of the form of Eq. III.6. A simplified version of Eq. III.6 is introduced that still captures the essential exponential decrease of soil temperature towards the ground surface,

$$T\left(z\right) = c_3 + A_0\, e^{z/d}, \tag{III.7}$$

where $z \leq 0$ and d was chosen as one third the depth of T_{deep}, with the boundary conditions $T\left(z=0\right) = T_0$, and $T\left(z=-3\,d\right) = T_{\text{deep}}$, to give

$$T\left(z\right) = T_0 + \frac{T_{\text{deep}} - T_0}{1 - e^{-3}}\left(1 - e^{z/d}\right), \tag{III.8}$$

where $z \leq 0$. The depth d was chosen to avoid any step in the model output variables during the start of the simulation, which is indicative of a system close

to a state of partial equilibrium. This is important since the short simulated period makes long-term model adjustments impractical. The solution was then a compromise between the need to simplify the problem and the need to model the soil temperature profile in a reasonable way.

The idealized terrain was initially set-up to represent an Alpine landscape consisting mainly of grasses, and so the vegetation and landuse type was set to 'grassland', giving, for winter, a surface albedo of 0.23, a surface emissivity of 0.92, an aerodynamic roughness length of 0.10 m, and a surface moisture availability of 0.3 (volume fraction).[8]

The soil type was set to 'silty clay loam', a relatively moist soil [Oke, 1987b], with dry, wilting point, field capacity and maximum soil moistures of 0.120, 0.120, 0.387 and 0.464 (volume fractions), respectively. It typically takes a couple of days for a soil to reach its field capacity, after drainage of water via the soil macropores following a rain event, the exact time period depending on the soil properties, the initial water content of the soil, and the initial water depth in the soil. Before the field capacity is reached the gravitational and capillary forces, which dominate the movement (redistribution) of soil water during infiltration and drainage, are both directed downwards. When the field capacity is reached, matric potential or water content gradients are in opposite directions in the upper and lower portions of the soil profile, preventing any significant net downward water flux [Nachabe, 1998]. Once the macropores are emptied, further drainage, by evaporation from the soil surface or through extraction by plants, removes water at a much slower rate from the soil micropores [Rowell, 1994]. The method was to provide the soil with a constant soil moisture value 10 % below the chosen soil field capacity, thereby placing the soil safely within the latter soil water redistribution regime. The simulation therefore considered a soil a few days after rainfall, which is reasonable given the winter period modelled, when frequent precipitation is typical in the Alps. The exact soil moisture profile is a complex problem and it is acknowledged that soil moistures are likely to decrease by small amounts with depth, however, over the sub-diurnal time period of interest any exchange of moisture between soil layers is negligible.

The model was run with periodic lateral boundary conditions. This was made possible by the relatively large extent of the flat plateaus in the x-direction and the y-independent valley geometry. If the valley geometry were not y-independent then any valley flow is expected to evolve in the down-valley direction precluding the use of a periodic boundary condition in this direction. The implemented valley geometry effectively eliminated any significant valley flow from the results. Without considering a far larger domain, pressure-induced flow cannot be represented. A 4-km deep implicit Rayleigh damping layer [Klemp *et al.*, 2008] was implemented at the top of the model

[8] see supporting information (§ III.5)

domain to prevent any significant wave reflections affecting the solution. The damping coefficient was set to 0.2 s^{-1}.

III.3 Results and discussion

III.3.1 Valley-averaged variation of cold-air-pooling processes

Time series, starting about one hour before sunset[9] of average valley-atmosphere temperature and cooling rate, denoted by $\langle T \rangle_{va}$, and $\langle R \rangle_{va} \equiv \langle \partial\theta_v/\partial t \rangle_{va}$, respectively, where $\partial\theta_v/\partial t \approx \partial T/\partial t$ (not shown), are displayed in Fig. III.4a. The time series were created by first averaging the model output across the y-dimension. The output fields on the model curvilinear grid were then interpolated onto a linear orthogonal framework (i.e., Cartesian system), which filled the two-dimensional valley space, with $\Delta x' = \Delta z' = 5$ m. $\partial\theta_v/\partial t$ was calculated from the model output θ_v field using centered finite differencing before re-gridding, to avoid numerical artifacts. The results are not sensitive to the choice of differencing scheme. A local bilinear interpolation was used, that relies on grid indexes, avoiding errors close to sloping ground associated with triangulation techniques using real heights. Such errors are caused by the maximum grid distortion in these regions, together with the rapidly changing fields when moving in a direction normal to the ground. Having said this, $\langle R \rangle_{va}$ has a low sensitivity to such errors (not shown). The sensitivity of the series to the new grid resolution, was tested using $\partial\theta_v/\partial t$ (see Fig. III.4b), which demonstrates a convergence of the results as the resolution is increased from 100 to 1 m. Figure III.4b shows that there is no noticeable difference between the 1 and 5 m results, and therefore all of the $\langle\rangle_{va}$ and $\langle\rangle_{vs}$ time series were created using the latter resolution, where the subscript vs stands for a valley section, in the (x, z) plane. Errors occurring in $\langle R \rangle_{va}$, as the resolution is decreased, are primarily caused by the misrepresentation of the valley atmosphere away from the valley slopes.

Figure III.4a shows a general steady cooling of the valley atmosphere through time. $\langle T \rangle_{va}$ is approximately 1 °C for the first 30 min or so of simulation, before decreasing at a near constant rate of roughly 0.25 K hr^{-1}, to reach a final value close to −1 °C, revealing a total 2 °C decrease of $\langle T \rangle_{va}$ during the simulated 8-hr period. The initial near-constant temperature is due to a balance between cooling from longwave radiation and combined heating from shortwave radiation and dynamical processes, when all terms are small. The change in $\langle T \rangle_{va}$ over this period is −0.043 K and in $\langle \theta_v \rangle_{va}$ is −0.046 K. In general, the subsequent decrease of $\langle T \rangle_{va}$ is caused by the reduction and loss of shortwave radiation effects, an increase in the cooling from longwave radiation, and the initiation of cooling from dynamical processes, as discussed in this section. The

[9] see supporting information (§ III.5)

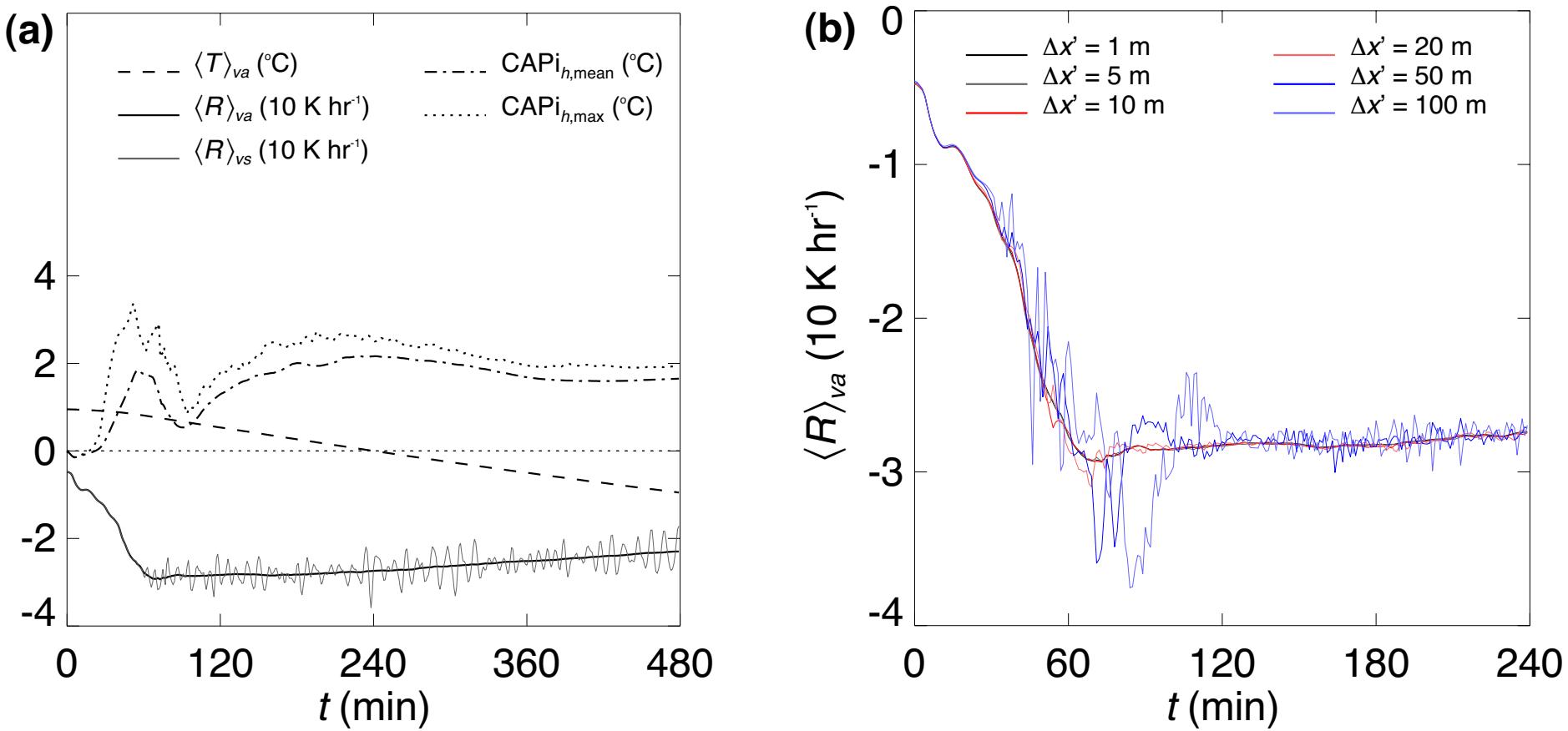

Figure III.4: Time series of **(a)** average valley-atmosphere temperature, denoted by $\langle T \rangle_{va}$, $\langle R \rangle_{va} \equiv \langle \partial\theta_v/\partial t \rangle_{va}$, where θ_v is virtual potential temperature, $\partial\theta_v/\partial t$ averaged over an $((x, z)$ slice taken half-way along y, denoted by $\langle R \rangle_{vs}$, $\mathrm{CAPi}_{h,\mathrm{mean}}$ and $\mathrm{CAPi}_{h,\mathrm{max}}$ (see text for details), and **(b)** $\langle R \rangle_{va}$ using a number of different Cartesian grid resolutions.

associated instantaneous cooling rate, $\langle R \rangle_{va}$, initially increases in magnitude relatively quickly, due to the changes in the forcing mechanisms, with $\langle R \rangle_{va}$ decreasing from -0.048 to -0.29 K hr^{-1} at $t = 73$ min. $|\langle R \rangle_{va}|$ then gradually decreases with $\langle R \rangle_{va}$ increasing to -0.23 K hr^{-1} at the end of the simulation. During this latter period there is a general reduction in the cooling from longwave radiation and dynamics effects. Possible oscillatory features can be seen in $\langle R \rangle_{vs} \equiv \langle \partial\theta_v/\partial t \rangle_{vs}$, taken halfway along the y-dimension, after $t = 60$ min (see Fig. III.4a). These features are discussed in Appendix C

III.3.1.a Cold-air-pool intensity

Due to the relatively large valley depth and possibly the chosen initial stratification, the simulated temperatures over the plateaus are always less than the temperatures over the valley floor, despite the enhanced cooling there, and in this respect a CAP is not simulated. This highlights the ambiguity that remains in the definition of a CAP, which typically refers to the relatively low air temperatures in a volume of air confined towards the bottom of a depression, compared to a reference air temperature above it.[10] This work has found evidence of slightly higher temperatures immediately above the shallow (less than 100-m deep) layer of air at the bottom of the valley (not shown). However, the sign of this temperature difference is quickly reversed by moving the reference further away from this layer. The approach taken here was to remove the hydrostatic variation in temperature from all points in the model domain, allowing for a comparison of model domain cooling rates to those over flat terrain at the same elevation. This revealed a region of enhanced cooling that expanded upwards from the bottom of the valley (see Sect. III.3.2.a), denoted by CAP_h, where the subscript h refersto the hydrostatic adjustment. The CAP intensity (CAPi), has therefore been denoted by CAPi_h. CAPi_h was calculated in two ways: as the difference between the model adjusted-plateau and valley floor average near-surface air temperatures, denoted by $\text{CAPi}_{h,\text{mean}}$, and also using the adjusted-maximum and minimum values from the two respective regions, denoted by $\text{CAPi}_{h,\text{max}}$. All temperatures were taken from the model first mass points at 0.76 and 0.81 m above the plateaus and valley floor, respectively (i.e., approximately at screen-level height). For the first 15 min both CAPi_h curves show negative values, that is the plateaus initially cooled faster than the valley floor (see Fig. III.4a). The maximum magnitude of the temperature difference is small, with $\text{CAPi}_{h,\text{mean}} = -0.15$ °C. After $t = 15$ min $\text{CAPi}_{h,\text{mean}}$ and $\text{CAPi}_{h,\text{max}}$ become positive and remain so for the remainder of the simulation, highlighting the enhanced cooling at the bottom of the valley compared to air adjacent to flat terrain in the stable decoupled conditions. Immediately after $t = 15$ min there is

[10] see supporting information (§ III.5)

a peak in both curves centered close to $t = 60$ min, before CAPi $_{h,\mathrm{mean}}$ and CAPi$_{h,\mathrm{max}}$ increase again at a progressively decreasing rate until about $t = 240$ min. Both CAPi$_h$ curves then gradually decrease until approximately $t = 360$ min before levelling off for the remainder of the simulation, suggesting that some form of equilibrium or partial equilibrium condition was reached. The maximum CAPi$_{h,\mathrm{max}}$ is 3.4 °C at $t = 52$ min, in contrast to the maximum CAPi$_{h,\mathrm{mean}}$ of 2.2 °C at $t = 228$ min.

III.3.1.b Cold-air-pool forcing mechanisms

Figure III.5a reveals that the $\langle\rangle_{va}$ accumulated temperature change due to net radiation only, $\langle\Delta\,\theta_{v_r}\rangle_{va}$, is nearly linear, and reaches a total value close to −1 K, where the subscript r is short for radiation. $\langle\Delta\,\theta_{v_r}\rangle_{va}$ at $t = 30$ min is small with a value of −0.047 K. Also shown is the $\langle\rangle_{va}$ cooling rate due to net radiation, denoted by $\langle R_r\rangle_{va}$, where $\langle R_r\rangle_{va} \approx \langle\partial T_r/\partial t\rangle_{va}$ (not shown). Initially $|\langle R_r\rangle_{va}|$ increases relatively rapidly with $\langle R_r\rangle_{va}$ decreasing from −0.081 to −0.13 K hr^{-1} at $t = 65$ min, before decreasing again only slightly to a rate of −0.135 K hr^{-1} at $t = 113$ min. After this time $|\langle R_r\rangle_{va}|$ decreases gradually with $\langle R_r\rangle_{va}$ increasing to −0.12 K hr^{-1} at the end of the simulation. Figure III.5a displays the $\langle\rangle_{va}$ contribution of $\Delta\,\theta_{v_r}$ and R_r to the total quantities, denoted by $\langle\Delta\,\theta_{v_r}/\Delta\,\theta_v\rangle_{va}$ and $\langle R_r/R\rangle_{va}$, respectively. The averaging must be done after the normalization to correctly represent the normalized model output fields. $\langle\Delta\,\theta_{v_r}/\Delta\,\theta_v\rangle_{va}$ increases for the first 5 min from approximately 102 to 148 %, before decreasing relatively rapidly to 77 %, at $t = 65$ min, after which it generally decreases at a progressively slower rate to reach a final value of 53 %. The initial increase of $\langle\Delta\,\theta_{v_r}/\Delta\,\theta_v\rangle_{va}$ balances the heating caused by dynamics effects (see Fig. III.5b). $\langle\Delta\,\theta_{v_r}/\Delta\,\theta_v\rangle_{va}$ completely dominates the cooling for the initial 30 min, with $\langle\Delta\,\theta_{v_r}/\Delta\,\theta_v\rangle_{va} = 103$ % at $t = 30$ min, and the subsequent rapid decrease of $\langle\Delta\,\theta_{v_r}/\Delta\,\theta_v\rangle_{va}$ accounts for the growing influence of the dynamics in the total temperature changes. Figure III.5b illustrates the difference between the total and radiation fields (i.e., the combined dynamics effects of advection and subgrid-scale turbulent mixing) for which the subscript d is used. $\langle\Delta\,\theta_{v_d}\rangle_{va}$ is near zero for the first 30 min of the simulation, in fact amounting to a very small positive temperature change of 0.00062 K. Over the same period shortwave radiation caused a temperature change, $\langle\Delta\,\theta_{v_{SW}}\rangle_{va}$, of 0.00525 K (see Fig. III.6), as expected to give $\langle\Delta\,\theta_v\rangle_{va}$. $\left|\langle\Delta\,\theta_{v_d}\rangle_{va}\right|$ then increases steadily to a final value close to −1 K, as expected.

$\langle R_d\rangle_{va}$ initially decreases from 0.033 to −0.16 K hr^{-1} at $t = 73$ min, changing from a small heating rate to a relatively large cooling rate. $|\langle R_d\rangle_{va}|$ then generally decreases with $\langle R_d\rangle_{va}$ increasing to a final value of −0.11 K hr^{-1}. The oscillatory features in $\langle R_d\rangle_{vs}$ (see Fig. III.5b) could not be found in the data for $\langle R_r\rangle_{vs}$, which reveals that the oscillations in $\langle R\rangle_{vs}$ (see Fig. III.4a) are caused by the dynamics alone. $\langle\Delta\,\theta_{v_d}/\Delta\,\theta_v\rangle_{va}$ first decreases from −2 to −48 % at $t = 5$ min, before increasing rapidly

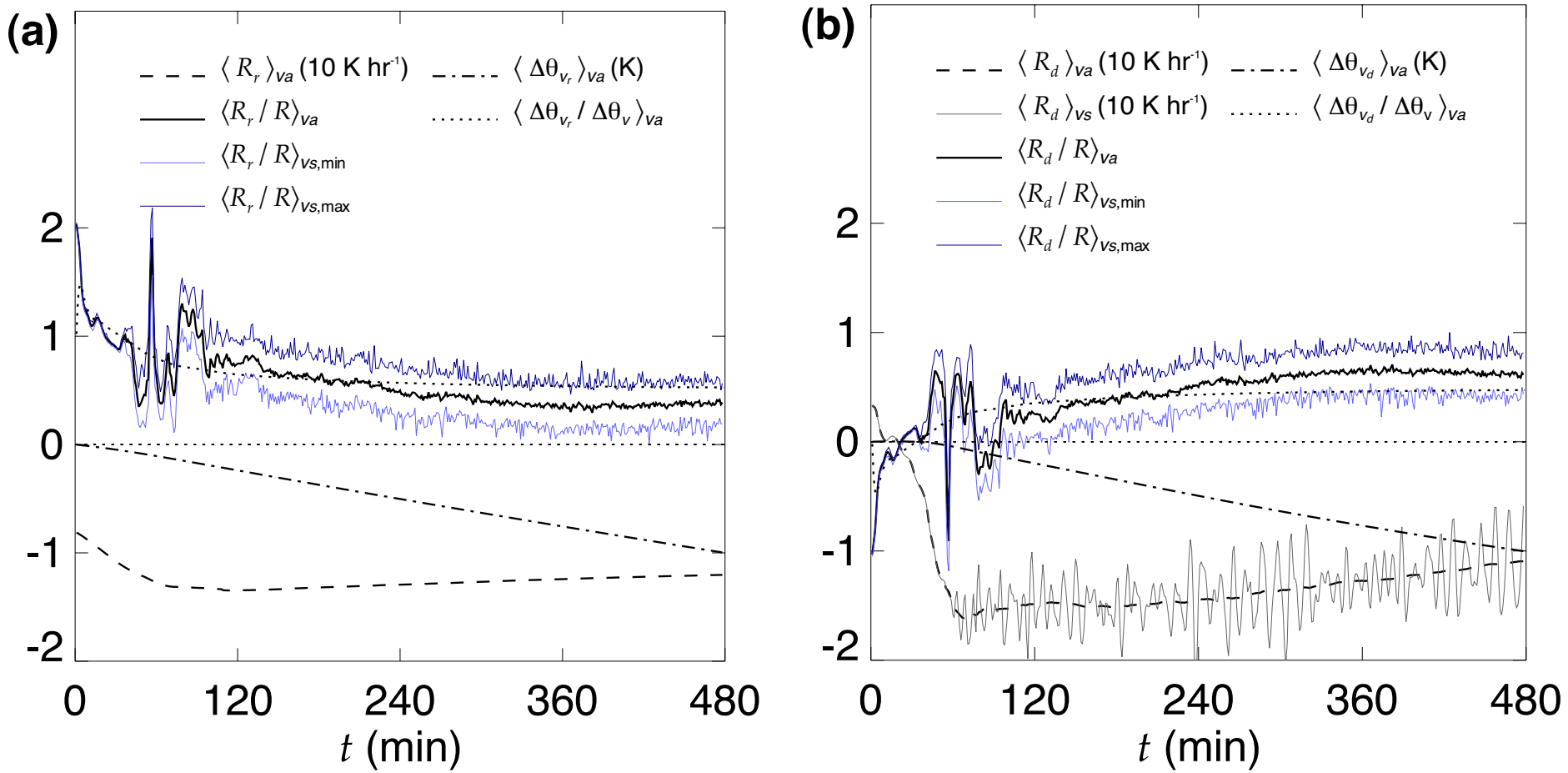

Figure III.5: Time series of **(a)** the average valley-atmosphere radiative part of $\partial\theta_v/\partial t \equiv R$, denoted by $\langle R_r \rangle_{va}$, $\langle R_r/R \rangle_{va}$, $\langle R_r/R \rangle_{vs,min}$ and $\langle R_r/R \rangle_{vs,max}$ obtained by using the operator $\langle\rangle_{vs}$ for every y position and searching across y at each time for the minimum and maximum $\langle R_r/R \rangle_{vs}$, $\langle \Delta\theta_{v_r} \rangle_{va}$, where $\Delta\theta_{v_r}$ is the accumulated change of θ_v due to net radiation, $\langle \Delta\theta_{v_r}/\Delta\theta_v \rangle_{va}$, where $\Delta\theta_v$ is the total accumulated change of θ_v, and **(b)** the same as **(a)** but considering dynamics quantities, as well as $\langle R_d \rangle_{vs}$ taken half-way along y.

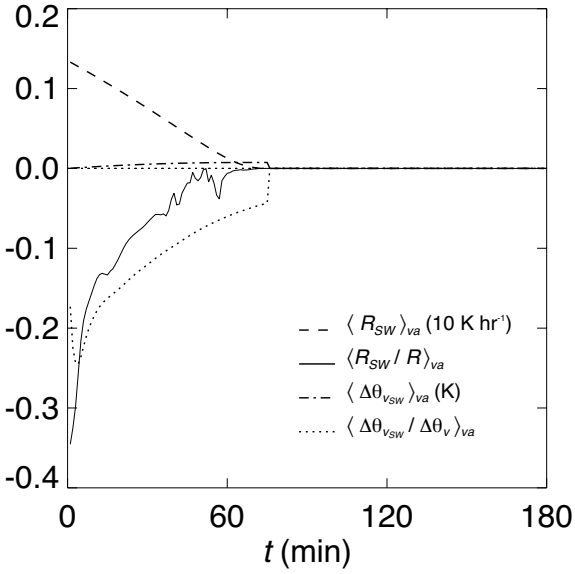

Figure III.6: Time series of $\langle R_{SW} \rangle_{va}$, $\langle R_{SW}/R \rangle_{va}$, $\langle \Delta\theta_{v_{SW}} \rangle_{va}$ and $\langle \Delta\theta_{v_{SW}}/\Delta\theta_v \rangle_{va}$, where R_{SW} and $\Delta\theta_{v_{SW}}$ are the instantaneous and accumulated changes of θ_v due to shortwave radiation.

until approximately $t = 75$ min, reaching 27 %, and then increasing only gradually to reach a final value of 47 %. The initial heating effect by the dynamics and the subsequent time it takes for the cooling by the dynamics to take effect, together with broadly similar rates of cooling from longwave radiation and dynamics, once the flow is established, results in $\langle \Delta\theta_{v_d}/\Delta\theta_v \rangle_{va} < \langle \Delta\theta_{v_r}/\Delta\theta_v \rangle_{va}$. The two forcing mechanisms are tightly coupled, and ultimately it is longwave radiation that causes the downslope flows (discussed in Sect. III.3.2.a). It would be interesting to investigate further the generality of this result, for instance by varying the initial conditions.

$\langle R_r/R \rangle_{va}$ and $\langle R_d/R \rangle_{va}$ are more variable than $\langle \Delta\theta_{v_r}/\Delta\theta_v \rangle_{va}$ and $\langle \Delta\theta_{v_d}/\Delta\theta_v \rangle_{va}$, and are formed of three fairly distinct regimes (see Fig. III.5). As above, there is first a 30-min period when longwave radiation almost completely dominates the cooling, with $\langle R_r/R \rangle_{va}$ decreasing from 203 to 90 %. After approximately $t = 30$ min there is a period of instability, lasting some 90 min, where $\langle R_r/R \rangle_{va}$ is of course exactly out of phase with $\langle R_d/R \rangle_{va}$. Finally, there is a gradual reduction of $\langle R_r/R \rangle_{va}$ from 75 % to a final contribution of 37 %. Figure III.5 also gives the maximum and minimum values of $\langle R_r/R \rangle_{vs}$ and $\langle R_d/R \rangle_{vs}$, by applying $\langle\rangle_{vs}$ to every y-position and searching across y at each time. Both plots demonstrate that there is little variation from $\langle R_r/R \rangle_{va}$ and $\langle R_d/R \rangle_{va}$ for about the first 30 min of the simulation, suggesting that the thermodynamics are constrained to develop in an essentially two-dimensional way during this period. The variation around $\langle R_r/R \rangle_{va}$ and $\langle R_d/R \rangle_{va}$ is generally larger during the period of instability, depending on the specific time considered. After $t = 120$ min, the variation around $\langle R_r/R \rangle_{va}$ and $\langle R_d/R \rangle_{va}$ is near constant over time, with the volume averages close to the centre of the variation defined be the maximum and

minimum values (defining a maximum variation of about 40 %). The simulation average for $\langle \Delta\theta_{v_r}/\Delta\theta_v \rangle_{va}$ and $\langle R_r/R \rangle_{va}$ is 64 and 58 %, respectively. The corresponding values for the period of gradual decline are 56 and 46 %. The maximum (minimum) values for $\langle \Delta\theta_{v_r}/\Delta\theta_v \rangle_{va}$ and $\langle R_r/R \rangle_{va}$ are 147 (53) and 203 (29) %, respectively. The times of these maximum (minimum) percentages are respectively 5 (480) and 1 (382) min. Figure III.6 shows that shortwave radiation has only a small modulating influence in the first hour or so of the simulation, decreasing the cooling due to net radiation, and increasing the rate of initial increase of $|\langle R_r \rangle_{va}|$. Hoch *et al.* [2011b] found values of about 30 % for $\langle \Delta\theta_{v_{LW}}/\Delta\theta_v \rangle_{va}$ and $\langle R_{LW}/R \rangle_{va}$, early in the night, from 1700 to 2200 LST, for the Arizona meteor crater, which is clearly different from the respective values of 56 and 46 % obtained for the period of gradual decline, from 1630 to 2230 UTC. One possible explanation is an over-estimation of $\langle R_{LW}/R \rangle_{va}$ by the one-dimensional radiative transfer scheme used for the simulation.

The RRTM longwave radiation scheme, used here, does not consider photon transport between atmospheric columns, and so nor reflections or emissions from surrounding terrain. The work by Hoch *et al.* [2011b] using the MYSTIC code, a 3D radiative transfer model, demonstrated that one-dimensional schemes will tend to over-estimate $\langle \rangle_{va}$ longwave radiative cooling rates, denoted by $\langle R_{LW} \rangle_{va}$ hereafter [see Fig. 6 and 7 in Hoch *et al.*, 2011b]. The 1900 LST MYSTIC simulation suggests there will be an error close to 0.05 K hr^{-1} in the $t = 270$ min (1900 UTC) $|\langle R_{LW} \rangle_{va}|$ value reported here, where $\langle R_{LW} \rangle_{va}$ is always negative. The 1900 LST MYSTIC simulation had a similar bulk atmospheric temperature profile to the 1900 UTC WRF model results from this work (not shown). Hoch *et al.* [2011b] assumed a temperature deficit of 4 K, which is larger than the corresponding value of about 2.5 K, for this work, obtained half-way up the western valley slope and considering the temperature change across the downslope flow, which is less than 50-m deep (not shown). However, the MYSTIC model results suggests that this is unlikely to have any significant effect on the error. Hoch *et al.* [2011b] made simulations for 1500, 1900 and 0600 LST, which revealed that the error is not constant in time. Although the WRF simulation made here, began at a similar time to the first MYSTIC simulation, the initial conditions were different, which makes even any linear approximation of the changing error impossible. This would nevertheless make an interesting topic of future research. Also, in the present work, the shortwave radiation decreased at approximately the same rate everywhere, since slope effects on shortwave radiation were not included. Including shadowing effects is likely to cause a different initiation of the flow [e.g. Lehner *et al.*, 2011], a subject of future work.

III.3.2 Local-scale features

III.3.2.a Cold-air-pool evolution

Details of the valley-atmosphere cooling are difficult to appreciate in the T or θ_v fields, due to the hydrostatic change of these quantities with z. However, both fields show the general cooling and stabilization of the valley atmosphere as the night progresses. The T or θ_v fields also indicate that in general the valley atmosphere cooling is horizontally homogeneous. This effect is also indicated by the $\Delta\,\theta_v$ field and gives a clearer picture of the cooling variation across the domain. Figure III.7 displays filled contour plots of $\langle \Delta\,\theta_v \rangle_y$ overlaid with streamlines. The streamlines were created by tracing the paths of massless particles through $\langle \mathbf{u}_{xz} \rangle_y$, by time integration, where $\mathbf{u}$ is the model wind field and $\mathbf{u}_{xz} \equiv (u, w)$. Each 'particle' was tracked from its seed point until the path left the input space or a maximum number of iterations was reached. After adding arrows at the seed points to reveal flow direction, the approach has the advantage of indicating the relative strength, direction and vorticity of the flow, across the input space. The filled contours were created using a 5-m grid resolution, justified above for the field averages, and the streamline seed points are positioned on the Cartesian grid with the same origin, with $\Delta\,x' = \Delta\,z' = 100$ m, placing a limit on the range of turbulent scales that can be revealed in these particular plots. Nevertheless, it was found that the displayed streamlines are a good representation of the streamlines generated from a finer seed-point mesh. The streamline algorithm uses $\langle \mathbf{u}_{xz} \rangle_y$ projected onto the 5-m grid to track the 'particle' trajectories from the seed points. u is the dominant component of $\mathbf{u}$, which together with the implemented idealized terrain and initial conditions, suggests that the major features of the flow exist in the (x, z) plane, and so the streamlines are a good representation of the dominant flow features. To give an idea of the absolute magnitudes of the flow in the following analysis, it should be noted that the established downslope flow has a typical speed of approximately 2 m s^{-1}.

Close inspection of Fig. III.7a reveals that the dark region immediately above the top half of the western valley slope, no more than 50-m deep, is the region of maximum flow, which hides a corresponding region of relatively large accumulated temperature decrease, with $\langle \Delta\,\theta_v \rangle_y \approx -1$ K, compared to the surrounding atmosphere that has $-0.1 < \langle \Delta\,\theta_v \rangle_y < 0$ K. $\Delta\,\theta_v$ is negative everywhere at all times. Figures III.7a and III.7b reveal a propagating intensification of the downslope flow, with a counter-clockwise vortex at the head of this flow, considering a northerly oriented rotation axis. The downslope flow was found to exist, albeit to a lesser degree, from within 5 min of $t = 0$ (not shown). There is evidence of relatively large cooling at the bottom of the valley at $t = 40$ min, with $-0.2 < \langle \Delta\,\theta_v \rangle_y < -0.1$ K within about 100 m above ground level, and with $\langle \Delta\,\theta_v \rangle_y \leq -2$ K within a few meters of the valley floor. This cooling is due to a combination of radiation and dynamics effects. The intensification of the

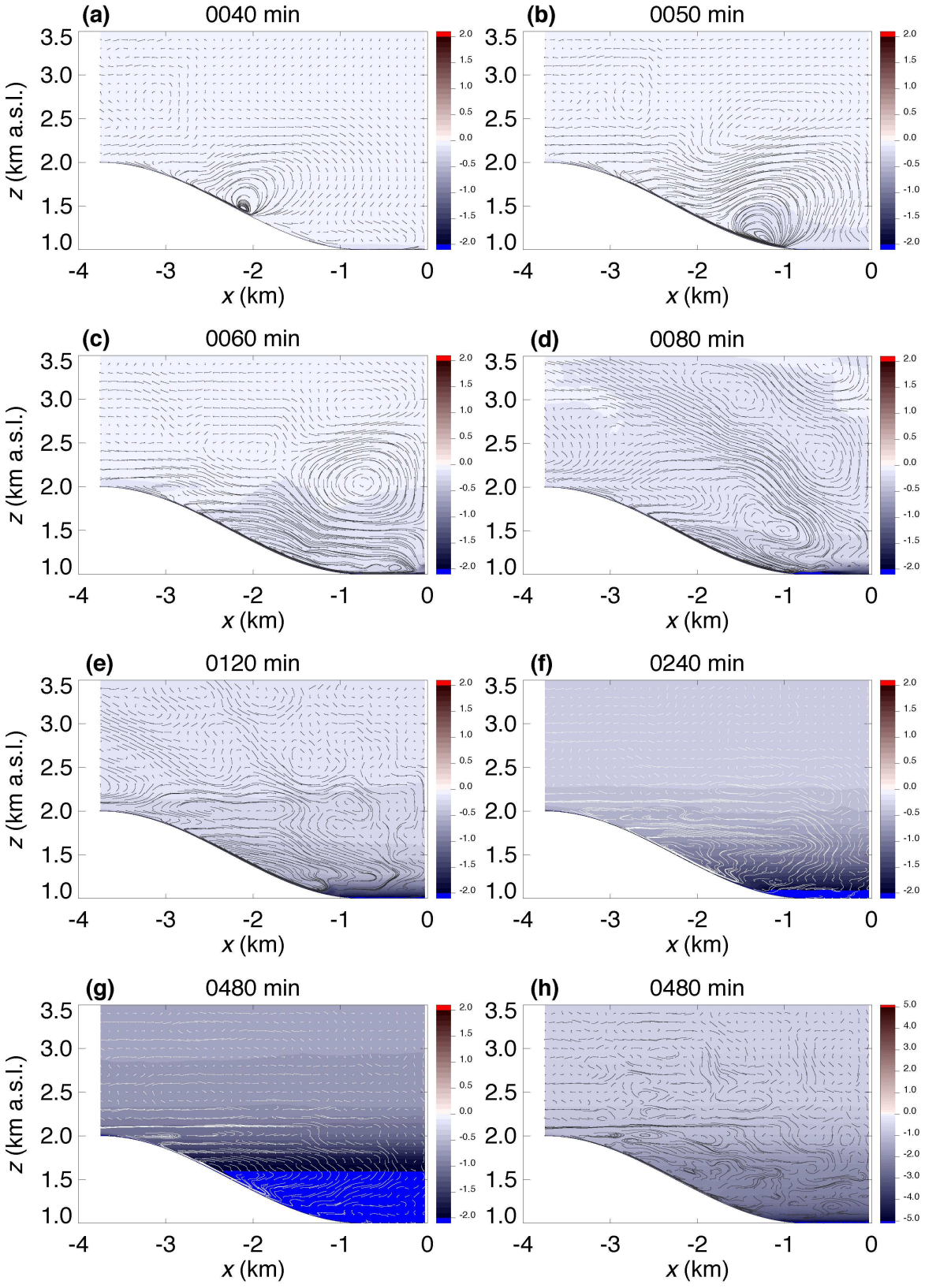

Figure III.7: Contour plots (**a**) to (**g**) of $\langle \Delta\theta_v \rangle_y$ (in K), with solid black or white streamlines over-plotted at $t = 40$, 50, 60, 80, 120, 240 and 480 min, and (**h**) $\Delta\theta_v$ (in K) taken half-way along the y-dimension at $t = 480$ min.

downslope flow is shown to generally disturb the quiescent valley atmosphere, creating further vortices away from the terrain, a general upward motion close to the valley axis, which is to be expected due to mass conservation, as well as a movement of air towards the slope behind the vortex at the head of the maximum flow region. Despite the variability in the system, this latter counter-clockwise half-valley-scale circulation becomes a quasi-permanent feature of the valley flow system. Figure III.7c shows the beginning of the reflection of the maximum flow region back towards the bottom of the slope, after colliding with the fluid from the eastern slope. A small-scale eddy about 100-m across, close to the centre of the valley, indicates the presence of turbulence in a shallow region less than 100-m deep.

Soon after $t = 60$ min the signature of internal gravity waves (IGWs) becomes clear, in and above the valley atmosphere (see Fig. III.7d), which supports the evidence of IGWs reported in Appendix C. The general direction of the wave vector $\langle \mathbf{k}_{xz} \rangle_y$, where $\mathbf{k}_{xz} \equiv (k_x, k_z)$, at this time, is clear, revealed by the upward and downward streamline regions, with $\langle \mathbf{k}_{xz} \rangle_y$ directed westwards to allow for an upward energy propagation. The streamlines indicate that $\langle \mathbf{k}_{xz} \rangle_y$ makes an angle of about 30° with the vertical, which agrees with $0.88 < \langle \omega'/N \rangle_{xz} < 0.92$ (see Appendix C), and that $2\,\pi/\langle k_z \rangle_y = \langle \lambda_z \rangle_y \approx 1$ km, which are very similar to the results of Chemel *et al.* [2009] and Largeron *et al.* [2013], and supports their finding that λ_z is set by the depth of the topography. An interesting feature of the flow are the vortices between the regions of upward and downward motions. A full description of the IGW field is beyond the scope of this work.

Figure III.7d also shows the further retreat of the maximum flow region back towards the bottom of the slope, which leaves behind it a region of relatively large $|\langle \Delta\,\theta_v \rangle_y|$ air, indicating the importance of the downslope flow for the valley bottom cooling in the early night. The downslope flow intensification mixes the region of large $|\langle \Delta\,\theta_v \rangle_y|$ at the bottom of the valley higher into the atmosphere. By $t = 120$ min (see Fig. III.7e), the maximum flow region has retreated further, with a clear deflection of the downslope flow, close to the bottom of the slope, as it comes into contact with air of a similar or greater density. Figures III.7f and III.7g show the further growth of the CAP_h and subsequent retreat of the downslope flow maximum region back up the western slope. The streamlines in these latter plots were made white for clarity, however, the apparent loss of the IGW signature is deceiving. From $t = 120$ min onwards, streamlines run westward beginning close to the centre of the valley in a near-horizontal region approximately 100-m deep, positioned about 100 m above the plateau height (see Fig. III.7f and III.7g), and develop together with a valley atmosphere capping inversion (not shown). This flow feature is linked to the quasi-permanent counter-clockwise flow system noted above.

The return flow above the downslope flow over the bottom half of the slope is clear

in Fig. III.7f, revealed by the S-shaped streamlines adjacent to the ground. There is evidence of flow separation above the developing CAP_h during the early night (see Fig. III.7d to III.7f), though the feature is difficult to see later in the night, when there is clear evidence of flow penetration into the developing CAP_h (see Fig. III.7g). The colour scale in Fig. III.7a through III.7g was chosen to make clear the development of the CAP_h, however, the detail of the cooling at the very bottom of the valley is lost after $t = 120$ min. Figure III.7h indicates the relatively large cooling effect within the first 100 m of the valley bottom, compared to the atmosphere above, the effect intensifying as the night progresses. Streamlines for an (x, z) slice of the domain, taken half-way along the y-dimension, reveals the localized variability in the dynamics along y. The dominant flow features are still apparent. However, the turbulent nature of the flow is more clear, and it would be interesting to investigate further the exact mixing characteristics of the valley atmosphere, as well as the ability of the valley-flow system to mix scalars into the free atmosphere.

III.3.2.b Cold-air-pool forcing mechanisms

Figure III.8 shows contour plots of $\langle R_r/R \rangle_y$, with streamlines over-plotted, as above. R is found to have both signs, whereas, R_r is always negative, with the exception of a few rare cases of radiative heating at the very bottom of the valley atmosphere (not shown). As pointed out above, the air temperatures are always less than at $t = 0$, despite the occasional heating rate. This means that, in general, $\langle R_r/R \rangle_y > 1$ corresponds to a cooling atmosphere due to radiative processes, despite heating from the dynamics, and $\langle R_r/R \rangle_y < 0$ corresponds to a heating atmosphere due to the dynamics overcoming radiative cooling. A clockwise circulating vortex, with rotation axis into the page, can be seen in Fig. III.8a, centered at approximately $(x = -3.1 \text{ km}, z = 2.75 \text{ km})$. The region of bright red colour on the eastern edge of this vortex corresponds to $\langle R_r/R \rangle_y > 1$, and the streamlines suggest this is caused by the downward advection of air from about $z = 3$ km. Γ is less than the dry adiabatic rate, denoted by Γ_d, everywhere at $t = 0$, and in this region Γ decreases slightly with time, however, downward advected parcels of air will experience compressional warming at Γ_d, since there is no liquid water in the atmosphere. This will result in warmer parcels displacing cooler ones and $\langle R_d \rangle_y > 0$. Evidently the heating from the dynamics is not large enough to overcome the radiative cooling in this case. The opposite effect can be seen on the western side of the vortex where, $0 < \langle R_r/R \rangle_y < 1$, due to $\langle R_d \rangle_y < 0$, due to the expansion and cooling of parcels as they rise higher through the atmosphere, adding to the radiative cooling. The patterns in R generally correspond to those in R_d, which is expected given the uniformity of R_r (not shown). $R_d < 0$ corresponds to enhanced total cooling, whereas $R_d > 0$ corresponds to reduced total cooling or a warming (that is $R > 0$). As well as the absence of liquid water, these compressional effects rely on

$\Gamma < \Gamma_d$ (i.e., a stable atmosphere), and overturning and mixing is implied whenever $\Gamma > \Gamma_d$, which occurs close to the ground at times towards the valley bottom (not shown). Γ is near constant in space and time above $z = 2.5$ km, where the main cause of cooling variability is reversible compression effects, potentially affected by the horizontal advection of air. Below $z = 2.5$ km, where the dynamics is controlled by the downslope flows, the sources of cooling variability are more complex, as further explained below.

The 'blue' region positioned mainly behind the largest vortex, at the front of the downslope flow maximum region, indicating $\langle R \rangle_y > 0$ and $\langle R_d \rangle_y > 0$, is likely caused, at least in part, by compressional effects, as above. The 'blue' region corresponds to the area where the streamlines indicate the maximum downward transport of air. Close inspection of the field immediately above the valley floor reveals that the enhanced cooling here, noted above, is due to a combination of radiation and dynamics effects. Figures III.8b and III.8c correspond roughly to the times of minimum and maximum $\langle R_r/R \rangle_{va}$, during the period of instability, shown in Fig. III.5a, at $t = 47$ and 57 min, with values of 35 and 191 %, respectively. The cause of these extreme values is now clear. Considering the valley atmosphere only, Fig. III.8b shows a greater upward transport of air together with a larger 'blue' region, compared to Fig. III.8c, where the streamlines have been generally tilted towards the horizontal and the 'blue' region, carried with the flow, has been partly forced upwards and out of the valley atmosphere by the colliding opposite flows. The relatively intense upward motion occurs when the downslope flow intensification reaches the bottom of the slope. The situation is perhaps similar to the minimum 9 % radiative cooling rate contribution found by Hoch *et al.* [2011b] during a midnight air-intrusion into the Arizona meteor crater. Interestingly, the time of minimum $\langle R_r/R \rangle_{va}$, during the period of instability, occurs only 5 min before the time of maximum $\mathrm{CAPi}_{h,\max}$.

The large changes in $\langle R_r/R \rangle_y$ occurring over small distances adjacent to the valley floor, at $t = 60$ min, in general, are well correlated with nearby unstable air, which complements the evidence of turbulence in this region provided by the small-scale eddy, noted above. An animation of an (x, z) slice of R_r/R, taken half-way along y, reveals that the smallest of these turbulent features generally originate from the front of the downslope flow maximum region and are transported down the slopes towards the valley centre. This effect is not clear in $\langle R_r/R \rangle_y$, after approximately $t = 80$ min (when the variability across y increases), due to the averaging operation, which makes the analysis of small-scale features difficult. Figures III.8d and III.8e show clearly that $\langle \mathbf{k}_{xz} \rangle_y$ tilts towards the ground as the waves move closer to the plateau, which agrees well with the analysis of $\langle \omega'/N \rangle_{xz}$, also revealed in the patterns of ω' (see Appendix C). The thermodynamics effects of the IGWs are clear, with regions of $\langle R_d \rangle_y > 0$ occurring in the downward streamline regions of the waves, caused by counter-rotating vortices

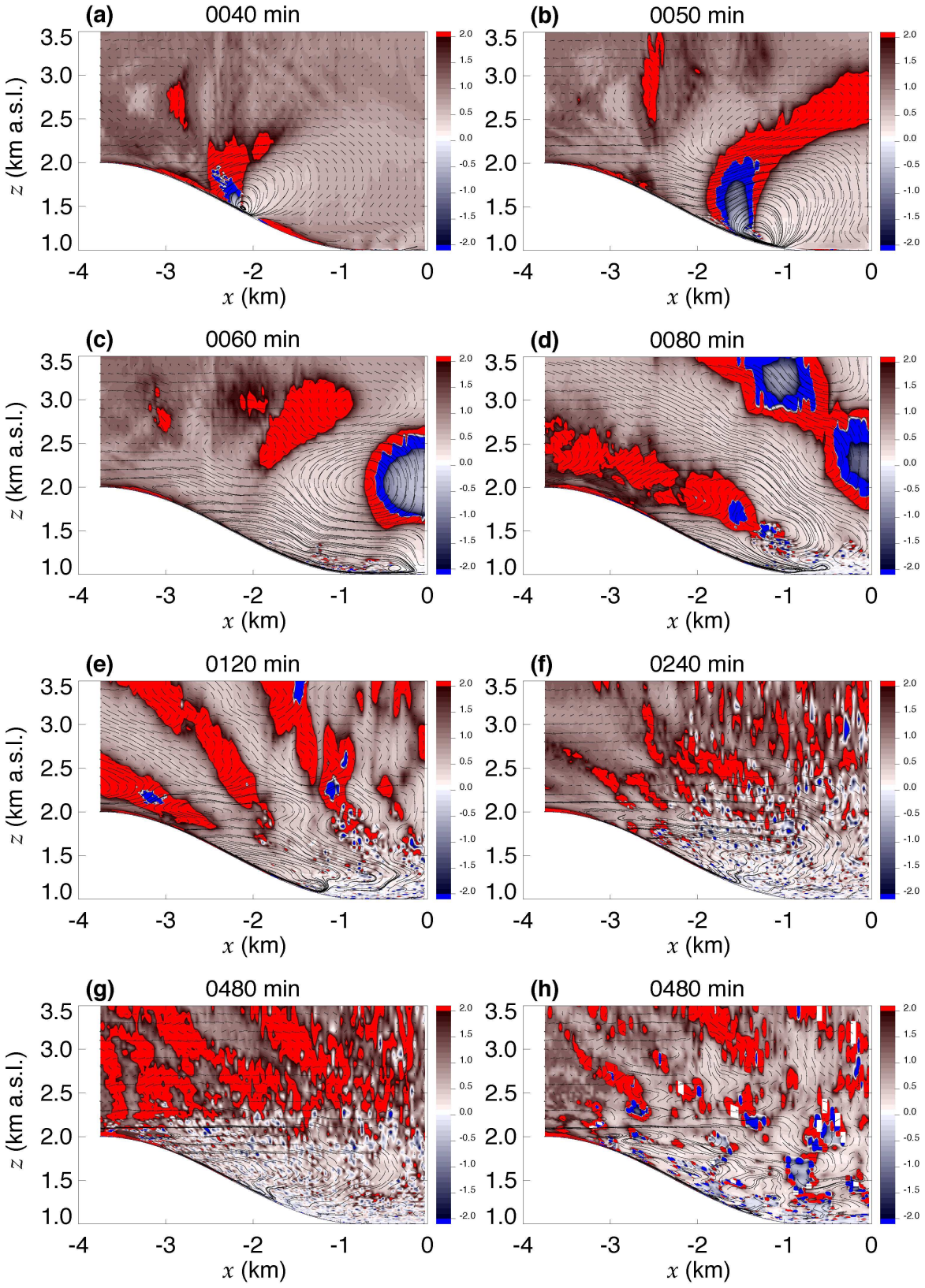

Figure III.8: Contour plots (**a**) to (**g**) of $\langle R_r/R \rangle_y$, with black streamlines over-plotted at t = 40, 50, 60, 80, 120, 240 and 480 min, and (**h**) R_r/R taken half-way along the y-dimension at t = 480 min.

between the upward streamline regions, where $\langle R_d \rangle_y < 0$. Close inspection of the (x, z) slices, as above, for all time, has revealed a general westward movement of regions with reduced cooling, or $\langle R \rangle_y > 0$, that are inter-spaced by regions of enhanced cooling, over the top half of the slope. Analysis of the streamlines indicates that in many cases these features are caused by westward propagating vortices, together with their associated compressional effects, as explained above. The instances where no vortex can be found reveal the occurrence of near-laminar advective effects. The westward transport of heating effects and vortices is caused by the quasi-permanent anti-clockwise circulation, and shallow region of near-horizontal streamlines close to the plateau height. Many of the heating features are absorbed into the downslope flow region. Higher above the plateaus there is also an apparent westward movement of compressional heating and cooling regions, but in fact this effect is due to the propagating IGWs that modulate the flow. Figures III.8f and III.8h provide some evidence of these effects. Figure III.8h is for an (x, z) slice, providing a representation of the turbulent flow field, as well as suggesting the continued presence of IGWs above the valley atmosphere at the end of the simulated period. Figures III.8d through III.8g make clear the dominance of cooling by the dynamics within the developing CAP_h (see Fig. III.7). Both radiation and dynamics effects appear to be important for the upward expansion of CAP_h. The general existence of relatively small-scale effects above the CAP_h suggests that the cold-air-pooling processes cause an interaction between the valley air and the free atmosphere above, although the degree of this effect remains unclear.

The minimum R_r within the valley atmosphere is -3.19 K hr^{-1}, occurring immediately adjacent to the ground. Generally, the greatest cooling in R_r is adjacent to the ground, with R_r decreasing steadily with distance from the surface (not shown). In comparison, Hoch *et al.* [2011b] found a maximum cooling rate of -1.25 K hr^{-1} close to the ground surface.

III.4 Summary

The purpose of this work was to unravel the physical processes controlling cold-air pools in complex terrain. For this purpose, the WRF numerical model was used to examine the variation of key cold-air-pooling forcing mechanisms in an idealized alpine-valley domain with a width of order 10 km under decoupled stable conditions.

The total average valley-atmosphere cooling results from a complex balance/interplay between radiation and dynamics effects. There are three fairly distinct regimes in the evolution of cold-air-pooling processes. Starting about one hour before sunset, there is an initial 30-min period when the downslope flows are initiated and longwave radiation almost completely dominates the cooling. A period of instability follows, when there

is a competition between radiation and dynamics effects, lasting some 90 min. Finally, there is a gradual reduction of the contribution of radiative cooling to total average valley-atmosphere cooling, $\langle R_r/R \rangle_{va}$, from 75 % to a final contribution of 37 %. The maximum cold-air-pool intensity corresponds to the time when cooling by radiation effects is at a minimum, within the period of instability. The initial heating effect by the dynamics and the subsequent time it takes for the dynamics effects to cool the valley atmosphere, together with broadly similar rates of cooling from radiation and dynamics, once the flow is established, results in $\langle \Delta\theta_{v_d}/\Delta\theta_v \rangle_{va} < \langle \Delta\theta_{v_r}/\Delta\theta_v \rangle_{va}$.

Further work is needed to investigate further the generality of this result, for example, by varying the initial conditions. The simulation average is approximately 64 % for $\langle \Delta\theta_{v_r}/\Delta\theta_v \rangle_{va}$, and 56 % for the period of gradual decline. For the latter time period, Hoch *et al.* [2011b] found a value of about 30 % for $\langle \Delta\theta_{v_{LW}}/\Delta\theta_v \rangle_{va}$. One possible explanation of the difference is the overestimation of radiative heat loss by the one-dimensional radiative transfer scheme used for this work, even though the effects of different terrain geometries and initial conditions considered by the two studies can not be ruled out.

Some of the intricacies of the valley mixing have been revealed. There are places where the dynamics dominate the cooling and radiation effects are minor.

Internal gravity waves have been identified in and above the valley atmosphere. An analysis of ω' complements the work of Chemel *et al.* [2009] and Largeron *et al.* [2013]. It has been found that $0.88 < \langle \omega'/N \rangle_{xz} \approx \langle \omega' \rangle_{xz}/\langle N \rangle_{xz} < 0.92$ for $-2.25 \leq x \leq 2.25$ km, $2.5 \leq z \leq 3.5$ km a.s.l., and $0.80 < \langle \omega'/N \rangle_{xz} \approx \langle \omega' \rangle_{xz}/\langle N \rangle_{xz} < 0.835$ for $-3.75 \leq x \leq 3.75$ km, with the same z range. The difference is caused by lower values of ω' above the top of the valley slopes, associated with a tilting of the wave vector towards the ground as the waves approach the plateaus, also apparent in the streamlines. The ratios decrease with t, as N increases, in agreement with the findings of Largeron *et al.* [2013].

III.5 Supporting information

1 See Appendix A for further discussion about the choice of vertical grid resolution, including a comparison between the numerical model results and available observations.

→ This item corresponds to a point in § III.2.1.

2 Note that Moeng *et al.* [2007] followed the earlier work of Moeng & Wyngaard [1988], who determined a reasonable value for the constant C_k for LES. C_k is used to model the subgrid-scale eddy diffusivities, using $K_M = C_k \Delta_g e^{1/2}$ and $Pr_e = K_M/K_H$, where K_M and K_H are the subgrid-scale eddy diffusivities for

momentum and scalars, respectively, $\Delta_g = (\Delta x\, \Delta y\, \Delta z)^{1/3}$ is the effective grid size, e is kinetic energy per unit mass, and Pr_e is the subgrid-scale Prandtl number. The value of 0.1 assigned to the constant C_k is smaller than the default value used in the WRF model, which was tuned for mesoscale cloud simulations [Takemi & Rotunno, 2003].

→ This item corresponds to a point in § III.2.1.

3 It should perhaps be emphasised that the idea of this study was to improve understanding of cold air pooling processes in alpine terrain. A range of terrain types exist in alpine terrain, so the Chamonix valley was used to help fix the simulation's initial and boundary conditions, including the length scales of the idealised valley. However, it is not claimed that the model set-up accurately simulates the exact evolution of the Chamonix valley atmosphere, which would presumably require a more tailored model set-up than that provided. It would be interesting to compare the results of the simulation completed for this study to those from simulations more tailored to the Chamonix valley.

→ This item corresponds to a point in § III.2.2.

4 The amount of acceptable grid distortion in a simulation, effectively the upper limit of c_2, depends on what errors are acceptable for a particular problem. The sizes of errors in the approximation of horizontal gradients will depend not only on how distorted the curvilinear grid is but also on the sizes of field variations where the grid is distorted. The initial field variations will depend on the model initial and boundary conditions, however, subsequent variations will depend to some extent on the computational errors themselves. Whether or not substantial errors are important for a simulation will depend on what the simulation is being used for. The parameter c_2 is commonly set in the range of 1–5 for simulations of complex terrain atmospheres Zhong & Chow [2013], since this range has been found to generate reasonable numerical results when evaluated against available observations and analytical solutions.

→ This item corresponds to a point in § III.2.3.

5 A test of the sensitivity of the numerical model results of interest to the horizontal grid resolution formed part of the model set-up. This sensitivity test is presented and discussed in Appendix B.

→ This item corresponds to a point in § III.2.3.

6 The impact of using different initial static stabilities, on the results found by this study, should be investigated, which might represent the case of long-lived elevated inversions and/or regions of enhanced cooling. Such cases can occur, for

example, under calm conditions during winter in snow covered terrain Chazette *et al.* [e.g. 2005]. Some previous work has investigated the effects of long-lived regions of enhanced cooling on pollutant concentrations [e.g. Silcox *et al.*, 2012] (see also Chapter V). A more detailed investigation into the effects of increasing γ on the thermodynamics of nocturnal valley atmospheres would be useful.

→ This item corresponds to a point in § III.2.4.

7 The simulation performed for this study considers the development of a region of enhanced cooling and its interactions with downslope flows during the early night. The evolution of the valley atmosphere for the full nocturnal period for the case considered should be quantified in future work. A future simulation of a diurnal or multi-diurnal period would enable investigation into the daytime valley thermodynamics. Downslope flows and regions of enhanced cooling have been reported during daylight hours in some locations [e.g. Chazette *et al.*, 2005]. A multi-diurnal simulation could be used to investigate the formation of long-lived regions of enhanced cooling and elevated inversions. The results of such a simulation could be used as initial conditions for sensitivity studies considering shorter time periods.

→ This item corresponds to a point in § III.2.4.

8 The choice of land-use type for this study was limited by the high vertical grid resolution, required to resolve the downslope flows with reasonable accuracy. Setting the land-use type to short grass avoided placing the lowest layer of the model grid within the vegetation, which would have rendered the surface-layer parameterisation inappropriate.

The constant landuse type used for this work is likely to be an over-simplification for some terrain depressions, where land-surface type varies significantly across the terrain. Variations in landuse can cause variations in surface parameters, such as the aerodynamic roughness length, and surface fluxes. Some discussion of this point was provided in § I.2.3.d. Further work should quantify the effects of varying landuse across terrain depressions. It would be of great interest to investigate the effects, on the results presented herein, of forest cover and/or an urban area at the bottom of the idealised valley.

Using the IBM [Lundquist *et al.*, 2012] to model forests is impractical for the mesoscale domain considered by this study. An extremely high horizontal resolution would be required to resolve individual trees; a resolution more typical of CFD simulations. The accurate representation of forests would require the implementation of a new parameterisation scheme in the numerical model used for this study, for example, following Ross & Baker [2013]. Given the horizontal res-

olution used for the simulation completed for this work, the IBM could be used to resolve a simplified urban area at the bottom of the implemented idealised valley. Another option could be to modify an existing urban parameterisation scheme, such as the Martilli scheme [Martilli *et al.*, 2002].

→ This item corresponds to a point in § III.2.4.

9 The simulation completed for this work avoided the additional complexity of shadowing effects. This allows the significance of shadowing on the development of cold air pools to be quantified in future work. Shadowing is likely to cause a different initiation of the downslope flows. Nadeau *et al.* [2012] took observations in an Alpine valley with a roughly similar configuration and orientation to that considered by this work. Near-zero flow speeds were observed close to sunset during what was termed the 'early-evening calm' period (see also Acevedo & Fitzjarrald [2001] and Mahrt *et al.* [2001]). The initiation of the downslope flows was found to be controlled by the movement of a shading front from the bottom towards the top of the valley slopes.

→ This item corresponds to a point in § III.3.1.

10 Whiteman *et al.* [1998] essentially made the same observation when analysing radiosonde soundings made in the Colorado plateau, which has the characteristics of a basin atmosphere. The Colorado plateau covers an area of approximately 225,000 km^2 and is surrounded by a fragmented ring of mountains that to the west are 1500-m high.

→ This item corresponds to a point in § III.3.1.a.

III.6 Chapter link

This chapter has clarified the key forcing mechanisms controlling the cooling of the nocturnal valley atmosphere for the alpine case considered and has focused on valley-atmosphere average quantities. This first chapter has targeted the first main objective of this work (see § I.6). In the next chapter a more thorough investigation of cooling processes within the valley atmosphere is made, including an analysis of the four-dimensional evolution of the region of enhanced cooling and its interactions with slope flows. The next chapter therefore targets the second main objective of this work (see § I.6) and is a reproduction of Burns & Chemel [2014b].

IV

Interactions between Downslope Flows and a Developing Cold-Air Pool

This chapter is a reproduction of Burns & Chemel [2014b] and maps onto the second objective of this work (see § I.6).

Paul Burns · Charles Chemel

Received: 27 November 2013 / Accepted: 29 July 2014

Abstract A numerical model has been used to characterize the development of a region of enhanced cooling, in an alpine valley with a width of order 10 km, under decoupled stable conditions. The region of enhanced cooling develops largely as a region of relatively dry air that partitions the valley atmosphere dynamics into two volumes, with air flows partially trapped within the valley by a developing elevated inversion. Complex interactions between the region of enhanced cooling and the downslope flows are quantified. The cooling within the region of enhanced cooling and the elevated inversion is almost equally partitioned between radiative and dynamics effects. By the end of the simulation, the different valley atmosphere regions approach a state of thermal equilibrium with one another, though this can not be said of the valley atmosphere and its external environment.

Keywords Cold-air pools · Downslope flows · Numerical simulation

P. Burns
Centre for Atmospheric & Instrumentation Research (CAIR),
University of Hertfordshire, College Lane, Hatfield, AL10 9AB, UK
email: p.burns@herts.ac.uk

C. Chemel
National Centre for Atmospheric Science (NCAS), Centre for Atmospheric & Instrumentation Research (CAIR),
University of Hertfordshire, College Lane, Hatfield, AL10 9AB, UK

IV.1 Introduction

Mountain and hill environments (i.e., complex terrain) have been estimated to cover 34 % of Earth's land surface (excluding the Antarctic and Greenland glaciers), directly supporting some 39 % of the growing global human population [Maybeck *et al.*, 2001]. Those people not living in these environments may nevertheless partially depend upon

them, for example, for a wide range of goods and services including water and energy resources, for biodiversity maintenance, as well as for recreational opportunities [Blyth *et al.*, 2002].

Downslope flows and cold-air pools (CAPs) are well known atmospheric phenomena of complex terrain, particularly under stable decoupled conditions, typical of nocturnal hours and the winter months in sheltered locations. Under these conditions it is known that downslope flows, together with in situ cooling by longwave radiative heat loss to space, control the evolution of CAPs [e.g. Whiteman, 2000]. In even 'moderate terrain' the temperature variations caused by CAPs can be large. For example, Gustavsson *et al.* [1998] reported near-surface air temperature variations close to 7 K over horizontal length scales of order 1 km, in terrain with elevation variations less than 100 m. In some places the air temperatures decreased by 8.5 K in 1 h following sunset. Such temperature variations are currently not well represented in weather forecast models [Price *et al.*, 2011], however, they have an important effect on road transport, aviation safety, and agricultural practices [e.g. Price *et al.*, 2011]. CAPs must be considered for the effective management of atmospheric pollutants [Anquetin *et al.*, 1999; Brulfert *et al.*, 2005; Chazette *et al.*, 2005; Szintai *et al.*, 2010; Chemel & Burns, 2014], and likely have an important modulating effect on climate change estimates [Daly *et al.*, 2009]. It is thought that cold-air-pooling processes are capable of affecting the wider atmosphere [Noppel & Fiedler, 2002; Price *et al.*, 2011]. For the foreseeable future, the representation of the effects of downslope flows and CAPs in both high-resolution forecast models and low-resolution climate and earth-system models, is likely to require varying levels of parametrization, which requires a sound understanding of the underlying physical processes.

Considerable progress has been made at documenting the characteristics of downslope flows and CAPs [see Zardi & Whiteman, 2013, for a review, and references therein]. However, the two-way interactions between downslope flows and CAPs has so far received little attention. Catalano & Cenedese [2010] used a large-eddy simulation (LES) to carry out a sensitivity study on cold-air pooling within three idealized valleys, which all had a depth of 500 m, and with widths and slope angles ranging between 7 and 13 km, and 5 and 10°, respectively. The depth of the CAP was derived by locating the point along vertical profiles of potential temperature θ, taken through the CAP at different times, which approximately corresponded to the θ-value of a near-neutral profile simulated at sunset. The causes of cooling within and above the CAP were not fully investigated. It was stated that the downslope flows interact with the developing CAP, however, this interaction needs to be further quantified. Burns & Chemel [2014a] used a LES to quantify the partitioning of cooling between radiative and dynamics effects (i.e., the combined effects of advection and subgrid-scale mixing), by averaging across the full volume of the valley atmosphere. This paper develops the work

of Burns & Chemel [2014a] by analyzing the spatial variation of cooling mechanisms within the valley atmosphere, and by considering the complex interactions between the downslope flows and the developing region of enhanced cooling.

The present paper considers cold-air-pooling processes in a valley atmosphere that is not subject to any synoptic forcing, which approximates the case of weak synoptic flows, or where the valley atmosphere is shielded from larger-scale flows by the terrain and possibly by stable layers. The set-up of the model and the design of the numerical simulation are presented in Sect. IV.2. Numerical results are analyzed in Sect. IV.3 and a summary is given in Sect. IV.4.

IV.2 Design of the Numerical Simulation

The numerical simulation presented herein was performed with the Weather Research and Forecasting (WRF) model [Skamarock *et al.*, 2008], version 3.4.1, which is specifically designed for research and operational forecasting on a range of scales. The model set-up used for this paper has been described and justified in full by Burns & Chemel [2014a]. A brief summary of the model set-up is provided here.

An idealized 1 km deep U-shaped valley, with its axis orientated south-north, was implemented with a maximum slope angle of 27.6°, flanked on either side by a horizontal plateau extending 2.25 km from the top of the valley slopes (see Fig. IV.1). The sinusoidal terrain was made uniform in y, though y was given a length of 1.2 km. The floor of the valley was given a half-width of 750 m and the x-dimension slope length was set to 3000 m. The terrain approximates the environment of the lower Chamonix Valley, located in the French Alps (45.92 °N, 6.87 °E).

The model was run in LES mode, with the vertical dry-hydrostatic-pressure coordinate discretized by 101 points. These points were stretched across the vertical coordinate z using a hyperbolic tangent function [Vinokur, 1980], which provided a vertical grid resolution Δz of approximately 1.5 m adjacent to the ground. The top of the model domain was set to a height of 12 km above sea level (a.s.l.). The model horizontal grid resolution, $\Delta x = \Delta y$, was set to 30 m, resulting in 402 and 42 points in x and y, respectively. A turbulent kinetic energy 1.5-order closure scheme [Deardorff, 1980] was used to model the subgrid scales. The constant C_k in the subgrid-scale parametrization scheme was set to 0.10 [Moeng *et al.*, 2007]. Because of the anisotropy of the grid, the width of the filter for the subgrid scales was modified following Scotti *et al.* [1993] [see also Catalano & Cenedese, 2010].

Time integration was performed using a third-order Runge-Kutta scheme using a mode-splitting time integration technique to deal with the acoustic modes. The model time step Δt and acoustic time step were 0.05 and $\Delta t/10$ s, respectively. The parameter β, used to damp vertically propagating sound waves, was set to 0.9 [see

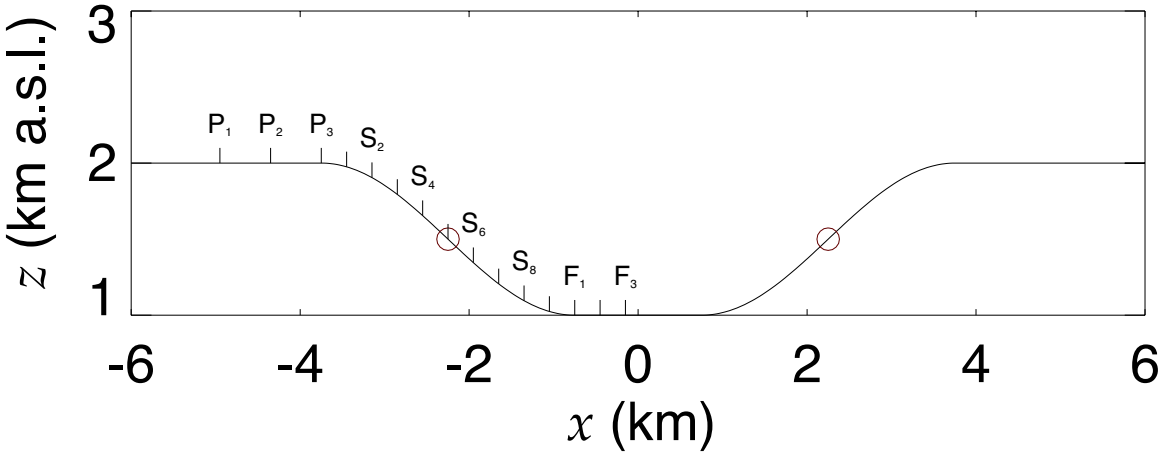

Figure IV.1: Variation of terrain height with x, orientated west-east. The terrain is uniform along y (into the page), orientated south-north, though y was given a length of 1.2 km. Symbols adjacent to the ground mark the positions where the downslope flows were analyzed in detail (see Sect. IV.3). The spacing between the analysis points is constant within each sub-section of the terrain [i.e. plateau (P), slope (S), and valley floor (F)]. The red circles mark the slope inflection points.

Dudhia, 1995]. Momentum and scalar variables were advected using a fifth-order Weighted Essentially Non-Oscillatory (WENO) scheme with a positive definite filter [Shu, 2003], with no artificial diffusion. Earth's rotation effects were neglected.

Model shortwave and longwave radiation physics were represented by the Dudhia [1989] scheme and the Rapid Radiation Transfer Model (RRTM) [see Iacono *et al.*, 2008], respectively. Slope effects on surface solar flux, and slope shadowing effects, were deactivated. The National Severe Storms Laboratory (NSSL) scheme [Mansell *et al.*, 2010] was used to parameterize microphysical processes. The revised MM5 Monin-Obukhov scheme, by Jiménez *et al.* [2012], simulated the atmospheric-surface layer, which was coupled to the community Noah land-surface model [Chen & Dudhia, 2001].

The simulation was provided with an initial weakly-stable linear lapse rate in virtual potential temperature, $\gamma_0 \equiv \partial\theta_v/\partial z\,|_{t=0} = 1.5$ K km^{-1}, an environmental lapse rate slightly less than the adiabatic rate. Therefore the simulation represents cases where there is no pre-existing residual layer, or stable layers, in the valley atmosphere at the start of the night, indicative of well-mixed post-convective conditions. The model was run for an 8 h period starting at 1430 UTC on 21 December, that is about 1 h before sunset at the latitude of the Chamonix valley. The atmosphere at the bottom of the valley was assigned an initial $\theta_v = 288$ K, a temperature of about 6 °C. The model skin temperatures T_0 were initialized by extrapolating the first three air temperatures above the ground. A random negative thermal perturbation was added to T_0 with a minimum value of -0.05 K, applied at the initial time across the valley slopes of the domain. The atmosphere was initialized with a constant relative humid-

ity of 40 %, preventing the occurrence of liquid water in the atmosphere. The wind field was zero everywhere at the initial time, simulating decoupled conditions.

The model deep soil temperature, at a depth of 8 m, is denoted T_{deep}. At the bottom of the valley T_{deep} was set to the annual mean surface air temperature of 281.4 K (8.25 °C). T_{deep} was varied with altitude across the idealized terrain at a rate of -2 K km^{-1}. The soil temperature, between the boundary values of T_0 and T_{deep}, was initialized by assuming that $T(z) = c_4 + A_0\, e^{z/d}$, where c_4 and A_0 are constants given the boundary conditions $T(z = 0) = T_0$ and $T(z = -3d) = T_{deep}$, where $z \leq 0$. The vegetation and landuse type were set to 'grassland', giving, for winter, a surface albedo of 0.23, a surface emissivity of 0.92, an aerodynamic roughness length of 0.1 m, and a surface moisture availability of 0.3 (volume fraction). The soil type was set to 'silty clay loam', a relatively moist soil [Oke, 1987b], with dry, wilting point, field capacity and maximum soil moistures of 0.120, 0.120, 0.387 and 0.464 (volume fractions), respectively. The soil was initialized with a constant soil moisture value 10 % below the chosen soil's field capacity, thereby placing the soil within the desired soil water redistribution regime that occurs after soil drainage [Nachabe, 1998]. The model results therefore consider a soil a few days after rainfall.

The model was run with periodic lateral boundary conditions, with a 4 km deep implicit Rayleigh damping layer [Klemp *et al.*, 2008] implemented at the top of the model domain. The damping coefficient was set to 0.2 s^{-1}.

IV.3 Results and Discussion

The methods used to define the region of enhanced cooling, denoted by CAP$_h$ hereafter, and downslope flows, as well as several other physical regions in and above the valley atmosphere, will first be presented in Sect. IV.3.1 and IV.3.2. Each section will end with a broad description of the evolution of the physical features defined therein. The details of the patterns introduced in Sect. IV.3.1 and IV.3.2 will be addressed in Sect. IV.3.3, which requires a consideration of the complex interactions that take place between the CAP$_h$ and downslope flows. The analysis of the system's complexities informs the analysis of its bulk features, which is given in Sect. IV.3.4. Inevitably, the latter section also informs the analysis of Sect. IV.3.3.

The subscript h in CAP$_h$ refers to the hydrostatic adjustment made to θ_v in order to reveal the region of enhanced cooling. The CAP$_h$ is evident in the field $\Delta\theta_v \equiv \theta_v - \theta_v\,(t = 0)$, where $\theta_v\,(t = 0)$ is the hydrostatic variation of θ_v.

IV.3.1 Defining the region of enhanced cooling

This section focuses on defining the CAP_h, however, a number of additional volumes that are useful for the analysis below are also defined. The CAP_h encompasses the ground-based inversion (GBI), which cools significantly more than the rest of the CAP_h, enabling the GBI to be defined within the CAP_h. The growth of the CAP_h is partly controlled by phenomena occurring in volumes close to the top of the valley atmosphere (discussed below), therefore these volumes have also been defined (see Fig. IV.2a).

The top height of the GBI (z_{GBI}) was tracked by locating the point above the valley floor where $\langle T \rangle_{xy}$ ceased increasing, where T is the air temperature. The averaging operator $\langle\ \rangle_{xy}$ denotes an average across the (x, y) plane, restricted here to the valley floor (i.e. $-0.75 \leq x \leq 0.75$ km). This average is justified by the fact that the iso-surfaces of the model scalar fields are near-horizontal planes above the valley floor (not shown).

In general, the top height of the CAP_h was tracked using both the θ_v field and atmospheric water-vapour mass-mixing ratio field q_v. The accumulated change of θ_v ($\Delta\theta_v$) and the atmospheric stability γ, both averaged across the full y-dimension (denoted by $\langle \Delta\theta_v \rangle_y$ and $\langle \gamma \rangle_y$, respectively) reveal that in general the CAP_h develops with a capping inversion (CI) at its top (see Sect. IV.3.3.a for examples of $\langle \gamma \rangle_y$), which can be tracked. For each t the algorithm searched for the maximum $\langle \partial\gamma/\partial z \rangle_{xy}$ above z_{GBI}, thus locating the lower edge of the CI, with this height denoted $z_{CI\downarrow}$. The top of the CI, denoted by $z_{CI\uparrow}$, was then found by searching upwards above $z_{CI\downarrow}$ for the minimum $\langle \partial\gamma/\partial z \rangle_{xy}$. $\langle \Delta\theta_v \rangle_y$ and $\langle q_v \rangle_y$ reveal that in general the CAP_h evolves as a region of relatively dry air surmounted by a thin layer of relatively humid air (not shown). Evidently, the transport of relatively dry air by the downslope flows, from higher altitudes towards the valley floor, is a greater effect than the surface moisture flux, for the model set-up used for this study. The relatively dry downslope flows displace and mix humid parcels adjacent to the valley floor upwards. These humid parcels are forced higher as the valley fills with relatively dry air.[1] The lower edge of the layer of high-q_v air, denoted $z_{HL\downarrow}$, where HL stands for humid-layer, was located by searching above z_{GBI} for the maximum $\langle \partial q_v/\partial z \rangle_{xy}$. The upper edge of the layer ($z_{HL\uparrow}$) was then located by searching upwards above $z_{HL\downarrow}$ for the minimum $\langle \partial^2 q_v/\partial z^2 \rangle_{xy}$.

Soon after $t = 60$ min a narrow region of relatively well-mixed air develops close to the top of each slope and spreads roughly horizontally toward the valley axis. The top and bottom of this layer are denoted by $z_{UML\downarrow}$ and $z_{UML\uparrow}$, respectively, where UML stands for upper mixed layer (see Fig. IV.2a). This region is characterized by high-shear and vortices and lies directly beneath the region of near-horizontal streamlines,

[1] see supporting information (§ IV.5)

directed from the valley axis towards the plateaux, noted by Burns & Chemel [2014a]. These features contribute to the development of an elevated inversion and trap air within the valley; they play an important role in the development of the CAP_h (see Sect. IV.3.3.b).

Throughout the simulation a thin layer of relatively stable air develops above $z_{UML\uparrow}$, where the top of this layer is denoted by $z_{USL\uparrow}$, where USL stands for upper stable layer. The heights defining the UML and USL were defined in essentially the same way as the heights defining the CI and HL.

The curves in Figure IV.2a compare well with the vertical structure of their corresponding fields away from the valley slopes. Close to the slopes the fields tend to curve upwards away from the horizontal, resulting in some under-estimation of field heights. Intense mixing takes place close to the sloping ground where the downslope flows interact with the dense air of the CAP_h. This can result in the CI being ill defined in this region when it can still be defined further away from the slopes.

The curves demarking the CI and HL in Fig. IV.2a indicate that the CAP_h expands upwards through the valley atmosphere after $t \approx 60$ min. The GBI is also shown to gradually deepen after $t \approx 120$ min.[2] There are a number of complexities in the curves of Fig. IV.2, for example, there are significant differences in the heights of the curves for the CI and HL after $t = 120$ min. A number of discontinuities exist in the curves for the CI, and the GBI top height includes a maximum point before $t = 120$ min. These complexities are the result of the varying interactions between the downslope flows and developing CAP_h, which will be discussed in Sect. IV.3.3.

IV.3.2 Defining the Downslope Flows

The components of the velocity field $\mathbf{u}$ in WRF are given with respect to the Cartesian coordinate system (x, y, z). By applying an orthogonal transformation to (x, y, z) with rotation/slope angle α, a slope-orientated coordinate system (s, y, n) is introduced, with s directed downslope and n pointing away from the slope. In accord with the usual geometric convention, α is defined to be negative for clockwise rotations, from the line defined by x. The components of $\mathbf{u}$ along s and n, denoted by u_s and u_n, respectively, were obtained from $\langle \mathbf{u}_{xz} \rangle_y$, $\mathbf{u}_{xz} \equiv (u, w)$. The analysis also considers u_s and u_n averaged across the depth of the downslope flows, denoted by $\langle u_s \rangle_n$ and $\langle u_n \rangle_n$, respectively. The upper limit for the average across n (n_{df}) was calculated by searching within 100 m above the ground for the first point where u_s falls below 20 % of its maximum value $u_{s,j}$ (the downslope flow jet speed, located at n_j), that is, where $u_s < c_4\, u_{s,j}$, $c_4 = 0.2$. A 100-m long normal vector was constructed for each x point with a resolution of 1 m, approximately Δz in this region. A more exact estimate of

[2] see supporting information (§ IV.5)

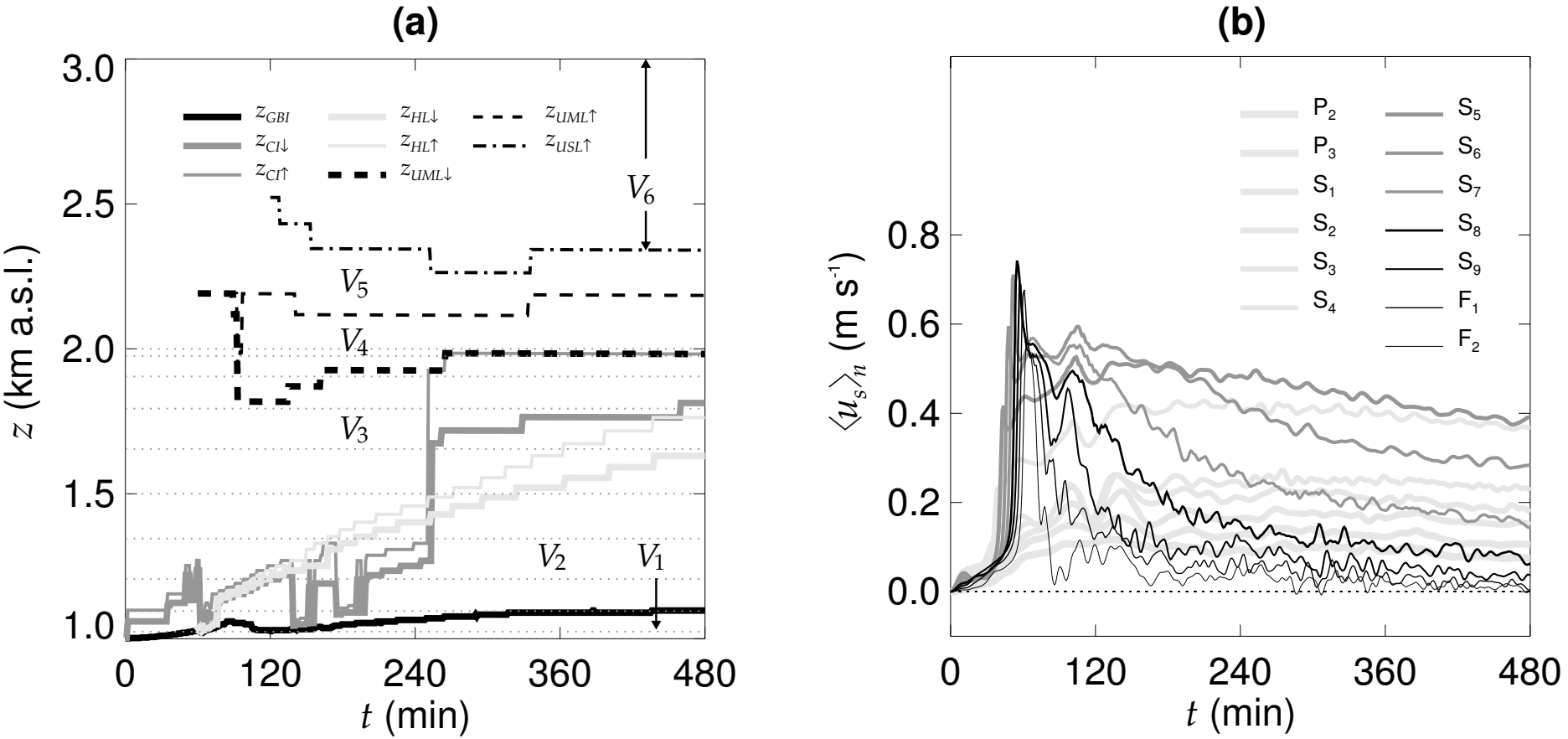

Figure IV.2: Time series of **(a)** the height of the ground-based inversion, z_{GBI}, the lower and upper boundaries of the capping inversion (denoted by $z_{CI\downarrow}$ and $z_{CI\uparrow}$, respectively), the humid layer (defined by $z_{HL\downarrow}$ and $z_{HL\uparrow}$), and the upper mixed layer (defined by $z_{UML\downarrow}$ and $z_{UML\uparrow}$). The top edge of the upper stable layer is denoted by $z_{USL\uparrow}$ (see text for details). Horizontal dotted lines mark the heights of the analysis points shown in Fig. IV.1. Six volumes are defined by V_1 : 1 km $< z < z_{GBI}$, $V_2 : z_{GBI} < z < z_{HL\downarrow}$, $V_3 : z_{HL\uparrow} < z < z_{UML\downarrow}$, $V_4 : z_{UML\downarrow} < z < z_{UML\uparrow}$, $V_5 : z_{UML\uparrow} < z < z_{USL\uparrow}$, and $V_6 : z_{USL\uparrow} < z < 3$ km. The volumes were limited along x between the top of each slope (i.e. $-3.75 \leq x \leq 3.75$ km) and allowed to encompass the full y-dimension, and **(b)** the layer-averaged downslope flows $\langle u_s \rangle_n$ (defined in Sect. IV.3.2) at the analysis points defined in Fig. IV.1. Note that after $t = 180$ min $\langle u_s \rangle_n$ increases from P_2 to S_5 before decreasing between S_5 to F_2.

n_{df} where $u_s = c_4\, u_{s,j}$ was then obtained by linear interpolation. The value of c_4 is arbitrary, chosen to avoid any large under- or over-estimations of n_{df}. If $c_4\, u_{s,j}$ could not be found, then the n-point associated with the maximum (minimum) $\partial^2 u_s/\partial n^2$ was used for the western (eastern) slope. This latter method focuses on the shape of the downslope flow profile rather than on relative flow speeds. The algorithm, designed for cases with a fairly distinct downslope flow jet, was found to work effectively away from the slope extremities (not shown).

Figure IV.2b shows $\langle u_s \rangle_n$ for the analysis points P_2 to F_2 defined in Fig. IV.1. Figure IV.2b reveals the essential spatial and temporal structure of the y- and n-averaged downslope flow field. The curves for the points over the valley slope reveal the initial propagation of the downslope flow maximum region down the slope, which reaches the valley floor close to $t = 60$ min. Burns & Chemel [2014a] demonstrated the presence of an anticyclonic vortex (with rotation axis along y) at the front of this maximum region, which is an example of a microfront, a phenomenon discussed more generally by Mahrt [2014], whom observed them in shallow fog layers. A general increase of $\langle u_s \rangle_n$ is evident moving from the western plateau to the western slope inflection point (S_5), followed by a general decrease of $\langle u_s \rangle_n$ towards the valley floor. One exception is the curve for S_5 before $t \approx 180$ min. A clear increase and decrease of $\langle u_s \rangle_n$ occurs over time for points located below S_3, with the decrease shown to begin earlier in time for points further down the slope. This is consistent with the retreat of the region of maximum downslope flows back up the western slope as the CAP_h expands upwards, noted by Burns & Chemel [2014a] and implied by Catalano & Cenedese [2010].

IV.3.3 Co-evolution of the region of enhanced cooling and downslope flows

IV.3.3.a Initial evolution of the region of enhanced cooling

$\langle \gamma \rangle_y$, and $\langle \Delta\theta_v \rangle_y$ with over-plotted streamlines (as in Fig. IV.3b), reveal that the CI is first formed soon after $t = 60$ min, when the region of maximum downslope flows reaches the valley floor. At this time the accelerated flows transport cold (low-θ_v) air (relative to the atmosphere away from the ground along x) along the slopes towards the valley floor, and mix it approximately 200 m into the atmosphere, generally increasing γ in this region. These flows also partly mix the pre-existing largely radiatively cooled air-layer, adjacent to the valley floor, higher into the atmosphere, noted by Burns & Chemel [2014a]. After the intensification of the downslope flows their effect on the CAP_h is more complex. At these later times the downslope flows are comprised of a layer of relatively cold (low-θ_v) air close to the ground, however, the top part of the downslope flows contains relatively warm (high-θ_v) air. The downslope flows advect

higher-θ_v air from above that increases $\Delta\theta_v$ in the top part of the downslope flows that is less affected by the cooling surface. Despite this advection of warm air into the CAP_h the downslope flows on average have a cooling effect on the CAP_h (see Sect. IV.3.4). This is due to both the transport of cold air close to the ground and the bulk rising motions induced to conserve mass, which causes adiabatic cooling.

Figures IV.2a and IV.4a show that the intensification of the downslope flows causes both a rapid increase in the depth and a reduction in the intensity or strength (denoted by I_{GBI}), of the GBI between $t = 60$ and 85 min (with z_{GBI} rising from 1026 to 1060 m a.s.l., and I_{GBI} decreasing from 2.64 to 1.50 K), supporting the pattern of mixing stated above.

Mixing from the dynamics creates a relatively well-mixed region within the CAP_h, which defines the CI, that is the mixing is non-uniform within the CAP_h (see Fig. IV.3). Hence, the CI cannot exist before the downslope flow intensification and the curves for $z_{CI\downarrow}$ and $z_{CI\uparrow}$ are difficult to interpret before this event. This intensification of the dry downslope flows displaces humid air adjacent to the valley floor upwards. Mixing caused by the downslope flows tends to re-sort parcels according to their moisture content, forcing moist lighter parcels above dry heavier ones. Therefore $z_{HL\downarrow}$ and $z_{HL\uparrow}$ are undefined during the first 60 min of simulation. Despite the difficulty interpreting $z_{CI\downarrow}$ and $z_{CI\uparrow}$ before $t = 60$ min, the algorithm captures the upward displacement of air and the general perturbation of the lower valley atmosphere. This coincides with the initiation of internal gravity waves (IGWs) in and above the valley atmosphere, effects noted by Burns & Chemel [2014a].

$\langle\Delta\theta_v\rangle_y$, $\langle\gamma\rangle_y$ and $\langle q_v\rangle_y$ indicate that between $t \approx 70$ and 180 min the CAP_h expands upwards, together with its CI, carrying the layer of relatively high-q_v air to greater heights. Over the same time period mixing processes gradually erode the CI, close to the top of the CAP_h, so that by $t \approx 180$ min it is not well defined (compare Fig. IV.3a and IV.3c). This is reflected in Fig. IV.2a by a large sudden decrease in $z_{CI\downarrow}$ and $z_{CI\uparrow}$; at this time the algorithm used to track the CI finds a lower layer of relatively high γ that does not demark the top of the CAP_h. After this discontinuity a layer of high γ is found by the algorithm at a lower height range than the CI height range before the discontinuity, but is soon eroded away. A similar behaviour occurs close to $t = 140$ min (discussed below), however, between $t = 140$ and 180 min a CI is present at the top of the CAP_h, which can be reasonably estimated by $z_{HL\downarrow}$.

Figure IV.2a suggests that the early development of the CAP_h erodes away the top of the GBI, decreasing z_{GBI} from a maximum of 1060 m a.s.l. at $t = 85$ min to a minimum of 1026 m a.s.l. at $t = 121$ min. This coincides with the time period when the maximum region of the downslope flows is forced back up the slopes by the CAP_h (see Fig. IV.4b). Relatively intense mixing close to the front of this maximum region erodes away the top of the GBI (as also indicated by the streamlines in Fig. IV.3b).

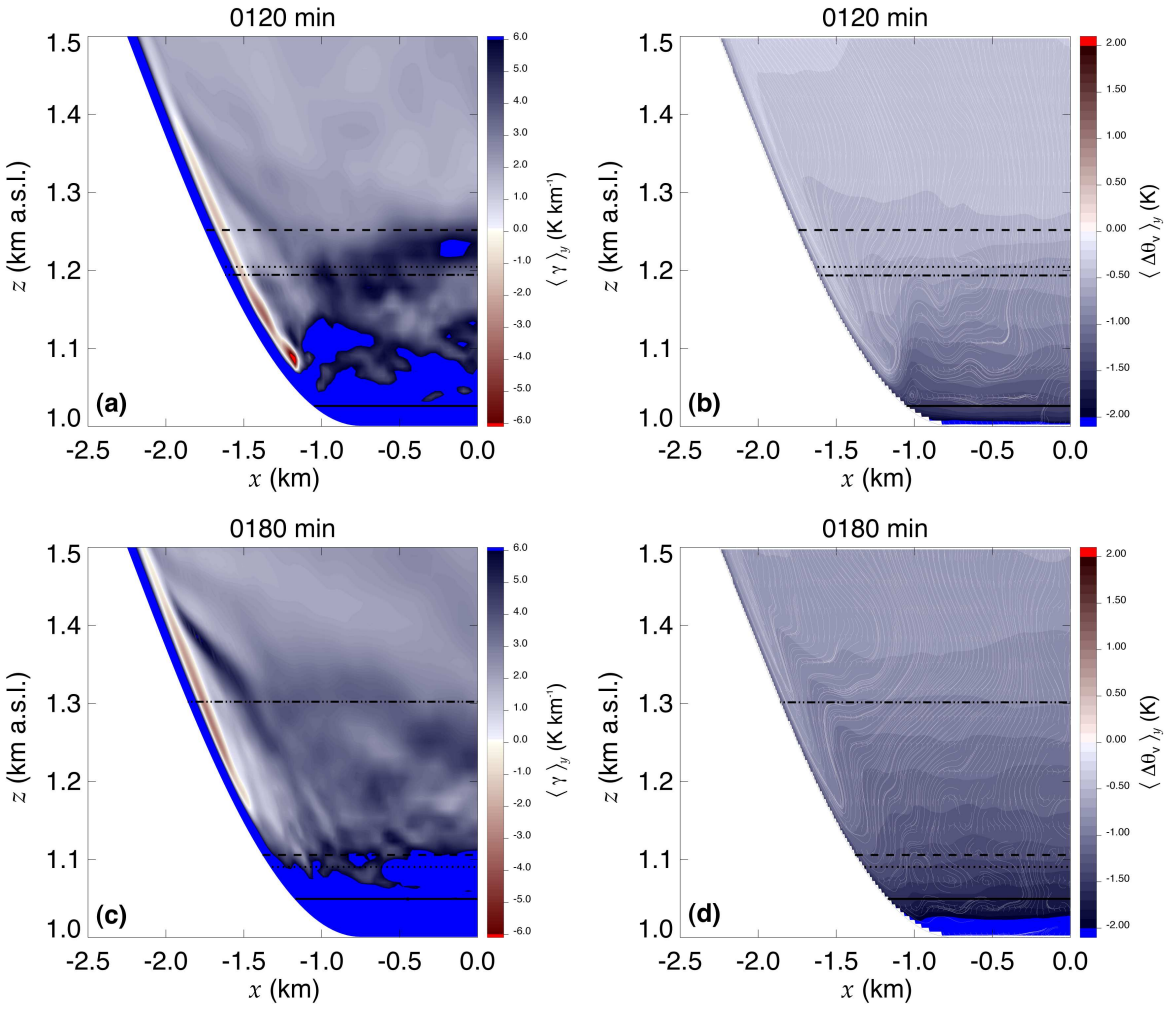

Figure IV.3: Contour plots of **(a)** $\partial\theta_v/\partial z$ averaged across the model y-dimension $\langle\gamma\rangle_y$ and **(b)** the accumulated change of θ_v from $t = 0$, averaged across y, $\langle\Delta\theta_v\rangle_y$, with over-plotted streamlines, both at $t = 120$ min, and **(c)** and **(d)** the same type of plots as for **(a)** and **(b)** but at $t = 180$ min. The solid, dashed, dotted and dash-dotted lines mark, respectively, the heights of the ground-based inversion z_{GBI}, the upper and lower boundaries of the capping inversion ($z_{CI\uparrow}$ and $z_{CI\downarrow}$), and the approximate height where the downslope flows are neutrally buoyant. The latter corresponds to $F_b \approx 0$ and is used later in this section. The streamlines were created using $\langle\mathbf{u}_{xz}\rangle_y$, $\mathbf{u}_{xz} \equiv (u, w)$, projected onto a 5-m linear orthogonal mesh, where the resolution of the new grid was justified by Burns & Chemel [2014a]. The streamlines were seeded on the Cartesian grid, with the same origin, with a resolution of 35 m, which is generally close to the model grid resolution in this region of the atmosphere.

Figure IV.4b compares $z_{HL\downarrow}$ to a number of downslope flow characteristics in order to investigate some of the interactions between the CAP_h and the downslope flows. The curves denoted by $\max(u_{s,j})$, $\max(\langle u_s\rangle_n)$, and $\max(\langle u_n\rangle_n)$ show the heights corresponding to the greatest $u_{s,j}$, $\langle u_s\rangle_n$ and $\langle u_n\rangle_n$, respectively. These curves show the initial propagation of the downslope flow maximum region down the western slope (matching the patterns in Fig. IV.2b).

It should be noted that the simulation completed for this work avoided the ad-

ditional complexity of shadowing effects. This allows the significance of shadowing on the development of cold air pools to be quantified in future work. Shadowing is likely to cause a different initiation of the downslope flows. Nadeau *et al.* [2012] took observations in an Alpine valley with a roughly similar configuration and orientation to that considered by this work. Near-zero flow speeds were observed close to sunset during what was termed the 'early-evening calm' period [see also Acevedo & Fitzjarrald [2001] and Mahrt *et al.* [2001]]. The initiation of the downslope flows was found to be controlled by the movement of a shading front from the bottom towards the top of the valley slopes.

Between $t \approx 60$ and 180 min it is clear that as the CAP_h top height increases (reasonably estimated by $z_{HL\downarrow}$ during this period) so does the height of $\max(\langle u_s \rangle_n)$ and $\max(u_{s,j})$, which quantifies the initial retreat of the downslope flow maximum region back up the valley slopes. This retreat of the maximum region matches the patterns of decreasing $\langle u_s \rangle_n$ below slope point S_3, noted in Sect. IV.3.2. Time series of the mass flux computed from the above defined flow speeds show essentially the same patterns as those already discussed.

The sudden decrease of $z_{CI\downarrow}$ and $z_{CI\uparrow}$ at $t \approx 140$ min is associated with the development of a relatively well-mixed layer, immediately above z_{GBI}, with this layer generally expanding upwards over time with the CAP_h (compare Fig. IV.3a and IV.3c). Figure IV.3 indicates that the development of relatively well-mixed regions within the CAP_h are generally associated with regions where $\langle \mathbf{u}_{xz} \rangle_y$ and $\nabla_{xz} \langle \mathbf{u}_{xz} \rangle_y$ are relatively large, where ∇_{xz} is the (x, z) part of ∇. These regions promote both explicit mixing and shear-induced subgrid-scale mixing, where the latter essentially relies on elements of $\nabla(\nabla \mathbf{u})$ [see Skamarock *et al.*, 2008]. The streamlines give a rough idea of relative flow strengths, so the above observation was confirmed by an analysis of $|\langle \mathbf{u}_{xz} \rangle_y|$ (not shown).[3] An exact correspondence between the stability of the atmosphere, flow strengths and flow gradients is not expected due to the averaging process. It is also not expected that a particular flow configuration will immediately alter the atmospheric stability, which may take time to adjust to the flow regime. The relatively well-mixed regions generally correspond to regions of large $-\langle \mathbf{u}' \cdot \nabla \theta_v' \rangle_y$, the Reynolds stress term for the conservation of energy (not shown),[4] where the perturbations were computed by averaging across y. This is justified by the fact that only small variations of $\mathbf{u}$ occur along y, due to the 2D geometry and near-y-independent thermal forcing at the ground-air interface.

$\langle u_n \rangle_n$ approximates the net mass flux along n and so $\max(\langle u_n \rangle_n)$ suggests that detrainment of air from the slopes, considering the resolved flow, reaches a maximum not far above z_{GBI}, which is generally supported by an analysis of the streamlines of

[3] see supporting information (§ IV.5)
[4] see supporting information (§ IV.5)

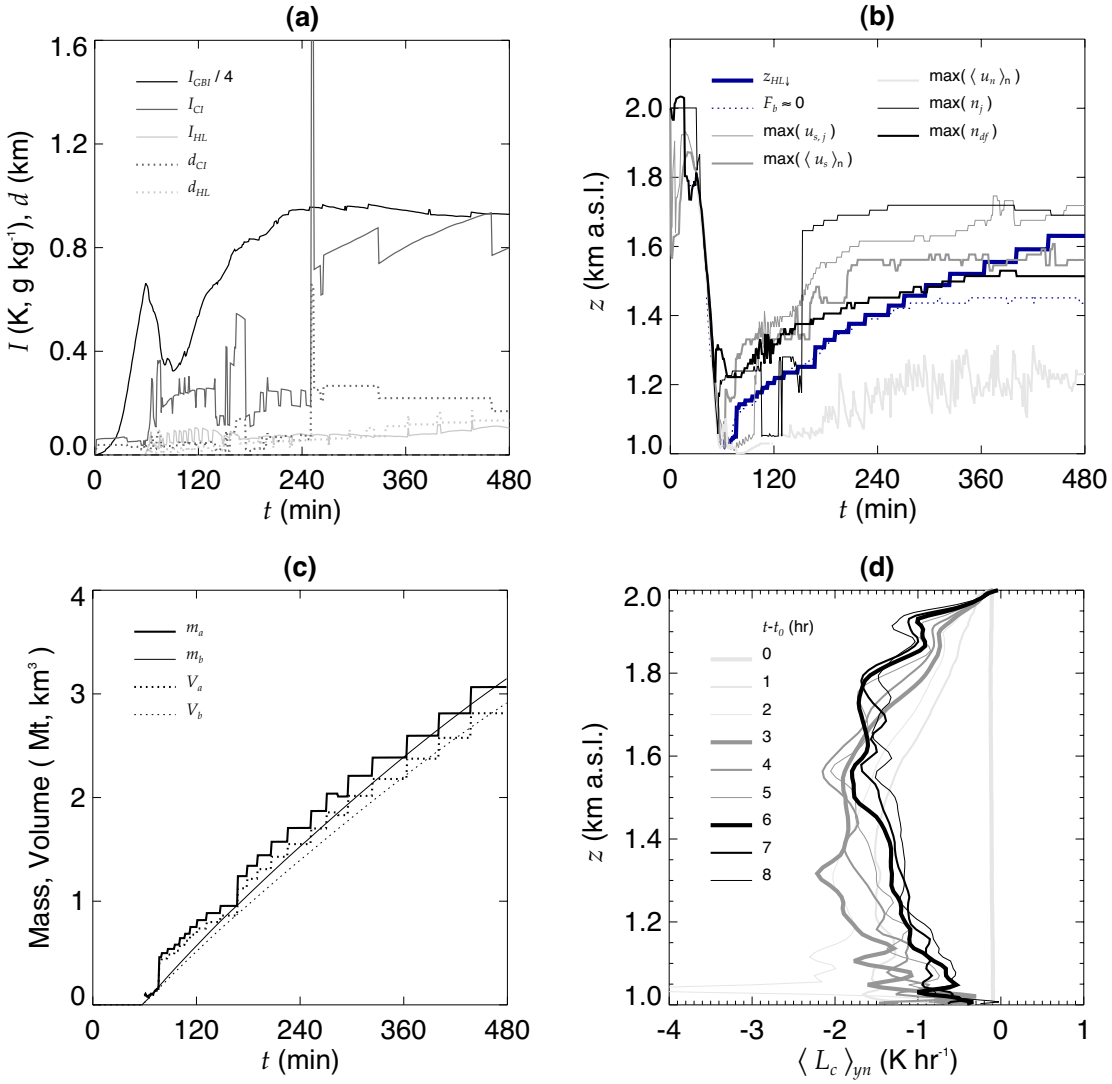

Figure IV.4: Time series of **(a)** the intensity (strength) of the ground-based inversion, capping inversion and humid layer, denoted I_{GBI}, I_{CI} and I_{HL}, respectively. I_{GBI} and I_{CI} were defined as the difference in $\langle\theta_v\rangle_{xy}$ across the layers, and I_{HL} as the difference in $\langle q_v\rangle_{xy}$ between the centre and bottom of the layer. The depths of the capping inversion and humid layer are also shown, denoted by d_{CI} and d_{HL}, respectively, **(b)** $z_{HL\downarrow}$ compared against a number of downslope flow characteristics. These include the height of the greatest downslope flow jet speed, denoted by max($u_{s,j}$). The height of the greatest layer-averaged flow along and normal to the slope is denoted by max($\langle u_s\rangle_n$) and max($\langle u_n\rangle_n$), respectively. The height where $u_{s,j}$ is furthest from the ground along n (i.e., the greatest n_j) is denoted by max(n_j). The height where the depth of the downslope flow is greatest is denoted by max(n_{df}). The height where the downslope flows are neutrally buoyant is also provided (i.e., where $F_b \approx 0$), see text for details. **(c)** Time series of the mass and volume of air below $z_{HL\downarrow}$, denoted by m_a and V_a, respectively, and the accumulation of mass and volume, across $z_{HL\downarrow}$, from the downslope flows, denoted by m_b and V_b (see text for details). **(d)** shows the hourly variation with height (by moving along s) of the two-dimensional layer-averaged diabatic cooling rate $\langle L_c\rangle_{yn}$.

$\langle \mathbf{u}_{xz} \rangle_y$ (see Fig. IV.3).

An analysis of $\langle u_n \rangle_n$ reveals some detrainment of air above $z_{HL\downarrow}$, however, the amount of detrained air in this region is much smaller than below $z_{HL\downarrow}$ (see Fig. IV.5a). Figure IV.5a shows the variation of $\langle u_n \rangle_n$ with height (i.e. along s), for $t = 90$, 180 and 300 min. The horizontal dotted-lines correspond to $z_{HL\downarrow}$ at the three different times ($z_{HL\downarrow}$ increases with time). A greater detrainment effect might be expected for a greater γ_0. Below $z_{HL\downarrow}$, multiple maxima and minima of $\langle u_n \rangle_n$ indicates a layering effect as the downslope flows detrain into the valley atmosphere, inducing wind shears and mixing. A similar layering effect was found by Neff & King [1989] who observed the formation of a CAP that grew from the floor of the De Beque Canyon, located along the Colorado River, USA. Reduced entrainment (or slight detrainment) is evident within the elevated inversion, as well as enhanced entrainment below it. This is generally inline with the analytical theory laid out by Vergeiner & Dreiseitl [1987]. This reduction of entrainment or slight detrainment suggests that the elevated inversion helps to shield the valley atmosphere from flows above. The importance of this effect remains unclear. A slight entrainment of air is evident immediately below $z_{HL\downarrow}$ during approximately the last hour of simulation.

Generally detrainment occurs below a level approximately 100 m above $z_{HL\downarrow}$. This detrainment occurs both above and below the height where the downslope flows are neutrally buoyant (i.e., where the buoyancy force $F_b = \langle g\, \theta'_v / \theta_{v_a} \sin\alpha \rangle_n = 0$). F_b is expressed in slope orientated coordinates (as above) for a Boussinesq fluid. g is the acceleration due to Earth's gravitational field, $\theta'_v(s,n,t) = \langle \theta_v \rangle_y - \theta_{v_a}$, is the perturbation from the ambient θ_v-field $\theta_{v_a}(z,t) = \langle \theta_v \rangle_{xy}$, where the averaging operators are those used in Sect. IV.3.1. The approximation $\rho'/\rho_r \approx -\theta'_v/\theta_{v_a}$ has been used, where ρ' is the perturbation from a constant reference density ρ_r. $F_b \approx 0$ was located by first finding the maximum and minimum F_b, and then searching from the maximum towards the minimum position.

Generally entrainment occurs above a level approximately 100 m above $z_{HL\downarrow}$. These detrainment and entrainment effects are evident in the streamlines of $\langle \mathbf{u}_{xz} \rangle_y$. Significant variations of $-\langle \mathbf{u}' \cdot \nabla \theta'_v \rangle_y$ close to the ground surface essentially mirror the changes of $\langle u_n \rangle_n$. $-\langle \mathbf{u}' \cdot \nabla \theta'_v \rangle_y$ indicates negligible mixing close to the ground surface in the entrainment region but enhanced mixing within about 200 m from the slopes in the detrainment region.[5] Enhanced shear-induced mixing is likely to occur where the downslope flows detrain and where they 'spring-back' after 'over-shooting' $F_b \approx 0$. This region of enhanced shear is evident in the streamlines of $\langle \mathbf{u}_{xz} \rangle_y$ (see Fig. IV.3). A similar pattern of entrainment and detrainment, as well as the 'spring-back' effect were found by Baines [2008], studying gravity currents flowing down a steep uniform slope in irrotational stratified liquids, in what was termed the 'plume regime'.

[5] see supporting information (§ IV.5)

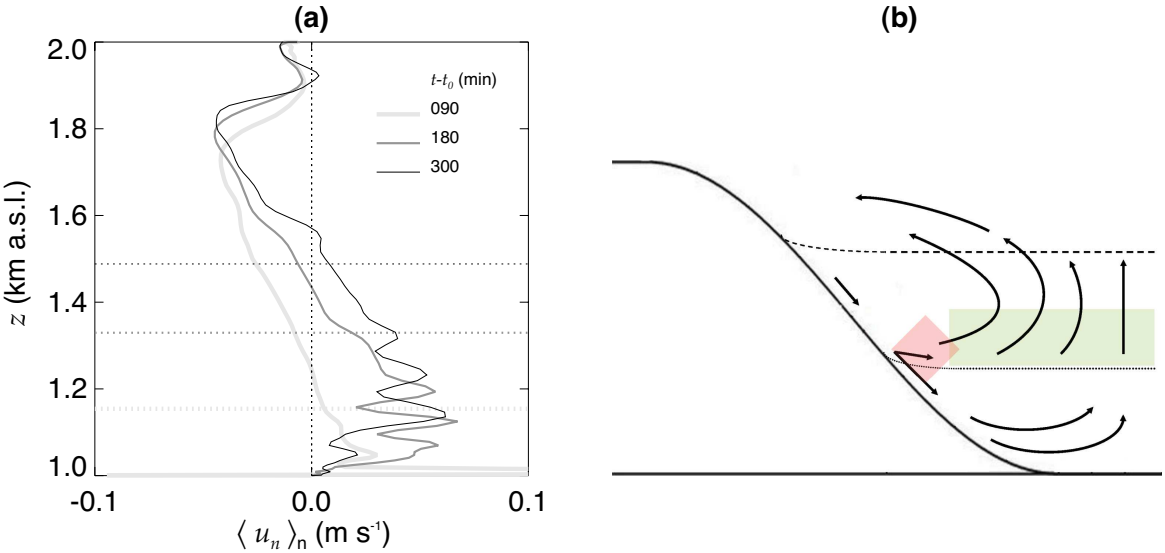

Figure IV.5: **(a)** Variation of $\langle u_n \rangle_n$ along the western slope at three times, as indicated. Horizontal dotted-lines mark the height of $z_{HL\downarrow}$ at the three times ($z_{HL\downarrow}$ increases with time), and **(b)** a schematic illustrating the mechanisms that 'accelerate' the cooling in the upper portion of the valley atmosphere after $t = 180$ min. Arrows indicate flow direction, the dotted and dashed lines represent $z_{HL\downarrow}$ and $z_{CI\downarrow}$, respectively. The transparent red square and green rectangle indicate regions of enhanced mixing/detrainment and longwave radiative divergence, respectively. The latter corresponds to a region of relatively moist air.

The streamlines in Fig. IV.3 indicate that the thin regions of unstable air above the downslope flows are linked to the return flows associated with the spring-back effect. The return flows transport low-θ_v air from the bottom of the valley. The downslope flows advect higher-θ_v air downslope that increases $\Delta\theta_v$ in the top part of the downslope flows. The combination of these two effects results in $\gamma < 0$. It is interesting to note that the return flows are restricted to the part of the slope below $z_{HL\downarrow}$.

The mass flux from the downslope flows at the slope point corresponding to $z_{HL\downarrow}$ can be accumulated over time and compared to the mass in the volume of atmosphere beneath $z_{HL\downarrow}$, obtained using a Cartesian coordinate system. The resolution of the regular grid was 5 m, which was justified by Burns & Chemel [2014a]. Figure IV.4c shows that the mass within the CAP$_h$ below $z_{HL\downarrow}$ (m_a), is approximately equal to the accumulated mass from the downslope flows (m_b). The downslope flow mass flux was assumed to be symmetric about the valley axis. It was noted in Sect. IV.3.1 that $z_{HL\downarrow}$ is likely to be an under-estimation of the height of the humid layer close to the slopes, and so the point used to estimate the mass flux is likely to be slightly within the region of relatively dry air. Mass may be mixed into this region before reaching the mass flux point, and some slight under-estimation of the accumulation of mass from the downslope flows might be expected. Volumes V_a and V_b in Fig. IV.4c, calculated in a similar

manner as m_a and m_b, demonstrate that the fluid is approximately incompressible. This analysis shows that q_v is an effective tracer of the flow field. Between $t = 60$ and 180 min $z_{HL\downarrow}$ is a reasonable estimate of the CAP_h top height and so Fig. IV.4c confirms that the growth of the CAP_h during this period is almost entirely due to the flux of mass from the downslope flows into the CAP_h. After $t \approx 180$ min the development of the CAP_h is more complex and it is not possible to state that the upward expansion of the CAP_h is essentially due to the flux of mass from the downslope flows into the CAP_h (see Sect. IV.3.3.b).

It seems reasonable to suggest that a significant along-valley flow is likely to remove cooled air from the bottom of the valley and transport it to relatively flat regions (e.g. a plain). This is likely to reduce the speed of expansion of the CAP_h as well as its maximum height, however, this needs to be confirmed by future research.

IV.3.3.b Development of the region of enhanced cooling

The gradual erosion of the CI is essentially caused by the interactions of the downslope flows with the expanding CAP_h, which forces the downslope flows back up the valley slopes, but is mixed and eroded as it does so. Relatively intense mixing occurs below the front of the downslope flow maximum region. Further mixing occurs across the regions of high-curvature associated with larger-scale circulations (see Fig. IV.3b and IV.3d). Although the streamlines indicate a flow across the CI (away from the slopes), at $t = 120$ min (when the CI height range approximates that of the HL), Sect. IV.3.3.a demonstrated that any such flow must be small. The valley atmosphere dynamics are largely partitioned into two volumes, defined by $z_{HL\downarrow}$.

It appears that the erosion of the CI is accelerated as it comes into contact with the most energetic part of the flow (close to analysis points S_5 and S_6, compare Fig. IV.2a and IV.2b), and is broken up soon after $t = 180$ min. Between $t \approx 180$ and 300 min the top of the CAP_h is difficult to define. $z_{HL\downarrow}$ does not always correspond to the CI or to the CAP_h top height after $t = 180$ min. This suggests a rapid near-vertical transfer of heat energy, starting close to $t = 180$ min, between the CAP_h (the top of which is reasonably estimated by $z_{HL\downarrow}$ at $t = 180$ min), and the atmosphere above $z_{HL\downarrow}$. This process corresponds well with the analysis of bulk cooling trends (see Sect. IV.3.4).

Vertical motions are initially restricted by the narrow region of near-horizontal flows close to the plateau height, as well as the UML immediately below it. The latter region contributes to the development of an elevated inversion several hundred meters deep, extending below the UML, which restricts vertical motions further. Detrainment of air above $z_{HL\downarrow}$ is likely to converge close to the valley axis causing rising motions which will cool the atmosphere adiabatically. Air parcels will be forced laterally on reaching the elevated inversion, before being entrained into the downslope flows. This process is likely to be enhanced as the detrainment of fluid increases (see Fig. IV.5a).

Air flows below $z_{HL\downarrow}$ and above $z_{CI\downarrow}$ generally do not have such a strong vertical component reducing cooling by adiabatic expansion. This is therefore another likely process that blurs the difference between the cooling of the lower and upper valley atmosphere, making it difficult to define the top of the CAP_h between $t \approx 180$ and 300 min.

The elevated inversion also partially traps the layer of relatively high-q_v air beneath it ($z_{HL\uparrow}$ converges with $z_{CI\downarrow}$ towards the end of the simulation). The early development of the CAP_h concentrates the available water vapour into the top portion of the valley atmosphere. A greater amount of water vapour in the atmosphere increases the bulk radiative cooling [Hoch *et al.*, 2011a]. This is therefore another process that reduces the difference in cooling between the lower and upper valley atmosphere. A schematic is provided in Fig. IV.5b that summarizes the three identified processes that contribute to a more gradual variation of $\Delta\theta_v$ with height.

Several processes may contribute to the development of the elevated inversion. The vortices in the UML generally transport lower-θ_v air upwards and higher-θ_v air downwards, which tends to increase γ above and below the vortices. The circulation above $z_{HL\downarrow}$ generally transports relatively low-θ_v air into this region of the atmosphere from below. Radiative cooling decreases with z (not shown) as expected from Stefan's Law, mainly due to decreasing T with z, resulting in radiative divergence and increasing stratification.

A discontinuity in $z_{CI\downarrow}$ and $z_{CI\uparrow}$ occurs at $t \approx 250$ min. This is due to the destruction of the regions of relatively high γ lower in the valley atmosphere, and the establishment of the elevated inversion. Close to $t = 240$ min it becomes possible to identify a reasonably well defined decrease in $\langle \Delta\theta_v \rangle_y$ close to the top of the valley atmosphere, and by $t = 300$ min it is clear that the top of the CAP_h corresponds well with $z_{CI\downarrow}$. The CAP_h expands up to the bottom of the elevated inversion by the end of the simulation (i.e. 81 % of the valley depth).

After $t \approx 270$ min the change of $\max(\langle u_s \rangle_n)$ and $\max(u_{s,j})$ are less sensitive to the change in $z_{HL\downarrow}$ (see Fig. IV.4b) and closer to the change in $z_{CI\downarrow}$ (see Fig. IV.2a), a better estimate of the CAP_h top height during this period. The two maximum quantities generally lie somewhere between the two heights. Interestingly the height of $\max(\langle u_s \rangle_n)$ is generally less than $\max(u_{s,j})$ after $t = 180$ min, which corresponds to the time of interaction between the CAP_h and the most energetic region of the downslope flows. Both quantities lie above the height where $F_b \approx 0$. It seems that although there is flow penetration well below the height of $F_b \approx 0$ (see Fig. IV.3), the most energetic part of the flow is always above this level.

Figure IV.4b shows that $\max(n_{df})$ is generally less than $\max(\langle u_s \rangle_n)$ and $\max(u_{s,j})$, but has a similar trend. The algorithm used to compute $\max(n_{df})$ avoided finding points towards the bottom of the slope, not far above z_{GBI}. Large values of n_{df}

occur in this region where the downslope flows detrain above z_{GBI}. The algorithm considers the downslope flow before it is disrupted towards the base of the slope. A minimum point occurs in n_{df} towards the top of the slope (corresponding to a region of minimum entrainment or slight detrainment within the elevated inversion). This allowed $\max(n_{df})$ to be found by first moving along s whilst $n_{df}(s+1) < n_{df}(s)$ and then continuing along s whilst $n_{df}(s+1) > n_{df}(s)$. The algorithm shows an increase of n_{df} from the top of the slope. Figure IV.4b shows that $\max(n_j)$ is generally not sensitive to the CAP_h. $\max(n_j)$ was found by searching above z_{GBI} in order to avoid the bottom of the slope where n_j is not always well defined.

The decrease of $\langle u_s \rangle_n$ at points S_5 to S_8 compares well to the above analysis. At points S_8 and S_7 the decrease of $\langle u_s \rangle_n$ corresponds to either the rise of $z_{HL\downarrow}$ or $z_{CI\downarrow}$ (when the two heights are very similar). At point S_6 the more rapid decrease of $\langle u_s \rangle_n$ after $t = 190$ min corresponds to the rise of $z_{HL\downarrow}$. This occurs when the CI has already been eroded but largely before the rapid vertical transfers of heat energy, when $z_{HL\downarrow}$ still gives a reasonable estimate of the CAP_h top height. The accelerated decrease of $\langle u_s \rangle_n$ at point S_5 appears to precede the arrival of $z_{HL\downarrow}$ (by about one hour), presumably due to the rapid vertical transfer of heat energy. It was noted in Sect. IV.3.2 that the curve for $\langle u_s \rangle_n$ at S_5 does not follow the general trends before $t = 180$ min. This indicates that without the development of the CAP_h the region of the most energetic flows lies below the inflection point.

The main spatial and temporal variations of $\langle u_s \rangle_n$, illustrated in Fig. IV.2b, generally match those of the layer-averaged diabatic cooling $\langle L_c \rangle_{yn} = \partial \langle \theta_v \rangle_{yn} / \partial t + \langle u_s \rangle_n \, \partial \langle \theta_v \rangle_{yn} / \partial s$ (see Fig. IV.4d). As the CAP_h engulfs a slope point the fluid in the downslope flow is brought closer to a thermal equilibrium with its environment, that is, the driving buoyancy force of the downslope flows F_b is reduced or nearly vanishes, and in some cases $F_b < 0$ (see below).

IV.3.3.c Downslope flow momentum budget and internal variability

Figure IV.6 displays time series of the components F_i of the layer-averaged downslope flow momentum balance (for u_s), from the Eulerian perspective, using y-averaged fields, at slope points S_1 to S_8. The components F_i correspond to the momentum balance for an irrotational, Boussinesq fluid, that is Eq. IV.1,

$$\left\langle \frac{\partial u_s}{\partial t} = - \overbrace{u_s \frac{\partial u_s}{\partial s}}^{F_{adv-s}} - \overbrace{u_n \frac{\partial u_s}{\partial n}}^{F_{adv-n}} - \overbrace{\frac{1}{\rho_r} \frac{\partial p'}{\partial s}}^{F_p} + \overbrace{g \frac{\theta_v'}{\theta_{v_a}} \sin\alpha}^{F_b} - \overbrace{\frac{\partial \tau_{sj}}{\partial X_j}}^{F_f} \right\rangle_n , \qquad \text{(IV.1)}$$

[e.g. Holton, 2004], which includes along-slope and slope-normal advection F_{adv-s} and F_{adv-n}, respectively, the pressure force F_p, buoyancy force F_b, and subgrid-scale dif-

fusion, denoted by F_f.[6] Note that if the fields are not y-averaged it is possible to consider advection along y (F_{adv-v}), however, this term has no significant effect on the budget. p' is the perturbation pressure field, computed after applying $\langle\ \rangle_{xy}$ to the full pressure field p, where the averaging operator is that used in Sect. IV.3.1. τ_{sj} is the subgrid-scale stress tensor expressed using summation notation, where the index $j = \{s, n\}$, with $X_s \equiv s$, $X_n \equiv n$.

Figure IV.6 quantifies the influence of the CAP$_h$ on the downslope flows. F_b is shown to nearly vanish or to change to a negative force at slope points S_5 to S_8. The times of these events correspond almost exactly to the arrival of $z_{HL\downarrow}$ at each point (shown by a vertical dashed line). $z_{HL\downarrow}$ does not reach the slope points above S_5, and F_b remains significantly above zero at these positions. There is some reduction of F_b at all points; the degree of this reduction generally decreases with height, reflecting the decreasing influence of the CAP$_h$ with altitude. As expected there is a close correlation between F_b, $\langle L_c \rangle_{yn}$ and $\langle u_s \rangle_n$ (see also end of the previous section).

Figures IV.6b to IV.6f (slope points S_2 to S_8) show time periods where there is an approximate balance between F_b, $F_{adv} = F_{adv-s} + F_{adv-n}$ and F_f. The approximate start and end times of these periods are marked by single solid vertical lines and two solid vertical lines, respectively. Downslope flows resulting from a balance between F_b, F_{adv-s} and F_f were classified as 'shooting flows' by Mahrt [1982]. F_{adv-n} cannot be neglected for the system considered by this work; the fluid normal to the slope is not in hydrostatic balance, a condition that presumably would require a more gentle slope. The occurrence of two solid vertical lines marks the beginning of a period where there is an approximate balance between F_b and F_f, classified by Mahrt [1982] as 'near-equilibrium flows'. The approximate end of such a period is marked by a set of three vertical solid lines. Note that there is a short period of near-equilibrium flows at S_8 and a near-equilibrium flow regime is reached by the end of the simulation at S_4, however, in both cases the vertical lines were omitted for clarity.

There is therefore a transition from shooting flows to near-equilibrium flows at slope positions reached by $z_{HL\downarrow}$, with a more rapid evolution of the flow occurring with distance down the slope. After $z_{HL\downarrow}$ reaches a slope point F_{adv-s} generally changes to a positive force. This reflects the fact that the region of maximum downslope flows retreats back up the western slope ahead of $z_{HL\downarrow}$; the maximum region of the downslope flows becomes a source of momentum for points below it. F_{adv-n} follows F_{adv-s}; a convergence of fluid along the slope (i.e., $F_{adv-s} > 0$) must result in detrainment given that the fluid is approximately incompressible (see Sect. IV.3.3.a). The correspondence between flow convergence along s and detrainment is confirmed by a comparison of Fig. IV.2b and Fig. IV.5a. $\langle \partial u_s / \partial n \rangle_n < 0$ (not shown), due to the typical profile of the downslope flows, more specifically the close proximity of the cold-air jet to the ground

[6] see supporting information (§ IV.5)

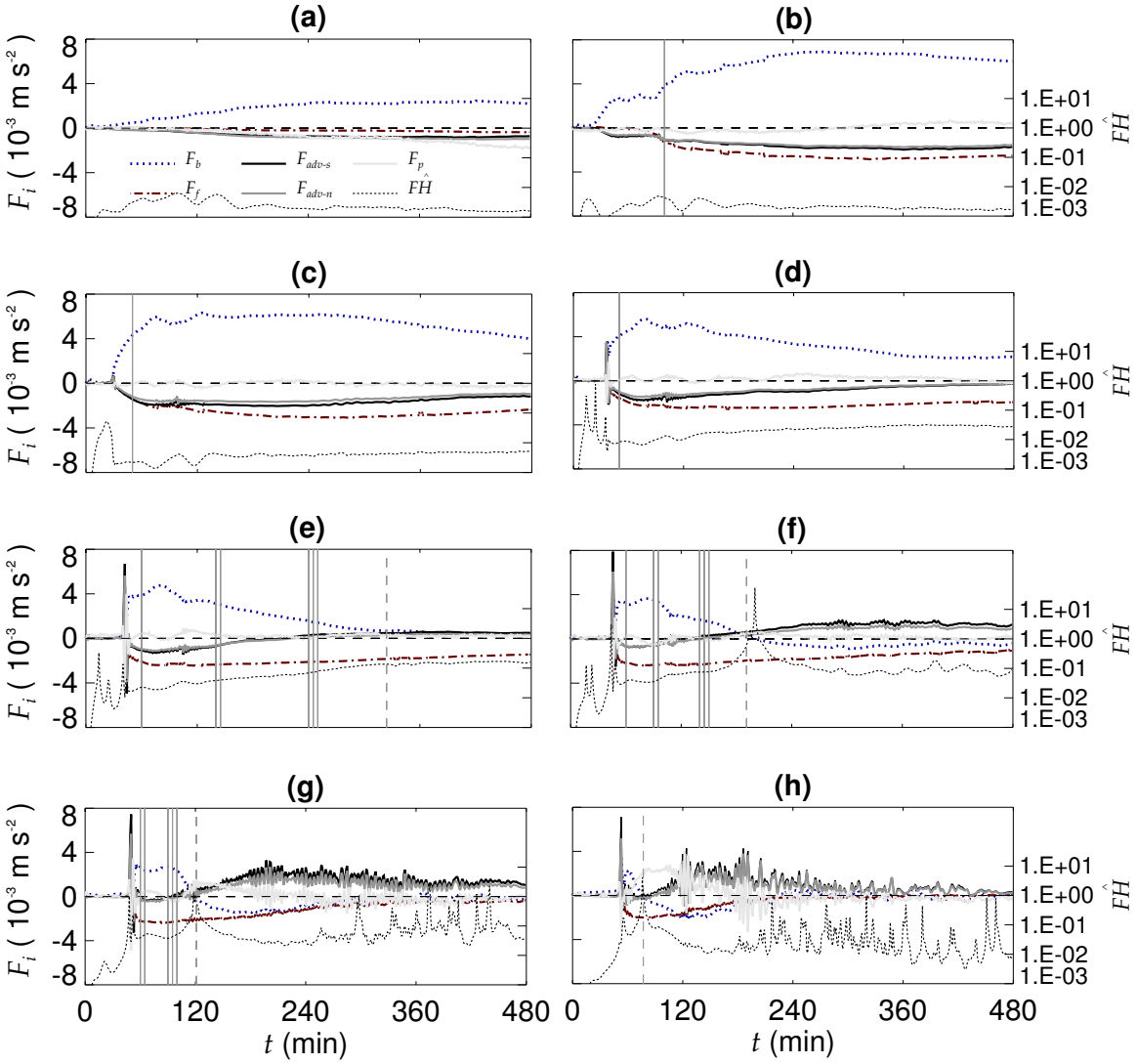

Figure IV.6: Time series **(a)** to **(h)** of the components F_i of the layer-averaged downslope flow momentum balance (for u_s), using y-averaged fields, from the Eulerian perspective, at slope points S_1 to S_8, respectively. The analysis points were defined in Fig. IV.1. F_i corresponds to the momentum budget for an irrotational, Boussinesq fluid, and includes the buoyancy force F_b, subgrid-scale diffusion F_f, along-slope and slope-normal advection F_{adv-s} and F_{adv-n}, respectively, and the pressure force F_p. A black dashed horizontal line marks the zero level. The grey dashed vertical lines mark the arrival times of $z_{HL\downarrow}$. Solid grey vertical lines partition the flow into different regimes; one line marks the start of the shooting flow regime, two lines mark the end of this regime and the start of the near-equilibrium flow regime, which ends with the occurrence of three lines. The modified Froude number $F\hat{H}$ is over-plotted for comparison [see Mahrt [1982] and the text for details].

surface. Therefore the two advection terms tend to follow one another. Detrainment below $z_{HL\downarrow}$ is presumably aided by $F_b < 0$ in this region.

The modified Froude number $F\hat{H}$ [Mahrt, 1982] has been over-plotted for comparison, where $F = U^2/(g'H)$ is the Froude number. U and H are the speed and depth scales of the downslope flow, set to $\langle u_s \rangle_n$ and n_{df}, respectively. $g' = g\,\delta\theta_v/\theta_{v_a}$ is the 're-

duced gravity', where $\delta\theta_v$ is the temperature deficit scale of the flow; g' was extracted from F_b. The non-dimensional height $\hat{H} = H/\Delta Z_s$, where ΔZ_s is the height change made by the slope ($\hat{H} \ll 1$ here). As expected $F\hat{H} < 1$ for both the shooting-flow and equilibrium-flow regimes. $F\hat{H}$ generally increases down the slope, with values of $F\hat{H} = \mathcal{O}(1)$ occurring at times when either $F_b \approx 0$ and $F_{adv} \neq 0$, or when $F_b \approx F_{adv}$ when the budget is not dominated by the two terms.

Small time variations can be seen on most of the curves of Fig. IV.2b. A fast Fourier transform has been used to investigate these variations further. It is not possible to apply the spectral analysis to $\langle u_s \rangle_n$ since the averaging along y distorts the true flow variations. Instead the spectral analysis was applied to $\langle \tilde{u_s} \rangle_n$, where $\tilde{u_s}$ was derived from u and w taken halfway along y. The general trends in $\langle \tilde{u_s} \rangle_n$ are the same as those in $\langle u_s \rangle_n$, however, there are significant differences in the amplitude of the variations (see Fig. IV.7a). Figure IV.7a shows $\langle \tilde{u_s} \rangle_n$ for slope points S_5 to S_7 and demonstrates that the expanding CAP_h induces relatively large variations in $\langle \tilde{u_s} \rangle_n$ as it reaches each point. The arrival time of $z_{HL\downarrow}$ is marked by concentric circles, which correspond to $t = 121$, 191 and 324 min, respectively ($z_{HL\downarrow}$ increases with time). Some negative values of $\langle \tilde{u_s} \rangle_n$ occur for point S_7 at times when the downslope flows are not well defined due to their interactions with the dense air towards the valley floor. Note that the variations in $\langle \tilde{u_s} \rangle_n$ are very similar to those in $\langle u_s \rangle_n$ above S_5. Below S_7 $\langle \tilde{u_s} \rangle_n$ and $\langle u_s \rangle_n$ become increasingly variable.

Close inspection of Fig. IV.7a reveals that the variations have a frequency in the range of approximately 0.002 to 0.005 rad s^{-1} (i.e., a period in the range of 20 to 50 min). Figure IV.7b to Fig. IV.7l show the spectra of $\langle \tilde{u_s} \rangle_n$ for analysis points S_1 to F_2. An analysis of these spectra reveals that the range of frequencies evident in Fig. IV.7a clearly dominates the spectrum at points S_4 to S_8, if the frequencies below 0.002 rad s^{-1} (due to longer-term trends) are disregarded. Above S_4 and below S_8 it is harder to see this effect. Peaks close to 0.002 rad s^{-1} above S_4 are due to variations that occur during the establishment of the flow, which takes longer in this region of the slope (see Fig. IV.2b). It is clear that it is not possible to find a single dominant frequency. It is possible that the type of oscillations predicted by McNider [1982b] contribute to the dominant range of frequencies identified above, however, it is difficult to confirm this. The assumptions made to arrive at the model derived by McNider [1982b] are generally not valid for the flow system considered by this work.[7] There are other candidates that may cause variations in the downslope flow. There is high shear where the flow springs back after over-shooting $F_b = 0$, which may cause Kelvin-Helmholtz (KH) instabilities. There is a region of unstable air below $z_{HL\downarrow}$ (see Sect. IV.3.3.a), which may also trigger KH instabilities. Interesting elongated features orientated downslope are evident in the flow below S_5 (see Fig. IV.8), which

[7] see supporting information (§ IV.5)

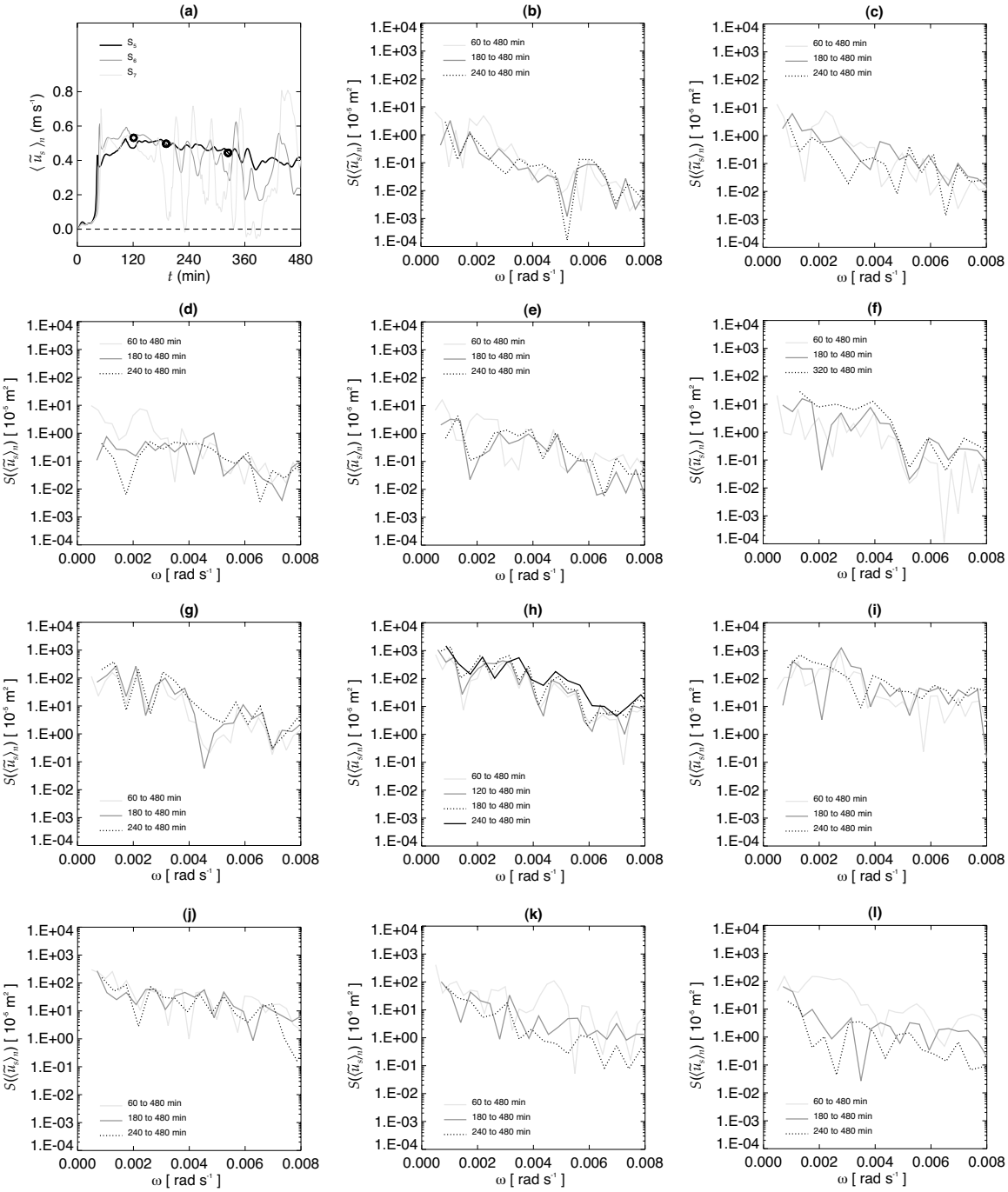

Figure IV.7: **(a)** Time series of the layer-averaged downslope flows $\langle \tilde{u_s} \rangle_n$ at slope points S_5 to S_7. $\tilde{u_s}$ was derived from u and w taken halfway along y. The arrival times of $z_{HL\downarrow}$ are marked by concentric circles ($z_{HL\downarrow}$ increases with time). **(b)** to **(l)** Spectra of $\langle \tilde{u_s} \rangle_n$ at analysis points S_1 to F_2, respectively. The spectra were determined for different time periods to analyze the time variation of the spectra, which was limited by the resolution of the WRF model output (1 min).

are approximately coincident with the region where there is a clear range of dominant frequencies, the region of high shear and where there exists a region of unstable air. Confirmation of the exact causes and nature of the variations found in $\langle \tilde{u_s} \rangle_n$ is beyond the scope of this work but would make an interesting topic of future research. The

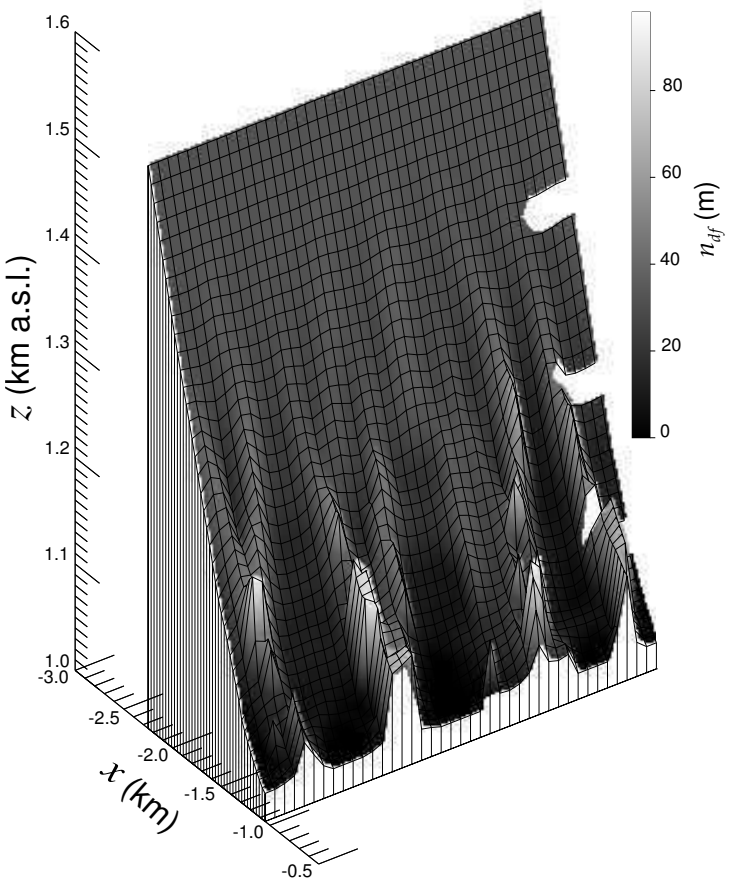

Figure IV.8: Height of the downslope flow top surface at $t = 240$ min, between slope points S_5 and S_9 (defined in Fig. IV.1), where intermediate point heights are indicated by the notches on the right of the figure. Grid intersections indicate the horizontal grid resolution $\Delta x = \Delta y = 30$ m. The surface uses the full y-dimension that was given a length of 1.2 km. Shading is scaled by the depth of the downslope flows (n_{df}) to help reveal the pattern.

variations in the flow may be formed from a combination of processes.

IV.3.4 Bulk cooling mechanisms and atmospheric characteristics

The various heights defined in Sect. IV.3.1 enable the subdivision of the valley atmosphere into a number of volumes, shown in Fig. IV.2a. This provides one means of investigating the varying cooling mechanisms in different regions of the valley atmosphere. The volumes were allowed to encompass the full y-dimension and limited along x between the top of each slope (i.e. $-3.75 \leq x \leq 3.75$ km).

Figure IV.9a shows $\langle R_r \rangle_V / \langle R \rangle_V$, where R_r is the time-rate of change of θ_v ($\partial\theta_v/\partial t \equiv R$), due to radiation. The operator $\langle\ \rangle_V$ refers to a volume average across any of the defined volumes. Volume averages were computed by first applying $\langle\ \rangle_y$, before pro-

jecting the variables onto a linear orthogonal mesh with a resolution of 5 m, that filled the valley space. $\langle R_r \rangle_{V_1} / \langle R \rangle_{V_1}$ confirms that radiative effects generally dominate the instantaneous cooling within the GBI. Between $t \approx 30$ and 100 min instantaneous cooling from the dynamics (i.e., the combined effects of advection and subgrid-scale mixing) is dominant. After this time radiative divergence generally dominates the instantaneous cooling as the region of maximum downslope flows is forced away from the GBI. Figure IV.9b shows $\langle \Delta\theta_{v_r} \rangle_V / \langle \Delta\theta_v \rangle_V$, where $\Delta\theta_{v_r}$ is the change in temperature from $t = 0$ due to radiative effects. $\langle \Delta\theta_{v_r} \rangle_{V_1} / \langle \Delta\theta_v \rangle_{V_1}$ remains close to 0.5 due to the dominance of instantaneous cooling by the dynamics when the temperature changes are close to their maximum (see Fig. IV.9c).

$\langle R_r \rangle_V / \langle R \rangle_V$ and $\langle \Delta\theta_{v_r} \rangle_V / \langle \Delta\theta_v \rangle_V$ for V_2 and V_3 confirm that the cooling is almost equally partitioned between radiative and dynamics effects within the CAP_h and the elevated inversion. Figure IV.9b shows that $\langle \Delta\theta_{v_r} \rangle_{V_2} / \langle \Delta\theta_v \rangle_{V_2}$ is always less than 0.5 after approximately $t = 85$ min. This explains the decrease of $\langle \Delta\theta_{v_r} / \Delta\theta_v \rangle_{va}$ over time found by Burns & Chemel [2014a], where $\langle\ \rangle_{va}$ is an average across the full valley atmosphere.

After $t = 300$ min, $z_{CI\downarrow}$ appears to be a more accurate measure of the CAP_h top height, however, the effect of using $z_{HL\downarrow}$ in place of $z_{CI\downarrow}$ does not change the results qualitatively. The small difference decreases over time as $z_{HL\downarrow}$ moves closer to $z_{CI\downarrow}$. $\langle \Delta\theta_{v_r} \rangle_V / \langle \Delta\theta_v \rangle_V$ can be expected to lag behind $\langle R_r \rangle_V / \langle R \rangle_V$, which is evident in the data. Large variations in $\langle R_r \rangle_V / \langle R \rangle_V$ occur at varying times before $t = 180$ min when these volumes are not well defined. It should be noted that some over-estimation of radiative cooling is likely to be present in the results, which rely on the use of a one-dimensional radiative transfer scheme [Hoch *et al.*, 2011a].

The partitioning of the accumulated temperature changes within the GBI and CAP_h, between radiative and dynamical effects, occurs largely within the first two hours of simulation. This corresponds to the time period of maximum instantaneous temperature changes (see Fig. IV.9c). This partitioning effect is also true for the full valley atmosphere [Burns & Chemel, 2014a].

The cooling within volumes V_4 to V_6 (see Fig. IV.9a and IV.9b), at the top of or above the valley atmosphere, is almost completely dominated by radiative effects. $\langle \Delta\theta_{v_r} \rangle_V / \langle \Delta\theta_v \rangle_V$ for V_4 and V_5 generally decrease over time, suggesting an interaction between the CAP_h and the valley atmosphere above, and an interaction between the latter and the free atmosphere above the valley. As the CAP_h expands higher the dynamics are able to increasingly cool air at greater elevations.

Figures IV.9c and IV.9d show the general reduction of cooling rates and accumulated temperature changes with height within and above the valley atmosphere. A minimum point in the time series of $|\langle R \rangle_{V_1}|$ (see Fig. IV.9c) occurs close to $t = 100$ min when it falls below that of $|\langle R \rangle_{V_2}|$, which follows an initial peak in $|\langle R \rangle_{V_1}|$ close to

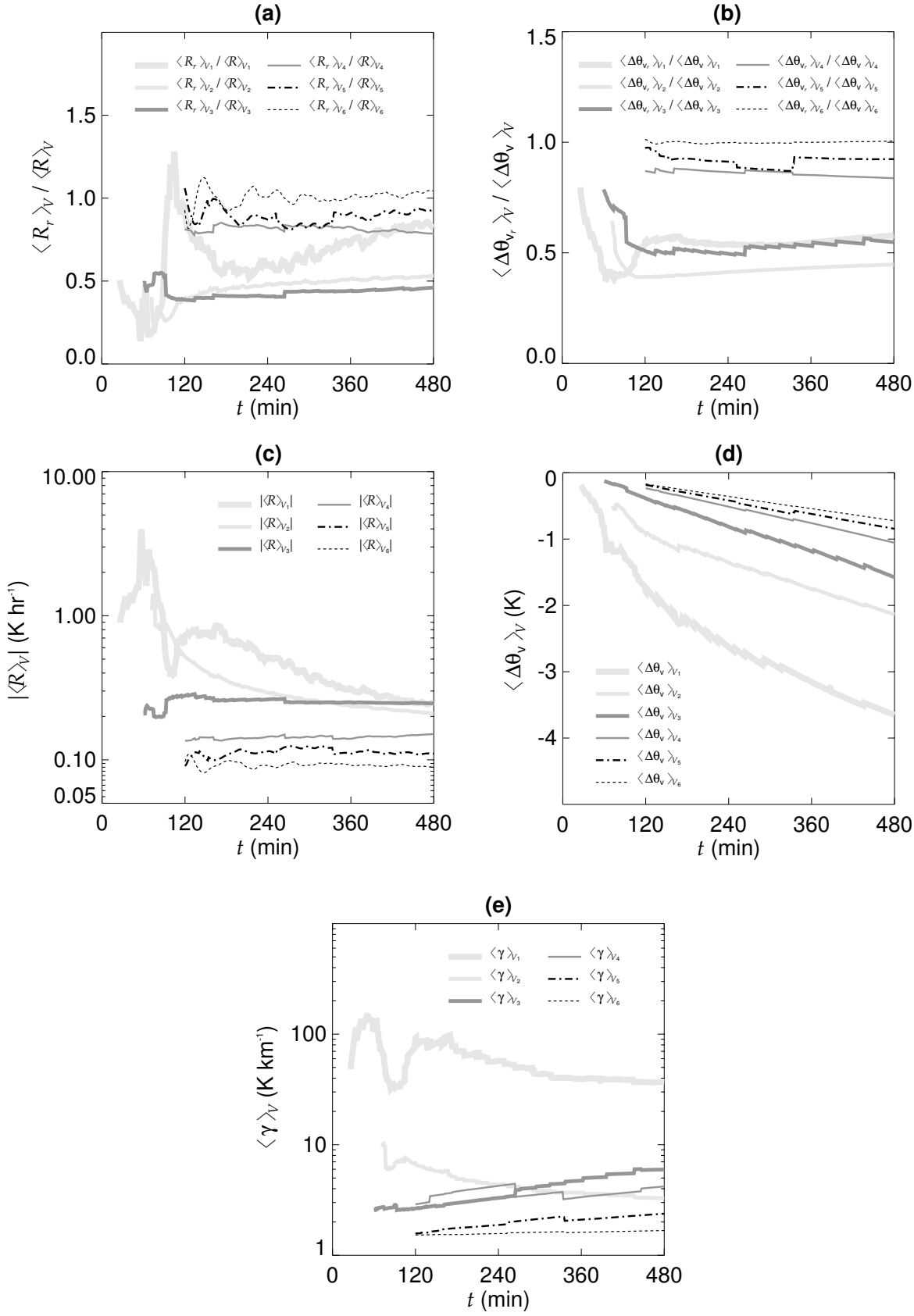

Figure IV.9: Time series of volume averages for V_1 to V_6 (defined in Fig. IV.2a) of **(a)** $\langle R_r \rangle_V / \langle R \rangle_V$, where R_r is the time-rate of change of virtual potential temperature ($\partial\theta_v/\partial t \equiv R$) due to radiation, **(b)** $\langle \Delta\theta_{v_r} \rangle_V / \langle \Delta\theta_v \rangle_V$, where $\Delta\theta_{v_r}$ is the accumulated change of virtual potential temperature ($\Delta\theta_v$) due to radiation, **(c)** the absolute magnitude of R, where $\langle R \rangle_v < 0$, **(d)** $\Delta\theta_v$, and **(e)** $\gamma \equiv \partial\theta_v/\partial z$.

$t = 60$ min. $|\langle R \rangle_{V_1}|$ first peaks close to the arrival time of the region of maximum downslope flows. $|\langle R \rangle_{V_1}|$ then decreases rapidly during the time period when the region of maximum downslope flows displaces the GBI vertically, reducing its intensity by advective and mixing processes (Sect. IV.3.3.a). This reduction in intensity follows the reduction in average atmospheric stability (see Fig. IV.9e). The advection and mixing of higher-θ_v air from above reduces $|\langle R \rangle_{V_1}|$. As the region of maximum downslope flows is forced back up the valley slopes (see Fig. IV.4b) $|\langle R \rangle_{V_1}|$ and $\langle \gamma \rangle_{V_1}$ increase once again. The absolute magnitude of $\langle R \rangle_V$ for V_1 to V_3 are shown to nearly converge by the end of the simulation (see Fig. IV.9c) indicating that these regions tend towards a state of thermal equilibrium with one another. The average accumulated temperature change within the GBI is close to double the change within the rest of the valley atmosphere, which cools by about twice as much as the free atmosphere above.

Careful inspection of Figure IV.9d reveals a slight reduction in the rate of increase of $|\langle \Delta\, \theta_v \rangle_{V_2}|$ after $t \approx 180$ min. Fig. IV.9c shows the average cooling rate in V_2 to approximate that of V_3 by $t \approx 240$ min and to fall below the cooling rate of V_3 by $t \approx 300$ min. These bulk features correspond very well to the details discussed in Sect. IV.3.3.b.

Figure IV.9e shows that the atmospheric stability of all the defined regions is greater than γ_0 at the end of the simulation. For example, on average, $\gamma \approx 25\,\gamma_0$, $2\,\gamma_0$ and $4\,\gamma_0$ within the GBI, CAP_h and elevated inversion, respectively, by the end of the simulation. The average atmospheric stability of the GBI is approximately an order of magnitude greater than the majority of the rest of the valley atmosphere, or the free atmosphere above, with the exception of the elevated inversion after $t \approx 300$ min. The average stability of both the GBI and CAP_h are shown to decrease after $t \approx 120$ min, which is in-line with the observations of Neff & King [1989].

$\langle \gamma \rangle_{V_3}$ is shown to increase more rapidly than $\langle \gamma \rangle_{V_4}$, whilst $\langle \gamma \rangle_{V_2}$ decreases, which quantifies the development of the elevated inversion and the UML. $\langle \gamma \rangle_{V_5}$ increases at a greater rate than $\langle \gamma \rangle_{V_6}$ quantifying the development of the USL. Close to $t = 240$ min, $\langle \gamma \rangle_{V_2}$ falls below $\langle \gamma \rangle_{V_3}$, which corresponds to the destruction of the lower layers of relatively high γ and the establishment of the elevated inversion, discussed in Sect. IV.3.3.b.

IV.4 Summary

A numerical model has been used to characterize the development of a region of enhanced cooling and some of its interactions with downslope flows, in an idealized alpine valley with a width of order 10 km, under decoupled, stable and poorly-drained conditions.

After the initial intensification of the downslope flows, a region of enhanced cooling was found to expand up through the valley atmosphere. Initially this expansion is fairly gradual and almost entirely due to the flux of mass into the region from the downslope flows. The region is relatively dry with a capping inversion at its top, defined by variable mixing. A layer of moist air is carried above the region and concentrated into the top half of the valley atmosphere.

The downslope flows first displace the ground-based inversion vertically and weaken it before the region of enhanced cooling forces the most energetic region of the downslope flows back up the valley slopes, which initially erodes away the top of the ground-based inversion. By the end of the simulated 8-h period the ground-based inversion expands to a depth of approximately 100 m, which compares very well to the observations of Chemel & Chollet [2006].

The growth of the region of enhanced cooling is accelerated when the expanding region encounters the most energetic part of the downslope flows some 2 h after sunset. This results in enhanced mixing close to the top of the region of enhanced cooling, the final destruction of the initial capping inversion, and a relatively rapid near-vertical transfer of heat energy. From 2 h after sunset the region of enhanced cooling does not essentially expand due to the flux of mass into the dry region of air.

A region of near-horizontal streamlines lies above a layer of vortices close to the top of the valley atmosphere. The latter directly contributes to the development of an elevated inversion. This elevated inversion is also likely formed by the transport of low-potential temperature air from below and by radiative divergence. These features at the top of the atmosphere partially trap air flows within the valley atmosphere. These valley-atmosphere flows are largely partitioned between two volumes, defined by the top of the region of relatively dry air. The expanding region of dry air concentrates the available water vapour into the upper part of the valley atmosphere, increasing the cooling there due to radiative processes. At the same time the re-circulation of air above the region of dry air is intensified causing enhanced adiabatic cooling. Therefore, there appear to be three key processes that blur the difference in cooling between the upper and lower parts of the valley atmosphere. These processes make it difficult to define the top of the region of enhanced cooling between 2 and 4 h after sunset.

The entrainment and detrainment patterns of the simulated downslope flows are comparable to those observed during the laboratory experiments of density currents in the ‘plume regime’ made by Baines [2008]. Generally entrainment of air into the slope flows occurs above the region of dry air and detrainment of air from the downslope flows occurs below the top of this region. The detrainment of air appears to be caused by several processes. The flows will tend to leave the slope close to their levels of neutral buoyancy. Detrainment is enhanced by shear-induced mixing in the region where the flows ‘spring-back’ after ‘over-shooting’ their level of neutral buoyancy. Return

flows occur where the flows spring-back and are largely restricted to the region of dry air. The downslope flows are deflected above the ground-based inversion, which is generally an order of magnitude more stable than the atmosphere above it (except for the elevated inversion after 4 h following sunset). An analysis of the detrainment of air from the downslope flows reveals a layering effect that will generate shears and mixing within the region of enhanced cooling. The return flows help to create a region of unstable air above the downslope flows by transporting low potential temperature air from below. At the same time the downslope flows advect high potential temperature air downslope causing warmer temperatures in the top part of the downslope flows less affected by the cooling ground surface.

As the CAP_h engulfs the slopes, the downslope flows mix with it, reducing their negative buoyancy, causing them to slow down. With a lower temperature deficit the ability of the downslope flows to lose thermal energy to the sloping surface is reduced. A significant increase and decrease of the downslope flow speeds occurs over time for slope points engulfed by the region of dry air. From 2 h after sunset the downslope flow speeds generally increase from the top of the slopes towards the slope inflection points, and decrease after this point towards the valley floor. The flow field before 2 h after sunset reveals that, without the influence of the region of enhanced cooling, the maximum region of the downslope flows is below the slope inflection points. There is a transition from shooting flows to near-equilibrium flows at slope points reached by the region of dry air, with a more rapid evolution of the flow occurring with distance down the slope. The expansion of the region of enhanced cooling increases the height of the maximum downslope flow depth.

The expanding region of enhanced cooling has been found to initiate relatively large variations of the downslope flows with periods ranging between approximately 20 and 50 min. Disregarding variations due to longer-term flow changes, this range of periods has been found to dominate the spectra of the downslope flows engulfed by the region of dry air, away from the bottom of the slope. The exact nature and causes of these flow variations remains unclear. These flow variations are approximately coincident with a region of high shear, a region of unstable air, and a region of elongated flow features orientated downslope.

After the initial intensification of the downslope flows, the instantaneous cooling in the ground-based inversion is generally dominated by radiative effects. This occurs as the maximum region of the downslope flows is forced further away from the ground-based inversion. The normalized temperature changes within the ground-based inversion remain close to 0.5 due to the initial dominance of cooling from the dynamics when temperature changes are close to their maximum. The cooling within the region of enhanced cooling and within the elevated inversion is almost equally partitioned between radiative and dynamics effects. The partitioning of the cooling between the

two processes occurs largely within an hour following sunset.

The cooling at the top of or above the valley atmosphere is almost completely dominated by radiative effects, but with generally an increasing contribution to the cooling by the dynamics. This suggests some interaction between the valley atmosphere and the free atmosphere above, as the region of enhanced cooling evolves.

The average temperature changes within the ground-based inversion are approximately double those of the rest of the valley atmosphere, which cools by about twice as much as the free atmosphere above. The three lowest volumes tend towards a state of thermal equilibrium with one another by the end of the simulation, however, at this time they are not in a state of thermal equilibrium with their external environment.

The average atmospheric stability of all defined volumes is greater than the initial atmospheric stability at the start of the simulation. The final stability within the ground-based inversion, the region of enhanced cooling and the elevated inversion is close to 25, 2 and 4 times the initial atmospheric stability, respectively. The stability of the ground-based inversion and the region of enhanced cooling decreases after approximately an hour following sunset. This bulk decrease in atmospheric stability has not been widely reported in the scientific literature, however, the observations of Neff & King [1989] show a similar effect.

It should be stated that these results are for a particular valley geometry, and set of initial and boundary conditions. A future sensitivity study should test the generality of these results.

IV.5 Supporting information

1 Under the right atmospheric conditions this layer of relatively moist air can be expected to condense into cloud. This has important implications for road and aviation safety. Under the right conditions a relatively thin region of reduced visibility should be expected to expand through a depression atmosphere through the night. The expanding region of enhanced cooling may also cause a spatial and temporal evolution of ground frost, snow and ice cover.

→ This item corresponds to a point in § IV.3.1

2 Note that z_{GBI} reaches a maximum height close to 100 m by the end of the simulation, which compares very well to the observations of Chemel & Chollet [2006].

Chazette *et al.* [2005] recorded 450-m deep GBIs in the Chamonix valley lasting all day during winter with snow cover under calm synoptic conditions. A few field campaigns conducted in terrain with similar scales to those considered herein have recorded GBIs with depths of $\mathcal{O}(1)$ km [e.g. Gohm *et al.*, 2009; Daly *et al.*, 2009]. The exact cause of these deep GBIs is not fully clear. One candidate

is the rapid stabilisation of the boundary layer over snow-covered terrain under quiescent synoptic conditions. If these conditions persist then the stability of the boundary layer may build enough to generate such deep temperature inversions. The advection of relatively high-θ air in the top portion of terrain depressions may also help to create deep temperature inversions. It is worth highlighting that the initial atmospheric stability of the idealised simulation conducted for this study was relatively weak; deeper temperature inversions may have been generated if this were not the case. It would be useful to investigate these effects in future work.

→ This item corresponds to a point in § IV.3.1

3 The analysis of the absolute magnitude of the wind field $|\langle \mathbf{u}_{xz} \rangle_y|$ is provided in Appendix D.

→ This item corresponds to a point in § IV.3.3.a

4,5 The analysis of resolved turbulent mixing (i.e., the Reynolds 'stress' for the conservation of heat energy, $-\langle \mathbf{u}' \cdot \nabla \theta_v' \rangle_y$) is provided in Appendix D.

→ This item corresponds to a point in § IV.3.3.a

6 A consideration of the downslope flow momentum budget has enabled a comparison of the downslope flow profiles generated by the numerical model with the analytical solution derived by Prandtl [1942]. This comparison is provided in Appendix E.

→ This item corresponds to a point in § IV.3.3.c

7 The parameters used to create Fig. I.6 in § I.3.1, Chapter I are appropriate for the downslope flows simulated at S_5. The range of oscillation periods shown in Fig. I.6 is similar to the range of dominant frequencies evident in Fig. IV.7 for slope points S_4 to S_8. Although the solution derived by McNider [1982a] contains some of the essential physics of the problem, it is strictly not valid for the flow system considered by this study.

→ This item corresponds to a point in § IV.3.3.c

IV.6 Chapter link

This chapter has elucidated the early evolution of the region of enhanced cooling for the alpine case considered together with some of its interactions with slope flows. An important question for society and the environment is how do these processes affect the evolution of pollutants within the valley? This is the subject of the next chapter, which targets the third objective of this work (see § I.6), and is a reproduction of Chemel & Burns [2014].

V

Pollutant Dispersion in a Developing Valley Cold-Air Pool

This chapter is a reproduction of Chemel & Burns [2014] and maps onto the third objective of this work (see § I.6).

Charles Chemel · Paul Burns

Received: 13 November 2013 / Accepted: 13 November 2014

Abstract Pollutants are trapped and accumulate within cold-air pools, thereby affecting air quality. A numerical model is used to quantify the role of cold-air-pooling processes in the dispersion of air pollution in a developing region of enhanced cooling (denoted CAP for simplicity) within an alpine valley under decoupled stable conditions. Results indicate that the negatively buoyant downslope flows transport and mix pollutants into the valley to depths that depend on the temperature deficit of the flow and the ambient temperature structure inside the valley. Along the slopes, pollutants are generally entrained above the CAP and detrained within the CAP, largely above the ground-based inversion layer. The ability of the CAP to dilute pollutants is quantified. The analysis shows that the downslope flows fill the valley with air from above, which is then largely trapped within the CAP, and that dilution depends on where the pollutants are emitted with respect to the positions of the top of the ground-based inversion layer and the CAP, and on the slope wind speeds. Over the lower part of the slopes, the CAP-averaged concentrations are proportional to the slope wind speeds where the pollutants are emitted, and diminish as the CAP deepens. Pollutants emitted within the ground-based inversion layer are largely trapped there. Pollutants emitted farther up the slopes detrain within the CAP above the ground-based inversion layer, although some fraction, increasing with distance from the top of the slopes, penetrates into the ground-based inversion layer.

Keywords Cold-air pools · Downslope flows · Numerical simulation · Pollutant dispersion

C. Chemel
National Centre for Atmospheric Science (NCAS), Centre for Atmospheric & Instrumentation Research (CAIR), University of Hertfordshire, College Lane, Hatfield, AL10 9AB, UK

P. Burns
Centre for Atmospheric & Instrumentation Research (CAIR),
University of Hertfordshire, College Lane, Hatfield, AL10 9AB, UK
email: p.burns@herts.ac.uk

V.1 Introduction

Cold-air pools (CAPs) in regions of hilly and mountainous terrain refer to layers of cold air confined towards the bottom of landscape depressions [see, for instance, Whiteman, 2000]. CAPs frequently occur during nocturnal hours and the winter season in basins and poorly-drained valleys decoupled from the atmosphere above, which is the case considered herein. Previous work has considered the case of coupled conditions where larger-scale non-local flows (e.g. synoptic weather systems) perturb the complex terrain atmosphere [e.g. Vosper & Brown, 2008; Whiteman *et al.*, 2010; Dorninger *et al.*, 2011; Haiden *et al.*, 2011; Lareau & Horel, 2014]. The mechanisms by which the atmosphere cools in complex terrain under decoupled stable conditions have been discussed in several observational and modelling studies [see Zardi & Whiteman, 2013, for a review, and references therein]. However, much remains to be understood about the relative roles of turbulent and radiative flux divergences and advection. Vosper *et al.* [2014] discussed results from a numerical model simulation of the formation of a CAP in early March 2010 in the Clun Valley, United Kingdom, a narrow valley with depth between 75 and 150 m, using horizontal grid spacings of 100 m and a vertical grid resolution of 2 m close to the ground surface. Results of the simulation indicated that parametrized subgrid-scale turbulent mixing dominates the cooling of the air adjacent to the ground while the cooling above is dominated by the advection of cold air away from the surface into the interior valley atmosphere.

Burns & Chemel [2014a,b] analyzed results from a numerical simulation of a developing region of enhanced cooling (referred to as CAP thereafter, for simplicity) in an idealized 1-km deep narrow U-shaped valley at the latitude of the Chamonix valley, France. This terrain is in contrast with the small-scale terrain considered in the works cited above, as well as the case of much larger basin landforms that have also been investigated [e.g. Cuxart & Jiménez, 2007; Martínez & Cuxart, 2009; Martínez *et al.*, 2010]. Burns & Chemel [2014a,b] used horizontal grid spacings of 30 m and a vertical grid resolution of about 1.5 m adjacent to the ground. The simulation started about 1 h before sunset on a winter day. After 1 h of relatively rapid valley-atmosphere cooling, driven mainly by radiative cooling, the cooling rate of the valley atmosphere decreased during the simulated 8-h period as a result of a complex balance/interplay between radiation and dynamical effects [Burns & Chemel, 2014a]. Within 1 h following sunset, the valley-atmosphere instantaneous cooling was almost equally partitioned between dynamics (i.e., advection and subgrid-scale turbulent mixing) and radiative cooling. Burns & Chemel [2014b] investigated the interactions between the downslope flows and the developing CAP. As the CAP deepened, a 100-m deep strongly stratified ground-based inversion layer was left above the valley floor. As the developing CAP engulfed the slopes, the downslope flows within the CAP could not maintain their

negative buoyancy by losing heat to the underlying surface, and detrained into the developing CAP, largely above the ground-based inversion layer, thereby mixing the CAP atmosphere.

Much research has been devoted to improving understanding of the dispersion of air pollution in complex terrain and much progress has been made. A number of previous studies have focused on daytime conditions or have considered daily-averaged quantities. Chazette *et al.* [2005] documented the vertical distribution of ozone, nitrogen oxides and aerosols in the Chamonix valley, France, during daylight hours on winter days when a strongly stratified ground-based inversion layer had developed during the night or persisted throughout the day. Pollutants were found to be largely trapped near their sources in the lower most stable part of the inversion layer (i.e., below 150 m above the ground), thereby affecting air quality, and to be essentially isolated from the air above. Such trapping of pollutants close to the ground surface was observed, during morning hours of winter days, in the Inn valley, Austria [Harnisch *et al.*, 2009; Schnitzhofer *et al.*, 2009], and in the Adige valley, Italy [de Franceschi & Zardi, 2009]. Lehner & Gohm [2010] used an idealized numerical simulation to investigate the daytime tracer transport in the Inn valley. Prolonged multi-day episodes of high daily-averaged aerosol concentrations have been observed close to the ground during winter in the Cache valley, Utah, USA [Malek *et al.*, 2006]. The pollution events were well correlated with the presence of ground-based stable layers. Silcox *et al.* [2012] reported observations of elevated daily-averaged aerosol concentrations during days with persistent, multi-day CAPs in the Salt Lake valley, Utah, USA. Aerosol concentrations were found to be linearly correlated with the valley heat deficit, a measure of the overall atmospheric stability within the valley. Under most conditions, atmospheric stability increased with time during CAP events, causing air pollution to intensify from sources within the ground-based inversion layer. Hence, the highest concentrations were usually found in the longest lasting CAPs. Concentrations were generally observed to decrease with increasing elevation, with decreases in ground-level concentrations of up to 30 % for differences in elevation of about 300 m.

Previous investigations of nocturnal air pollution in complex terrain have frequently used near-ground point samples and (quasi-) vertical profiles, often focusing on the ground-based inversion layer. Raga *et al.* [1999] described the occurrence of high near-ground ozone concentrations at night in the Mexico City basin, Mexico, due to the return of ozone-rich air, carried by downslope flows, following the advection of pollution above the basin by daytime upslope winds. A similar effect was observed by King *et al.* [1987] who released tracers over the slopes of the Los Angeles basin, California, USA. Lee *et al.* [2003] reported similar events in the Phoenix valley, Arizona, USA, when the lower layers of the valley atmosphere were weakly stratified. However, when a strongly stratified ground-based inversion layer developed, downslope flows detrained

near the top of the growing inversion layer.

The full spatial and temporal variations of pollutants during CAP events remain to be examined, presumably owing to the challenges in modelling CAPs [Baker *et al.*, 2011] and making extensive observations of CAPs. The present study builds on previous research by explicitly studying the dispersion of air pollution within an alpine valley during nocturnal hours, under decoupled poorly-drained conditions. The work quantifies how the complex interactions between the downslope flows and the developing region of enhanced cooling, studied by Burns & Chemel [2014a,b], affect the dispersion of pollutants emitted at different locations over the slopes of the valley. The region of enhanced cooling includes both the ground-based inversion and the region of enhanced cooling that expands above this layer. The design of the numerical experiment is presented in Sect. V.2, numerical results are analyzed in Sect. V.3, and a summary follows in Sect. V.4.

V.2 Design of the numerical experiment

The numerical simulation presented herein was performed with the Weather Research and Forecasting (WRF) model [Skamarock *et al.*, 2008], version 3.4.1, run in a large-eddy simulation (LES) mode (i.e., with no boundary-layer parametrization scheme). The WRF model was set-up exactly as in Burns & Chemel [2014a] with the inclusion of additional prognostic passive tracers (referred to as pollutants), governed by the tracer-conservation equation

$$\frac{\partial C_i}{\partial t} + \mathbf{u} \cdot \nabla C_i = \frac{1}{\rho} \nabla \cdot (\rho \, \kappa \, \nabla C_i) + Q_i, \tag{V.1}$$

where C_i is the concentration (volume mixing ratio) of pollutant P_i, $\mathbf{u}$ is the velocity field, ρ is the air density, κ is the eddy diffusivity for heat and mass, and Q_i is the source emission rate of pollutant P_i. A turbulent kinetic energy 1.5-order closure scheme [Deardorff, 1980] was used to model the subgrid scales. The constant C_k in the subgrid-scale parametrization scheme was set to 0.10 [see Moeng *et al.*, 2007]. Also, because of the anisotropy of the grid, the width of the spatial filter was modified in the present simulation following Scotti *et al.* [1993]. A brief summary of the model set-up is given below. Dynamics and physics options are not detailed hereafter and the reader is referred to Burns & Chemel [2014a].

The model domain encompasses an idealized deep narrow U-shaped valley, with its axis orientated south-north in the y-direction (see Fig. V.1). All points in the domain are located at 45.92 °N and 6.87 °E, corresponding to the location of the Chamonix valley, France, and the size of the valley approximates that of the lower Chamonix valley. It is 1 km deep and flanked on either side by a horizontal plateau extending

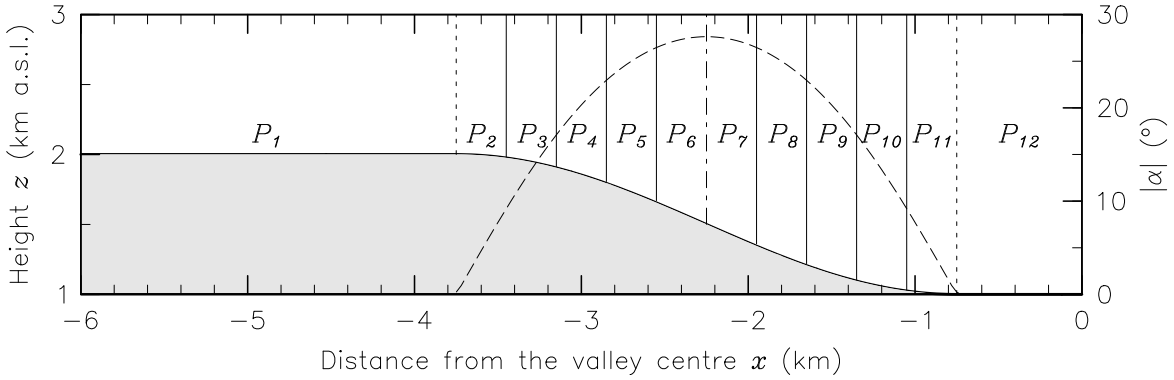

Figure V.1: Terrain height (curved solid line) along the x-direction orientated west-east. The terrain is symmetric about $x = 0$ and uniform in the along-valley direction y (into the page), orientated south-north, though the domain extends 1.2 km in the y-direction. The dashed line indicates the absolute value of the slope angle $|\alpha|$. The vertical dotted lines mark the top and bottom of the slopes and the vertical dashed-dotted line marks the slope inflection point, which is located half-way along the slopes. The regions where the pollutants P_i, $i \in [1..12]$, are emitted within the model layer adjacent to the ground are also indicated (see text for details).

2.25 km from the top of the valley slopes. The width of the valley floor is 1.5 km, the slopes are about 3.2 km long and the maximum slope angle is 27.6°. The terrain is uniform in the along-valley direction y, though the domain extends 1.2 km in this direction. The model top is located at 12 km above sea level (a.s.l.).

The two-dimensional terrain and the absence of any large-scale pressure differences along y mean that the simulation avoids the additional complexity of along-valley winds. The simulation considers the case of poorly-drained valleys. McKee & O'Neal [1988] presented observations of both very weak and strong along-valley winds in different valleys. Analytical theory was used to demonstrate that the different wind speeds can be explained by different down-valley changes in the width to (cross-sectional) area ratio W_v/A_v of the valleys, neglecting any variation in the surface energy budgets. Valleys with W_v/A_v increasing down the valley lead to increasing cooling rates in the down-valley direction, leading to the formation of cooler air further down the valley, which effectively blocks the down-valley flow. McKee & O'Neal [1988] demonstrated that the magnitude of the forcing mechanism outlined above (termed the intra-valley force) can exceed the magnitude of forces due to mountain-plain temperature differences or the magnitude of forces due to temperature differences caused by sloping valley floors.

The domain is discretized using a terrain-following grid of type Arakawa-C with 101 staggered grid points along the z-direction, pointing upwards, with a vertical grid resolution Δz of about 1.5 m adjacent to the ground surface, stretching continuously to the model top using a hyperbolic tangent function. Δz was selected, on the basis of a sensitivity study, to capture the downslope flows. The horizontal grid resolution

Δx is 30 m, resulting in 402 and 42 staggered grid points in the x- and y-directions, respectively. Δx was selected as a compromise between minimizing errors in the approximations of horizontal gradients due to grid distortion [Mahrer, 1984] and keeping the runtime practical. The even number of horizontal grid points makes the model grid symmetric about its mass points.

The numerical model simulated an 8-h period, starting about 1 h before sunset at time $t = 0$ on a winter day (21 December). To obtain numerically stable results, the vertical grid resolution and maximum flow speed demanded a model timestep $\Delta t = 0.05$ s. The acoustic timestep was set to $\Delta t/10$. Given the steep slopes of the valley considered herein, the model parameter β, used to damp vertically propagating sound waves, was set to 0.9 [see Dudhia, 1995].

Since we consider decoupled stable conditions, no synoptic forcing was prescribed at the initial time, that is, the velocity field was set to zero across the domain. The initial model atmosphere was weakly stratified, with a lapse rate in virtual potential temperature, $\partial\theta_v/\partial z = 1.5$ K km^{-1}, corresponding to an environmental lapse rate slightly less than the adiabatic rate. This initial state is typical of conditions where there is no pre-existing residual layer, or inversions, in the valley atmosphere at the start of the night, indicative of well-mixed post-convective conditions. Whiteman *et al.* [1997] and Whiteman & Zhong [2008] provide examples of such near-adiabatic lapse rates in complex terrain close to sunset. The near-surface air at the valley floor was assigned an initial $\theta_v = 288$ K, a temperature of approximately 279.3 K (about 6 °C), typical 1 h before sunset at this time of year in the Chamonix valley. This temperature value was taken from the Pollution in Alpine Valleys (POVA) dataset [see Brulfert *et al.*, 2005; Burns & Chemel, 2014a].

The atmosphere was initialized with a constant relative humidity of 40 %, corresponding to a relatively dry atmosphere, which avoided the complexity of cloud formation, while allowing for the expected overall slight reduction in water vapour with height due to entrainment of drier air from above during daytime and evapotranspiration from the surface. It is acknowledged that large variations in water content can occur in the atmosphere and that this moisture profile is a particular and idealized case. Hoch *et al.* [2011a] used a three-dimensional radiative transfer model to demonstrate that large changes in the water content of valley atmospheres (similar in scale and temperature structure to that considered herein) affect the magnitude of the valley-atmosphere instantaneous radiative cooling rates. Increasing the water vapour mass mixing ratio from 3.25 to 4.875 g kg^{-1} (that is a 50 % increase) increased the cooling rates by approximately 17 %. The effects of different initial moisture profiles should be quantified in future work, and the possibility of cloud and fog formation also needs to be considered in future work. At the same time, cloud formation generally reduces heat loss from the complex terrain atmosphere at night [Cuxart & Jiménez,

2012], which has implications, for instance, for agriculture.

Periodic lateral boundary conditions were used. This was made possible by the relatively large extent of the flat plateaux in the x-direction, the symmetry of the domain about the centre of the valley, the y-independent valley geometry and largely y-independent forcing at the ground surface. A 4-km deep implicit Rayleigh damping layer [Klemp *et al.*, 2008] was implemented at the top of the model domain to prevent any significant wave reflections affecting the solution. The damping coefficient was set to 0.2 s^{-1}. Forcing at the ground surface was provided by the revised MM5 Monin-Obukhov surface-layer scheme by Jiménez *et al.* [2012] coupled to the community Noah land-surface model [Chen & Dudhia, 2001]. The idealized terrain was set-up to represent an Alpine landscape consisting mainly of short grasses and the soil type was set to 'silty clay loam'. Setting the land-use type to short grass avoided placing the lowest layer of the model grid within the vegetation, which would have rendered the surface-layer parametrization inappropriate. Although many valleys are wooded, an accurate consideration of forested slopes would require the implementation of a new parametrization scheme in the WRF model, which is beyond the scope of the present work. The initial soil moisture was set constant at a value 10 % below the soil's field capacity [0.387 (volume fraction)], simulating soil conditions a few days after rainfall. This is reasonable given the winter period modelled, when frequent precipitation is typical in the Alps. For a detailed account of the initialization of the soil temperature and moisture, see Burns & Chemel [2014a]. The skin temperature was initialized by second-order extrapolation of the air temperature at the first three layers above the ground.

The initial atmospheric and surface conditions avoided the complexity of dewfall or frostfall during the simulated period. Whiteman *et al.* [2007] demonstrated that these processes can significantly reduce the atmosphere cooling rates within small-scale landscape depressions. Whiteman *et al.* [2007] made tethered balloon soundings in the Gruenloch basin, Austria, a depression with a width and depth of approximately 1 km and 150 m, respectively. The basin atmosphere water vapour mixing ratio fell by 2–3 g kg^{-1} overnight, resulting in a latent heat release that was 33–53 % of the overall basin sensible heat loss. Theory was used to indicate that the effects of dewfall and frostfall are less during winter, when ambient air temperatures are lower. It is unclear whether dewfall and frostfall have such a large impact in larger-scale topography, such as that considered herein. A random negative thermal perturbation, with a minimum value of −0.05 K, was applied to the skin temperature at the initial time across the valley slopes to make the flow three-dimensional and reduce the spin-up time of the simulation.

Pollutants were emitted within the model layer adjacent to the ground surface on the plateaux (pollutant P_1), equally-spaced strips along the slopes (pollutant P_i,

$i \in [2..11]$) and the valley floor (pollutant P_{12}). The regions where the pollutants are emitted are indicated in Fig. V.1, noting that the surface areas S_i of these regions are different. Each pollutant P_i was emitted from the start of the simulation at a constant rate R_i ($= \rho\, Q_i\, \Delta z / M$, where M is the molar mass of air) such that $R_i\, S_i = 1.845 \times 10^{-5}$ mol s^{-1}. In this way, the same mass of pollutant was emitted for each pollutant. The initial volume mixing ratio for all the pollutants was set to 1 pptv to provide a constant background against which concentrations can be compared. The along-valley-averaged volume mixing ratio of pollutant P_i is denoted by C_i hereafter for simplicity and its deviation from the constant background is denoted by C_i'.

We consider the dispersion characteristics of passive tracers, which over the length and time scale considered, can reasonably be expected to represent the trends of pollutant concentrations for species such as carbon monoxide.

V.3 Results and discussion

V.3.1 Dispersion characteristics of the downslope flows

Figure V.2 presents an overview of the along-valley-averaged downslope flow, its forcing mechanisms and dispersion characteristics along the western slope at time $t = 480$ min. Downslope flows develop as the result of ground-surface cooling along the slopes, which makes the air adjacent to the slopes negatively buoyant. The cooling of the slope surfaces is due to a net negative surface energy budget. The bottom two plots in Fig. V.2 show the surface energy budget and the cooling rate at the ground surface. At that time, there is no shortwave radiation and the net longwave radiation budget is negative, leading to a cooling by radiative heat loss. The radiative deficit is most effectively replenished by conduction from the soil, warming the surface. The sensible heat flux is directed downwards, cooling the air adjacent to the surface, while the latent heat flux is directed upwards as a result of the availability of soil moisture for evaporation, cooling the surface. The residual $\Delta\, Q_S$ of the energy budget, which represents changes of energy storage, is negative. This loss of energy results in a cooling at the surface (that is $\partial T_0 / \partial t < 0$, where T_0 is the skin temperature). Even though $\partial T_0 / \partial t$ is proportional to $\Delta\, Q_S$ at every time and point in the model domain, this is not necessarily the case when averaged along the valley axis.

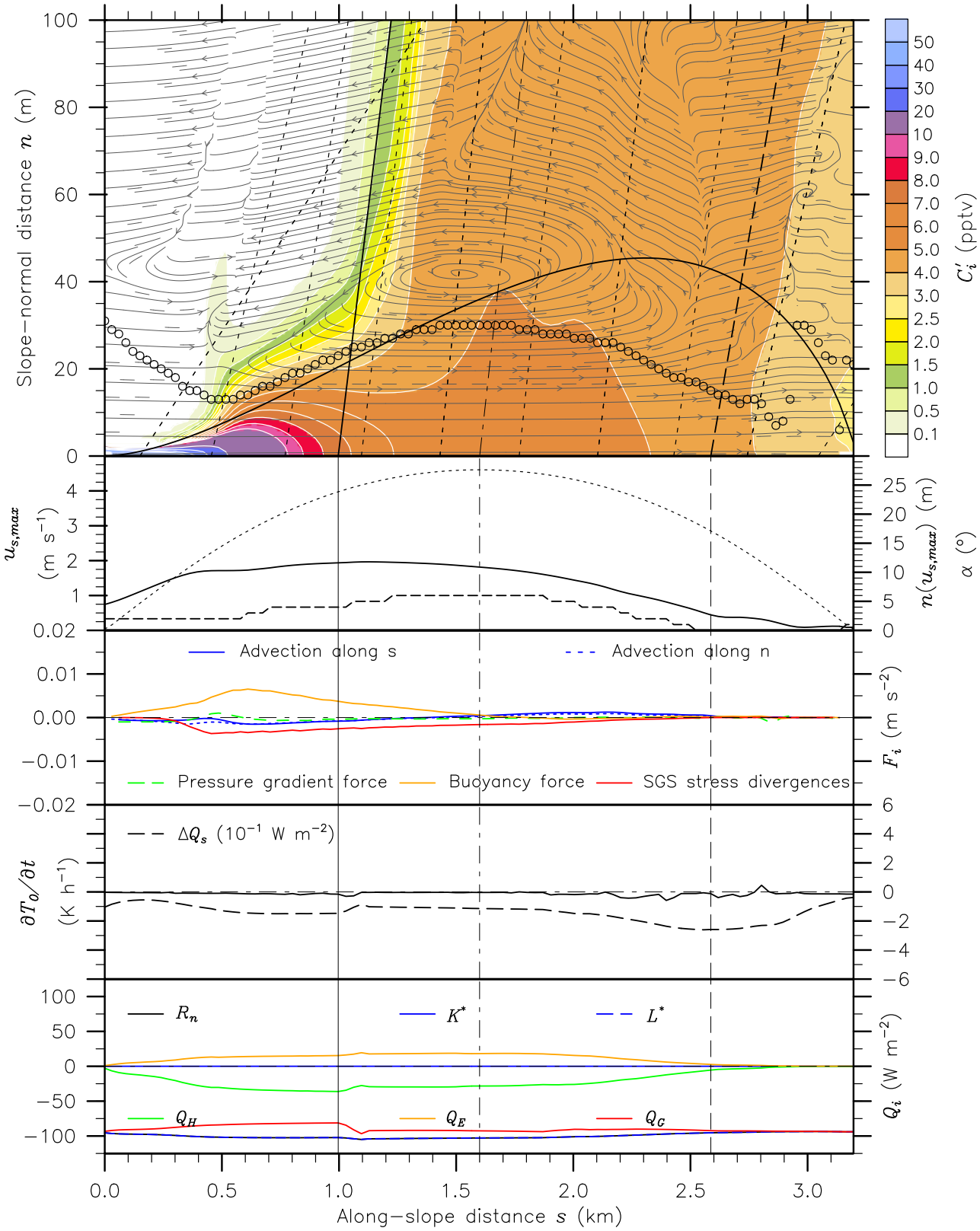

Figure V.2: Overview of the along-valley-averaged downslope flow, its forcing mechanisms and dispersion characteristics along the western slope at time $t = 480$ min. See overleaf for plot details.

Figure V.2: The top plot displays contours of the concentration C_1' of pollutant P_1, with streamlines superimposed. The circles indicate the depth of the downslope flow, calculated as the distance n along the normal at which the along-slope velocity component u_s decreases to 20 % of its maximum value, denoted by $u_{s,max}$. The dotted lines show horizontal lines. The dashed and straight solid lines mark the position of the top of the ground-based inversion layer and region of enhanced cooling, respectively. The dashed-dotted line indicates the location half-way along the slope. The curved solid line represents the depth of the downslope flow as inferred by $0.75\,E\,s$, where E is the entrainment coefficient and s is the along-slope distance from the top of the slope (see text for details). The plots below display $u_{s,max}$ (solid line), its distance along the normal $n\,(u_{s,max})$ (dashed line), the slope angle α (dotted line), the forcing terms F_i in the momentum budget for the tendency of u_s, averaged across the depth of the downslope flow, the cooling rate at the ground surface $\partial T_0/\partial t$, and the components Q_i (sensible heat Q_H, latent heat Q_E and conduction to the underlying soil Q_G) of the surface energy budget $R_n = Q_H + Q_E + Q_G + \Delta\,Q_S$, where $R_n = K^\star + L^\star$, $K^\star$ and $L^\star$ are net allwave, shortwave and longwave radiation, respectively, and $\Delta\,Q_S$ is the residual.

The downslope flows accelerate or decelerate along the slopes as a result of the balance between the forcing terms in the momentum budget (see the middle plot in Fig. V.2). Above the CAP, the dominant forcing mechanism is the buoyancy force, which is balanced mainly by the subgrid-scale (SGS) stress divergences (i.e., diffusion) and the advection terms. The most appropriate thermodynamics measure of the CAP top height (that is the height of the top of the humid layer) was determined following Burns & Chemel [2014b]. Given the relatively large vertical height of the sloping surface ΔZ_s compared with the typical height scale of the flow H (yielding $\widehat{H} = H/\Delta Z_s \ll 1$) and the relatively small Froude number [$F = U^2/(g' H) < 1$, where U is the typical velocity scale of the flow and g' is the reduced gravity], this balance corresponds to the type of flow that McNider [1982a] classified as a shooting flow. As the downslope flow penetrates into the CAP, the relative contribution of advection becomes less important. In this condition, the flow is classified as an equilibrium flow. This regime was reported in the numerical model experiments performed by Burkholder *et al.* [2009] over a steep slope with a constant slope angle of 20°. As the air flows down the slopes within the CAP, it reaches its level of neutral buoyancy and is detrained, largely above the ground-based inversion layer. The top height of the ground-based inversion layer was calculated as the level at which the temperature gradient reverses from positive to negative.

Cuxart *et al.* [2007] also reported the occurrence of shooting flows over a gentle (less than 2°) nearly two-dimensional slope on the island of Majorca, Balearic Islands, Spain, located in the western Mediterranean region, about 200 km off the Iberian peninsula. A mesoscale non-hydrostatic model was used to model one night in January 1999 at a horizontal resolution of 1 km and a vertical resolution adjacent to the ground surface of 3 m. Atmospheric microphysical processes were not considered. It was indicated that along approximately the first 5 km of the slope mountain waves perturbed the downslope flow, however, beyond this point the downslope flow existed in quiescent conditions. Beyond the 5-km mark the downslope evolution of the momentum budget (computed using a two-layer hydraulic model) during the early night generally follows the same pattern as that shown in Fig. V.2. The increase in downslope flow depths, associated with the disruption of the downslope flows over the lower slopes, is evident in both sets of results. There is more variability in the momentum budget presented in Cuxart *et al.* [2007], which, at least partly, can be attributed to relatively abrupt changes in the slope angle (compared to the smoothly changing slope considered herein).

The top two plots of Fig. V.2 show that the maximum speed of the downslope flow and the position of this maximum along the normal to the slope decrease with distance from the top of the slope within the CAP, while the depth of the flow is almost constant over the same section of slope above the ground-based inversion layer. Above

the CAP, the depth of the flow follows closely that inferred (for neutral conditions) by $0.75\,E\,s$ [Manins & Sawford, 1979], where E is the entrainment coefficient, estimated to be $0.05\ (\sin|\alpha|)^{2/3}$ [Briggs, 1981] based on the data reported by Ellison & Turner [1959], where α is the slope angle, and s is the along-slope distance from the top of the slope. This entrainment process corresponds to the plume-like regime of downslope flows over steep slopes analyzed by Baines [2005]. Within the CAP, the air above the downslope flow is not entrained but detrained, as indicated by the streamlines, and so the above semi-empirical estimation for the depth of the downslope flow is no longer appropriate.

The top plot in Fig. V.2 shows the dispersion characteristics of the downslope flow. Consistent with results of numerical model simulations of tracer dispersion over a uniform slope with a constant slope angle of 20°analyzed by Nappo *et al.* [1989], pollutant P_1, released at ground-level on the plateaux, spreads through the entire depth of the downslope flow above the CAP. In this region there is a two-layer structure to the pollutant concentration within the downslope flow, essentially defined by the height of the cold-air jet maximum $n\,(u_{s,max})$. The two-layer thermal structure of the downslope flow was discussed more generally by Burns & Chemel [2014b]. Figure V.2 shows that above the CAP pollutant concentrations are higher below than above $n\,(u_{s,max})$. This indicates a near-decoupling of the air below the cold-air jet maximum from the air above it. Within the CAP the pollutant concentration within the downslope flow is nearly uniform. It seems reasonable to suggest that this is caused by relatively large oscillations of the downslope flow speed within the CAP, as shown by Burns & Chemel [2014b]. These oscillations are likely to be associated with relatively intense mixing events, thereby mixing pollutants across the cold-air jet maximum. This is similar to an effect found by Cuxart & Jiménez [2007], who completed a LES of a cold-air jet over the Duero river basin on the Iberian peninsula, Spain. The cold-air jet, together with intermittent bursts of turbulence within the cold-air jet, were observed during the Stable Atmospheric Boundary Layer Experiment in Spain-1998 [SABLES-98; Cuxart *et al.*, 2000]. Good agreement between the LES results and the observations from SABLES-98 was found. Cuxart & Jiménez [2007] suggested that the mixing events could be explained by the 'Businger mechanism' [Businger, 1973], which is different to that suggested to cause the change in pollutant dispersion shown in Fig. V.2. However, this does not necessarily preclude the Businger mechanism from existing in the system considered herein.

Figure V.2 shows that the concentration C_1' of pollutant P_1 decreases by an order of magnitude as the pollutant reaches the top of the CAP. As the pollutant penetrates into the CAP and flows down the slope within the CAP, it is mixed and detrained out of the downslope flow. The isopleths within the CAP show that concentrations are slightly higher above the ground-based inversion layer than below, indicating that

some fraction penetrates into the ground-based inversion layer, despite its strong atmospheric stability.

To investigate the fate of the pollutants emitted along the slopes, Fig. V.3 presents cross-valley vertical cross-sections of along-valley-averaged pollutant concentrations at the same time ($t = 480$ min). Pollutant P_{11}, emitted at the bottom of the slopes within the ground-based inversion layer, is largely trapped there (see Fig. V.3f). Pollutant P_9, emitted farther up at the centre of the bottom half of the slopes (that is above the ground-based inversion layer), penetrates into the ground-based inversion layer, where its concentrations are highest, although some fraction detrains above it (see Fig. V.3e). Pollutant P_7, emitted just below the top half of the slopes, detrains within the CAP and concentrates just above the ground-based inversion layer (see Fig. V.3d). The pollutants emitted over the top half of the slopes display a similar behaviour to one another, with detrainment increasing with distance from the top of the slopes (see Fig. V.3a to V.3c). The concentrations of all pollutants above the CAP are relatively small with, at this time, no clear evidence of detrainment above the CAP top as defined by the top of the humid layer.

At that time ($t = 480$ min), an elevated inversion layer has developed close to the height of the plateaux, and the layer above the CAP is a region of increased atmospheric stability compared to the stability within the CAP [Burns & Chemel, 2014b]. As pointed out by Vergeiner & Dreiseitl [1987], an elevated inversion layer favours trapping. The argument is as follows: because of the enhanced atmospheric stability of the elevated inversion, the downslope flow mass flux is weaker in the elevated inversion than below. The airmass within the CAP is pushed up as the CAP grows, and when this airmass encounters the elevated inversion layer, it is transported towards the slopes at the lower boundary of the inversion layer, although some fraction is mixed within this layer.

The overview of the downslope flow, its forcing mechanisms and dispersion characteristics presented in this section calls for a quantification of the ability of the CAP to dilute pollutants, which is the purpose of the following section.

V.3.2 Dispersion characteristics of the developing CAP

Figure V.4 shows time series of the along-valley- and hourly-averaged concentrations of each pollutant P_i, averaged between the ground and the top height of the ground-based inversion layer, denoted by $\langle C_i \rangle_{\mathrm{GBI}}$, averaged between the top height of the ground-based inversion layer and that of the CAP, denoted by $\langle C_i \rangle_{\mathrm{CAP}}$, and the slope winds averaged over the depth of the downslope flows and over the region of the slopes where pollutant P_i is emitted. The stepwise character of the time series is due to the algorithm used to track the positions of the top of the ground-based inversion layer

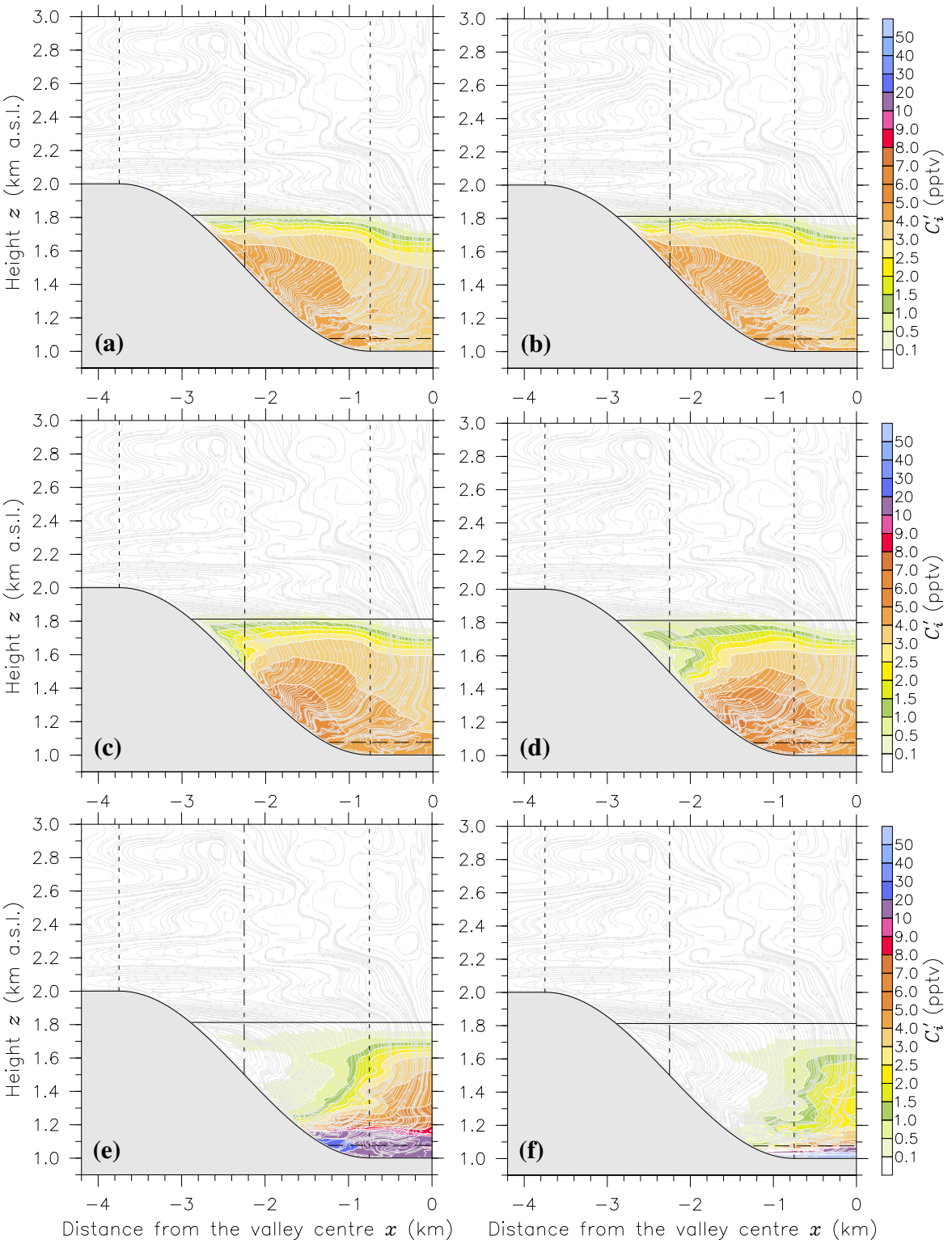

Figure V.3: Contour plots (**a**) to (**f**) of the along-valley-averaged concentration C_i' of pollutant P_i at time $t = 480$ min for $i = 2, 4, 6, 7, 9$ and 11, respectively, with streamlines superimposed. The horizontal dashed and solid lines mark the position of the top of the ground-based inversion layer and region of enhanced cooling, respectively. The vertical dotted lines mark the top and bottom of the western slope and the vertical dashed-dotted line indicates the location half-way along the slope.

and CAP [see Burns & Chemel, 2014b]. Once the flow is well established, about 1 h after sunset, the time evolutions of $\langle C_1 \rangle_{\mathrm{GBI}}$ and $\langle C_1 \rangle_{\mathrm{CAP}}$ follow closely those of the top height of the ground-based inversion layer and CAP, respectively. This shows that the downslope flows fill the valley with air from above, which is then trapped within the CAP.

The time evolution of the pollutant concentrations depends on where the pollutants are emitted with respect to the positions of the top of the ground-based inversion layer and CAP. Once the flow is well established, the concentrations of the pollutants emitted over the top half of the slopes (pollutants P_2 to P_6) are almost equal and constant with time, when averaged within the ground-based inversion layer, and almost equal but increasing steadily with time, when averaged within the CAP. The pollutants emitted towards the bottom of the slopes (pollutants P_9 to P_{12}) display a different behaviour. Their concentrations increase with time and distance from the top of the slopes, when averaged within the ground-based inversion layer, and decrease with time and distance from the top of the slopes, when averaged within the CAP.

Pollutants emitted within the ground-based inversion layer are largely trapped there. When pollutants are emitted at increasing distance above the ground-based inversion layer, their concentrations averaged within the ground-based inversion layer $\langle C_i \rangle_{\mathrm{GBI}}$, decrease because of dilution increasing with distance from their sources. More specifically, for the pollutants emitted over the lower part of the slopes $\langle C_i \rangle_{\mathrm{GBI}}$ is inversely proportional to the slope wind speeds where the pollutants are emitted, denoted by $\overline{u_s}|_i$. Since the slope wind speeds there decrease with distance from the top the slopes, this shows that the concentrations of these pollutants contain a factor proportional to the inverse of the distance from the sources, arising from 'plume' dispersion. This decrease in the slope wind speeds is due to their interaction with the growing CAP. The reader is referred to Burns & Chemel [2014b] for a detailed account of the influence of the developing CAP on the slope winds for the present simulation. The CAP-averaged concentrations $\langle C_i \rangle_{\mathrm{CAP}}$ are proportional to $\overline{u_s}|_i$ over the lower part of the slopes (pollutants P_9 to P_{12}), and diminish as the CAP deepens.

Mahrt *et al.* [2010] also reported diminishing slope winds on clear nights over the gentle lower slope (with a slope angle of about 5°) of Tussey Ridge, Pennsylvania, USA. Near-surface observations, over the lowest 50 m of the approximately 300-m high ridge, indicated that the slope winds diminished to a light and variable condition as the night progressed, assumed to be due to the influence of the deepening CAP engulfing part of the slope.

The overall increase of $\langle C_{12} \rangle_{\mathrm{GBI}}$ during the early night generally reflects the trend of pollutant concentration at screen-level height over the valley floor (not shown). A general increase in benzene concentration during the first half of the night of 1 February 2006, observed close to the floor of the Inn valley, Austria, was reported by

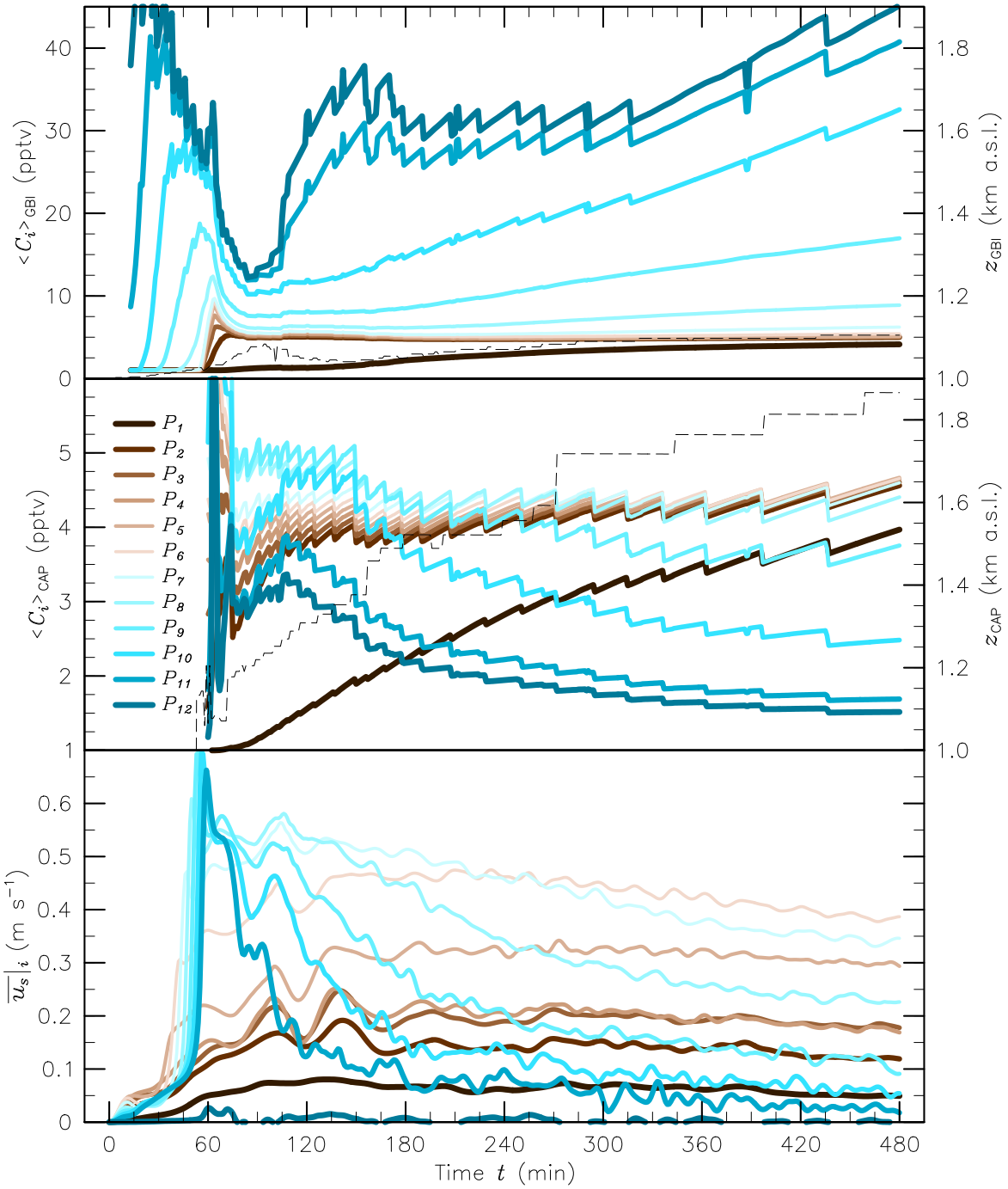

Figure V.4: Time series of the along-valley-averaged concentrations of pollutant P_i, $i \in [1..12]$, averaged between the ground and the top height of the ground-based inversion layer, denoted by $\langle C_i \rangle_{\mathrm{GBI}}$, averaged between the top height of the ground-based inversion layer and that of the region of enhanced cooling, denoted by $\langle C_i \rangle_{\mathrm{CAP}}$, and the slope winds averaged over the depth of the downslope flows and over the region of the slopes where pollutant P_i is emitted, denoted by $\overline{u_s}|_i$. The dashed lines in the top two plots indicate the top heights of the ground-based inversion layer z_{GBI} and region of enhanced cooling z_{CAP}.

Schnitzhofer *et al.* [2009]. The Inn valley has a similar width and depth to the geometry considered herein, although is more complex with tributary valleys and frequent

valley winds. The trend in benzene concentration noted above was observed during calm synoptic anticyclonic conditions with clear skies (except for scattered thin cirrus clouds). Wind speeds close to the ground were small (less than 1 m s^{-1}), although radiosonde data provided by Harnisch *et al.* [2009] suggest that a significant down-valley wind jet (maximum speed of approximately 7 m s^{-1}) existed about 400 m above the valley floor. Kitada & Regmi [2003] demonstrate the importance, in some cases, of valley and plain-to-mountain winds in the vertical and horizontal dispersion of air pollutants. Schnitzhofer *et al.* [2009] argued that the nocturnal increase in benzene concentrations was due to the development of a ground-based inversion layer, trapping pollutants close to the ground. In contrast to the observation of Schnitzhofer *et al.* [2009], Gohm *et al.* [2009] and Harnisch *et al.* [2009] provided data showing a general decrease in aerosol concentrations after sunset, observed on the same night and at the same location in the Inn valley. The trend in aerosol concentrations was in phase with that of vehicle numbers passing through the area. This suggests that the evolution of emissions and/or chemistry can be as important in controlling concentrations as the evolution of near-ground static stability. It is worth noting that shorter-term reductions (about an hour) are evident in $\langle C_{12} \rangle_{\mathrm{GBI}}$ (e.g. close to $t = 180$ min); a result of the interactions between the downslope winds and the ground-based inversion layer.

Figure V.5 presents vertical profiles of hourly-averaged pollutant concentrations, averaged across the valley floor, away from the slopes. The profiles show a marked build-up of pollution within about 100 m above the valley floor for the pollutants emitted towards the bottom of the slopes (pollutants P_9, P_{11} and P_{12}), which are engulfed by the ground-based inversion layer. Their concentrations decrease sharply with height across the ground-based inversion layer. The pollutants emitted farther up the slopes are almost well mixed within the CAP, suggesting detrainment through the entire depth of the CAP, as can be seen in Figs. V.2 and V.3. This well-mixed behaviour is also promoted by the slow decrease in atmospheric stability of the CAP above the ground-based inversion layer, once the flow is well established (about 1 h after sunset), from about 8 K km^{-1} (i.e., a value about 5 to 6 times larger than at the start of the simulation) to about 5 K km^{-1} at the end of the simulated 8-h period [Burns & Chemel, 2014b]. Pollutant P_1, emitted on the plateaux, is less concentrated within the CAP than the pollutants emitted at the top of the slopes, indicating that the downslope flows do not draw air only from the plateaux but also entrain air from above the slopes.

Table V.1 reports measures of the dilution of each pollutant within the developing CAP. The ratio $\langle C_{i,1} \rangle_{\mathrm{f}} / C_{i,max}$, where $\langle C_{i,1} \rangle_{\mathrm{f}}$ is the hourly-averaged concentration of pollutant P_i, averaged across the valley floor, within the model layer adjacent to the ground surface and $C_{i,max}$ is the maximum hourly-averaged concentration of pollutant P_i within the model domain (almost constant over time). This ratio is a measure of

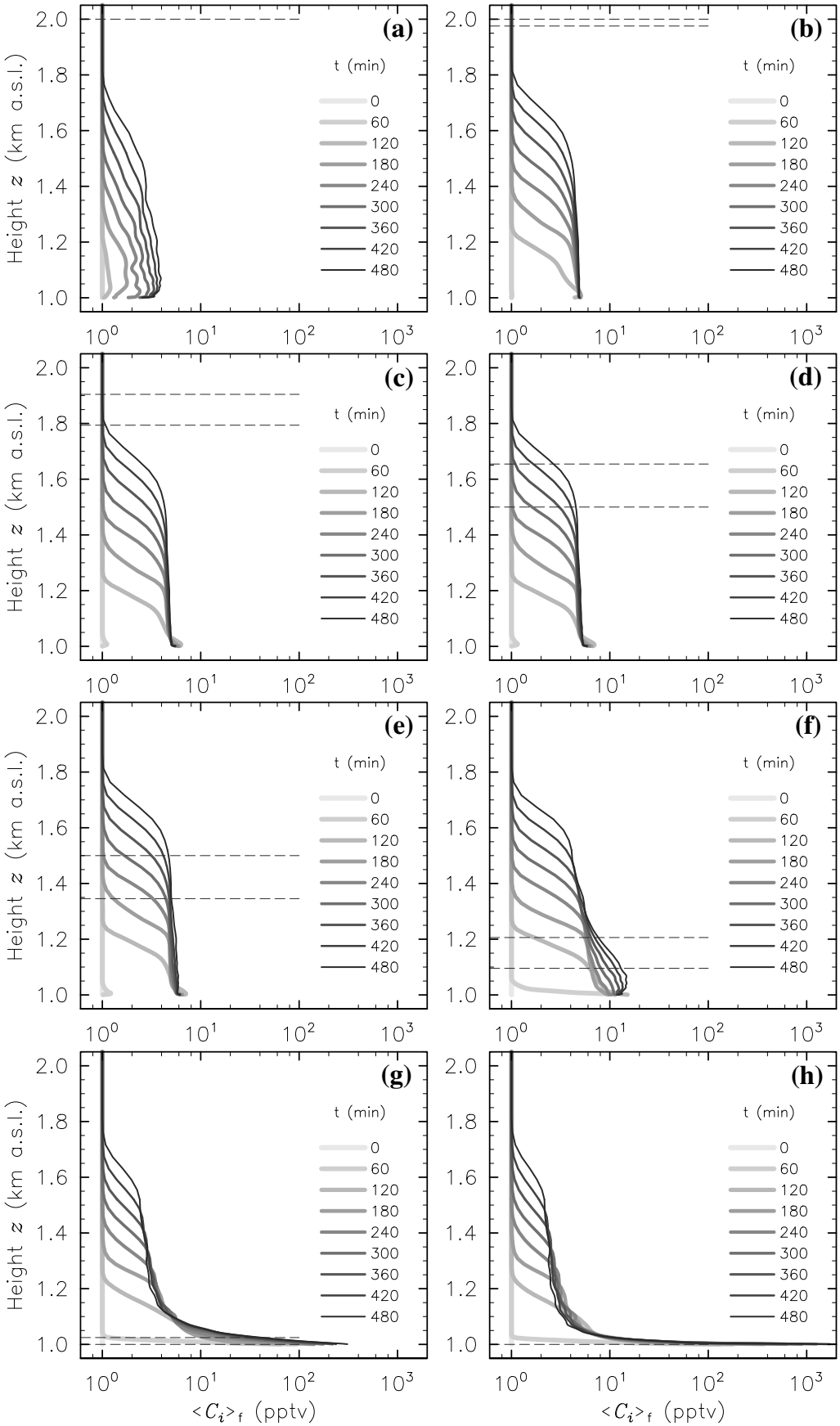

Figure V.5: Vertical profiles (**a**) to (**h**) of the hourly-averaged concentration of pollutant P_i, averaged across the valley floor, denoted by $\langle C_i \rangle_{\mathrm{f}}$, at times $t = 0$, 60, 120, 180, 240, 300, 360, 420 and 480 min for $i = 1, 2, 4, 6, 7, 9, 11$ and 12, respectively. The dashed lines mark the boundaries of the height range over which the pollutant P_i is emitted.

t (min)	P_1	P_2	P_3	P_4	P_5	P_6	P_7	P_8	P_9	P_{10}	P_{11}	P_{12}
$(\langle C_{i,1}\rangle_f / C_{i,max}) \times 100$ *(%)*												
120	0.4	2.9	9.2	35.9	54.5	67.8	72.1	88.8	76.5	80.0	56.9	65.4
240	0.5	4.7	23.7	44.7	57.6	62.5	59.2	54.3	44.2	39.2	46.0	76.1
360	0.8	5.1	24.8	42.6	51.8	53.3	48.3	41.2	33.5	31.0	29.2	72.6
480	0.8	5.1	24.7	39.7	47.7	47.8	43.1	35.4	20.9	16.7	18.0	82.5
$(\langle C_{i,\mathrm{GBI}}\rangle_f / \langle C_{i,1}\rangle_f) \times 100$ *(%)*												
120	113.6	86.9	76.6	74.0	73.0	72.6	73.8	66.6	48.5	23.9	11.0	4.7
240	123.4	93.4	84.1	80.4	78.2	77.4	79.0	78.2	73.4	42.3	4.4	0.8
360	119.9	95.9	89.1	86.2	84.5	84.1	86.3	88.1	84.0	36.0	2.6	0.3
480	144.3	98.2	91.5	88.6	86.9	87.4	93.2	102.8	107.3	41.5	1.7	0.2
$(\langle C_{i,\mathrm{CAP}}\rangle_f / \langle C_{i,1}\rangle_f) \times 100$ *(%)*												
120	97.1	30.0	25.9	24.6	23.8	23.4	23.8	19.4	11.5	4.6	2.0	1.0
240	54.6	20.4	18.5	17.7	17.1	16.6	16.4	14.0	9.7	4.4	0.7	0.2
360	39.5	20.4	18.9	18.2	17.6	17.1	16.4	13.5	8.5	3.3	0.4	0.1
480	38.9	20.7	19.3	18.6	18.0	17.5	16.7	13.5	8.4	3.1	0.3	0.0

Table V.1: Ratios $\langle C_{i,1}\rangle_f / C_{i,max}$, $\langle C_{i,\mathrm{GBI}}\rangle_f / \langle C_{i,1}\rangle_f$ and $\langle C_{i,\mathrm{CAP}}\rangle_f / \langle C_{i,1}\rangle_f$, for pollutants P_i, $i \in [1..12]$, at times $t = 120$, 240, 360, 420 and 480 min, where $\langle C_{i,1}\rangle_f$, $\langle C_{i,\mathrm{GBI}}\rangle_f$ and $\langle C_{i,\mathrm{CAP}}\rangle_f$ are the hourly-averaged concentrations of pollutant P_i, averaged across the valley floor, within the model layer adjacent to the ground surface, at the top height of the ground-based inversion layer and at the top of the CAP, respectively, and $C_{i,max}$ is the maximum hourly-averaged concentration of pollutant P_i within the model domain

the overall dilution from the emission sources to the valley floor. This ratio generally decreases with time for all the pollutants [except those emitted at the very top of the slopes (pollutants P_1 to P_3)]. Over time the pollutants are mixed through and out of the ground-based inversion layer. Unexpected increases and decreases of this ratio are noted from $t = 120$ to 240 min, which is approximately the time when the top of the CAP reaches the height of the strongest slope winds [see Burns & Chemel, 2014b, for details of the complex interactions between the downslope flows and the developing CAP]. For pollutant P_{12}, emitted at the valley floor, the ratio is less than 100 %, indicating that its concentration is not uniform across the valley floor, and consistent with pollutants being lifted up at the centre of the valley, as discussed above. The dilution from the emission sources is found to be inversely proportional to the slope wind speeds where the pollutants are emitted, as can be seen in Figs. V.2 and V.4. At the end of the simulated 8-h period, the concentration of the pollutants emitted on the steepest slopes, where the slope winds are the strongest, is about 40 % smaller at the valley floor than at the emission source.

The ratio $\langle C_{i,\mathrm{GBI}}\rangle_f / \langle C_{i,1}\rangle_f$, where $\langle C_{i,\mathrm{GBI}}\rangle_f$ is the hourly-averaged concentration of pollutant P_i, averaged across the valley floor, at the top height of the ground-based inversion layer, is a measure of the overall vertical dilution within the ground-based

inversion layer. This ratio generally increases with time for all the pollutants, except those emitted at the very bottom of the slopes (pollutants P_{10} to P_{12}). This shows that the gradient of concentration decreases over time, suggesting a build-up of pollution above the ground-based inversion layer, which is increasingly mixed over time, as noted above. The concentrations of the pollutants emitted within the ground-based inversion layer decrease sharply with height. For example, the concentration of pollutant P_{12} decreases by almost two orders of magnitude from the valley floor to the top of the ground-based inversion layer.

The ratio $\langle C_{i,\mathrm{CAP}}\rangle_\mathrm{f}/\langle C_{i,1}\rangle_\mathrm{f}$, where $\langle C_{i,\mathrm{CAP}}\rangle_\mathrm{f}$ is the hourly-averaged concentration of pollutant P_i, averaged across the valley floor, at the top of the CAP, is a measure of the overall vertical dilution within the CAP. This ratio depends on where the pollutants are emitted with respect to the positions of the top of the ground-based inversion layer and CAP, and on the slope wind speeds, as for $\langle C_i\rangle_\mathrm{GBI}$ and $\langle C_i\rangle_\mathrm{CAP}$ (see Fig. V.4). It generally increases with time for the pollutants emitted over the top half of the slopes (pollutants P_2 to P_6) and decreases with time for the pollutants emitted over the bottom half of the slopes (pollutants P_7 to P_{11}). This is explained as follows: the pollutants emitted within the ground-based inversion layer are largely trapped there. The pollutants emitted farther up the slopes detrain within the CAP above the ground-based inversion layer, although some fraction, increasing with distance from the top of the slopes, penetrates into the ground-based inversion layer.

V.4 Summary

The purpose of our study was to quantify the role of cold-air-pooling processes in the dispersion of air pollution in the developing valley CAP studied by Burns & Chemel [2014a,b]. The key findings are summarized below.

- The overview of the downslope flow, its forcing mechanisms and dispersion characteristics presented in Sect. V.3.1 showed that the negatively buoyant downslope flows transport and mix pollutants into the valley to depths that depend on the temperature deficit of the flow and the ambient temperature structure inside the valley. Along the slopes, pollutants are generally entrained above the CAP and detrained within the CAP, largely above the ground-based inversion layer. The downslope flow was found to have a clear two-layer structure above the CAP comparing very well with the numerical model results of Cuxart & Jiménez [2007], where the latter agreed well with relevant observations. Within the CAP the pollutants were found to be well mixed across the downslope flow layer, likely caused by relatively intense variations of the downslope flow within the CAP.

- The ability of the CAP to dilute pollutants was quantified in Sect. V.3.2. The analysis indicated that the downslope flows fill the valley with air from above, which is then trapped within the CAP, and that the air is drawn not only from the plateaux but also from above the slopes. Once the flow is well established, about 1 h after sunset, the pollutants within the ground-based inversion layer are continuously replenished by the downslope flows, despite its strong atmospheric stability. Dilution depends on where the pollutants are emitted with respect to the positions of the top of the ground-based inversion layer and CAP, and on the slope wind speeds. Over the lower part of the slopes, the CAP-averaged concentrations are proportional to the slope wind speeds where the pollutants are emitted, and diminish as the CAP deepens. Diminishing downslope winds within expanding CAPs have been observed at points in the atmosphere [e.g. Mahrt *et al.*, 2010]. Pollution accumulates within the ground-based inversion layer for the pollutants emitted towards the bottom of the slopes, which are engulfed by the ground-based inversion layer. This compares well to the observations reported by Schnitzhofer *et al.* [2009], however, stands in contrast to those of Gohm *et al.* [2009] and Harnisch *et al.* [2009], indicating that the evolution of emissions and/or chemistry can be as important as the evolution of static stability. Their concentrations decrease sharply with height across the ground-based inversion layer. The concentration of the pollutant emitted on the valley floor decreases by almost two orders of magnitude from the valley floor to the top of the ground-based inversion layer by the end of the simulated 8-h period. The pollutants emitted farther up the slopes detrain within the CAP above the ground-based inversion layer, although some fraction, increasing with distance from the top of the slopes, penetrates into the ground-based inversion layer. The concentration of the pollutants emitted on the steepest slopes, where the slope winds are the strongest, is about 40 % smaller at the valley floor than at the emission source at the end of the simulated 8-h period.

The results presented herein have important practical implications for the assessment and management of pollution in the atmosphere and in other fluid analogues. It is hoped that the present work will provide an impetus to investigate pollutant dispersion in cold-air pools.

VI

Summary & Conclusions

Downslope flows and regions of enhanced cooling have important impacts on society and the environment. Parameterisation of these often subgrid-scale phenomena in numerical models requires a sound understanding of the underlying physical processes, which has been the overarching aim of this work. A numerical model has been used to characterise the development of a region of enhanced cooling and some of its interactions with downslope flows, in an idealised alpine valley with a width and depth of order 10 and 1 km, respectively, under decoupled, stable and poorly-drained conditions.

This study has considered a region of enhanced cooling rather than a region of cold air, where the latter is appropriate for relatively small-scale terrain (i.e. hill environments). This work has focused partly on removing the uncertainty surrounding the forcing mechanisms controlling the evolution of regions of enhanced cooling. Perhaps one of the most important and interesting results of the study is the generally near-equal partitioning of cooling between radiative and dynamics effects within the valley atmosphere, for the case considered.

A second key focus of the work has been to quantify some of the interactions between the developing region of enhanced cooling and the downslope flows. A number of other physical regions affecting the developing region of enhanced cooling have also been considered. This part of the study has revealed the large complexity of even idealised cases. Thirdly, the study has focused on how these interactions and processes affect the dispersion of passive pollutants emitted close to the ground surface, which has important implications for both people and the environment (see Chapter I). Some of the key identified interactions and processes are listed below (see Chapters III to IV for more detail). To make the work more accessible for the reader Figure VI.1 illustrates the key interactions and processes that have been listed.

- The ground surface acts as a heat sink by radiating thermal energy to space, inducing downslope flows along the valley slopes (see A and B in Fig. VI.1).
- The downslope flows generally deepen over the top half of the slopes as they entrain air from their environment (see C). The analytical model of Manins

& Sawford [1979] gives a good estimate of the downslope flow height in this region. Over approximately the same part of the slope the flows accelerate due to buoyancy exceeding friction forces. In this region pollutants emitted close to the slope are largely trapped below the cold-air jet maximum height, revealing the two-layer structure of the flow in this region. The latter feature compares well to some previous numerical results and observations [Cuxart & Jiménez, 2007].

- The downslope flows are disrupted by the region of enhanced cooling (denoted by CAP_h, which generally corresponds to a region of relatively dry air. Above the CAP_h the downslope flows are in a 'shooting-flow' regime. For regions of the slope engulfed by the region of dry air the downslope flows enter a transient near-equilibrium flow regime preceding the arrival of the dry region. The momentum budget along the slope computed for this work is similar to that of a study of a gentle slope [Cuxart *et al.*, 2007]. Relatively large variations in the flow speeds occur as they enter the region of dry air (see D). Pollutants were found to be well mixed across the downslope flow layer within the CAP_h, likely caused by the relatively large flow variations. These variations have dominant periods ranging from approximately 20 to 50 min but cannot be solely explained by the analytical model described by McNider [1982a]. A capping inversion in potential temperature exists at the top of the CAP_h (denoted by CI), defined by variable mixing, until 2 h after sunset. The CI is not always well defined close to the slopes (see D) due to intense mixing there, when it still exists further away from the slopes. A layer of moist air is carried above the CI, with pollutants largely trapped within the CAP_h. These layers tend to curve upwards as they approach the slopes. Internal gravity waves (IGWs) are induced by the unstable flows with a highly non-monochromatic wave field occurring within the valley atmosphere (see E).

- The entrainment and detrainment patterns of the simulated downslope flows are comparable to those observed during the laboratory experiments of density currents in the 'plume regime' made by Baines [2008]. Detrainment occurs within the CAP_h as the downslope flows approach and exceed their level of neutral buoyancy. In this region the analytical model of Manins & Sawford [1979] does not accurately estimate the downslope flow height. A layering effect of the flows occurs within the CAP_h, similar to some previous observations [Neff & King, 1989], inducing wind shears and mixing (see F). Horizontal distances have been exaggerated for clarity.

- A return flow occurs mostly within the CAP_h where entrainment occurs. The return flows increase the wind shear close to the sloping surface, where the flows

'spring-back' after 'over-shooting' their levels of neutral buoyancy, encouraging detrainment through shear-instabilities. The return flows enable a thin layer of unstable air to develop close to the sloping ground, presumably also enhancing detrainment and mixing (see G). These features, together with the large flow variations noted above, are coincident with elongated flow structures orientated downslope.

- The downslope flows are generally deflected above the ground-based inversion (denoted by GBI), which is generally an order of magnitude more stable than the atmosphere above it (see H). Some dense air does penetrate into the GBI, especially during the early night when the GBI is displaced upwards and weakened by mixing, before the downslope flows are forced to retreat back up the valley slopes. Some observations exist of diminishing downslope flows within expanding regions of enhanced cooling [Mahrt *et al.*, 2010]. Pollutants were found to generally accumulate within the GBI throughout the night similar to some previous observations in the Alps [Schnitzhofer *et al.*, 2009], but in contrast to others made at the same time and location [Gohm *et al.*, 2009; Harnisch *et al.*, 2009]. This indicates that the evolution of emissions and/or chemistry can be as important as the evolution of static stability. Shorter-term (about an hour) simulated reductions in tracer concentrations occured within the GBI due to the interactions between the downslope flows and the GBI. By the end of the simulated 8-h period the GBI expands to a depth of approximately 100 m, which compares very well to the observations of Chemel & Chollet [2006]. Pollutants concentrations decrease by almost two orders of magnitude across the depth of the GBI. Pollutants emitted above the GBI are increasingly trapped within the region as the emission source moves towards the layer. The concentration of pollutants within the CAP_h, emitted over the lower half of the slopes, increases as the emission source moves away from the GBI. The concentration of pollutants within the CAP_h is very similar when varying the location of the emission source over the top half of the valley slopes.

- A region of near-horizontal streamlines, directed from the valley axis towards the plateaux, occurs above the valley atmosphere. A well-mixed region with many vortices begins to occur below it (but still generally above the valley atmosphere). These features partially trap air flows within the valley and the vortices start the formation of an elevated inversion, further preventing vertical motions (see I). The valley atmosphere dynamics are largely partitioned into two volumes defined by the top of the region of dry air. The wave vectors of IGWs above the valley clearly tilt towards the plateaux (see J).

- Close to 2 h after sunset the CAP_h encounters the most energetic region of

the downslope flows causing enhanced detrainment above the region, the final destruction of the lower CI, and relatively rapid near-vertical transfers of heat energy (see K in middle schematic).

- Enhanced vertical motions occur above the region of dry air (see L) which are then resisted as parcels reach the strengthening elevated inversion (see M). Enhanced adiabatic cooling occurs between these vertical limits that helps to reduce the difference in cooling between the lower and upper parts of the valley atmosphere. Moisture is also concentrated above the dry air but mainly below the elevated inversion increasing cooling by radiative divergence. Air motions within the dry air region are also tilted towards the horizontal in-line with the detrainment processes taking place there (see N). These processes make it difficult to define the top of the CAP_h between approximately 2 and 4 h after sunset.

- Close to 7 h after sunset the CAP_h reaches the bottom of the elevated inversion in potential temperature (see right schematic). Fig. VI.1 shows the expansion of the CAP_h up through the valley atmosphere during the early night.

- The average accumulated temperature change within the GBI is close to double the change within the rest of the valley atmosphere, which cools by about twice as much as the free atmosphere above. The stability of the GBI and CAP_h decrease after 1 h following sunset, similar to some previous observations [Neff & King, 1989]. The stability of the atmosphere is greater at the end of the simulation than the initial condition.

It is important to note that some of the interactions and processes noted above may be particular to the case considered here, at least in their prominence. Research aimed at developing a parameterisation scheme for complex terrain processes has advanced understanding of atmospheric processes in complex terrain to the benefit of society.

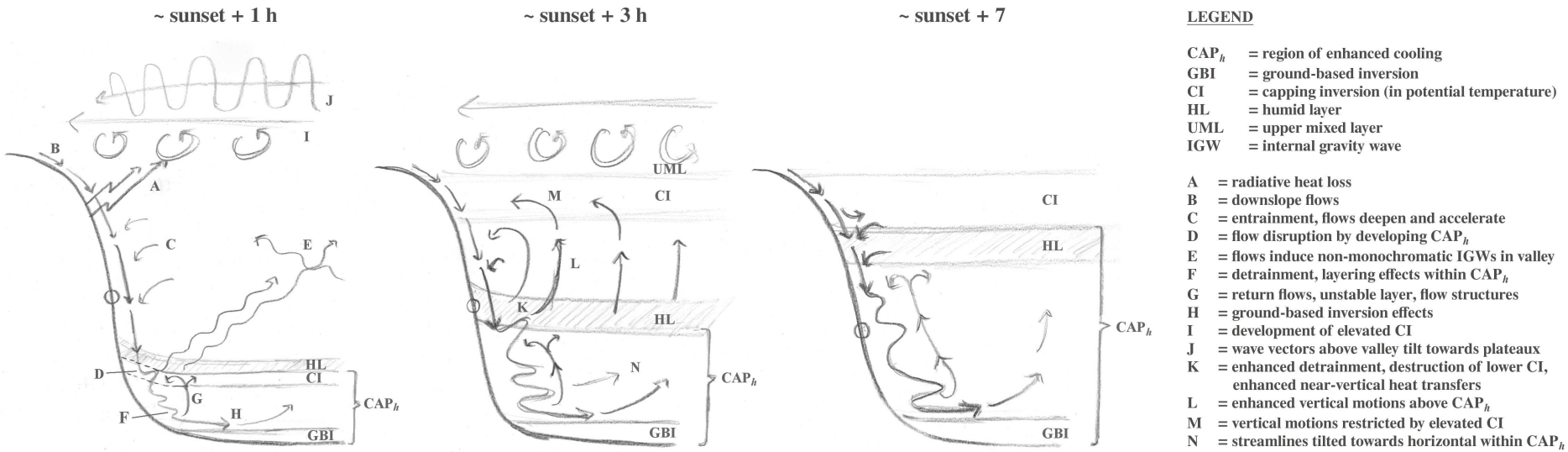

Figure VI.1: Schematic showing some of the key identified interactions and processes that have been detailed in Chapters III to V. The schematics from left to right represent the valley atmosphere at approximately sunset + 1 h, sunset + 3 h, and sunset + 7 h, respectively. Horizontal distances have been exaggerated for clarity. The approach has been to not repeat all features at each approximate time considered but rather to include those features key to the changes occurring at each time. The text symbols and abbreviations used in the figure are briefly explained or defined in the figure legend, see text for full details.

As well as the results corresponding to the key objectives of this study, several other important findings were made during the course of the study, for example, during the literature review and the numerical model set-up:

The numerical model results have been compared to the analytical solution of the downslope flow profile derived by Prandtl [1942] at a point half-way down the model slope. The comparison has revealed that the analytical solution produces downslope flows approximately half as deep and fast as those generated by the numerical model. The cause of the difference in flow depths is most likely due to the assumption of a quasi-hydrostatic atmosphere and the use of a constant eddy viscosity by the analytical model, a result also found by [Grisogono & Oerlemans, 2001]. The use of a constant eddy viscosity in the model dervied by Prandtl [1942] is also likely to under-estimate flow speeds in the cold-air jet. Furthermore, the analytical model assumes a balance between buoyancy and friction forces, which is not appropriate at the point considered during the first few hours of simulation when buoyancy accelerates parcels along the slope. In future work it would be useful to include the model derived by [Grisogono & Oerlemans, 2001] in the comparison conducted here.

The sensitivity of the valley-average temperature changes to numerical horizontal grid resolution was tested by varying the grid resolution between 1500 and 30 m. The results indicate that current operational forecasting models will significantly underestimate the valley-average cooling for the case considered herein. By the end of the simulation, the change of average temperature for the 30-m case is very similar to that of the 50 and 75-m cases, but approximately twice that of the 750-m and 1500-m cases, with the 250-m case seeming to represent an intermediate case between two regimes. Initial investigations suggests that the cause of the different temperature changes is closely tied to the representation of downslope flows in the different simulations. Coarser resolutions appear to generate weaker downslope flows, reducing the ability of the system to cool the atmosphere enclosed within the terrain, which increases net radiative heat losses from the valley atmosphere.

Future work might begin by extending the analysis conducted herein to the full nocturnal period, before sampling more of the parameter space.

A

Appendix

Constraints on numerical model grid resolution

The Nyquist-Shannon sampling theorem states that a signal bandlimited (e.g., by using a Fourier transform), to a maximum frequency f_{max} can be exactly reconstructed by sampling the bandlimited signal at a frequency $f_s \geq 2\, f_{max}$. A downslope flow with a CAJ located 1 m a.g.l., represented by a bandlimited signal, is likely to contain frequencies greater than $1/2$ m^{-1}, given that the flow profile around the CAJ is non-linear. If the shape of the downslope flow profile is assumed to be linear, then the bandlimited signal representing this profile may be exactly reconstructed by sampling the bandlimited signal at a frequency of $f_s = 1$ m^{-1}. In this case the numerical model vertical resolution Δz should be set to 1 m. Although using the Nyquist frequency to approximate the required numerical model grid resolution theoretically avoids anti-aliasing problems, some numerical modelling studies indicate that an even greater resolution may be required in practice. For example, Skamarock [2004] and Skamarock & Klemp [2008] have suggested that the 'effective resolution' is $6\,\Delta z$ to $8\,\Delta z$, indicating the length scale of the smallest accurately resolved features in a numerical model.

Using an 'effective resolution' was not practical for the downslope flow system and relatively large sub-mesoscale domain considered by this study. Increasing the vertical resolution demands an increase in the horizontal resolution to avoid grid distortion errors associated with the approximation of horizontal gradients, increasing integration times. As a compromise, the approach taken here was to use a vertical resolution that results in a CAJ feature that approximately corresponds to the available observations. A vertical resolution adjacent to the ground surface of approximately 1.5 m was used (see Chapter III for more details on how the terrain-following hydrostatic pressure coordinate was stretched across the vertical coordinate).

Figure A.1 displays hourly profiles of the simulated downslope flow speed u_s and near-ground virtual potential temperature perturbation θ'_v from the ambient field, in a slope-orientated coordinate system (s, y, n). Downslope flow profiles, ordered left to

right and top to bottom, correspond to the terrain points P_2 to F_1, respectively (see top figure). The idealised valley, given in a Cartesian coordinate system (x, y, z), is 1-km deep (along z), with the valley floor located 1 km a.s.l. and y is directed into the page. The relationship between the two coordinate systems is defined in § I.3, and the idealised terrain is fully described in Chapter III. u_s and θ'_v were computed from y-averaged fields (see § IV.3.2 and IV.3.3.a for an exact definition). The slope angle α is given for each point.

Figure A.1 demonstrates that the numerical simulation performed for this study generated downslope flows with length scales comparable to what is found in the available observations. Excluding the slope extremities, where the downslope flows are not well defined, the flows are shown to be between approximately 15 and 30-m deep, with a CAJ maximum wind speed located between 2 and 8 m a.g.l. These values are similar to those reported by Doran & Horst [1983] and Helmis & Papadopoulos [1996]. The necessary restrictions applied to Δz, the fact that the observations are point samples, and differences between the simulated and observed initial and boundary conditions makes a more thorough comparison difficult.

If a lower maximum slope angle had been considered then a lower vertical grid resolution adjacent to the ground surface could have been used. The downslope flows observed by Whiteman & Zhong [2008] had a CAJ located 10–15 m a.g.l. Setting $8\,\Delta z = 10$ m, for this example, results in an approximate maximum required $\Delta z = 1.25$ m. It is unclear what Δz is required to accurately simulate down-valley and/or drainage flows, since although the CAJ in these flows is significantly higher [$\mathcal{O}(100)$ m] than in downslope flows, drainage flows are often fed by downslope flows. It seems reasonable to suggest that drainage flows forced largely by mountain-to-plain pressure differences will be less dependent on an accurate representation of downslope flows than drainage flows forced mostly by local horizontal temperature differences over sloping ground. However, it should be noted that both forces frequently affect drainage flows and it may be impractical to separate them, at least for certain locations and time periods.

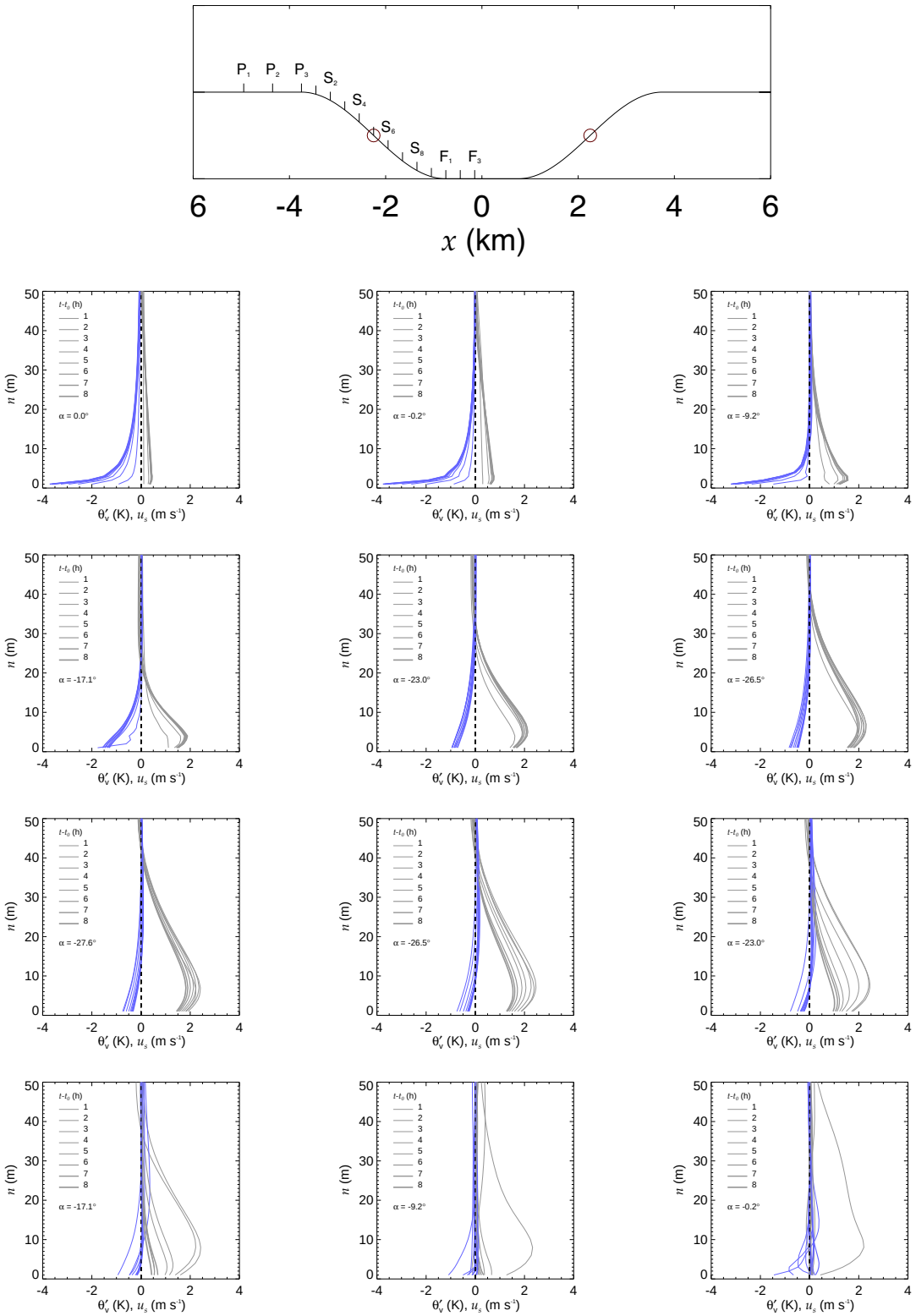

Figure A.1: Hourly profiles of downslope flow speed u_s and near-ground virtual potential temperature perturbation (θ'_v) from the ambient field, in a slope-orientated coordinate system (s, y, n). Downslope flow profiles, ordered left to right and top to bottom, correspond to the terrain points P_2 to F_1, respectively (see top figure). The idealised valley, given in a Cartesian coordinate system (x, y, z), is 1-km deep (along z), with the valley floor located 1 km a.s.l, and y is directed into the page. The slope angle α is given for each point.

To give an idea of the variation of Δz in the numerical simulation performed for this study, consider a vertical line at the centre of the valley. Δz ranges between approximately 1.5 and 60 m along the line through the valley atmosphere. This Δz, together with the expected flow characteristics from observational studies (discussed above), means that close to the terrain slopes, it is unlikely that the simulation resolved all of the significant eddies, with a significant energy content, that play an important role in controlling the flow characteristics. Therefore in this region of the domain the model cannot strictly be classified as a LES. Interestingly, Figure A.1 demonstrates that the subgrid-scale diffusion scheme, together with the implemented surface-layer scheme, generates reasonable flow characteristics close to the terrain slopes. The shape of the downslope flows, generated by the simulation performed for this study, should be checked against the results of higher resolution numerical simulations. Given the implemented Δz, it seems likely that the simulation presented herein (see Chapters III and IV) has generally resolved the eddies with the largest energy content away from the terrain slopes. In this region of the atmosphere it is likely that the subgrid-scale parameterisation scheme mainly acts to dissipate energy to the inertial range (as in a LES).

→ This appendix corresponds to a point in § III.2.1

B
Appendix

Consideration of sensitivity to model grid resolution

An important step towards completing the numerical model set-up, used for this study, was to choose the model's horizontal grid resolution. This was achieved by comparing the output from numerical model simulations implemented with different horizontal grid resolutions, but with the same stretched η coordinate (see previous section and Chapter III), and searching for a convergence of the results. Table B.1 shows the horizontal resolutions $\Delta x = \Delta y$ that were tested, together with the corresponding required number of grid points in the x and y directions. The lengths of x and y were held approximately constant at 12000 and 1200 m, respectively. The number of processors used is also provided together with the approximate time taken to complete the simulations using the available resources. As Δx is reduced below 30 m the simulations become very expensive (not shown). For example, the simulation takes over a week to run for $\Delta x = \Delta y = 7.5$ m (assuming that an optimised parallel computation is performed, requiring the use of significant national HPC resources).

Δx	x points	x length (m)	y points	y length (m)	processors	wall time (h)
30	402	12030	42	1230	144	52
50	242	12050	26	1250	88	35.3
75	162	12075	18	1275	32	38.2
150	82	12150	10	1350	8	34.4
250	50	12250	6	1250	5	22.3
750	18	12750	3	1500	2	8.7
1500	10	13500	3	3000	1	7.2

Δx is the grid resolution along the the model domain's x axis, with $\Delta x = \Delta y$. The 2^{nd} column shows the number of staggered grid points along the x axis for each Δx, the 3^{rd} column shows the total lengths of the domains along the x axis, and similarly for the 4^{th} and 5^{th} columns. The number of processors used to carry out the parallel computations are given in the 6^{th} column and the time taken to complete the computations (i.e. wall time) is given in the final column.

Table B.1: Numerical model parameters

Figure B.1 **(a)** shows the average valley-atmosphere instantaneous total cooling

rate $\langle R \rangle_{va}$ for the different implemented Δx, and demonstrates the general convergence of the results that was found.

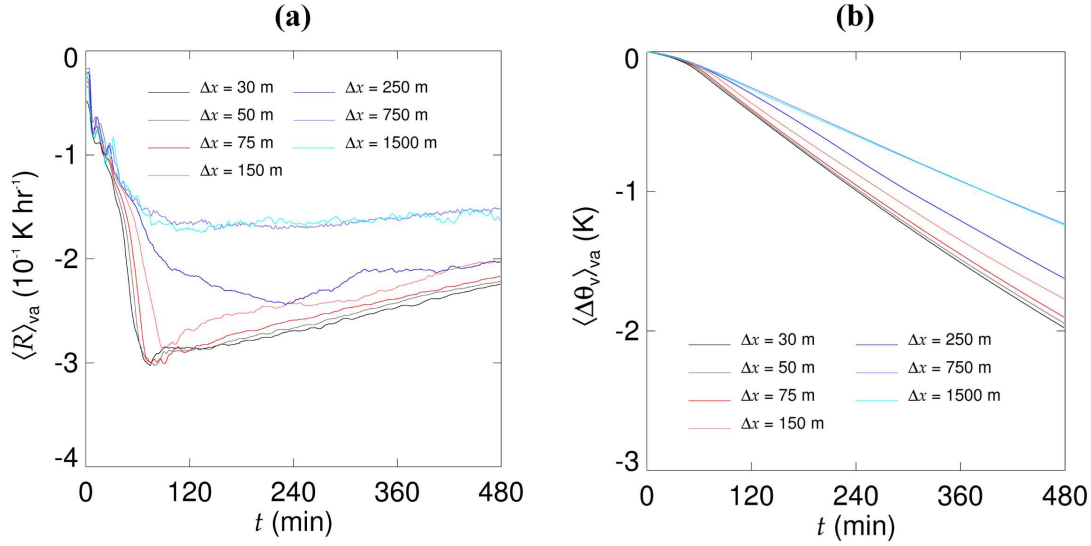

Figure B.1: Time series; **(a)** average valley-atmosphere instantaneous total cooling rate $\langle R \rangle_{va}$ for a number of different horizontal numerical grid resolutions Δx, with the same η coordinate in each case, see text for details, and **(b)** the same as for **(a)** but considering the accumulated change of θ_v from $t = 0$ ($\Delta \theta_v$). The simulation started approximately one hour before sunset close to the winter solstice.

After calculating θ_v from the model output θ field, R was calculated by using centered finite differencing; the form of R was not sensitive to the choice of differencing scheme. After averaging R across the model y-dimension, R was then interpolated onto a linear-orthogonal framework from the model's curvilinear grid. The finite differencing was carried out before the re-griding to avoid introducing numerical artifacts. A bilinear interpolation scheme was used, which only uses data points in the immediate vicinity of a target point to carry out the interpolation, constraining the interpolation to the numerical model output as far as possible. The bilinear interpolation scheme relied on grid indexes, avoiding errors close to sloping ground associated with triangulation techniques using real heights. Such errors are caused by the maximum grid distortion in these regions, together with the rapidly changing fields when moving along n. The new grid was given the same origin as the model curvilinear grid, however, a resolution $\Delta x' = \Delta z' = 5$ m was used. The final step was to average over the interpolated 2D valley space to generate the time series shown in Fig. B.1.

The sensitivity of the time series to the chosen $\Delta x'$ and $\Delta z'$ for each Δx was tested, for example, see Fig. III.4 in Chapter III for the $\Delta x = 30$ m results. Figure III.4 demonstrates that the time series converges as $\Delta x'$ is reduced from 100 to 1 m, where $\Delta x' = \Delta z'$ was used. This was found to be the case for all the Δx considered (not

shown). Errors occurring in $\langle R \rangle_{va}$, as $\Delta x'$ is increased, are primarily caused by the misrepresentation of the valley atmosphere away from the valley slopes. The sensitivity of $\langle R \rangle_{va}$ to errors occurring when using triangulation techniques instead of grid indexes is small. Presumably this is partly caused by the relatively small portion of the total valley volume that these near-ground errors affect, for the model set-up used for this study. This may not be the case for a smaller topographic depression.

The sensitivity of the time series to varying $\Delta z'$ (i.e. decreasing $\Delta z'$ from 100 to 1 m as above), but setting $\Delta x' = \Delta x$, was also tested (not shown). The results were very similar to that when considering $\Delta x' = \Delta z'$, indicating that the interpolation scheme operated in a reasonable way.

It would be preferable to avoid carrying out any interpolation, however, the alternative is at least as complicated as the technique outlined above, and is also prone to approximations and error. One approach that would work for the numerical model set-up used for this study, would be to find, for every x, the nearest model grid point below an arbitrary level, such as the plateau height, thereby roughly limiting any average to the valley space. Since the grid cells in the curvilinear space have varying volumes, a weighted average would need to be carried out. Therefore the volumes of the cells would need to be found or approximated. A quick comparison of the two methods can be made by assuming that the model output geometric heights are given at the corners of the model grid cells, which is not true. Volumes can then be approximated by assuming that the grid cell (x, z) areas are trapeziums. The resulting valley average is very similar to that obtained by re-gridding (not shown). Not weighting the average generates significantly different results to those presented in Figure B.1.

Figure B.1 **(a)** and **(b)** show the average valley-atmosphere instantaneous total cooling rate and accumulated change of θ_v from $t = 0$ (denoted by $\Delta \theta_v$), respectively, for the different tested Δx. The figures show a general convergence of the results as Δx is reduced from 1500 to 30 m, with very similar results for the 30, 50, and 75 m resolutions. The lowest horizontal resolution tested approximates the greatest horizontal numerical grid resolution found in current operational mesoscale forecasting models. Figure B.1 demonstrates that current mesoscale operational forecasting models will significantly underestimate $\langle R \rangle_{va}$ and $\langle \Delta \theta_v \rangle_{va}$, in the scale of complex terrain considered by this study. Initially, the increase in $|\langle R \rangle_{va}|$ is similar for all Δx, but soon diverges by approximately $t = 60$ min. At this time $|\langle R \rangle_{va}|$ for $\Delta x = 30$ m is approximately twice that of the $\Delta x = 1500$-m case. All curves then show a relatively gradual reduction of $|\langle R \rangle_{va}|$, however, the rate of change of $\langle R \rangle_{va}$ is significantly reduced for the 750 and 1500 m resolutions. The shape of the curve of the 250-m case is noticeably different from the others, seeming to represent an intermediate case between two regimes. The curves for all cases are shown to gradually converge after $t = 60$ min. The opposite effect can be seen in Fig. B.1 **(b)**, which displays a gradual

divergence of the results over time from the different Δx. By the end of the simulation, the accumulated change in θ_v for the $\Delta x = 30$-m case is almost twice that of the 1500 and 750-m cases.

An interesting question is what does cause the different cooling effects shown in Fig. B.1? The valley geometry is significantly misrepresented for large Δx ($\Delta x > 250$ m). For these cases the volume of atmosphere enclosed by the valley topography is significantly reduced. If the net loss of radiation to space at the ground surface is assumed to be similar for all cases then it is tempting to predict greater temperature changes for smaller enclosed volumes of atmosphere, however, this does not appear to be the case. Indeed an opposite trend is evident in the results.

$\langle \Delta\theta_v \rangle_{va}$ essentially represents the change in heat energy content of the valley atmosphere between $t = 0$ and some future time t'. Equation (B.1) summarises the causes of temperature changes (and changes in heat energy) at a point in the model atmosphere

$$\int_0^{t'} \frac{\partial \theta_v}{\partial t} dt = -\int_0^{t'} \mathbf{u} \cdot \nabla\theta_v \, dt + \int_0^{t'} S_r \, dt + \int_0^{t'} S_f \, dt, \tag{B.1}$$

When averaged across the valley atmosphere Eq. (B.1) is equivalent to $\langle \Delta\theta_v \rangle_{va}$. The first term on the right-hand side represents the change of heat energy content at a point due to advection. S_r and S_f are heat sinks from radiative divergence and subgrid-scale diffusion, respectively. Equation (B.1) is not implemented in the WRF model, where the equations are complicated by grid transformations etc.; it has been used here to clarify the description.

Since $\langle \Delta\theta_v \rangle_{va}$ decreases for increasing Δx the sum of the terms on the right-hand side of Eq. (B.1) (after applying $\langle\ \rangle_{va}$) must also decrease. Initial investigations indicate decreasing downslope flow speeds for increasing Δx, which presumably will reduce the transfer of heat energy towards the ground surface. The ground surface acts as a heat sink by removing energy to space by thermal radiation (neglecting any absorption and re-emission of longwave radiation back towards the ground by the valley atmosphere). Weaker downslope flows are likely to reduce upward vertical transport in the central valley atmosphere due to mass conservation, reducing cooling by the upward advection of low-θ_v air from below. These two effects are likely to generally reduce $|S_f|$ and $|-\mathbf{u} \cdot \nabla\theta_v|$, respectively. A reduction in $\langle \Delta\theta_v \rangle_{va}$ results in generally warmer valley atmospheres indicating that the total emission of infra-red radiation by the valley atmosphere to space will be greater for increasing Δx. The atmosphere above the valley is not affected significantly by cold-air pooling processes, and so the radiative flux of thermal energy into the valley atmosphere from above is likely to be similar for all Δx. This is likely to lead to increasing losses of heat energy from the valley atmosphere by radiative transport as Δx increases. The situation is likely to

be more complex than the theory outlined above and these initial ideas need to be confirmed by future research.

Much uncertainty remains about the forcing mechanisms [summarised in Eq. (B.1)] controlling the evolution of regions of enhanced cooling in terrain depressions. Chapter III aims to help remove some of this uncertainty by considering the cooling due to dynamics effects [the sum of the first and last terms on the right-hand side of Eq. (B.1)] and radiative processes, focusing on a consideration of the valley atmosphere as a whole.

→ This appendix corresponds to a point in § III.2.3

C
Appendix

Fourier analysis

It is clear that $\langle R \rangle_{vs}$ satisfies the Dirichlet conditions, and so a Fourier series will converge to the signal. A fast Fourier transform (FFT) of the form

$$g_\omega = \frac{1}{N_p} \sum_{n=0}^{N_p-1} f_n \, e^{\imath \, 2 \, \pi \, \omega \, n / N_p}, \tag{C.1}$$

with $\omega = 0, \ldots, N_p - 1$, was applied to $\langle R \rangle_{vs}$, taken half-way along y, after $t = 60$ min, where ω is the discrete set of angular frequencies, and N_p the number of points in the discrete time series f_n. Figure C.1a reveals that the harmonic with ω close to 0.01 rad s^{-1}, a period close to 10.48 min (see Fig. III.4a), dominated the signal, with $2 \, |g_\omega|^2 = S\left(\langle R \rangle_{vs}\right) = 4.01 \; 10^{-12}$ K^2. The zero frequency, the signal mean, was removed, as was the fundamental frequency, which is statistically not well defined and otherwise dominated the signal. The FFT normalizes g_ω by N_p, in order that Parseval's theorem applies, that is, in discrete form, $1/N_p \sum_{n=0}^{N_p-1} |f_n|^2 = \sum_{\omega=0}^{N_p-1} |g_\omega|^2$, where the total energy of the signal is the same in both the real and phase-space domains. For a real signal $\sum_{\omega=0}^{N_p-1} |g_\omega|^2 = \sum_{\omega=0}^{N_p/2-1} 2 \, |g_\omega|^2$. An in-depth spectral analysis is beyond the scope of this work, however, it is reasonable to argue that the dominant peak, found above, is the signature of internal gravity waves (IGWs). It was confirmed that the oscillations in $\langle R \rangle_{vs}$ are caused by the dynamics and not radiative processes (see Sect. III.3.1.b).

All points in the $\partial \theta_v / \partial t$ field within 100 m of the sloping valley sidewalls were then removed and $\langle \rangle_{vs}$ was applied to the resulting field, in the same way as for $\langle \partial \theta_v / \partial t \rangle_{vs}$, which provided a time series, denoted by $\langle R_2 \rangle_{vs}$, free from any signature of an oscillating downslope flow. Figure C.1b displays the above FFT applied to $\langle R_2 \rangle_{vs}$, which, when compared to Fig. C.1a, shows that the oscillations in $\langle R \rangle_{vs}$ are likely the result of IGWs propagating through the stable valley atmosphere. Largeron *et al.* [2013] demonstrated that it is the unstable and/or oscillatory downslope flow that initiates the IGWs. Further investigation, using the dominant frequency identified

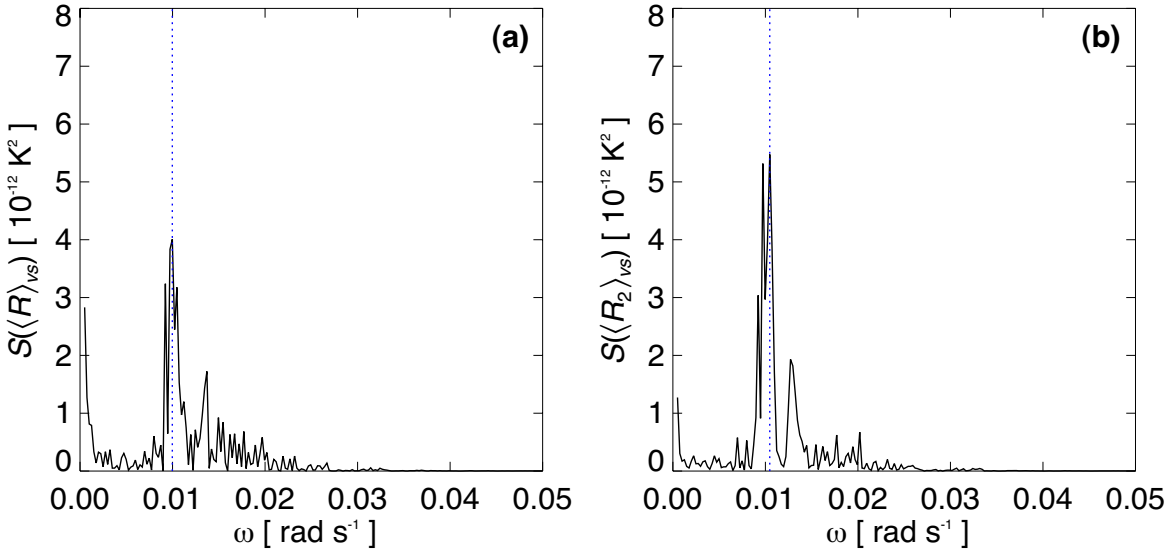

Figure C.1: Spectrum of the time series, after $t = 60$ min, of **(a)** $\langle R \rangle_{vs}$ and **(b)** $\langle R_2 \rangle_{vs}$, taken half-way along y, where the vertical dotted lines mark the frequencies with the largest amplitude in the spectrum (see text for details).

above, denoted by $\omega'_{\langle R_2 \rangle_{vs}}$, where ω' denotes the frequency with the largest amplitude in the spectrum of a time series, considering all times after $t = 60$ min, is difficult since $\langle R_2 \rangle_{vs}$ does not provide an accurate representation of the wave field (not shown). The problem is due to the averaging operation rather than the chosen proxy variable, which is representative of the wave field for positions above 200 m from the terrain surface (see Fig. C.2). The symmetry of the terrain and initial conditions makes the model output qualitatively symmetric about the valley axis, and therefore only the western side of the valley atmosphere is presented to make clear any features of interest.

An initial analysis of ω' across an (x, z) slice taken half-way along y (see Fig. C.2a) indicates that the wave field within the valley atmosphere is non-uniform. The reasons behind this heterogeneity have not been fully quantified, but seem likely to include wave-wave interactions [Largeron *et al.*, 2013], which strictly precludes the use of IGW linear theory in this region, as well as the use of a single representative ω' for the valley atmosphere. ω', as defined above, is not required to be a clearly dominant frequency, and an initial analysis indicates that the dominance of ω' is less clear wherever there is a relatively large and rapid spatial change in ω' (not shown). It is interesting that the waves in the valley atmosphere, above 200 m from the terrain surface, are restricted to approximately $0.005 \leq \omega' \leq 0.014$ rad s^{-1}. The wave field above $z = 2.5$ km a.s.l. (i.e., 500 m above the plateaus), and for $-2.25 \leq x \leq 2.25$ km (between the slope inflection points), is quasi-monochromatic (see Fig. C.2a), which permits the use of a single representative ω'. Using a similar model set-up to that used here, Chemel *et al.* [2009] found $\omega'/N_0 \approx 0.8$–0.9 at two locations a few hundred metres above the valley atmosphere, where N_0 is the Brunt-Väisälä frequency at $t = 0$. The sensitivity

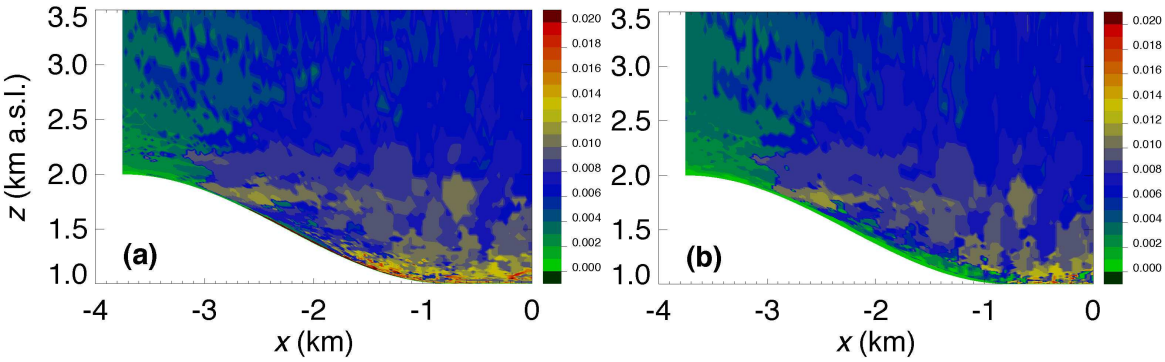

Figure C.2: Contour plots of ω' (in rad s^{-1}), the frequency with the largest amplitude in the spectrum of the time series, after $t = 60$ min, of **(a)** $\partial\theta_v/\partial t$ and **(b)** w, across an (x, z) slice taken half-way along y.

study by Largeron *et al.* [2013] extended the work by Chemel *et al.* [2009] and found $0.8 < \langle\omega'\rangle_y/N_0 < 0.9$ for a similar location above the valley atmosphere, where $\langle\rangle_y$ indicates an average across y. These results were found to correspond to IGWs radiated by any turbulent field with no dominant frequency component. For the model set-up used here, N is near-constant in space above 2.5 km a.s.l., for the full simulated period (not shown), resulting in $0.88 < \langle\omega'/N\rangle_{xz} \approx \langle\omega'\rangle_{xz}/\langle N\rangle_{xz} < 0.92$, with the ratio decreasing with t as N increases slightly. The averages were made across $-2.25 \leq x \leq 2.25$ km, $2.5 \leq z \leq 3.5$ km a.s.l., where the upper z limit was chosen to lie well below the Rayleigh damping layer at 8 km a.s.l. Largeron *et al.* [2013] also found the ratio to generally decrease with increasing N. Extending the x range to include the regions of lower ω' above the top of each slope, with $-3.75 \leq x \leq 3.75$ km, gives $0.80 < \langle\omega'/N\rangle_{xz} \approx \langle\omega'\rangle_{xz}/\langle N\rangle_{xz} < 0.835$. The two ranges of $\langle\omega'/N\rangle_{xz}$ correspond reasonably well with those reported by Chemel *et al.* [2009] and Largeron *et al.* [2013].

→ This appendix corresponds to a point in § III.3.1

D
Appendix

Resolved turbulent diffusion of heat

Figure D.1 shows the absolute magnitude of the wind field $|\langle \mathbf{u}_{xz} \rangle_y|$ (see Chapter IV for symbol definitions), at $t = 120$ and 180 min, corresponding to the times considered in Fig. IV.3 (§ IV.3.3.a). Figure D.1**(a)** shows a region of relatively large $|\langle \mathbf{u}_{xz} \rangle_y|$ between $z \approx 1.05$ and 1.2 km a.s.l, which corresponds very well to the relatively well-mixed region below the CI shown in Fig. IV.3**(a)**. Figure D.1**(b)** shows that by $t = 180$ min the region of relatively large $|\langle \mathbf{u}_{xz} \rangle_y|$ has moved to a higher altitude range (between $z \approx 1.2$ and 1.4 km a.s.l.), associated with the retreat of the maximum region of the downslope flows back up the valley slopes, causing the near-destruction of the CI by $t = 180$ min.

Figure D.2 shows contour plots of the time-rate of change of temperature due to resolved turbulent diffusion of heat (i.e., the Reynolds 'stress' term for the conservation of heat energy, $-\langle \mathbf{u}' \cdot \Delta\theta_v' \rangle_y$) at $t = 120$ and 180 min. Figure D.2**(a)** shows a region of relatively large $-\langle \mathbf{u}' \cdot \Delta\theta_v' \rangle_y$ below $z \approx 1.2$ km a.s.l, which corresponds very well to the relatively well-mixed region below the CI shown in Fig. IV.3**(a)**. Figure D.2**(b)** shows that the region of relatively large $-\langle \mathbf{u}' \cdot \Delta\theta_v' \rangle_y$, within about 200 m of the valley slope, has expanded further up the slope. This is essentially due to the expansion of the region of enhanced cooling which disrupts the downslope flows, repelling them back up the valley slopes, but is mixed and eroded as it does so.

Figure D.3 is the same as Fig. D.2 except for $t = 240$ and 480 min. Both figures show negligible mixing close to the ground surface in the entrainment region (above the region of enhanced cooling) but enhanced mixing within about 200 m from the slopes in the detrainment region within the region of enhanced cooling.

→ This appendix corresponds to points in § IV.3.3.a

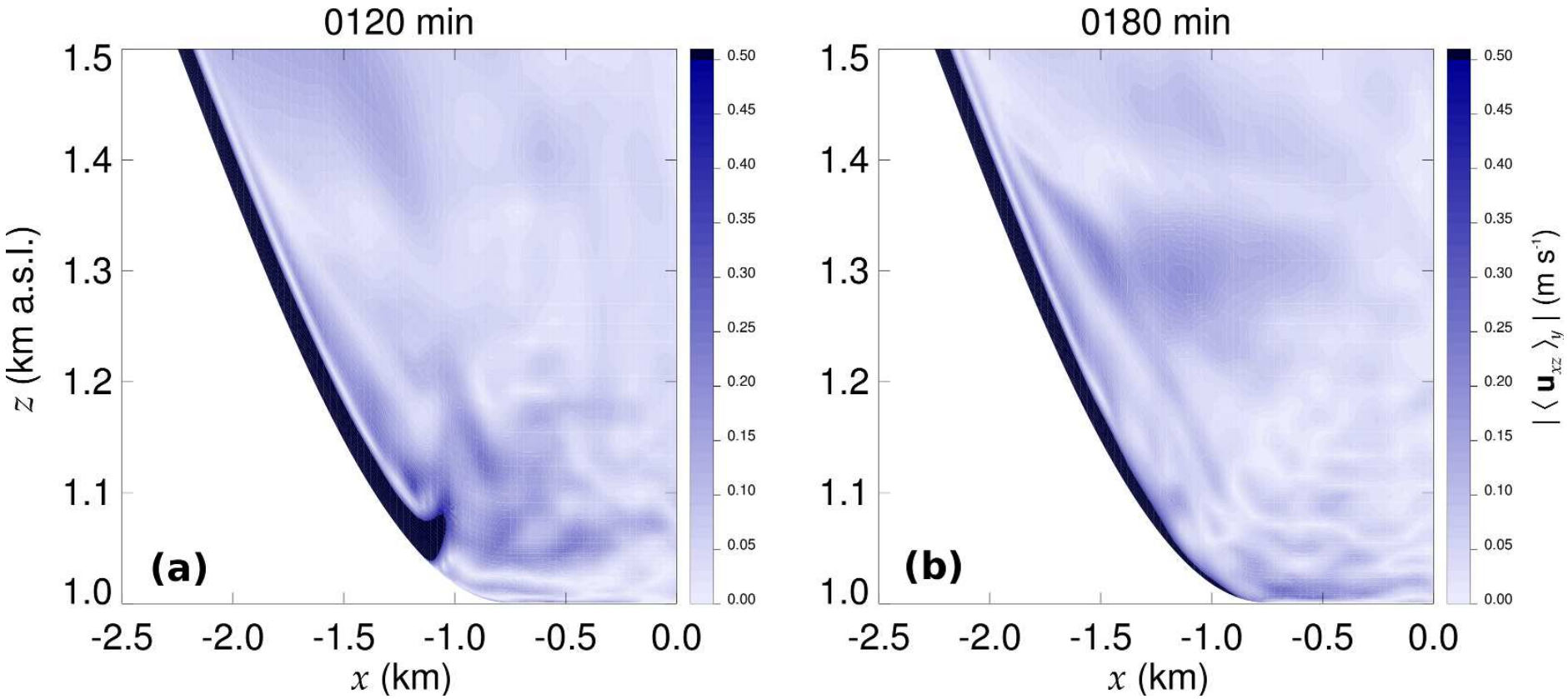

Figure D.1: Contour plots of the absolute magnitude of the wind field $|\langle \mathbf{u}_{xz} \rangle_y|$ at $t = 120$ min **(a)**, and $t = 180$ min **(b)**, see Chapter IV for symbol definitions.

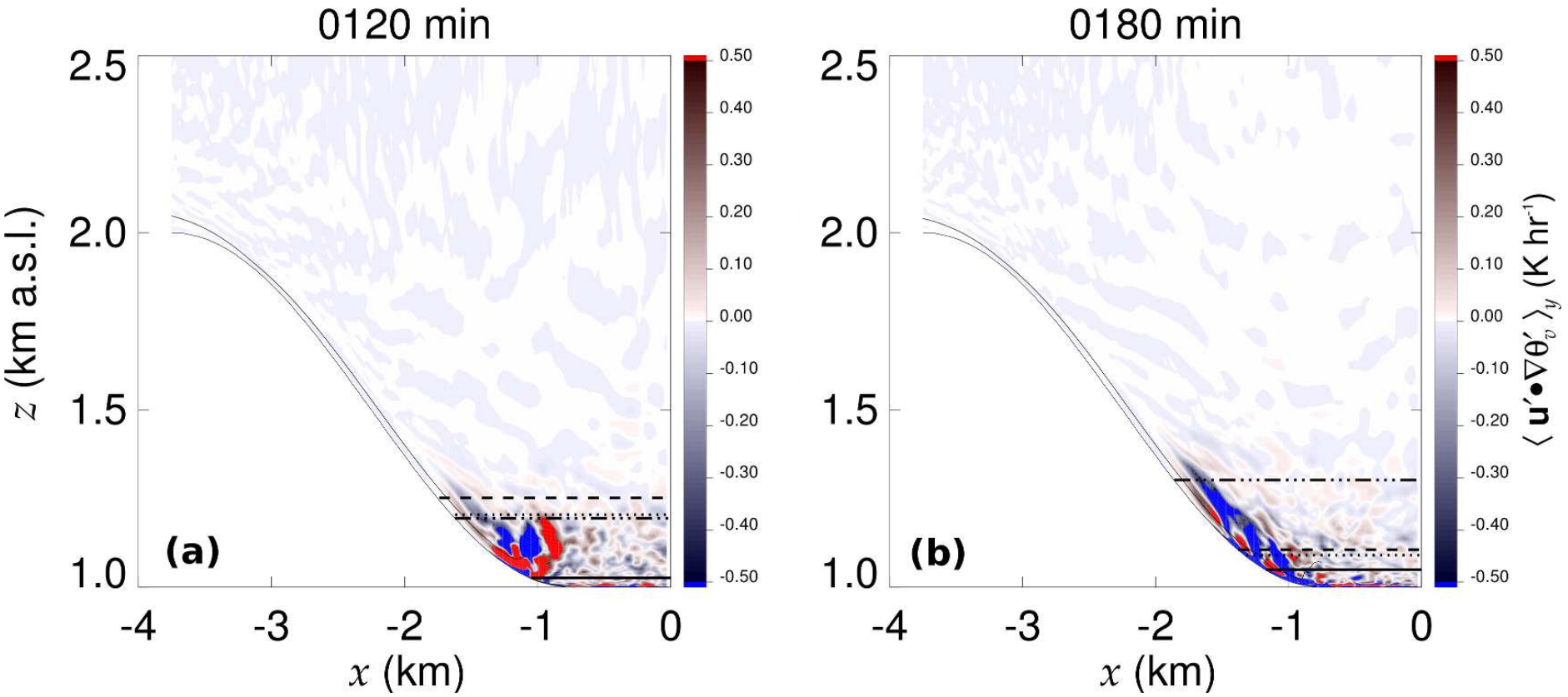

Figure D.2: Contour plots of the time-rate of change of temperature due to resolved turbulent diffusion of heat (i.e., the Reynolds 'stress' term for the conservation of energy, $-\langle \mathbf{u}' \cdot \Delta\theta_v' \rangle_y$) at $t = 120$ min **(a)**, and $t = 180$ min **(b)**. The horizontal solid, dashed, dotted and dash-dotted lines demark, respectively, the top height of the ground-based inversion z_{GBI}, the upper and lower boundaries of the capping inversion ($z_{CI\uparrow}$ and $z_{CI\downarrow}$), and the approximate height where the downslope flows are neutrally buoyant (i.e., $F_b \approx 0$). The curved line close to the western valley slope approximates the top height of the downslope flow layer along the slope (as defined in Chapter IV).

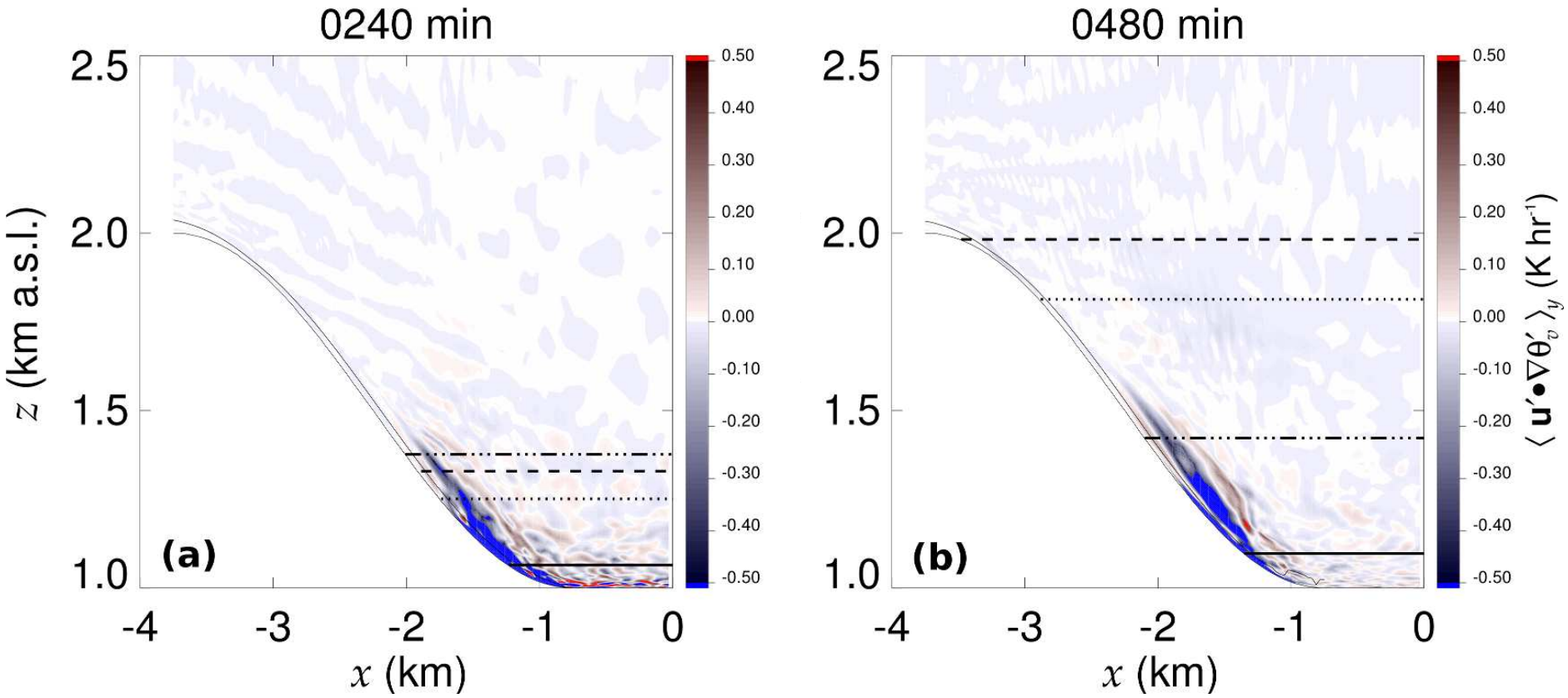

Figure D.3: Contour plots of the time-rate of change of temperature due to resolved turbulent diffusion of heat (i.e., the Reynolds 'stress' term for the conservation of energy, $-\langle \mathbf{u}' \cdot \Delta\theta_v' \rangle_y$) at $t = 240$ min **(a)**, and $t = 480$ min **(b)**. The horizontal solid, dashed, dotted and dash-dotted lines demark, respectively, the top height of the ground-based inversion z_{GBI}, the upper and lower boundaries of the capping inversion ($z_{CI\uparrow}$ and $z_{CI\downarrow}$), and the approximate height where the downslope flows are neutrally buoyant (i.e., $F_b \approx 0$). The curved line close to the western valley slope approximates the top height of the downslope flow layer along the slope (as defined in Chapter IV).

E

Appendix

Downslope flow profiles: a comparison between numerical and analytical solutions

Figure E.1**(a)** shows hourly profiles of the downslope flow speed u_s and virtual potential temperature perturbation from the ambient state θ'_v in (s, y, n, t) from the numerical solution at point S_5 (reproduced from Appendix A for convenience). S_5 is the western slope inflection point. In Figure E.1**(a)** the downslope flow is approximately 40-m deep with $u_{s,j} \approx 2$ m s^{-1} at $n_j \approx 6$ m, driven by $\theta'_v \approx 0.5$ K immediately adjacent to the slope.

Figure E.1**(b)** is a plot of the analytical model derived by Prandtl [1942] (reproduced here from § I.3.2 for convenience). The parameters used to create Fig. E.1**(b)** (reproduced in the caption) are appropriate for the downslope flow at point S_5. The values for ν_t and κ_t were taken from the numerical model vertical eddy viscosity fields for momentum and heat, respectively. The fields were averaged across the model y dimension and approximately across the depth of the downslope flow layer.

Whilst the flow profiles from the analytical model are roughly similar to those of the numerical model, there are some clear differences. In particular the downslope flow is approximately twice as deep and fast in the numerical model compared to the analytical solution. The first difference is likely to be caused by entrainment of air into the downslope flow, which is not accounted for in the analytical model that assumes a quasi-hydrostatic atmosphere. The vertical eddy viscosity fields for momentum and heat show generally increasing eddy viscosities from the ground surface throughout the downslope flow layer (not shown). This is likely to generate a deeper profile with a stronger cold-air jet closer to the ground (generally evident in the results). By modifying the model derived by Prandtl [1942] to include a gradually varying eddy diffusivity Grisogono & Oerlemans [2001] found a better representation of downslope flow depths observed and modelled over a gentle slope (0.1°). Furthermore, the analytical model of Prandtl [1942] assumes a balance between buoyancy and friction forces. However, it is shown in § IV.3.3.c that parcels of air at S_5 are accelerated for the first few hours

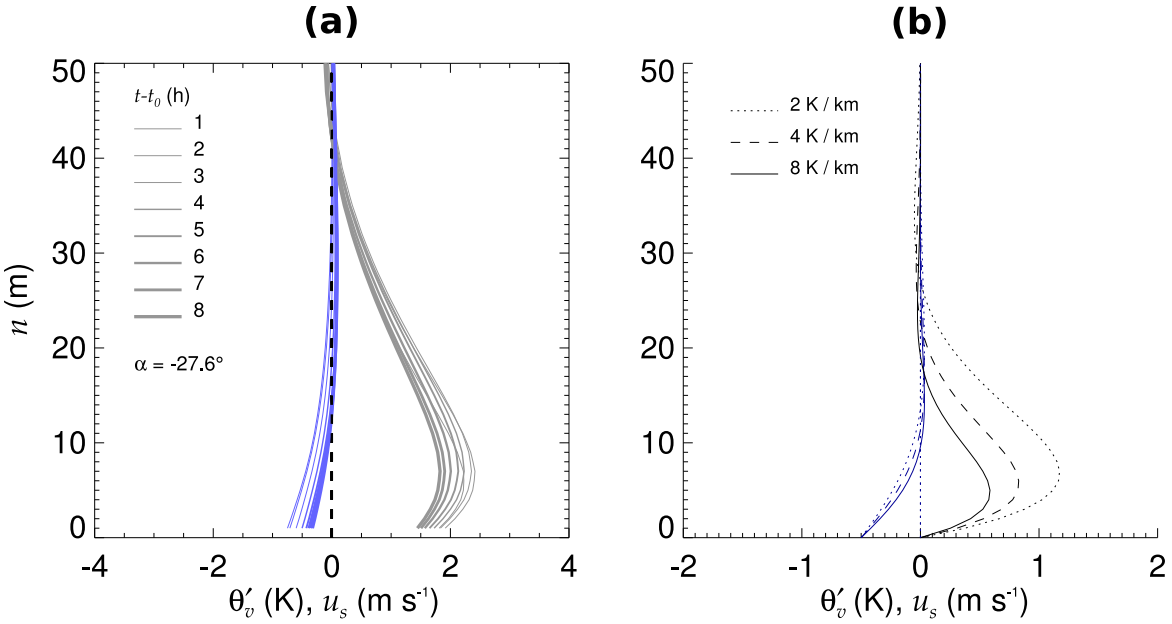

Figure E.1: Profiles of downslope flow speed and virtual potential temperature perturbation from the ambient state in a slope-orientated coordinate system (s, y, n); **(a)** hourly profiles from the numerical simulation performed for this study at point S_5, **(b)** profiles of stationary downslope flow speed and potential temperature perturbation from the analytical model of Prandtl [1942], for three ambient stratifications. The required constants were set as $A_2 = -0.5$ K, $\alpha = 27.6°$, $\theta_0 = 288$ K, $\delta z = 500$ m, $\nu_t = 0.08$ s^{-1}, and $\kappa_t = 0.25$ s^{-1}.

of simulation by buoyancy that is not fully countered by friction or pressure forces. It seems reasonable to suggest that a greater amount of kinetic energy close to the ground can be mixed to greater heights.

It is worth noting that θ'_v immediately adjacent to the slope, and n_j, are similar in the two models. n_j is generally slightly greater in the analytical model (disregarding the ambient stability of 8 K km^{-1}, which is not appropriate for S_5), which follows the arguments above.

It should be noted that part of the differences may exist due to the necessary limits placed on the numerical model grid resolution. Ideally the comparison should be confirmed by using a full LES code for the same domain as that used herein, however, this is at least approaching the limits of current computing platforms. For practical reasons it would be worth investigating the possibility of including only the near-slope region in a full LES simulation.

→ This appendix corresponds to points in § IV.3.3.c

List of tables

List of figures

List of symbols, acronyms and abbreviations

Roman symbols

(x, y, z, t)	Cartesian coordinate system
(s, y, n, t)	Slope-orientated linear-orthogonal coordinate system
$(\hat{x}, \hat{y}, \hat{z}, \hat{t})$	Curvilinear coordinate system
(u, v, w)	Velocity components in Cartesian coordinate system (m s^{-1})
(u_s,u_y,u_n)	Velocity components in slope orientated coordinate system. The components along s and n were derived from y-averaged fields, unless otherwise stated. Velocity components for a single y-point are denoted using a tilde superscipt, e.g. $\tilde{u_s}$, units (m s^{-1})
Δ, δ	Difference
$\Delta\, p_a$	Large-scale pressure change associated with the mountain-to-plain wind measured above the complex terrain atmosphere (Pa)
$\Delta\, x'$, $\Delta\, z'$	Cartesian grid resolution when interpolating WRF model output (m)
$\Delta\, z_{\Delta\, x}$	Change of height when moving between neighbouring x points (m)
$\Delta\, z_{s,\mathrm{min}}$	Minimum acceptable vertical-grid resolution adjacent to the ground according to Eq. (III.5)
$\Delta\, Z_s$	Height change made by slope (m)
$\Delta\, z_s$	Vertical grid resolution adjacent to the ground surface (m)
Δ_g	Effective grid size (m)
$\hat{H}$	Non-dimensional height

$\overline{\overline{\zeta}}$	A Tensor of order 2 and rank 1, known as a Dyad
∂T_r	Infinitesimal change of temperature due to net radiation (K)
A_0	Maximum amplitude of surface heat wave (K)
A_1	Maximum amplitude of velocity oscillation (m s^{-1})
A_2	Maximum temperature difference between near-slope air and ambient air (K)
A_v	Valley cross-sectional area (m)
c_1	Stretching coefficient (constant) for curvilinear coordinate
c_2	Parameter (constant) allowing for a range of grid cell distortions
c_3	Soil temperature when $z \to -\infty$, equivalent to $\langle T_0 \rangle$ (K)
c_4	Coefficient (constant) used to estimate top height of downslope flow layer
C_d	Turbulent exchange coefficient for momentum
C_h	Turbulent exchange coefficient for heat
$C_{i,1}$	Hourly-averaged concentration of passive pollutant P_i in model mass point adjacent to the ground surface (volume mixing ratio)
$C_{i,\mathrm{CAP}}$	Hourly-averaged concentration of passive pollutant P_i at the top height of the humid layer, a measure of the top height of the region of ehanced cooling, units (volume mixing ratio)
$C_{i,\mathrm{GBI}}$	Hourly-averaged concentration of passive pollutant P_i at the top height of the ground-based inversion layer (volume mixing ratio)
$C_{i,max}$	Maximum hourly-averaged concentration of passive pollutant P_i in model domain, which is almost constant over time (volume mixing ratio)
C_i	Concentration of passive pollutant P_i (volume mixing ratio). Note that C_i refers to a y-averaged value after § V.2
C_i'	Along-valley averaged deviation from constant background concentration of tracer (volume mixing ratio)
C_k	Constant in Deardorff [1980] subgrid-scale turbulent kinetic energy scheme, used in the WRF model

C_{p_d}	Heat capacity at constant pressure for dry air (J K^{-1})
c_{p_d}	Specific heat capacity at a constant pressure for dry air (J K^{-1} kg^{-1})
C_q	Turbulent exchange coefficient for moisture
C_{v_d}	Heat capacity at constant volume for dry air (J K^{-1})
$\text{CAPi}_{h,max}$	Cold-air pool intensity, computed by making a hydrostatic adjustment and using maximum and minimum air temperatures adjacent to the plateau and valley floor, respectively (K)
$\text{CAPi}_{h,mean}$	Cold-air pool intensity, computed by making a hydrostatic adjustment and averaging air temperatures, adjacent to the ground, over the plateau and valley floor (K)
CAPi	Cold-air pool intensity (K)
d	Damping depth used to initialise the WRF model soil temperature (m)
D_h	Thermal diffusivity of soil, set constant (m^2 s^{-1})
E	Downslope flow entrainment coefficient
e	Kinetic energy (J kg^{-1})
e_s	Saturated vapour pressure (Pa)
F	Froude number
f	A scalar function
$F\hat{H}$	Modified Froude number
F_θ	Diabatic sources and sinks of heat energy in Eq. (II.31) (kg K m^{-2} s^{-1})
F_{adv-n}	Advection force per unit mass along n (m s^{-2})
F_{adv-s}	Advection force per unit mass along s (m s^{-2})
F_{adv-v}	Advection force per unit mass along y (m s^{-2})
F_b	Buoyancy force per unit mass (m s^{-2})
f_c	Coriolis parameter (rad s^{-1})
F_{f_x}	Friction force per unit mass along x (m s^{-2})

F_f	Subgrid-scale diffusion (m s^{-2})
F_i	Components of layer-averaged downslope flow momentum balance per unit mass (for u_s), from the Eulerian perspective, using y-averaged fields, with $i = 1, \ldots, 5$, units (m s^{-2})
f_{max}	Maximum frequency of a signal after it has been bandlimited (s^{-1})
f_n	Discrete time series
F_p	Pressure force per unit mass (m s^{-2})
F_{r_a}	Flux of rainwater through a surface above the complex terrain atmosphere (kg m^{-2} s^{-1})
f_{rps}	Frequency (s^{-1})
F_{s_a}	Flux of snow mass through a surface above the complex terrain atmosphere (kg m^{-2} s^{-1})
f_s	A sampling frequency (s^{-1})
F_v	Vertical forces, per unit mass, excluding pressure and gravity (m s^{-2})
g	Magnitude of the acceleration due to gravity (m s^{-2})
g'	Reduced gravity (m s^{-2})
g_ω	Fourier transform of a discrete time series
H	Depth scale (m)
h	Ground surface height (m)
h_x	Change of terrain height along x (m)
h_y	Change of terrain height along y (m)
I	Index of average monthly synoptic conditions
$I_{\downarrow a}$	Irradiance downwelling through a surface above the complex terrain atmosphere (J s^{-1} m^{-2})
I_{GBI}	Strength (intensity) of ground-based temperature inversion (K)
k	Index for vertical coordinate, with $k = 1, \ldots, k_{max}$

K^*	Net shortwave radiation (W m^{-2})
K_H	Subgrid-scale eddy diffusivity for scalars (m^2 s^{-1})
K_M	Subgrid-scale eddy diffusivity for momentum (m^2 s^{-1})
k_t	Turbulent mixing coefficient (constant) in analytical model derived by McNider [1982a] (s^{-1})
L	Length scale (m)
l	Turbulence length scale (constant) in analytical model derived by Prandtl [1942] (m)
L, T, M, Θ	Dimensions of length, time, mass and temperature, respectively, represented as symbols, used to simplify the dimensional analysis in § I.4
L^*	Net longwave radiation (W m^{-2})
L_c	Local diabatic cooling rate (K s^{-1})
L_O	Obukhov length scale (m)
M	Molar mass of air (kg mol^{-1})
m_a	Mass below $z_{HL\downarrow}$ (a measure of the top height of the region of enhanced cooling) at some t (kg)
m_b	Accumulation of mass over time below $z_{HL\downarrow}$ (a measure of the top height of the region of enhanced cooling) from downslope flows (kg)
M_d	Molecular weight of dry air (kg mol^{-1})
M_s	Surface moisture (volume fraction)
M_w	Molecular weight of water (kg mol^{-1})
N	Buoyancy (or Brunt-Väisälä) frequency (rad s^{-1})
N_0	Buoyancy frequency at $t = 0$ (rad s^{-1})
N_a	Number of anticyclonic days in a month
N_c	Number of cyclonic days in a month
n_{df}	Distance from slope to top height of downslope flow layer along n (m)

n_j	Distance from slope to cold-air jet wind maximum along n (m)
N_p	Number of points in discrete time series
p	Pressure (Pa)
p'	Perturbation pressure, computed from y-averaged fields and after averaging the full pressure field across the valley floor (Pa)
p_0	Arbitrary pressure of 1000 hPa corresponding to mean sea level
p_{h_s}	Dry-hydrostatic pressure at ground surface (Pa)
p_{h_t}	Constant dry-hydrostatic pressure at domain top (Pa)
p_h	Dry-hydrostatic pressure (Pa)
P_i	Notation used in Chapter V to refer to different passive pollutants, or tracers, where the subscript refers to the emission region adjacent to the ground, with $i = 1, \ldots, 12$
P_j, S_{jj}, F_{jjj}	Points along x used for further analysis in Chapter IV; on the western plateau (P_j), slope (S_{jj}) and valley floor (F_{jjj}), with $j = 1, \ldots, 3$, $jj = 1, \ldots, 9$ and $jjj = 1, \ldots, 3$. Point intervals are equal within each sub-section of the terrain (i.e. P, S and F)
$\mathrm{PM}_{2.5}$	Particulate matter with a diameter less than 2.5 μm (μg m^{-3})
Pr_e	Subgrid-scale Prandtl number
Q_E	Flux of latent heat energy at the ground surface (W m^{-2})
Q_G	Flux of ground heat energy (W m^{-2})
Q_H	Flux of sensible heat energy at the ground surface (W m^{-2})
Q_i	Source emission rate of passive pollutant P_i (s^{-1}), except in Fig. V.2, where it refers to the components of the surface energy budget (W m^{-2})
ΔQ_S	Ground heat storage (W m^{-2})
q_{v_s}	Saturated water vapour mass-mixing ratio (kg kg^{-1})
q_v	Water vapour mass-mixing ratio (kg kg^{-1})

R	Rate of change of virtual potential temperature with respect to time (K s^{-1})
R_2	Rate of change of virtual potential temperature over time, excluding region of domain within 100 m of the slopes (K s^{-1})
R_D	Gas constant for a dry-air mix (J K^{-1} kg^{-1})
R_d	Rate of change of virtual potential temperature, over time, due to dynamics effects (K s^{-1})
R_i	Constant emission rate of passive pollutant P_i over surface area S_i (mol s^{-1} m^{-2})
R_{LW}	Rate of change of virtual potential temperature, over time, due to longwave radiation (K s^{-1})
R_n	Net radiation (W m^{-2})
R_r	Rate of change of virtual potential temperature, over time, due to net radiation (K s^{-1})
R_{SW}	Rate of change of virtual potential temperature, over time, due to shortwave radiation (K s^{-1})
RH	Relative Humidity (%)
Ro	Rossby number
S_i	Surface area of emission region for passive pollutant P_i (m^2)
S_x	x-dimension slope length (m)
S_y	y-dimension slope length (m)
T	Temperature (K)
t	Time (s)
T_0	Ground surface temperature (K)
T_2	2-m air temperature (K)
T_{deep}	Land-surface model deep-soil temperature (K)
T_d	Dew-point temperature (K)
T_{sgs}	Subgrid-scale temperature, either a surface temperature or the average temperature of a depression atmosphere (K)

U	Velocity scale (m s^{-1})
$\mathbf{u_a}$	Ambient wind (m s^{-1})
$u_{s,j}$	Notation used in Chapter IV for the maximum cold-air jet speed. The notation $u_{s,max}$ is used in Chapter V, units (m s^{-1})
V_a	Volume of air below $z_{HL\downarrow}$ (a measure of the top height of the region of enhanced cooling) at some t (m^3)
V_b	Volume of air that accumulates over time below $z_{HL\downarrow}$ (a measure of the top height of the region of enhanced cooling) from the downslope flows (m^3)
V_i	Physical volumes in complex terrain atmosphere, with $i = 1, \ldots, 6$
V_x	Half-width of valley floor (m)
W_v	Valley width (m)
x_j	Sequence of N elements, each a function of u_m, with $m = 1, \ldots, M$
z_{0h}	Thermal roughness length (m)
z_0	Aerodynamic roughness length (m)
$z_{CI\downarrow}$	Height of lower edge of capping inversion (m a.s.l.)
$z_{CI\uparrow}$	Height of upper edge of capping inversion (m a.s.l.)
z_{GBI}	Height of top height of ground-based temperature inversion (m a.s.l.)
$z_{HL\downarrow}$	Height of lower edge of humid layer (m a.s.l.)
$z_{HL\uparrow}$	Height of upper edge of humid layer (m a.s.l.). Note that this height is referred to as z_{CAP} in Chapter V, used to estimate the top height of the region of enhanced cooling
z_{ref}	Valley floor height (m)
$z_{UML\downarrow}$	Height of lower edge of upper-mixed layer (m a.s.l.)
$z_{UML\uparrow}$	Height of upper edge of upper-mixed layer (m a.s.l.)
$z_{USL\uparrow}$	Height of upper edge of upper-stable layer (m a.s.l.)
$\mathbf{F}$	Forces, per unit mass, excluding pressure and gravity (m s^{-2})

$\mathbf{f}$	A vector function
$\mathbf{F}_h$	Horizontal forces, per unit mass, excluding pressure and gravity (m s^{-2})
$\mathbf{k}_{xz}$	Wave vector in (x,z) plane (rad m^{-1})
$\mathbf{n}$	Normal unit vector
$\mathbf{r}$	Position vector
$\mathbf{u}$	Velocity (m s^{-1})
$\mathbf{u}_{xz}$	Wind velocity in (x,z) plane (m s^{-1})
$\mathbf{e}_x$, $\mathbf{e}_y$, $\mathbf{e}_z$	Unit (basis) vectors for Cartesian coordinate system

Greek symbols

θ	Potential temperature (K)
α	Slope angle (rad)
α_{ρ_d}	Inverse density for dry air (m^3 kg^{-1})
α_ρ	Inverse density (m^3 kg^{-1})
α_r	Albedo
β	Parameter (constant) used to damp vertically propagating sound waves in the WRF model
$\Delta\,\theta_{v_d}$	Change in virtual potential temperature due to dynamics effects (K)
$\Delta\,\theta_{v_{LW}}$	Change in virtual potential temperature due to longwave radiation (K)
$\Delta\,\theta_{v_r}$	Change in virtual potential temperature due to net radiation (K)
$\Delta\,\theta_{v_{SW}}$	Change in virtual potential temperature by shortwave radiation (K)
$\dot{\eta}$	Terrain-following hydrostatic-pressure coordinate velocity component (m s^{-1})
$\dot{\pi}$	Hydrostatic-pressure coordinate velocity component (m s^{-1})

ϵ	Ratio of molecular weights of water and dry air
ϵ_r	Emissivity
η	Terrain-following hydrostatic-pressure coordinate
Γ	Atmospheric lapse rate (K m^{-1})
γ	Atmospheric stability (K m^{-1})
γ_0	Initial lapse rate in virtual potential temperature in WRF model (K m^{-1})
Γ_d	Dry adiabatic lapse rate (K m^{-1})
κ	Eddy diffusivity for heat and mass (m^2 s^{-1})
κ_t	Turbulent mixing coefficient for heat (m^3 s^{-2} K^{-1})
μ	Mass of fluid in column of atmosphere per unit area (kg m^{-2})
ν	Kinematic viscosity (m^2 s^{-1})
ν_t	Turbulent eddy viscosity (m^2 s^{-1})
ω	Angular frequency (rad s^{-1})
ω'	Angular frequency with largest amplitude in the spectrum of a time series (rad s^{-1})
Ω	Earth's angular speed (rad s^{-1})
ω_d	Damped oscillation frequency (rad s^{-1})
Ω_v	Vertical component of Earth's angular speed (rad s^{-1})
Φ	Latitude (rad)
ϕ	Gravitational potential (m^2 s^{-2})
π	Hydrostatic-pressure coordinate (Pa)
ρ	Density (kg m^{-3})
ρ'	Perturbation density from constant reference value (kg m^{-3})
ρ_r	Constant reference density (kg m^{-3})

τ_{sj}	Subgrid-scale stress tensor expressed using summation notation, where the index $j = \{s, n\}$, with $X_s \equiv s$, and $X_n \equiv n$, with units (m^2 s^{-2})
θ'	Potential temperature perturbation from ambient state (K)
θ_0	Constant reference temperature (K)
θ_a	Ambient/base-state potential temperature (K)
θ_{v_a}	Ambient virtual potential temperature, computed by averaging across valley floor (K)
θ_v	Virtual potential temperature (K)
θ'_v	Perturbation from ambient virtual potential temperature field (using y-averaged fields), except where it appears in the Reynolds stress term where it denotes a perturbation from the y-averaged field (K)
φ	Constant phase shift in analytical model derived by McNider [1982a] (rad)
ς	Ratio of heat capacities for constant pressure and constant volume for dry air
ζ	Any variable

Operators

$\left(\frac{\partial \zeta}{\partial \zeta}\right)_\zeta$	Partial differentiation with constant variable stated (same form for d/d)
$\approx$	Approximately equal to
$\overline{\zeta}$	Layer-averaged quantity
$\langle\zeta\rangle$	Mean quantity
$\langle\zeta\rangle_{\mathrm{f}}$	Average across the valley floor
$\langle\zeta\rangle_n$	Average along n, across the downslope flow layer
$\langle\zeta\rangle_{va}$	Average made across full valley space
$\langle\zeta\rangle_{vs,min}$	Minimum $\langle\zeta\rangle_{vs}$ in domain (similar notation for the maximum case)

$\langle\zeta\rangle_{vs}$	Average made across (x,z) at some y
$\langle\zeta\rangle_V$	Volume average across any of the volumes V_i defined in Chapter IV, with $i = 1, \ldots, 6$. Note that $\langle\zeta\rangle_{V_1}$ and $\langle\zeta\rangle_{V_2}$ are equivalent to $\langle\zeta\rangle_{\mathrm{GBI}}$ and $\langle\zeta\rangle_{\mathrm{CAP}}$, respectively, where the latter two notations are used in Chapter V
$\langle\zeta\rangle_{xy}$	Average across (x,y) plane
$\langle\zeta\rangle_y$	Average across y dimension
$\mathcal{O}$	On the order of
$\mid \zeta \mid$	Absolute magnitude
∇	Gradient
∇^2	Laplacian
∇_η	Gradient using terrain-following hydrostatic-pressure coordinate
∇_π	Gradient using hydrostatic-pressure coordinate
∇_{xz}	(x,z) part of ∇
$\sum$	Summation
$\cdot$	Scalar product
$\times$	Cross product
$\otimes$	Tensorial (dyadic) product
$\rightarrow$	Tending to
d	Total differential
d/d	Material derivative
∂/∂	Partial derivative
$\max(\zeta)$	Time series of heights of the maximum value of different downslope flow characteristics
$S(\ )$	Spectrum of a time series

Acronyms and abbreviations

1D	One dimension(al)

2D	two dimensions/two dimensional
3D	Three dimensions/three dimensional
a.g.l.	above ground level
a.m.s.l.	above mean sea level
AFWA	Air Force Weather Agency
ARPS	Advanced Regional Prediction System
ARW	Advanced Research WRF
ASCOT	Atmospheric Studies in Complex Terrain
CAJ	Cold-air jet
CAP_h	Region of enhanced cooling, where subscript h refers to a hydrostatic adjustment
CAP	Cold-air pool
CAPS	Center for Analysis and Prediction of Storms
CFD	Computational fluid dynamics
CI	Capping inversion
COLPEX	Cold-Air Pooling Experiment
ESRL	Earth System Research Laboratory
EUMETSAT	European Organisation for the Exploitation of Meteorological Satellites
FAA	Federal Aviation Administration
FFT	Fast Fourier transform
GBI	Ground-based temperature inversion
GCM	Global climate model
HL	Humid layer
HPC	High-performance computing
IBM	Immersed-boundary method

IGW	Internal gravity wave
KH	Kelvin-Helmholtz
LES	Large-eddy simulation
LIDAR	Light detection and ranging
LSM	Land surface model
LST	Local standard time
MMM	Mesoscale and Microscale Meteorology
MYSTIC	Monte Carlo code for the physically correct tracing of photons in cloudy atmospheres
NCAR	National Centre for Atmospheric Research
NCEP	National Center for Environmental Prediction
NMM	Non-hydrostatic Mesoscale Model
NOAA	National Oceanic and Atmospheric Administration
NRL	Naval Research Laboratory
NSSL	National Severe Storms Laboratory
NWP	Numerical weather prediction
POVA	POllution in Alpine Valleys
RADAR	Radar detection and ranging
RANS	Reynolds-averaged Navier-Stokes
RHS	Right-hand side
RRTM	Rapid Radiation Transfer Model
SABLES	Stable Atmospheric Boundary-Layer Experiment in Spain
SELF	Slope Experiment near La Fouly
SGS	Subgrid-scale
SODAR	Sonic detection and ranging
TAF	Topographic amplification factor

UML	Humid layer
USGS	United States Geological Survey
USL	Upper stable layer
UTC	Coordinated Universal Time
VTMX	Vertical Transport and Mixing Experiment
WENO	Weighted Essentially Non-Oscillatory
WRF	Weather Research and Forecasting
WVS	Winter Visibility Study

Definitions

Microscale	Length scales of the order of 1 km or less
Sub-mesoscale	Length scales of the order of 1 to 10 km
Mesoscale	Length scales of the order of 10 to 100 km
Synoptic scale	Length scales of the order of 1000 km

List of references

Acevedo, O.C. & Fitzjarrald, D.R. (2001). The early evening surface-layer transition: Temporal and spatial variability. *J. Atmos. Sci.*, **58**, 2650–2667. III.5, IV.3.3.a

Anquetin, S., Guilbaud, C. & Chollet, J.P. (1998). The formation and destruction of inversion layers within a deep valley. *J. Appl. Meteorol.*, **37**, 1547–1560. III.1

Anquetin, S., Guilbaud, C. & Chollet, J.P. (1999). Thermal valley inversion impact on the dispersion of a passive pollutant in a complex mountainous area. *Atmos. Environ.*, **33**, 3953–3959. I.1, III.1, IV.1

Baines, P.G. (2005). Mixing regimes for the flow of dense fluid down slopes into stratified environments. *J. Fluid Mech.*, **538**, 245–267. V.3.1

Baines, P.G. (2008). Mixing in downslope flows in the ocean-plumes versus gravity currents. *Atmos. Ocean*, **46**, 405–419. I.2.1.b, IV.3.3.a, IV.4, VI

Baker, K.R., Simon, H. & Kelly, J.T. (2011). Challenges to modeling "cold pool" meteorology associated with high pollution episodes. *Environ. Sci. Technol.*, **45**, 7118–7119. V.1

Banta, R.M., Shun, C.M., Law, D.C., Brown, W., Reinking, R.F., Hardesty, R.M., Senff, C.J., Brewer, W.A., Post, M.J. & Darby, L.S. (2013). Observational techniques: Sampling the mountain atmosphere. In F.F. Chow, S.F.J. De Wekker & B.J. Snyder, eds., *Mountain Weather Research and Forecasting: Recent Progress and Current Challenges*, Springer Atmospheric Sciences, chap. 8, Springer, New York, NY, USA. I.2, I.3

Beelen, R., Hoek, G., van den Brandt, P.A., Goldbohm, R.A., Fischer, P., Schouten, L.J., Jerrett, M., Hughes, E., Armstrong, B. & Brunekreef, B. (2008). Long-term effects of traffic-related air pollution on mortality in a Dutch cohort (NLCS-AIR Study). *Environmental Health Perspectives*, **116(2)**, 196–202. I.1

Belcher, S.E., Harman, I.N. & Finnigan, J.J. (2012). The Wind in the Willows: Flows in Forest Canopies in Complex Terrain. *Ann. Rev. Fluid Mech.*, **44**, 479–504. I.2.3.d

Blyth, S., Groombridge, B., Lysenko, I., Miles, L. & Newton, A. (2002). Mountain Watch: Environmental change and sustainable development in mountains. I.1, I.2.3.d, IV.1

Briggs, G.A. (1981). Canopy effects on predicted drainage flow characteristics and comparison with observations. In *Proc. of the Fifth AMS Symposium on Turbulence and Diffusion, Atlanta, GA, USA*, 113–115, American Meteorological Society, Boston, MA, USA. V.3.1

Brulfert, C., Chemel, C., Chaxel, E. & Chollet, J.P. (2005). Modelling photochemistry in alpine valleys. *Atmos. Chem. Phys.*, **5**, 2341–2355. I.1, I.1, I.2.3.c, I.4, III.1, III.3, IV.1, V.2, E

Buckingham, E. (1914). On physically similar systems; illustrations of the use of dimensional equations. *Phys. Rev.*, **4**, 345–376. I.4

Burkholder, B.A., Shapiro, A. & Fedorovich, E. (2009). Katabatic flow induced by a cross-slope band of surface cooling. *Acta Geophys.*, **57**, 923–949. V.3.1

Burns, P. & Chemel, C. (2014a). Evolution of cold-air-pooling processes in complex terrain. *Boundary-Layer Meteorol.*, **150**, 423–447. III, IV.1, IV.2, IV.3.1, IV.3.2, IV.3.3.a, IV.3, IV.3.3.a, IV.3.4, IV.3.4, V.1, V.2, V.2, V.2, V.4, E

Burns, P. & Chemel, C. (2014b). Interactions between downslope flows and a developing cold-air pool. *Boundary-Layer Meteorol.*, in press. III.6, IV, V.1, V.3.1, V.3.1, V.3.2, V.3.2, V.3.2, V.4

Businger, J.A. (1973). Turbulent transfer in the atmospheric surface layer. In D.A. Haugen, ed., *Proc. of the Workshop on Micrometeorology, Boston, MA, USA*, 67–100, American Meteorological Society, Boston, MA, USA. V.3.1

Catalano, F. & Cenedese, A. (2010). High-resolution numerical modeling of thermally driven slope winds in a valley with strong capping. *J. Appl. Meteorol. Climatol.*, **49**, 1859–1880. I.2.3.a, III.1, III.2.1, IV.1, IV.2, IV.3.2

Chazette, P., Couvert, P., Randriamiarisoa, H., Sanak, J., Bonsang, B., Moral, P., Berthier, S., Salanave, S. & Toussaint, F. (2005). Three-dimensional survey of pollution during winter in French Alps valleys. *Atm. Environ.*, **39**, 1035–1047. I, I.1, I.1, I.2.3.a, I.2.3.b, I.2.3.c, I.4, III.1, III.5, IV.1, IV.5, V.1

Chemel, C. & Burns, P. (2014). Pollutant Dispersion in a Developing Valley Cold-Air Pool. *Boundary-Layer Meteorol.*, in press. IV.1, IV.6, V

Chemel, C. & Chollet, J.P. (2006). Observations of the daytime boundary layer in deep alpine valleys. *Boundary-Layer Meteorol.*, **119**, 239–262. I.1, I.2.3.a, I.2.3.c, I.4, I.4, IV.4, IV.5, VI, E

Chemel, C., Staquet, C. & Largeron, Y. (2009). Generation of internal gravity waves by a katabatic wind in an idealized alpine valley. *Meteorol. Atmos. Phys.*, **103**, 187–194. III.3.2.a, III.4, C

Chen, F. & Dudhia, J. (2001). Coupling an advanced land-surface/hydrology model with the Penn State/NCAR MM5 modeling system. Part I: model implementation and sensitivity. *Mon. Weather. Rev.*, **129**, 569–585. III.2.1, III.2.4, IV.2, V.2

Chen, F. & Zhang, Y. (2009). On the coupling strength between the land surface and the atmosphere: From viewpoint of surface exchange coefficients. *Geophys. Res. Lett.*, **36**, L10404. III.2.1

Cheng, Y. & Brutsaert, W. (2005). Flux-profile relationships for wind speed and temperature in the stable atmospheric boundary layer. *Boundary-Layer Meteorol.*, **114**, 519–538. III.2.1

Cuxart, J. & Jiménez, M.A. (2007). Mixing processes in a nocturnal low-level jet: an LES study. *J. Atmos. Sci.*, **64**, 1666–1679. V.1, V.3.1, V.4, VI

Cuxart, J. & Jiménez, M.A. (2012). Deep radiation fog in a wide closed valley: study by numerical modeling and remote sensing. *Pure Appl. Geophys.*, **169**, 911–926. I.1, I.2.3.c, V.2

Cuxart, J., Yagüe, C., Morales, G., Terradellas, E., Orbe, J., Calvo, J., Fernandez, A., Soler, M.R., Infante, C., Buenestado, P., Espinalt, A., Joergensen, H.E., Rees, J.M., Vila, J., Redondo, J.M., Cantalapiedra, I. & Conangla, L. (2000). Stable atmospheric boundary-layer experiment in Spain (SABLES 98): a report. *Boundary-Layer Meteorol.*, **96**, 337–370. I.2.1.a, V.3.1

Cuxart, J., Jimenez, M.A. & Martineze, D. (2007). Nocturnal meso-beta basin and katabatic flows on a midlatitude island. *Mon. Weather. Rev.*, **135**, 918–932. V.3.1, VI

Dai, A., Wang, J., Ware, R.H. & Hove, T.V. (2002). Diurnal variation in water vapor over North America and its implications for sampling errors in radiosonde humidity. *J. Geophys. Res.*, **107**, 1–14. I.1, I.2.3.c

Daly, C., Smith, J.W., Smith, J.I. & McKane, R.B. (2007). High-Resolution Spatial Modeling of Daily Weather Elements for a Catchment in the Oregon Cascade Mountains, United States. *J. Appl. Meteorol. Climatol.*, **46**, 1565–1586. I.2.3.a

Daly, C., Conklin, D.R. & Unsworth, M.H. (2009). Local atmospheric decoupling in complex topography alters climate change impacts. *Int. J. Climatol.*, **30**, 1857–1864. I.1, I.1, I.2.2, I.2.3.a, III.1, IV.1, IV.5

de Franceschi, M. & Zardi, D. (2009). Study of wintertime high pollution episodes during the Brenner-South ALPNAP measurement campaign. *Meteorol. Atmos. Phys.*, **103**, 237–250. V.1

Deardorff, J.W. (1980). Stratocumulus-capped mixed layers derived from a three-dimensional model. *Boundary-Layer Meteorol.*, **18**, 495–527. III.2.1, IV.2, V.2, E

Defant, F. (1949). Zur theorie der Hangwinde, nebst Bemerkungen zur Theorie der Bergund Talwinde. *Arch. Meteor. Geophys. Bioklim.*, 421–450, [English translation: Whiteman, C. D. and Dreiseitl, E.: 1984, 'Alpine Meteorology: Translations of Classic Contributions by A. Wagner, E. Ekhart and F. Defant'. Technical Note PNL-5141/ASCOT-84-3, PNL, Richland, WA, USA, pp. 95–121]. I.1, E

Defant, F. (1951). Local winds. In T.M. Malone, ed., *Compendium of Meteorology*, 655–672, American Meteorological Society, 45 Beacon St., Boston, MA, USA. I.1, E

Doran, J.C. & Horst, T.W. (1981). Velocity and temperature oscillations in drainage winds. *J. Appl. Meteorol.*, **20**, 361–364. I.1, I.2.1.a

Doran, J.C. & Horst, T.W. (1983). Observations and models of simple nocturnal slope flows. *J. Atmos. Sci.*, **40**, 708–717. I.1, I.2.1.a, I.2.1.b, I.2.3.e, I.3.1, III.2.1, A

Doran, J.C., Fast, J.D. & Horel, J. (2002). The VTMX 2000 campaign. *B. Am. Meteorol. Soc.*, **83**, 537–554. I.2.1.a

Dorninger, M., Whiteman, C.D., Bica, B., Eisenbach, S., Pospichal, B. & Steinacker, R. (2011). Meteorological events affecting cold-air pools in a small basin. *J. Appl. Meteorol. Climatol.*, **50**, 2223–2234. V.1

Droulia, F., Lykoudis, S., Tsiros, I., Alvertos, N., Akylas, E. & Garofalakis, I. (2009). Ground temperature estimations using simplified analytical and semi-analytical approaches. *Solar Energy*, **83**, 211–219. III.2.4

Dudhia, J. (1989). Numerical study of convection observed during the winter monsoon experiment using a mesoscale two-dimensional model. *J. Atmos. Sci.*, **46**, 3077–3107. III.2.1, IV.2

Dudhia, J. (1995). Reply. *Mon. Weather. Rev.*, **123**, 2573–2575. III.2.3, IV.2, V.2

Eckman, R.M. (1997). Observations and numerical simulations of winds within a broad forested valley. *J. Appl. Meteorol.*, **37**, 206–219. I, I.1, I.2.1.a, I.2.3.e

Ellison, T.H. & Turner, J.S. (1959). Turbulent entrainment in stratified flows. *J. Fluid Mech.*, **6**, 423–488. V.3.1

Fairall, C.W., Bradley, E.F., Rogers, D.P., Edson, J.B. & Young, G.S. (1996). Bulk parameterization of air-sea fluxes for Tropical Ocean Global Atmosphere Coupled-Ocean Atmosphere Response Experiment. *J. Geophys. Res.*, **101**, 3747–3764. III.2.1

Fleagle, R.G. (1950). A theory of air drainage. *J. Meteor.*, **7**, 227–232. I, I.3, I.3.1

Forbes, R.M. & Hogan, R.J. (2005). Observations of the depth of ice particle evaporation beneath frontal cloud to improve NWP modelling. *Q. J. R. Meteorol. Soc.*, **132**, 865–883. I.1, I.2.3.c

Gohm, A., Harnisch, F., Vergeiner, J., Obleitner, F., Schnitzhofer, R., Hansel, A., Fix, A., Neininger, B., Emeis, S. & Schäfer, K. (2009). Air pollution transport in an alpine valley: results from airborne and ground-based observations. *Boundary-Layer Meteorol.*, **131**, 441–463. I.1, I.2.3.a, IV.5, V.3.2, V.4, VI

Green, F.H.W. & Harding, R.J. (1979). The effects of altitude on soil temperature. *Meteorol. Mag.*, **108**, 81–91. III.2.4

Green, F.H.W. & Harding, R.J. (1980). Altitudinal gradients of soil temperatures in Europe. *Trans. Inst. Br. Geogr.*, **5**, 243–254. III.2.4

Grisogono, B. & Oerlemans, J. (2001). Katabatic flow: analytic solution for gradually varying eddy diffusivities. I.3.2, VI, E

Grisogono, B., Kraljevic, L. & Jericevic, A. (2007). The low-level katabatic jet height versus Monin-Obukhov height. *Q. J. Roy. Meteorol. Soc.*, **133**, 2133–2136. III.2.1

Gryning, S.E., Mahrt, L. & Larsen, S. (1985). Oscillating nocturnal slope flow in a coastal valley. *Tellus*, **37A**, 196–203. I.1, I.2.3.e

Guardans, R. & Palomino, I. (1995). Description of Wind Field Dynamic Patterns in a Valley and Their Relation to Mesoscale and Synoptic-Scale Meteorological Situations. *J. Appl. Meteorol.*, **34**, 49–67. I.1, I.2.2

Gudiksen, P.H., Leone, J.M., King, C.W., Ruffieux, D. & Neff, W.D. (1992). Measurements and Modeling of the Effects of Ambient Meteorology on Nocturnal Drainage Flows. *J. Appl. Meteorol.*, **31**. I.1, I.2.1.a, I.2.3.e

Gustavsson, T., Karlsson, M., Bogren, J. & Lindqvist, S. (1998). Development of temperature patterns during clear nights. *J. Appl. Meteorol.*, **37**, 559–571. I, I.1, I.2.1.a, I.2.1.b, I.2.3.c, I.4, III.1, IV.1

Haiden, T., Whiteman, C.D., Hoch, S.W. & Lehner, M. (2011). A Mass Flux Model of Nocturnal Cold-Air Intrusions into a Closed Basin. *J. Appl. Meteorol. Climatol.*, **50**, 933–943. I.1, I.2.3.c, I.4, V.1

Harnisch, F., Gohm, A., Fix, A., Schnitzhofer, R., Hansel, A. & Neininger, B. (2009). Spatial distribution of aerosols in the Inn Valley atmosphere during wintertime. *Meteorol. Atmos. Phys.*, **103**, 223–235. V.1, V.3.2, V.4, VI

Heinemann, G. (2002). Aircraft-based measurements of turbulence structure in the katabatic flow over Greenland. *Boundary-Layer Meteorol.*, **103**, 49–81. I.1, I.2.1.b

Helmis, C.G. & Papadopoulos, K.H. (1996). Some aspects of the variation with time of katabatic flow over simple slope. *Q. J. R. Meteorol. Soc.*, **122**, 595–610. I.1, I.2.1.a, I.2.1.b, III.2.1, A

Hillel, D. (1982). *Introduction to Soil Physics*. Academic Press, New York, NY, USA, 364 pp. III.2.4

Hoch, S.W., Whiteman, D.C. & Mayer, B. (2011a). A systematic study of longwave radiative heating and cooling within valleys and basins using a three-dimensional radiative transfer model. *J. Appl. Meteorol. Climatol.*, **50**, 2473–2489. I.1, I.2.1.b, I.4, IV.3.3.b, IV.3.4, V.2

Hoch, S.W., Whiteman, D.C. & Mayer, B. (2011b). A systematic study of longwave radiative heating and cooling within valleys and basins using a three-dimensional radiative transfer model. *J. Appl. Meteorol. Climatol.*, **50**, 2473–2489. III.1, III.3.1.b, III.3.2.b, III.4

Holton, J.R. (2004). *An Introduction to Dynamic Meteorology*. Elsevier Academic Press. I.2.1.b, I.3, IV.3.3.c

Iacono, M.J., Delamere, J.S., Mlawer, E.J., Shephard, M.W., Clough, S.A. & Collins, W.D. (2008). Radiative forcing by long-lived greenhouse gases: calculations with the AER radiative transfer models. *J. Geophys. Res.*, **113**. III.2.1, IV.2

Jiménez, P.A., Dudhia, J., Gonzalez-Rouco, J.F., Navarro, J., Montávez, J.P. & García-Bustamante, E. (2012). A revised scheme for the WRF surface layer formulation. *Mon. Weather. Rev.*, **140**, 898–918. III.2.1, IV.2, V.2

Katurji, M. & Zhong, S. (2012). The Influence of Topography and Ambient Stability on the Characteristics of Cold-Air Pools: A Numerical Investigation. *J. Appl. Meteorol. Climatol.*, **51**, 1740–1749. I.2.1.b

Kiefer, M.T. & Zhong, S. (2013). The effect of sidewall forest canopies on the formation of cold-air pools: A numerical study. *J. Geophys. Res. Atmos.*, **118(12)**, 5965–5978. I.2.3.d, I.4

King, J.A., Shair, F.H. & Reible, D.D. (1987). The influence of atmospheric stability on pollutant transport by slope winds. *Atmos. Environ.*, **21**, 53–59. V.1

Kitada, T. & Regmi, R.P. (2003). Dynamics of air pollution transport in late wintertime over Kathmandu valley, Nepal: as revealed with numerical simulation. *J. Appl. Meteorol.*, **42**, 1770–1798. V.3.2

Klemp, J.B., Dudhia, J. & Hassiotis, A.D. (2008). An upper gravity-wave absorbing layer for NWP applications. *Mon. Weather. Rev.*, **136**, 3987–4004. III.2.4, IV.2, V.2

Lacis, A.A. & Hansen, J.E. (1974). A parameterization for the absorption of solar radiation in the Earth's atmosphere. *J. Atmos. Sci.*, **31**, 118–133. III.2.1

Lareau, N.P. & Horel, J.D. (2014). Dynamically induced displacements of a persistent cold-air pool. *Boundary-Layer Meteorol.*, in press. V.1

Largeron, Y., Staquet, C. & Chemel, C. (2013). Characterization of oscillatory motions in the stable atmosphere of a deep valley. *Boundary-Layer Meteorol.*, **148**, 439–454. III.3.2.a, III.4, C

Lee, L.A., Carslaw, K.S., Pringle, K.J., Mann, G.W. & Spracklen, D.V. (2011). Emulation of a complex global aerosol model to quantify sensitivity to uncertain parameters. *Atmos. Chem. Phys.*, **11**, 12253–12273. I.4

Lee, S.M., Fernando, H.J.S., Princevac, M., Zajic, D., Sinesi, M., McCulley, J.L. & Anderson, J. (2003). Transport and diffusion of ozone in the nocturnal and morning planetary boundary layer of the Phoenix valley. *Environ. Fluid Mech.*, **3**, 331–362. V.1

Lehner, M. & Gohm, A. (2010). Idealised simulations of daytime pollution transport in a steep valley and its vensitivity to thermal stratification and surface albedo. *Boundary-Layer Meteorol.*, **134**, 327–351. V.1

Lehner, M., Whiteman, D. & Hoch, S.W. (2011). Diurnal cycle of thermally driven cross-basin winds in Arizona's meteor crater. *J. Appl. Meteorol. Climatol.*, **50**, 729–744. III.3.1.b

Lemmelä, R., Sucksdorff, Y. & Gilman, K. (1981). Annual Variation Of Temperature At Depths 20 To 700 cm In An Experimental Field In Hyrylä, South-Finland During 1969 To 1973. *Geophysica*, **17**, 143–154. III.2.4

Lott, F. & Miller, M.J. (1997). A new subgrid-scale orographic drag parameterization: its formulation and testing. *Q. J. R. Meteorol. Soc.*, **123**, 101–127. I.1

Lundquist, K.A. (2010). *Immersed boundary methods for high-resolution simulation of atmospheric boundary-layer flow over complex terrain*. Ph.D. thesis, University of California, Berkeley, CA, USA, 159 pp. III.1

Lundquist, K.A., Chow, F.K. & Lundquist, J.K. (2012). An Immersed Boundary Method Enabling Large-Eddy Simulations of Flow over Complex Terrain in the WRF Model. *Mon. Weather. Rev.*, **140**, 3936–3955. II.1, III.5

Mahrer, Y. (1984). An improved numerical approximation of the horizontal gradients in a terrain-following coordinate system. *Mon. Weather. Rev.*, **112**, 918–922. III.2.3, V.2

Mahrt, L. (1982). Momentum balance of gravity flows. *J. Atmos. Sci.*, **39**, 2701–2711. IV.3.3.c, IV.6, E

Mahrt, L. (2014). Stably Stratified Atmospheric Boundary Layers. *Ann. Rev. Fluid Mech.*, 23–45. IV.3.2

Mahrt, L., Vickers, D., Nakamura, R., Soler, M.R., Sun, J.L., Burns, S. & Lenschow, D.H. (2001). Shallow drainage flows. *Boundary-Layer Meteorol.*, **101**, 243–260. III.5, IV.3.3.a

Mahrt, L., Richardson, S., Seaman, N. & Stauffer, D. (2010). Non-stationary drainage flows and motions in the cold pool. *Tellus*, **62A**, 698–705. V.3.2, V.4, VI

Malek, E., Davis, T., Martin, R.S. & J., S.P. (2006). Meteorological and environmental aspects of one of the worst national air pollution episodes (January, 2004) in Logan, Cache Valley, Utah, USA. *Atmos. Research*, **79**, 108–122. I.1, I.2, I.1, I.2.1.a, V.1, E

Manins, P.C. & Sawford, B.L. (1979). A model of katabatic winds. *J. Atmos. Sci.*, **36**, 619–630. I.3, V.3.1, VI

Mansell, E.R., Ziegler, C.L. & Bruning, E.C. (2010). Simulated electrification of a small thunderstorm with two-moment bulk microphysics. *J. Atmos. Sci.*, **67**, 171–194. III.2.1, IV.2

Martilli, A., Clappier, A. & Rotach, M.W. (2002). An urban surface exchange parameterization for mesoscale models. *Boundary-Layer Meteorol.*, **104**, 261–304. III.5

Martínez, D. & Cuxart, J. (2009). Assessment of the hydraulic slope flow approach using a mesoscale model. *Acta Geophys.*, **57**, 882–903. V.1

Martínez, D., Cuxart, J. & Cunillera, J. (2008). Conditioned climatology for stably stratified nights in the Lleida area. *Journal of Weather & Climate of the Western Mediterranean*, **5**, 13–24. I.2.2

Martínez, D., Jiminénez, M.A., Cuxart, J. & Mahrt, L. (2010). Heterogeneous Nocturnal Cooling in a Large Basin Under Very Stable Conditions. *Boundary-Layer Meteorol.*, **137**, 97–113. I.1, I.2.1.a, V.1

Maybeck, M., Green, P. & Vorosmarty, C. (2001). A new typology for mountains and other relief classes: An application to global continental water resources and population distribution. *Mountain Research and Development*, **21**, 34–45. I.1, IV.1

Mayer, B. (2009). Radiative transfer in the cloudy atmosphere. *Eur. Phys. J. Conf.*, **1**, 75–99. III.1

Mayer, B. & Kylling, A. (2005). The libRadtran software package for radiative transfer calculations: Description and examples of use. *Atmos. Chem. Phys.*, **5**, 1855–1877. III.1

McKee, T.B. & O'Neal, R.D. (1988). The role of valley geometry and energy budget in the formation of nocturnal valley winds. *J. Appl. Meteorol.*, **28**, 445–456. I.1, I.2.1.b, I.4, V.2

McNider, R.T. (1982a). A note on velocity fluctuations in drainage flows. *J. Atmos. Sci.*, **39**, 1658–1660. (document), I.2.3.a, I.3, I.3.1, I.6, I.3.1, I.3.2, IV.5, V.3.1, VI, E, E

McNider, R.T. (1982b). A note on velocity fluctuations in drainage flows. *J. Atmos. Sci.*, **39**, 1658–1660. I.2.1.b, IV.3.3.c

Moeng, C.H. & Wyngaard, J.C. (1988). Spectral analysis of large-eddy simulations of the convective boundary layer. *J. Atmos. Sci.*, **45**, 3575–3587. III.5

Moeng, C.H., Dudhia, J., Klemp, J. & Sullivan, P. (2007). Examining two-way grid nesting for large eddy simulation of the PBL using the WRF model. *Mon. Weather. Rev.*, **135**, 2295–2311. III.2.1, III.5, IV.2, V.2

Nachabe, M.H. (1998). Refining the definition of field capacity in the literature. *J. Irrigat. Drain. Eng.*, **124**, 230–232. III.2.4, IV.2

Nadeau, D.F., Pardyjak, E.R., W., H.C., Huwald, H. & Parlange, M.B. (2012). Flow during the evening transition over steep Alpine slopes. *Q. J. R. Meteorol. Soc.*, **124**. I.1, I.2.1.a, I.2.3.b, III.5, IV.3.3.a

Nappo, C.J., Rao, K.S. & Herwehe, J.A. (1989). Pollutant transport and diffusion in katabatic flows. *J. Appl. Meteorol.*, **28**, 617–625. V.3.1

Neff, W.D. & King, C.W. (1989). The Accumulation and Pooling of Drainage Flows in a Large Basin. *J. Appl. Meteorol.*, **28**, 518–529. I, I.1, I.2.1.a, I.2.1.b, I.2.3.a, I.2.3.e, IV.3.3.a, IV.3.4, IV.4, VI

Noppel, H. & Fiedler, F. (2002). Mesoscale heat transport over complex terrain by slope winds – a conceptual model and numerical simulations. *Boundary-Layer Meteorol.*, **104**, 73–97. I.1, I.1, I.3.1, III.1, IV.1

Oke, T.R. (1987a). *Boundary Layer Climates*. 2nd Edition, Routledge, London, UK. I.2.3.c, I.2.3.c, I.2.3.d

Oke, T.R. (1987b). *Boundary Layer Climates*. Routledge, London, UK, London, UK, 464 pp. III.2.4, III.2.4, IV.2

Pope, C.A.I., Burnett, R.T., Thun, M.J., Calle, E.E., D., K., Ito, K. & Thurston, G.D. (2002). Lung cancer, cardiopulmonary mortality, and long-term exposure to fine particulate air pollution. *Journal of the American Medical Association*, **287(9)**, 1132–1141. I.1

Prandtl, L. (1942). *Fuhrer durch die Stromungslehre*. Vieweg und Sohn, Braunschweig, Germany. I.3, I.3.2, I.7, I.3.2, IV.5, VI, E, E.1, E, E

Price, J.D., Vosper, S., Brown, A., Ross, A., Clark, P., Davies, F., Horlacher, V., Claxton, B., McGregor, J.R., Hoare, J.S., Jemmett-Smith, B. & Sheridan, P. (2011). COLPEX: field and numerical studies over a region of small hills. *B. Am. Meteorol. Soc.*, **92**, 1636–1650. I, I.1, I.1, I.1, I.2.1.a, I.2.3.e, I.4, III.1, IV.1

Princevac, M., Hunt, J.C.R. & Fernando, H.J.S. (2008). Quasi-steady katabatic winds on slopes in wide valleys: hydaulic theory and observations. *J. Atmos. Sci.*, **65**, 627–643. I.1, I.2.1.a

Raga, G.B., Baumgardner, D., Kok, G. & Rosas, I. (1999). Some aspect of boundary layer evolution in Mexico City. *Atmos. Environ.*, **33**, 5013–5021. V.1

Renfrew, I.A. & Anderson, P.S. (2002). The surface climatology of an ordinary katabatic wind regime in Coats Land, Antarctica. *Tellus*, **54A**, 463–484. I.1, I.2.1.a, I.2.1.b

Riabouchinsky, D. (1911). Méthode des variables de dimensions zéro et son application en aérodynamique. *L'Aérophile*, 407–408. I.4

Ross, A.N. & Baker, T. (2013). Flow Over Partially Forested Ridges. *Boundary-Layer Meteorol.*, **146(3)**, 375–392. I.2.3.d, III.5

Roth, M. (2000). Review of atmospheric turbulence over cities. *Q. J. R. Meteorol. Soc.*, **126**, 941–990. I.2.3.d

Rowell, D.L. (1994). *Soil Science: Methods & Applications*. Prentice Hall, Upper Saddle River, NJ, USA. III.2.4

Sakiyama, S. (1990). Drainage Flow Characteristics and Inversion Breakup in Twp Alberta Mountain Valleys. *J. Appl. Meteorol.*, **29**, 1015–1030. I.1, I.2.1.a, I.2.1.b, I.2.3.e

Schnitzhofer, R., Norman, M., Wisthaler, A., Vergeiner, J., Harnisch, F., Gohm, A., Obleitner, F., Fix, A., Neininger, B. & Hansel, A. (2009). A multimethodological approach to study the spatial distribution of air pollution in an alpine valley during wintertime. *Atmos. Chem. Phys.*, **9**, 3385–3396. V.1, V.3.2, V.4, VI

Scotti, A., Meneveau, C. & Lilly, D.K. (1993). Generalized Smagorinsky model for anisotropic grids. *Phys. Fluids*, **5**, 2306–2308. III.2.1, IV.2, V.2

Seemann, S.W., Li, J., Menzel, W.P. & Gumley, L.E. (2003). Operational Retrieval of Atmospheric Temperature, Moisture, and Ozone from MODIS Infrared Radiances. *J. Appl. Meteorol.*, **42**, 1072–1091. I.1, I.2.3.c

Sheridan, P.F., Vosper, S.B. & Brown, A.R. (2013). Characteristics of cold pools observed in narrow valleys and dependence on external conditions. *Q. J. Roy. Meteorol. Soc.*, in press. III.1

Shu, C.W. (2003). High-order finite difference and finite volume WENO schemes and discontinuous Galerkin methods for CFD. *Int. J. Comput. Fluid Dyn.*, **17**, 107–118. III.2.1, IV.2

Silcox, G.D., Kelly, K.E., Crosman, E.T., Whiteman, C.D. & Allen, B.L. (2012). Wintertime $PM_{2.5}$ concentrations during persistent, multi-day cold-air pools in a mountain valley. *Atmos. Environ.*, **46**, 17–24. I.1, III.5, V.1

Skamarock, W.C. (2004). Evaluating mesoscale NWP models using kinetic energy spectra. *Mon. Weather. Rev.*, **132**, 3019–3032. A

Skamarock, W.C. & Klemp, J. (2008). A time-split nonhydrostatic atmospheric model for weather research and forecasting applications. *J. Comp. Phys.*, **227**, 3465–3485. A

Skamarock, W.C., Klemp, J.B., Dudhia, J., Gill, D.O., Barker, D.M., Duda, M.G., Huang, X.Y., Wang, W. & Powers, J.G. (2008). A Description of the Advanced Research WRF Version 3. NCAR Technical Note NCAR/TN-475+STR, NCAR, Boulder, CO, USA, 125 pp. II.2, II.2.2, III.2, III.2.1, IV.2, IV.3.3.a, V.2

Skyllingstad, E.D. (2003). Large eddy simulation of katabatic flows. *Boundary-Layer Meteorol.*, **106**, 217–243. II.1, III.1

Smith, C.M. & Skyllingstad, E.D. (2005). Numerical simulation of katabatic flow with changing slope angle. *Mon. Weather. Rev.*, **133**, 3065–3080. III.1

Smith, S.A., Brown, A.R., Vosper, S.B., Murkin, P.A. & Veal, A.T. (2010). Observations and simulations of cold air pooling in valleys. *Boundary-Layer Meteorol.*, **134**, 85–108. III.1

Stephens, G.L. (1978). Radiation profiles in extended water clouds. Part II: Parameterization schemes. *J. Atmos. Sci.*, **35**, 2123–2132. III.2.1

Stiperski, I., Kavcic, I., Grisogono, B. & Durran, D.R. (2007). Including coriolis effects in the Prandtl model for katabatic flow. *Q. J. R. Meteorol. Soc.*, **133**, 101–106. I.3.2

Stull, R. (1988). An Introduction to Boundary Layer Meteorology. vol. 13 of *Atmospheric and Oceanographic Sciences Library*, Kluwer Academic Publishers, Dordrecht, The Netherlands, 666 pp. I.2.3.a

Szintai, B., Kaufmann, P. & Rotach, M.W. (2010). Simulation of pollutant transport in complex terrain with a numerical weather prediction–particle dispersion model combination. *Boundary-Layer Meteorol.*, **137**, 373–396. I.1, I.1, III.1, IV.1

Takemi, T. & Rotunno, R. (2003). The effects of subgrid model mixing and numerical filtering in simulations of mesoscale cloud systems. *Mon. Weather. Rev.*, **131**, 2085–2101. III.5

Thompson, B.W. (1986). Small-scale katabatics and cold hollows. *Weather*, **41**, 146–153. I.1, I.2.1.a, III.1

Tsonis, A.A. (2007). *An Introduction to Atmospheric Thermodynamics*. Cambridge University Press. I.2.3.c, I.2.3.c

UoW (2014). Upper Air Data. Published online at http://weather.uwyo.edu/upperair/, data provided by the University of Wyoming (UoW), College of Engineering, Department of Atmospheric Sciences. I.3, E

Vaschy, A. (1892). Sur les lois de similitude en physique. *Annales Télégraphiques*, **19**, 25–28. I.4

Vergeiner, I. & Dreiseitl, E. (1987). Valley winds and slope winds – Observations and elementary thoughts. *Meteorol. Atmos. Phys.*, **36**, 264–286. IV.3.3.a, V.3.1

Versteeg, H.K. & Malalasekera, W. (2007). *An Introduction to Computational Fluid Dynamics*. Pearson Education Ltd. II.1

Vinokur, M. (1980). On One-Dimensional Stretching Functions for Finite-Difference Calculations. NASA Contractor Report 3313, NASA, Washington, DC, USA, 56 pp. III.2.3, IV.2

Vosper, S.B. & Brown, A.R. (2008). Numerical Simulations of Sheltering in Valleys: The Formation of Nighttime Cold-Air Pools. *Boundary-Layer Meteorol.*, **127**, 429–448. I.2.3.e, I.4, III.1, V.1

Vosper, S.B., Hughes, J.K., Lock, A.P., Sheridan, P.F., Ross, A.N., Jemmett-Smith, B. & Brown, A.R. (2013). Cold-pool formation in a narrow valley. *Q. J. Roy. Meteorol. Soc.*, in press. III.1

Vosper, S.B., Hughes, J.K., Lock, A.P., Sheridan, P.F., Ross, A.N., Jemmett-Smith, B. & Brown, A.R. (2014). Cold-pool formation in a narrow valley. *Q. J. R. Meteorol. Soc.*, **140**, 699–714. V.1

Weigel, A.P., Chow, F.K. & Rotach, M.W. (2007). The effect of mountainous topography on moisture exchange between the 'surface' and the free atmosphere. *Boundary-Layer Meteorol.*, **125**, 227–244. I.1

Whiteman, C.D. (2000). *Mountain Meteorology: fundamentals and applications*. Oxford University Press, New York, NY, USA. I, I, III.1, III.2.4, IV.1, V.1

Whiteman, C.D. & Zhong, S. (2008). Downslope flows on a low-angle slope and their interactions with valley inversions. Part I: observations. *J. Appl. Meteorol. Climatol.*, **47**, 2023–2038. I, I.1, I.2.1.a, I.2.1.b, I.2.3.a, I.2.3.c, I.2.3.e, V.2, A

Whiteman, C.D., Zhong, S. & Bian, X. (1997). Wintertime Boundary Layer Structure in the Grand Canyon. *J. Appl. Meteorol.*, **38**, 1084–1102. I.1, I.2.1.a, I.2.3.a, I.2.3.e, V.2

Whiteman, C.D., Bian, X. & Zhong, S. (1998). Wintertime Evolution of the Temperature Inversion in the Colorado Plateau Basin. *J. Appl. Meteorol.*, **38**, 1103–1117. I.1, I.2.1.a, I.2.3.e, III.5

Whiteman, C.D., De Wekker, S.F.J. & Haiden, T. (2007). Effect of dewfall and frostfall on nighttime cooling in a small, closed basin. *J. Appl. Meteorol. Climatol.*, **46**, 3–13. I.1, I.2.3.c, V.2

Whiteman, C.D., Hoch, S.W., Lehner, M. & Haiden, T. (2010). Nocturnal Cold-Air Intrusions into a Closed Basin: Observational Evidence and Conceptual Model. *J. Appl. Meteorol. Climatol.*, **49**, 1894–1905. I.1, I.4, V.1

Wood, C.R., Lacser, A., Barlow, J.F., Padhra, A., Belcher, S.E., Nemitz, E., Helfter, C., Famulari, D. & Grimmond, C.S.B. (2010). Turbulent Flow at 190 m Height Above London During 2006-2008: A Climatology and the Applicability of Similarity Theory. *Boundary-Layer Meteorol.*, **137**, 77–96. I.1, I.2.3.d

World Health Organisation (2013). Health Effects of Particulate Matter: Policy implications for countries in eastern Europe, Caucasus and central Asia. Published online, ISBN 9789289000017. I.1

Zardi, D. & Whiteman, C.D. (2013). Diurnal Mountain Wind Systems. In F.F. Chow, S.F.J. De Wekker & B.J. Snyder, eds., *Mountain Weather Research and Forecasting: Recent Progress and Current Challenges*, Springer Atmospheric Sciences, chap. 2, Springer, New York, NY, USA. I, I.1, I.2, I.2.1.b, I.2.2, I.2.3.a, I.5, II.1, III.1, III.2.1, IV.1, V.1

Zhong, S. & Chow, F.F. (2013). Meso- and Fine-Scale Modeling over Complex Terrain: Parameterizations and Applications. In F.F. Chow, S.F.J. De Wekker & B.J. Snyder, eds., *Mountain Weather Research and Forecasting: Recent Progress and Current Challenges*, Springer Atmospheric Sciences, chap. 10, Springer, New York, NY, USA. III.5